The Water Enhanced Turbofan Engine

A preliminary study on the thermodynamic assessment and parametric analysis of the WET cycle performance

Martijn van Roij

Technische Universiteit Delft

TU Delft Delft University of Technology

Challenge the future

The Water Enhanced Turbofan Engine

A preliminary study on the thermodynamic assessment and parametric analysis of the WET cycle performance

by

Martijn van Roij

in partial fulfillment of the requirements for the degree of

Master of Science
in Aerospace Engineering

at the Delft University of Technology,
to be defended publicly on Tuesday 27th of May, 2025 at 14:00 in AE Lecture Room G.

Supervisors:	Dr. ir. Carlo De Servi,	TU Delft
	Dr. ir. Dabo Krempus,	TU Delft
Thesis committee:	Prof. dr. ir. Piero Colonna,	TU Delft
	Dr. ir. Carlo De Servi,	TU Delft
	Dr. ir. Feijia Yin,	TU Delft

Delft University of Technology

Preface

This thesis marks the end of my master's degree in Aerospace Engineering at TU Delft. Over the past three and a half years, I have explored many fascinating topics related to aviation, propulsion, and sustainability. Beyond academics, my time at TU Delft has shaped me both personally and professionally. The past 15 months have been marked by both challenges and growth. While not always easy, this period has profoundly influenced my perspective and will continue to shape the way I think and navigate life in the years to come. I am incredibly grateful for the opportunity to pursue my passion and study what has always fascinated me most: aircraft. Since high school, I have been interested in aviation and sustainability, making Aerospace Engineering at TU Delft a natural choice. Adjusting to the fast-paced environment was challenging at first, but I embraced every moment and continue to do so to this day. I wholeheartedly encourage any student to follow their curiosity and passion, as studying should ultimately be a source of energy and inspiration.

This work would not have been possible without the support, guidance, and encouragement of many people. Firstly, I would like to thank Carlo for his great guidance during my thesis and the modeling project before. I really appreciated the bi-weekly meetings, the fruitful discussions, and the valuable feedback. You always kept me positive and on the right track. Moreover, I would like to thank Dabo for his support and patience during the first part of my thesis, which was mainly dedicated to getting acquainted with pyCycle. Also, special thanks to Fabio, who helped me with the usage of Hexacode. Lastly, I extend my sincere gratitude to the members of my thesis committee for their time, expertise, and thoughtful feedback. Their willingness to be present and assess my work is greatly appreciated.

Finally, I would like to thank all my family, friends, and colleagues from Maasbree, Delft, Dresden, and beyond. I share many memories with you and I will cherish them throughout life. Additionally, I would like to thank the former ITM-Linde Electrolysis team for providing me with a wonderful internship experience. Special thanks also goes to Marcel Vogelsangs from MV Energietechniek for all the shared hydrogen projects, discussions, and memories. My interest and passion in hydrogen has grown significantly because of you. Last but certainly not least, I want to express my deepest gratitude to my parents, sister, and Steve. Your unwavering support has meant everything to me, helping me through difficult times and celebrating every success along the way. You mean the world to me, and I will always be grateful for your love and support!

Martijn van Roij
Delft, May 2025

Abstract

To reduce aviation's climate impact, the industry must significantly reduce greenhouse gas emissions, necessitating the development of more sustainable and efficient propulsion technologies. The Water-Enhanced Turbofan (WET) engine is such a promising future aero-engine concept. The engine integrates a Joule-Brayton cycle with a semi-closed Rankine steam cycle. Superheated steam is injected before the combustion chamber and downstream before the core nozzle. While previous studies have explored the fundamental thermodynamics of the concept and assessed its potential for reducing climate impact, this study explores the design space of the WET engine and examines key design parameters and their influence on cycle performance using NASA's pyCycle and OpenMDAO framework. Moreover, the high-fidelity in-house software Hexacode is used to model the heat recovery steam generator (HRSG). Based on the design exploration, a water-to-air ratio (WAR) of 0.20 is found optimal for the WET cycle, reducing the thrust-specific fuel consumption (TSFC) by 7.3% with respect to a LEAP-1A-type engine. The best design solution comes with a significantly higher bypass ratio, and lower overall pressure ratio and turbine inlet temperature. Nozzle velocity ratios higher than 1 have been demonstrated to enhance the overall engine efficiency. Besides this, the condenser is identified as the main critical component of the proposed engine concept, while the HRSG design becomes challenging at high water-to-air ratios. Fuel burn can be further reduced by increasing the OPR and steam injection temperature. Future work should focus on detailed condenser modeling and the integration of the thermodynamic cycle model with preliminary heat exchanger (HEX) design models to improve system-level performance predictions.

Contents

Nomenclature

Abbreviations

Symbol	Description
AEROHEX	Advanced Exhaust Gas Recuperator Technology for Aero-Engine Applications
AFR	Air-to-fuel ratio
APU	Auxiliary power unit
BPR	Bypass ratio
CEA	Chemical Equilibrium with Applications
CCE	Combined Cycle Engine
CCR	Heat Capacity Rate Ratio
CLEAN	Component Validator for Environmentally Friendly Aero-Engine
CORN	COnical Recuperative Nozzle
ECS	Environmental control system
EI	Emission index
FAR	Fuel-to-air ratio
FPR	Fan pressure ratio
FPT	Free power turbine
GHG	Greenhouse gas
HEX	Heat exchanger
HBTF	High bypass turbofan
HOF	Enthalpy of formation
HPC	High pressure compressor
HPT	High pressure turbine
HRSG	Heat recovery steam generator
HySIITE	Hydrogen Steam Injected Intercooled Turbine Engine
IAWPS	International Association for the Properties of Water and Steam
ICR	Intercooled recuperated
IRAE	Intercooled-recuperated aero engine
LEMCOTEC	Low Emissions Core-Engine Technologies
LH2	Liquid hydrogen
LHV/HHV	Lower / Higher heating value
LMTD	Log-mean temperature difference
LPC	Low pressure compressor
LPT	Low pressure turbine
MDAO	Multidisciplinary Design Analysis and Optimization
MPD	Multiple-Point Design
NEWAC	NEW Aero engine Core concepts
NPSS	Numerical Propulsion System Simulation (NPSS)
NTU	Number of transfer units
OPR	Overall pressure ratio
ORC	Organic Rankine cycle
PM	Particulate matter
PR	Pressure ratio
RF	Radiative forcing
RH	Relative humidity

Symbol	Description
SAC	Schmidt-Appleman criterion
SAF	Sustainable aviation fuel
SIRA	Steam injecting and recovering aero engine
SFC	Specific fuel consumption
SSL	Standard Sea Level conditions
SPD	Single point design
STARTREC	STraight AnnulaR Thermal RECuperator
TEG	Thermoelectric generator
TIT	Turbine inlet temperature
TSFC	Thrust-specific fuel consumption
UHC	Unburned hydrocarbons
VOC	Volatile organic compound
VR	Velocity ratio
WA model	Wet air model
WAR	Water-to-air ratio
WET/WETF	Water enhanced turbofan
WETS	Water enhanced turboshaft
WHR	Waste heat recovery
XDSM	Extended Design Structure Matrix

Indices

Symbol	Description
a	ambient
byp	bypass
comb	combustor
cond	condenser
exh	exhaust
f	fuel
g	gas
id	ideal
in	inlet
inj	injection
is	isentropic
liq	liquid
max	maximum
n	net
out	outlet
nozz	nozzle
poly	polytropic
prods	reaction products
prop	propulsive
r	reaction
reacts	reactants
rec	recovered
s	static
sat	saturated
stoich	stoichiometric
t	total
th	thermal
tot	total
vap	vapor

Roman Symbols

Symbol	Description	Unit
A	Area	$[m^2]$
C_p	Isobaric specific heat	$[J/kg/K]$
C_v	Isochoric specific heat	$[J/kg/K]$
F	Force	$[N]$
g	Gibbs free energy	$[J/mole]$
G	Schmidt-Appleman mixing slope	$[Pa/K]$
H	Enthalpy	$[J]$
I	Impulse function	$[N]$
h	Specfic enthalpy	$[J/kg]$
k/z	Mass fraction	$[-]$
$\dot{m}$	Mass flow rate	$[kg/s]$
M	Molar mass	$[kg/mole]$
m	Mass	$[kg]$
n	Molar concentration & (chemical amount)	$[mole/kg \ \& \ (mole)]$
N	Rotational speed	$[rpm]$
p	Pressure	$[Pa]$
$\dot{Q}$	Heat flow	$[J/s]$
R	Molecular specific gas constant	$[J/mol/K]$
S	Entropy	$[J/kg/K]$
SS	(Super)saturation parameter	$[-]$
T	Temperature	$[K]$
V	Velocity	$[m/s]$
$\dot{W}$	Work	$[J/s]$
W	Weight	$[N]$
x	Molar fraction	$[-]$

Greek Symbols

Symbol	Description	Unit
γ	Specific heat ratio	$[-]$
ϵ	Effectiveness	$[-]$
ζ	Recovery factor	$[-]$
η	Efficiency	$[-]$
λ	Hub-to-tip ratio	$[-]$
μ	Chemical potential	$[kg\ mol\ kg_{mix}^{-1}]$
ν	Stoichiometric coefficient	$[-]$
π	Lagrange multiplier	$[-]$
Π	Pressure ratio	$[-]$
ϕ	Equivalence ratio	$[-]$
ρ	Density	$[kg/m^3]$
τ	Torque	$[Nm]$

Constants

Symbol	Description	Value
g_c	Gravitational acceleration	9.80665 m/s
$\bar{R}_c$	Universal gas constant	8.31446 $J/mole/K$

Other symbols

Symbol	Description
$\mathfrak{R}$	Residual equation

Chemical species

Molecular formula	Name
Ar	Argon
H_2	Hydrogen
H_2O	Water
C	Carbon
CH_4	Methane
CO	Carbon monoxide
CO_2	Carbon dioxide
N_2	Nitrogen
NO_x	Nitrogen oxides
O_2	Oxygen
O_3	Ozone
SO_x	Sulfuric oxides
C_xH_y	Unburned hydrocarbons (UHC)
$C_{12}H_{26}$	Dodecane

List of Figures

List of Tables

1 Introduction

Aviation contributes to the 'anthropogenic' global warming by being responsible for around 2% of the global carbon dioxide (CO_2) emissions [1]. However, not only CO_2 should be taken into account for determining the radiative forcing. Other harmful aircraft-related emissions such as nitrogen oxides (NO_x) and water vapor interact with the atmosphere and subsequently have an impact on the climate. NO_x emissions at lower altitudes affect the local air quality and have an effect on both the methane (CH_4) and ozone (O_3) levels by undergoing complex chemical reactions at high altitudes, as shown in Subsection 2.3.4 [2]. Water vapor is present in the aero engine exhaust as product of the kerosene combustion and can cause contrail (cirrus) formation under given circumstances [3]. All of the three above-mentioned emission types have an effect on the radiative balance of the earth and can therefore cause global warming [4]. To meet the climate goals of 2050, the emissions caused by air transportation should also be reduced drastically in the upcoming decades. New aircraft technologies should be researched and eventually deployed to prevent emissions at various altitudes. Making the air transportation sector future-proof is not limited to only adapting the aircraft design. According to Afonso et al. [5], sustainable aviation can be categorized by considering six disciplines: aerodynamics, operations, materials & manufacturing, structures, energy, and propulsion. A novel aircraft concept that is currently being developed and tested by TU Delft is the Flying-V aircraft [6]. Although this promising concept contains sustainable elements from all disciplines determined by Afonso et al., the transition from current in-service aircraft to such a revolutionary new design may be too challenging as this entails the solution of several technological challenges. New technologies for conventional aircraft are thus needed to reduce the climate impact. Developments as such will further help enabling the transition towards novel aircraft concepts and a zero-emission future.

Regarding propulsion, one of such newest technologies that can be applied to conventional aircraft is the so-called Water Enhanced Turbofan (WET) concept proposed by MTU in 2021 [7, 8]. The WET engine is claimed to reach higher thermal efficiency and to allow for a significant reduction in emissions [9, 10, 11]. The WET engine process is similar to that of a conventional Brayton cycle up until the last turbine stage: the high-energy exhaust gas coming from the LPT is used to evaporate and superheat the liquid water in a bottoming water cycle. This superheated steam is to be injected directly in or just before the combustion chamber and this enhances the specific power of the engine and reduces NO_x emissions formation in the combustor. A condenser is to be integrated after the steam generator to condense the water from the exhaust stream needed at the steam injection point.

Despite the WET engine being seen as a promising new engine concept, some potential limitations have already been identified. Space restrictions, weight, system integration, and the water recovery potential are examples of possible bottlenecks of this WET concept [7]. Some of these limitations can be overcome by replacing kerosene with (liquid) hydrogen as energy source of the engine. Synergies may arise when combining fuel supply with the bottoming water cycle in the WET configuration as liquid hydrogen can be exploited as heat sink for the condensation of water. The effect of synergizing hydrogen combustion with thermodynamic cycle improvement for aero engines has been researched in the past, but mainly for engine configurations slightly different than the WET cycle [12, 13]. The engine configuration from the HySIITE project of Pratt & Whitney or the ENABLEH2 project is generally used as a reference for these analyses [14, 15]. The condenser in all these novel architectures is a vital component as it is needed for condensing the water from the exhaust gases as efficiently as possible. However, none of the aforementioned literature sources provide a detailed description regarding the methodology for modeling the condenser [7, 13, 16]. Two main activities should be considered to better understand the WET engine concept and the corresponding cycle architecture. First of all, the WET engine should be modeled to gain more insight into its thermodynamic efficiency and performance. Secondly, the effect of varying key engine features on the performance and heat exchanger characteristics should be assessed. The research objective can now be formulated:

Investigate the thermodynamic cycle efficiency and performance of the water-enhanced turbofan engine by modeling and simulating this concept in a state-of-the-art framework, namely pyCycle.

The corresponding main research question can be derived based on the above objective:

How does water injection and recovery affect the thermodynamic cycle efficiency and overall performance of a turbofan engine when compared to a conventional engine?

To answer the main research question, sub-questions are formulated to break down the main question into smaller, more manageable ones:

- *How can the WET engine thermodynamic cycle be modeled in pyCycle?*
- *What is the baseline performance and efficiency of a state-of-the-art turbofan engine considering on-design conditions?*
- *What is the engine performance and efficiency of the WET engine considering on-design conditions?*
- *Based on a sensitivity analysis, what are the most critical engine performance parameters for the WET engine?*

The thesis is structured as follows. To start, a literature review is provided in Chapter 2 regarding both heat recuperation in aero engines and the water-enhanced turbofan engine. Next, a summary covering the most important aspects of aero engine modeling and the selected modeling framework is outlined in Chapter 3. Chapter 4 discusses all the adjustments that have been made in pyCycle for modeling the WET engine architecture. The verification and validation process is extensively discussed in Chapter 5. Then, a reference turbofan engine cycle is established in Chapter 6 to create a benchmark for comparison. The actual WET engine results, sensitivity analysis, and comparison with the reference engine are presented in Chapter 7. Lastly, key conclusions and recommendations are given in Chapter 8.

2

State of the Art: Heat Recuperation in Aero Engines

This literature study explores the evolution and potential advancements in aero engine technologies aimed at reducing environmental impact and enhancing efficiency via heat recuperation methods. The chapter begins with a historical background in Section 2.1, tracing the development of aero engine heat recuperation and highlighting key technological milestones achieved thus far in the industry. It then delves into the potential of heat recuperation in modern aero engines, examining concepts such as the intercooled-recuperated aero engine (Subsection 2.2.1), combined cycle units (Subsection 2.2.2), and other innovative heat recovery solutions (Subsection 2.2.3). Finally in Section 2.3, the emerging concept of the water-enhanced turbofan engine, which offers promising benefits in terms of thermal efficiency and reduced environmental footprint is explained. Through a comprehensive review of these technologies, this chapter sets the foundation for understanding the current state of aero engine advancements and the challenges and opportunities they present for achieving future climate goals.

2.1. Historical Background

In gas turbine engines, energy recuperation, or waste heat recovery, has a longstanding history. The principle is centered on recuperating and converting the thermal energy produced by the gas turbine, which would, otherwise, be dissipated into the surrounding environment. While recuperation systems are currently extensively utilized in stationary gas turbine engines, their implementation within the aviation sector remains a challenge yet to be overcome. However, this does not imply that there have been no endeavors to design, produce, and operate recuperative aero engines. The 'Bristol Theseus' turboprop engine, produced in 1945, represents the first real effort to operate a recuperated aerospace engine [17]. After the revolutionary design of the Bristol Aeroplane Company, several other attempts were made to develop a recuperative engine. The implementation of a bottoming unit was mainly investigated for turboprop or turboshaft engines because of their higher maturity and proven reliability at that time with respect to turbofan engines. Although recuperative engines, such as the Allison T56, T78, T63 and Lycoming T53, have been tested thoroughly, none of them have actually flown [17, 18]. This changed in 1967 when a helicopter with the Allison T63 recuperative turboshaft engine made its first flight with a lower fuel consumption and increase in range [18, 19] as a result. Unfortunately, no other flight has taken place since this milestone despite the numerous successful tests later in the twentieth century.

Not only turboprop-, turboshaft, and turbojet engines have been researched to fit recuperative devices, but also the propfan and turbofan engines. Given that turbofan engines are the most commonly used in commercial aviation and are likely to remain so for the next decades, several promising recuperative concepts have been proposed and developed [20]. Some of the most promising concepts for future recuperative turbofan engines are discussed in Section 2.2.

In recent decades, the primary objectives in aero engine development have been improving performance and reducing costs. However, the climate targets set for 2030 and 2050 have shifted the focus towards sustainability in future aero engine designs. Emission reduction is now a crucial metric in engine design, and waste heat recovery is expected to be increasingly implemented in upcoming engines. Compared to the past, modern engines are larger, heat exchangers have become more compact, and advanced materials capable of withstanding high temperatures are now available [21, 22]. These advancements make the integration of heat exchangers in future aero engines more feasible, contributing to both reduced environmental impact and improved performance.

2.2. Heat Recuperation Possibilities in Turbofan Engines

In the twenty-first century, modern aircraft already widely embraced the turbofan engine. This engine type was expected to be integrated into future aircraft as well. Further improvement and optimization of the engine is needed to enhance the performance, hence reducing fuel consumption. Nevertheless, as the bypass ratio (BPR) continues to increase, along with the potential for higher overall pressure ratios (OPRs) and turbine inlet temperatures (TITs), advancements in modern combustion techniques, and highly efficient turbomachinery, the limitations in cycle efficiency are expected to be reached eventually. Besides this, the effect of air transportation on the climate got more global attention, and this led to emission restrictions for next-generation aircraft. This opened the door again to newer engine cycle architectures, including the potential for heat recovery. Pasini et al. were one of the pioneers in the quantitative evaluation of heat recovery potential in aero engines [23]. A preliminary cycle performance study was conducted for turboshaft, turboprop, and turbofan engines, incorporating a heat exchanger positioned after the last turbine stages. The study revealed that waste heat can enhance engine performance; however, the installation location and design of the heat exchangers require more detailed consideration. To date, multiple novel engine designs have been suggested to address the limitations imposed by traditional methods, namely the open-rotor concept, interstage turbine burner (ITB), the geared turbofan (GTF), the intercooled-recuperated aero engine (IRAE), the combined cycle engine (CCE) and the water enhanced turbofan (WET) engine. Since heat recuperation is a central focus of this thesis, only the last three architectures will be considered. [20, 24, 25, 26].

2.2.1. The Intercooled-Recuperated Aero Engine (IRAE)

An advanced cycle concept for high by-pass geared turbofan engines was proposed in 2005 by MTU Aero Engines, namely the intercooled-recuperated aero engine (IRAE) [24, 25]. The new engine architecture promises to improve thermal efficiency and to cut emissions significantly by recovering part of the exhaust thermal energy and use it upstream in the cycle. A schematic representation of this advanced concept is depicted in Figure 2.1.

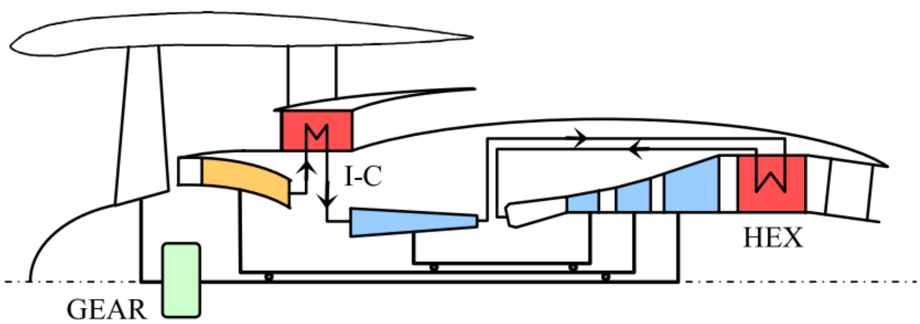

Figure 2.1: A schematic representation of the advanced intercooled-recuperated aero engine.

Although this engine still operates as an open Brayton cycle, it exhibits numerous differences from the conventional open Brayton cycle. Two heat exchangers (HEX) are needed for this concept: an intercooler (IC in Figure 2.1) and a recuperator (HEX in Figure 2.1). The intercooler is located between the low-pressure compressor (LPC) and high-pressure compressor (HPC), and its purpose is to cool the airflow with air from the bypass duct. This reduces the amount of HPC work necessary to reach a specific pressure ratio. When using the intercooler alone, the HPC exit temperature is lower, and

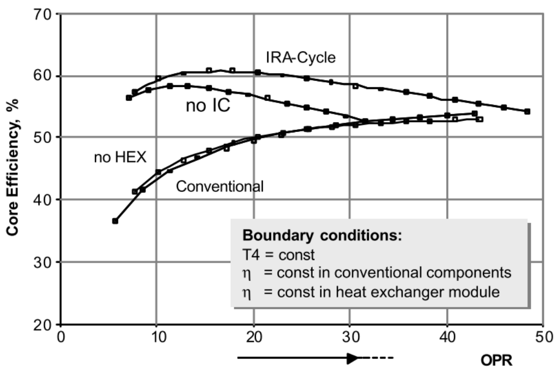

Figure 2.2: Thermal core efficiency of the conventional vs. alternative engine concepts [24].

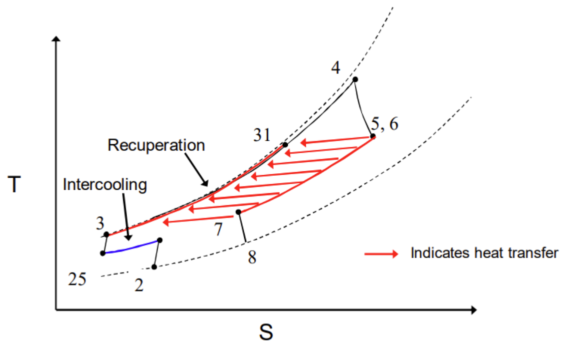

Figure 2.3: *T,s*-Diagram of the intercooled-recuperated aero engine concept [27].

more thermal energy, i.e., fuel, should be added to the combustion chamber for a fixed TIT. Thermal efficiency is, therefore, not improved when installing only the intercooler. Another disadvantage of the intercooler is the pressure drop on both streams, increasing the work amount of the HPC and lowering the thrust in the bypass duct. Nonetheless, the bypass air exit temperature is slightly higher, partially compensating for the pressure drops in the intercooler. To enhance the beneficial effects of the intercooler, a recuperator is installed downstream of the last turbine stage. Rather than releasing high-energy exhaust gases into the atmosphere, a major loss factor in modern aero engines, a portion of the exhaust energy can be supplied to the combustion air before it enters the combustor, then lowering fuel consumption. Thus, combining the intercooler and recuperator leads to a marked increase in thermal efficiency and cycle performance. This is shown in Figure 2.2 [24].

The effect of the intercooler and the recuperator on the IRA engine cycle is shown in the *T,s*-diagram in Figure 2.3 [27]. The intercooling process reduces the air temperature as indicated by station 25, after which the HPC compresses the air thus reaching station 3. Because of the recuperator, the inlet temperature of the combustor has risen from station 3 to station 31. Given a constant TIT, the exit temperature of the exhaust gas decreases significantly from station 5 to station 7. Not only is the thermal efficiency higher compared to a conventional Brayton cycle but emissions are also lowered with this architecture [28]. However, some critical notes should be made regarding the use of heat recuperators in modern high-BPR turbofan engines:

- The temperature difference between the turbine exit exhaust gases and the HPC discharge air should be large enough for all operating points as the recuperator becomes too large for small differences. Ensuring a sufficiently high turbine exit temperature is directly dependent on the TIT. During take-off, high TIT can be achieved, whereas this appears to be much more difficult during cruise conditions. A possible solution to maintain the TIT as constant as possible could be the integration of variable turbine inlet geometry [25, 28].

- As energy is extracted from the exhaust gases, less energy can be converted to engine thrust. This is not a major drawback as the core stream in an IRA engine generates only a small part of the thrust.

- The HPC discharge air is at a much higher pressure than the LPT exit air, indicating that the HEX should be sealed thoroughly to avoid leakages, which may cause matrix fuel fires.

- Additional manifolds, tubes, and other components are needed to implement the IRA concept in addition to the intercooler and recuperator. The performance enhancement due to the recuperation and intercooling should be more than the performance decrease due to the additional parasitic weight and volume required to install these components.

Following Boggia's initial analysis of the IRA engine [25], several efforts have been made to refine and enhance the concept, particularly focusing on the design of the recuperator and intercooler. Schoenenborn et al. from MTU provided extensive results regarding a first approach on the thermomechanical

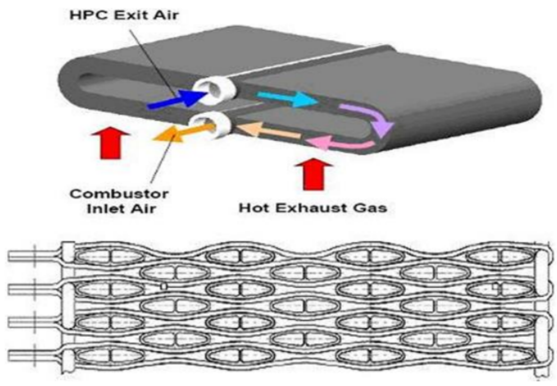

Figure 2.4: Geometry of the MTU recuperator for the IRA engine [25].

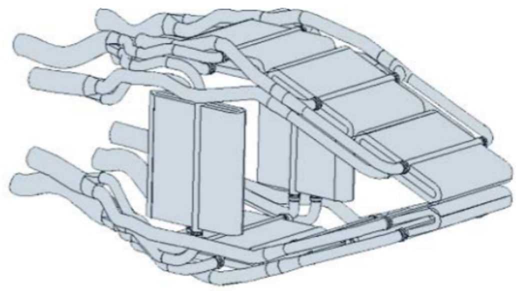

Figure 2.5: Recuperator system with piping to be integrated in the exhaust nozzle of a modern turbofan engine [25].

design of the recuperator and its integration in aero engines [29]. In addition, studies regarding minimization of HEX pressure drop, optimization of recuperator location in the nozzle and optimal HEX configuration have been conducted [22, 30, 31, 32, 33]. The recuperator features a bundle of tubes with an elliptical cross-section to reduce pressure- and aerodynamic losses. The layout of a single HEX is presented in Figure 2.4, while the integration of multiple such units within a recuperator system is illustrated in Figure 2.5 [25, 34]. The recuperator and its integration have continuously been updated and optimized during several European research projects, namely the CLEAN, AEROHEX, NEWAC, and LEMCOTEC. Two alternative recuperator concepts have been proposed and studied in addition to the MTU concept in Figure 2.5 [34, 35]:

1. *COnical Recuperative Nozzle (CORN)*: the recuperator's elliptic tubes are annularly and conically arranged within the hot-gas exhaust nozzle. Pressure losses can be reduced significantly as the inlet region of the HEX is relatively large, resulting in lower inlet velocities. The 'cold' air flows in the circumferential direction, whereas the hot exhaust gases flow axially.

2. *STraight AnnulaR Thermal RECuperator (STARTREC):* this concept has a straight annular design. The recuperator consists of several slices, with each slice having a different tube pitch to account for the change in density when the exhaust gas cools down. The tubes are again elliptical with a flow direction similar to that of the CORN concept.

The CORN and STARTREC concepts are illustrated at the left-hand side and right-hand side of Figure 2.6, respectively. A brief comparison between the MTU recuperator, the CORN, and STARTREC concept is provided in Table 2.1 below [36]. No absolute values are given regarding the specific fuel consumption (SFC) of the baseline cycle and the recuperator weight. Nonetheless, it is stated that the weight of the heat recovery system for each engine is about 1000 kg [25]. Furthermore, it is given that reducing the matrix weight of the recuperator by 20% causes the SFC to rise by roughly 0.2%.

Table 2.1: Comparison of performance and weight for the three recuperator concepts.

Concept	**SFC (compared to conventional TF engine)**	**Recuperator weight (compared to NEWAC)**
MTU NEWAC nozzle	- 12.3 %	0
CORN	-13.1 %	-5 %
STARTREC	- 9.1 %	-50 %

2.2.2. Combined-Cycle Engines

A combined-cycle (CC) engine is another alternative cycle architecture for recovering thermal energy from the exhaust gases that would otherwise be wasted into the atmosphere. The CCE generally consists of a primary Brayton cycle with an additional secondary power cycle. Known as the bottoming cycle of the engine, this secondary cycle aims to generate additional useful work from the thermal

Figure 2.6: The CORN (left) and STARTREC (right) recuperator concepts as proposed by Misirlis et al. [36]

power otherwise wasted from the primary or topping cycle system. Although many of the potential performance enhancements of the IRA engine also apply to CC engines, the cycle architecture differs substantially. The IRA engine consists only of an open Brayton cycle with the added intercooler and recuperated integrated into the bypass duct and the core nozzle, respectively. On the other side, a CC engine has two cycles: an open Brayton cycle and a (semi-)closed bottoming cycle. Zooming in on the closed bottoming cycle, its layout is dependent on numerous aspects, of which two are mentioned below:

1. **Working Fluid:** in contrast to industrial applications, the weight of the heat exchangers in aircraft is of significant importance in the design process. This opens the door for more advanced cycle fluids besides the conventional air and water cycles that are most common for industrial applications. Five distinct types of working fluids have been identified for use in aircraft bottoming cycles, namely: *water*, *air*, *ammonia-water mixture*, *organic fluids* and *supercritical* CO_2 [37].

2. **Power application:** a specific bottoming cycle layout can be selected based on the end use of the power produced by the bottoming unit. A secondary cycle could provide additional power to one of the shafts of the main engine, or supply to auxiliary systems of the aircraft. Examples of such auxiliary systems are the environmental control system (ECS), the auxiliary power unit (APU), or the anti-icing system.

Based on literature sources, Jacob performed a qualitative trade-off for the various bottoming cycle options for aircraft applications [37]. Four figures of merit (power density, implications for health and safety, quality and availability of relevant literature, and efficiency) have been assessed for each working fluid to end up with a ranking of the available options. Based on this approach, supercritical CO_2 (sCO_2) appeared to be the best choice for aero applications. Air, organic fluids, and water rank second, third, and fourth, respectively. As air shows really poor results on power density and efficiency, only the sCO_2-cycle unit and ORC unit are discussed here in more detail. The Kalina Cycle, i.e. a cycle with an ammonia-water mixture as working fluid, is not discussed, because of the low technical readiness level and high fluid and system complexity [38].

The Organic Rankine Cycle Unit

A bottoming (organic) Rankine cycle (ORC) is a promising concept for recovering thermal energy from the aircraft engine exhaust stream. The thermal energy can be recovered and converted into mechanical power or electricity by a generator. Perullo et al. initiated the research on integrating an ORC system in an aircraft engine [39]. A process flow diagram (PFD) of a bottoming ORC unit is provided in Figure 2.7 with the corresponding *T,s*-diagram in Figure 2.8 [40]. Red arrows indicate a relatively hot working fluid, whereas blue streams indicate relatively cold ones.

A bottoming ORC generally comprises an evaporator, a turbine, a possible regenerator, a condenser, and a pump. The function of the evaporator is to preheat (station 2-3 in Figure 2.8), evaporate (station 3-4), and superheat (station 4-5) the pressurized liquid working fluid. The superheated vapor then undergoes an expansion in the ORC turbine, where work is extracted from the fluid (station 5-6). Subsequently, the vapor is de-superheated (station 6-7), and finally, condensation takes place (station 7-1) in a condenser. In the pump, the subcooled liquid is pressurized (station 1-2) before being redirected to the evaporator again. A regenerator or recuperator may be installed between the expander

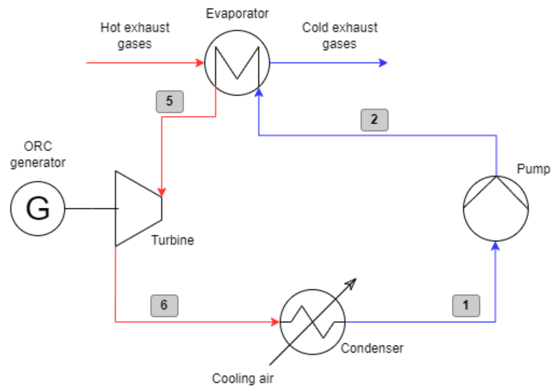

Figure 2.7: PFD of a bottoming ORC unit for waste heat recovery from aero engine exhaust.

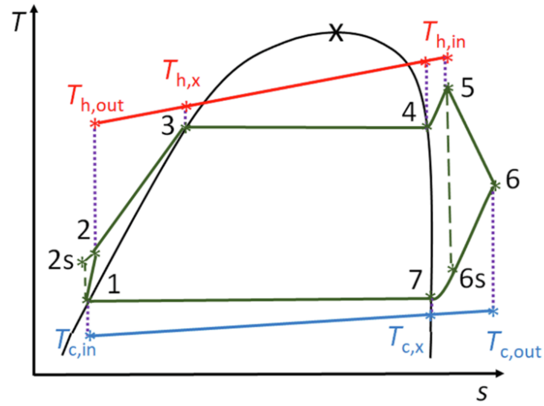

Figure 2.8: Typical *T,s*-diagram for a non-recuperative bottoming ORC unit [40].

and the condenser to preheat the working fluid before it enters the recuperator. Although higher thermal efficiency can be achieved with the regenerator, the weight imposes a significant disadvantage and can nullify the efficiency gain.

As seen from Figure 2.8, the cycle is similar to a steam Rankine cycle but with an organic working fluid instead of water. The shape of the liquid-vapor dome, as depicted in Figure 2.8, can, however, differ depending on the type of working fluid. Three types of working fluids can be distinguished for an ORC unit based on the saturation vapor line slope: *wet, dry, and isentropic fluids*. The type of working fluid directly affects the design and operating conditions of the turbine and the condenser. Considering organic fluids, the molecular weight and complexity often determine the slope of the saturation vapor line [41].

The idea of an ORC unit for aviation waste heat recovery systems has yet not received much attention, compared to the abundance of literature on ORC for land-based applications [42]. Regarding aero engine applications, Perullo et al. presented the first attempt at retrofitting an existing turbofan engine with an ORC unit [39]. They concluded that a reduction of TSFC can be achieved (1.1-2.2%) only when the turbine's work is used effectively, e.g. to give power to a compressor driving air to the ECS. The mass of the ORC unit was estimated to be 430kg. Besides this, the application of an ORC unit for a turboprop and reciprocating engine has been studied by [43, 44] and [45], respectively. The ARENA (airborne energy harvesting for aircraft) project currently focuses on applying an ORC unit within a turboelectric aircraft. This aircraft uses two turboshaft engines mounted in aft pods to supply power to an under-the-wing distributed propulsion system of electrically powered ducted fans. With a newly established multidisciplinary simulation framework, Krempus et al. studied the feasibility and integration of an ORC unit onboard a turboelectric aircraft [46]. Also, a combined cycle turbofan aircraft is assessed. It was found that the fuel mass could be reduced by almost 4% compared to the conventional turboelectric aircraft without compromising too much on aircraft weight and L/D. Heat exchanger size and HEX pressure drop are observed to be the critical performance parameters. The mass of the ORC unit was optimized and found to be 200kg. Next to the abovementioned application, Krempus et al. also investigated the possibility of integrating an organic Rankine cycle waste heat recovery system with an auxiliary power unit [47]. The redesigned CC-APU design reduces fuel usage for ground power provision by over a third compared to utilizing an APU without an ORC unit. The system has a 31% total cycle efficiency and a mass of 150 kg. System performance is again limited by condenser size and pressure drop in the exhaust gases.

To summarize, ORC as bottoming cycle for aero engines is a relatively new concept and has not yet been tested on real engines. However, some researchers investigated and modeled the effect of a bottoming ORC on engine performance. Although higher thermal efficiencies can be obtained with the ORC, the adverse effects of weight, system complexity, and spatial integration in the nacelle or aircraft remain significant. The need to improve this cycle further by, for example, superior working fluids or the application of a supercritical instead of a subcritical cycle is a possible way to compensate for the disadvantages of ORC units in aero engines.

The Supercritical CO_2 Cycle Unit

Another CC configuration for aero applications is investigated and assessed by De Servi et al. in 2017, namely a bottoming supercritical CO_2 (sCO_2) Brayton cycle to recover part of the engine exhaust heat in modern aero engines [48]. To the author's knowledge, this was the first research of a combined cycle applied in aero engines using supercritical carbon dioxide as a working fluid. However, the supercritical CO_2 bottoming cycle concept has already been studied for terrestrial and nuclear waste heat recovery applications [49], but integration in aircraft brings new difficulties and constraints.

The architecture of the combined cycle engine (CCE) as proposed by De Servi et al. is shown in Figure 2.9 and the corresponding *T,s*-diagram in Figure 2.10. From Figure 2.9 the conventional turbofan Brayton open-cycle can be identified. However, between the LPT and the core nozzle, a recuperator is integrated that is part of the bottoming sCO_2 cycle, namely the heater. The CO_2 is (super)heated to its supercritical state in the nozzle's HEXs (station $2_{a,WHR}$ to 3_{WHR} in Figure 2.10) and work is extracted from the working fluid in the sCO_2 turbine (station 3_{WHR} to 4_{WHR}. When expanded, the CO_2 passes through a regenerator to pre-heat the colder, pressurized CO_2 before being redirected to the heater (station 4_{WHR} to $4_{a,WHR}$). In the cooler, the CO_2 is cooled by the colder by-pass air to close the cycle and make the CO_2 denser (station $4_{a,WHR}$ to 1_{WHR}), which favors its compression (station 1_{WHR} to 2_{WHR}). After the compressor, the pressurized CO_2 is led to the regenerator, where it is pre-heated by the hotter CO_2 (station 2_{WHR} to 2_{aWHR}) before flowing to the main heat exchanger again. As well as in the ORC-based CCE, sCO_2 is used in a separate closed cycle in which the working fluid is not mixed with the main engine streams (both by-pass and core stream). This concept is, therefore, fundamentally different compared to the IRA engine from MTU, where the compressor discharge air is directed to and heated up in the nozzle's recuperator.

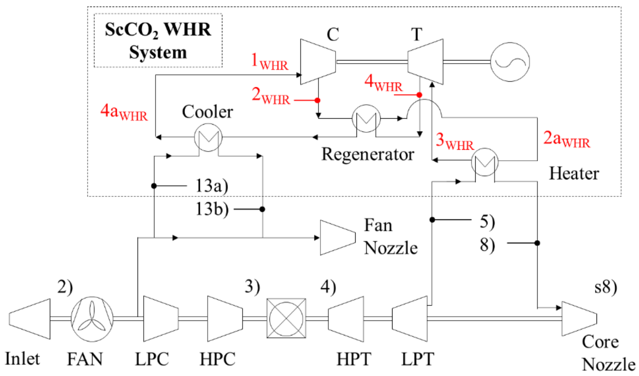

Figure 2.9: The layout of the supercritical carbon dioxide combined cycle engine configuration [48].

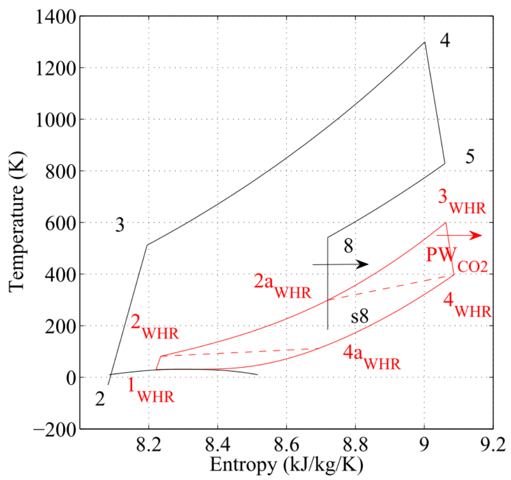

Figure 2.10: The T-s diagram of the combined cycle architecture with the bottoming sCO_2 Brayton cycle [48].

De Servi et al. performed a viability study of the sCO_2 CC engine using a thermodynamic analysis first [48]. The CCE was compared with the conventional and the IRA engine on the basis of TSFC and heat exchanger performance. It was concluded that the SFC value estimated for the CCE is significantly lower than that of the simple-cycle engine and outperforms the IRA engine for large pressure ratios ($OPR > 40$). Subsequently, a preliminary design study is carried out to analyze a CC GE90-94B turbofan engine with a sCO_2 WHR. The TSFC of the CCE was found to be about 2.8% less than that of the GE90-94B without considering the additional weight of sCO_2 WHR unit. Taking the latter into account did result in an increase of TSFC, nullifying the effects of the WHR unit. Nonetheless, this extensive study formed the basis for further development and research towards the sCO_2 combined-cycle engine.

In the past years, only a few researches have been conducted regarding sCO_2 cycles applied in aero engines. Apart from TU Delft, the University of Central Florida [50, 51], Cranfield University [52] and Florida State University [53] investigated the bottoming sCO_2 cycle unit in aero engines for WHR purposes. Jacob et al. from Cranfield University studied the implementation of a bottoming sCO_2 power cycle unit within a 2050-GTF engine [52]. Though only cruise was considered as a design point and no optimization of the CC parameters was performed, the HEX models were relatively detailed compared to previous studies. A reduction in fuel burn of 1.90% was found compared to the state-of-the-art GTF, similar to the reduction found by De Servi et al. (2.8%). However, the total weight of the bottoming cycle in the study of Jacob et al. is as large as the weight of the lightest component in the study of De Servi et al. Both researchers emphasize the need for (multi-disciplinary) integrated optimization techniques to combine cycle performance with component weight estimation and detailed HEX design. Yang et al. support this statement by suggesting that a parametric analysis gives a better picture of the CC engine than modeling it with scaling functions, as he has done in his work [53]. Lastly, a study about a sCO_2 WHR system in aircraft engines was performed by Vesely et al. in 2022 [50]. The effect of including the regenerative heat exchanger in the CC engine is studied and they found that the cycle efficiency can be doubled with the regenerator. However, a CC engine without a regenerator can use more heat from the exhaust stream, directly affecting the thrust. Again, pressure drop reduction via HEX design optimization is the main recommendation. Furthermore, system integration and the performance of the air cooler are studied more thoroughly in a follow-up study [51].

To summarize, the integration of a bottoming supercritical CO_2 unit within a turbofan engine reduces the specific fuel consumption by a few percent. However, the additional cycle weight is often not considered within the analysis. This almost nullifies the performance gain and makes the concept less attractive for future turbofan engines.

2.2.3. Other Recuperation Methods

The integration of an ORC or an sCO_2 cycle unit with a gas turbine is seen as a promising waste heat recovery method for aero engine applications. Although they are not as pertinent to this research, some other recovery options are found that could also be used with aero engines. A summary of these opportunities is given below:

- **Thermo-electric generators**: these devices can convert thermal energy directly into electrical energy without the intermediate step of producing mechanical energy. This heat recuperation method has not been widely studied because of its relatively low efficiency and power density. DLR performed a feasibility study regarding a thermoelectric generator between the hot core nozzle and the colder bypass stream. They reported a beneficial effect, between 0.05-0.1%, on fuel consumption and a power output of 1.65kW, which is significantly lower than for a CCE [54].
- **Air bottoming cycle:** These (mostly) open cycles have already been researched for application in aero engines. Already in 1996, it was found that the efficiency of an aero-derivative CC engine with an ABC unit could increase by 10.5 percent point [55]. Nevertheless, the power density was too small to be eligible for aero engines. Lastly, the ABC is also studied by other institutions, but all with the same result: a slight increase in efficiency either without considering the extra weight of the cycle or with the conclusion that the HEXs are too big to be fitted in the engine [56, 57].
- Other less promising and/or low readiness technologies, such as Kalina or Stirling cycles.

2.3. The Water Enhanced Turbofan Engine

Unfortunately, the previously mentioned recuperated turbofan designs have not been realized yet. The IRA engine requires extensive and complex piping to direct the pressurized compressor air through the recuperator aft of the LPT and back to the combustion chamber. Although continuous improvement of HEX performance and compactness, the weight and size of the HEXs would still nullify the beneficial thermodynamic effects of the IRA engine. Considering heat recuperation by an (organic) Rankine cycle unit or the supercritical CO_2 cycle unit, the problem with the heavy, bulky HEXs is not solved. Apart from bulky HEXs, the flammability of organic fluids and thermal instability are challenges in ORC units. In addition, the integration of a sCO_2 cycle unit in aero engine applications is hampered by the complex modeling behavior of supercritical fluids. The necessity to study novel heat recuperation alternatives persists until the shortcomings of previous WHR methods are sufficiently solved. MTU, therefore, proposed a new aero engine concept, the so-called Water Enhanced Turbofan (WET) engine. Whereas the IRA and CC engines attempt to enhance fuel efficiency, MTU focuses especially on reducing non-CO_2 emissions. This section discusses this new engine configuration, its opportunities, limitations, and environmental effects. Lastly, it provides an extensive summary of the available literature on this engine concept.

2.3.1. Concept

The WET engine was first proposed by MTU in 2021 as the steam injecting and recovering aero engine (SIRA) concept [7, 8]. The engine layout has been then adjusted multiple times throughout the last 3 years. The novel aero engine concept is now named WET (or WET) engine, as also adopted in this document. The original WET engine layout, as proposed by Schmitz et al. in 2021, is shown in Figure 2.11 below [7].

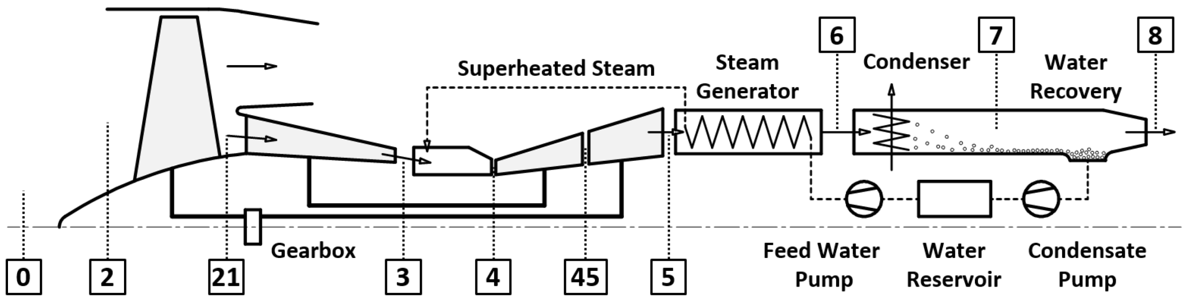

Figure 2.11: Schematic of the original WET engine concept proposed by MTU [7].

Before the combustion chamber, no radical design modifications are introduced with respect to the conventional high by-pass turbofan (HBTF) engine except for possible turbomachinery size changes. However, due to the injection of superheated steam in the combustion chamber, the thermodynamics and engine layout significantly differ aft of the combustion chamber. The wet combustion products expand through the HPT and LPT and flow through a heat recovery steam generator (HRSG) to evaporate and superheat the recovered liquid water. Throughout this document, the terms HRSG and evaporator are used interchangeably. The temperature of the combustion products is lowered in the HRSG but is still in a superheated state. The exhaust gases need to reach a saturated state before the water can be condensed in the so-called condenser. Afterward, the liquid water is collected in a water recovery system and is pumped to a reservoir, before being redirected to the HRSG. The superheated steam is then injected back in the engine core in or just ahead of the combustion chamber. Just like the IRA and CC engines, the WET engine incorporates multiple heat exchangers, and the problem of the size and weight of these devices are not solved for this new concept. In their first design, MTU chose the condenser to be located within the aircraft's fuselage, which resulted in extra piping systems to direct the HRSG exhaust stream from the engine via the wing to the aircraft's main body. The heat sink is provided by an external air blower that takes in ambient air. The core exhaust stream in this design is directed from the engine to the fuselage with the recovered water flowing back to the engine core to be injected. Because of the complexity and additional piping weight, the water recovery system was modified one year later as shown in Figure 2.12 [10]. From the figure, it can be observed that all WET engine components are integrated into the engine. The cooling of the condenser is provided by bypass air. Thus, the condenser is integrated into the bypass duct. Moreover, the core exhaust nozzle is located in the nacelle and the liquid water should be redirected to the engine core. The design, as shown in Figure 2.12, is seen as the baseline concept of the WET engine. A detailed description of each of the components in the engine, as well as their capabilities and limitations, is provided in the Subsection 2.3.3. Though MTU worked out the WET engine extensively, another similar concept has been proposed and researched. The project, initiated and led by Pratt & Whitney in 2022, is called the Hydrogen Steam Injected Intercooled Turbine Engine (HySIITE) project. Rather than using Jet-A as fuel, this project considers hydrogen as fuel, which has the advantage of producing more water per kilogram of fuel. This is beneficial for the water recovery system, especially during critical flight phases such as take-off and landing [7, 13]. A layout of the WET-like engine is depicted in Figure 2.13

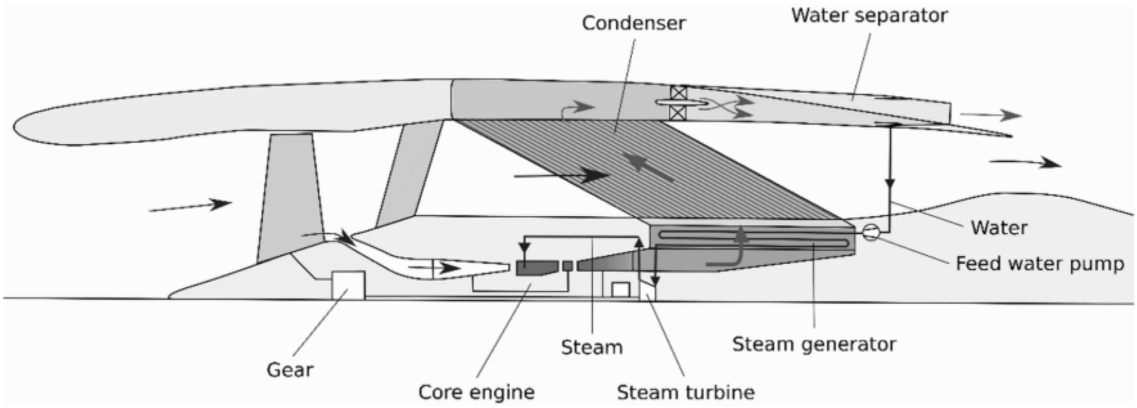

Figure 2.12: A revised design of the integration of some components in the WET engine [10].

[58]. Water is recovered from the condenser, pumped to the evaporator, and eventually injected as superheated steam both after the LPC and in the combustion chamber. Liquid hydrogen, the fuel of the engine, can be effectively used as a heat sink for the condenser, reducing the size of the air condenser in the WET engine. Although this water-enhanced concept shows some advantages over the WET concept of MTU, the project is led by a commercial company and technical data is scarce for this configuration. For this reason, the configuration proposed by MTU is used throughout this document.

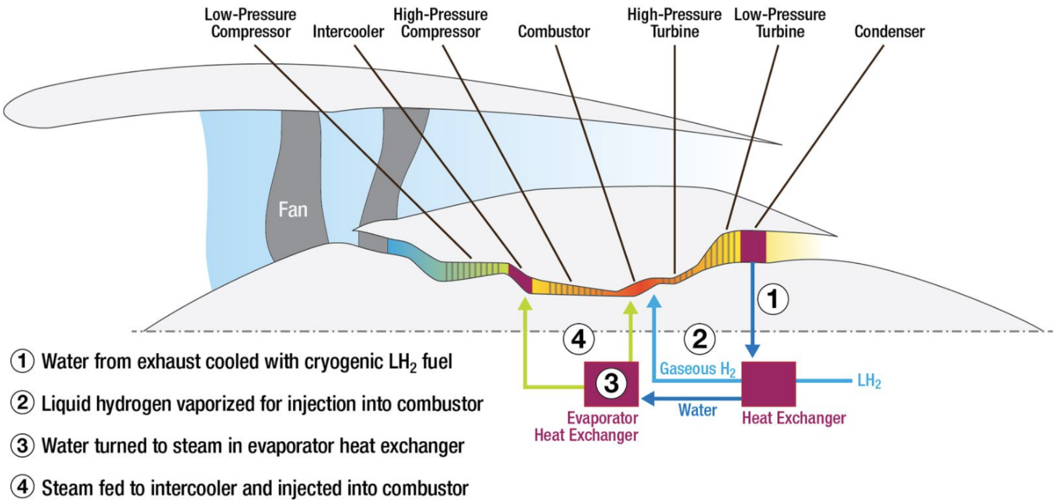

Figure 2.13: Engine configuration of the HySIITE project initiated by Pratt & Whitney, similar to the WET engine of MTU [58].

2.3.2. Key Thermodynamic Cycle and Performance Trends

Since introducing the Water-Enhanced Turbofan (WET) concept, research has primarily focused on its fundamental thermodynamics and potential environmental benefits [7, 10]. However, studies on the application of this concept to (high bypass) turbofan engines remain limited [16, 59, 60, 61]. Given the increasing focus on sustainable aviation propulsion, understanding the expected performance trends of WET turbofans is essential. The combination of water injection and exhaust heat recovery introduces distinct thermodynamic behaviors that influence key parameters such as OPR, TIT, TSFC, and component sizing. This section outlines the general trends anticipated for WET turbofan engines, based on existing research and parametric studies, to establish a foundation and basic understanding of the engine concept for interpreting the results in this study. At the end of this chapter, a table is provided that carefully summarizes the most relevant model details and findings for each WET engine study.

Overall Pressure Ratio (OPR)

Across all three studies, a clear trend emerges: increasing OPR improves thermal efficiency by enhancing compressor pressure ratio but at the cost of reducing the available heat for the steam cycle. Ziegler et al. (2023) show that the optimal OPR for TSFC in the traditional kerosene-fueled WET engine is lower than for a conventional turbofan due to a reduced engine core size as a result of steam injection [59]. Besides this, they found that the optimum OPR shifts to higher values with increasing TIT. DLR also investigated the new WET engine idea and contrasted a kerosene-fueled and hydrogen-fueled WET engine [16]. Görtz et al. indicate that hydrogen combustion further reduces the optimal OPR compared to the kerosene-fueled WET engine, as hydrogen's higher specific energy and water production increases the specific power density of the core. One year later, they found that for a kerosene-fueled WET turbofan, an OPR range of 30–37 balances efficiency and engine size constraints. Higher OPRs lead to reduced WAR and lower steam turbine power, as less heat is available for water evaporation. Thus, while higher OPR improves thermal efficiency, the diminishing availability of heat for the steam cycle and the challenge of integrating a high-pressure compressor in a compact core engine limit its practical range.

Turbine Inlet Temperature (TIT)

The effect of TIT on TSFC differs in the three studies mentioned above. Ziegler et al. (MTU) demonstrate that higher TIT reduces TSFC by up to 5% but requires careful optimization of WAR to maintain cooling effectiveness [59]. The OPR is observed to be coupled with TIT and increases therefore as well. Görtz et al. did not mention the effect of TIT on TSFC at cruise conditions but only investigated the TIT during take-off operation. Both OPR and TIT decrease when WAR increases; nonetheless, it is essential to maintain a high enough turbine exit temperature to ensure the feasibility of the heat recovery process. Contrary to the study by MTU, Görtz suggests later that an optimal TIT near 1600 K balances efficiency, component cooling, and cycle integration, with increasing TIT beyond this point leading to diminishing returns due to condenser size growth [60]. In their parametric study, both TSFC and mission fuel burn increases notably after a TIT of 1600 Kelvin, whereas a reduction does not improve the engine's performance. This supports their reasoning to prescribe an 'optimum' TIT of 1600 Kelvin. To summarize, the effect of TIT on the cycle performance is mainly dependent on input settings and engine constraints. However, it can be concluded that higher TIT allows more steam injection, enhances efficiency, and increases condenser size.

Bypass Ratio (BPR)

A common finding across all studies is that WET engines favor significantly higher BPRs than conventional turbofans, improving propulsive efficiency and reducing TSFC. Ziegler et al. do not report specifically about the optimal BPR range or its effect on cycle performance. However, it is mentioned that the condenser's cold-side outlet temperature determines the BPR and that the bypass flow is split into a cold stream and a hot stream that passes through the condenser [59]. Görtz et al. found that the BPR increases when introducing water into the core. Furthermore, DLR confirms that hydrogen combustion leads to an even larger optimal BPR due to increased steam content in the core, enabling higher workloads for the fan [16]. Lastly, DLR found that a BPR of approximately 22 offers the best trade-off between propulsive efficiency and integration feasibility. Further increases in BPR result in excessive nacelle drag and weight penalties, limiting practical implementation [60]. Thus, higher BPR is a defining characteristic of WET engines, with optimal values between 20–30, depending on integration constraints. Nevertheless, its optimum value is dependent on input parameters and design choices such as the prescribed velocity ratio, OPR, TIT, and WAR.

Nozzle Velocity Ratio

All three studies show that the nozzle velocity ratio ($VR_{nozzles}$) plays a critical role in fuel efficiency. It is defined as follows:

$$VR_{nozzles} = \frac{V_{id,byp}}{V_{id,core}} \tag{2.1}$$

The study of MTU indicates that the optimal velocity ratio differs from conventional turbofans, as the cooling effect of water injection alters core and bypass flow dynamics. However, the velocity ratio was not included among the design variables in their first studies [62, 10]. Therefore, no detailed information is provided regarding the effect of velocity ratio on the engine cycle [59]. Görtz et al. fixed the velocity ratio at a value of 0.9 and found a significant reduction of TSFC compared to a conventional turbofan engine [16]. The most detailed information can be found in the last papers of DLR. A velocity ratio larger than unity is considered the most beneficial, as it ensures lower TSFC for a higher bypass flow velocity while maintaining efficient condenser operation [60]. A parametric study is performed by varying the velocity ratio from 0.9 to 1.2, and a ratio of 1.1 is reported to ensure minimum fuel burn and optimal performance. Maintaining a higher nozzle velocity ratio (>1) is a key requirement for optimal WET cycle performance.

Water-to-Air Ratio (WAR)

The studies consistently highlight the importance of WAR optimization, as excessive water injection increases system weight (mainly by the evaporator and condenser), cooling demands, combustor complexity, and sizing problems. At the same time, too little water limits the efficiency benefits. Ziegler identifies that WAR at cruise should be lower than at takeoff, with an optimal value around 0.15 [59]. DLR shows in their first study that the optimal WAR is equal to 0.245 and that the TSFC of the WET engine is reduced by more than 11% compared to a conventional turbofan engine [16]. Higher WAR values enable a cooler, denser working fluid, increasing the specific work and favoring lower TIT, but could make water recovery or HEX sizing challenging when being too high. Later, Görtz et al. found an optimal cruise WAR of 0.123, with takeoff WAR reaching 0.158–0.161, ensuring proper steam injection while minimizing condenser load [16]. Therefore, a WAR range of 0.10-0.20 is expected to be ideal for WET engines, with a higher WAR at takeoff and lower WAR at cruise to optimize efficiency and reduce system weight.

Engine Size and Integration Challenges

All three studies confirm that while the WET engine improves efficiency, it introduces significant integration challenges due to additional heat exchangers and water circuits. Ziegler notes that the HRSG and condenser significantly increase engine weight, with condenser integration being the primary bottleneck [59]. Görtz (2023) suggests that using hydrogen as a heat sink reduces condenser size, making integration more feasible [16]. Görtz (2024, Part A) finds that the condenser is the main driver of engine length, with the total engine size influenced by the trade-off between heat exchanger effectiveness and nacelle aerodynamics [60]. A compact condenser design makes WET engines viable, as its size directly affects the complexity of engine integration and aircraft drag.

DLR also investigated the flow path of the WET engine together with a weight assessment and compared the results against those of a conventional geared turbofan [61]. Although mass and flow path details are not considered a priority in this study, it is important to have a basic understanding of these topics. DLR found that the WET core engine is 31% shorter than in a GTF due to the increased specific power output. However, heat exchangers add significant length, leading to a 36% total engine length increase and a 49% longer nacelle. Regarding engine mass, bare engine mass is 84% higher than that of a conventional GTF. The heat exchanger assembly accounts for nearly half of the total mass, with the condenser alone contributing 39%. Despite this, the core turbomachinery is 10.6% lighter as the booster compressor can be removed. Again, the effect of BPR and OPR on various engine components and cycle parameters is provided. Häßy et al. concluded that the WET concept remains technically feasible despite its size and mass penalties, offering efficiency and emission reductions. However, the authors highlighted the need for more detailed research regarding the condenser's optimal design.

Based on the literature discussed in this section, a summary can be made about the optimal range and constraints that apply to the most important design parameters of the WET engine.. The results are shown in Table 2.2 below [16, 59, 60, 61].

2.3.3. WET Components

In this subsection, the function of the WET engine components is given, along with their capabilities and possible limitations. A concise qualitative summary of the research conducted on some WET engine aspects is also provided. The modeling approach of the various (new) components is discussed in Chapter 3 and Chapter 4.

Table 2.2: Summary of expected design ranges of some important WET input parameters

Parameter	Unit	Cruise design range	Limiting factor
OPR	-	25 - 35	HRSG heat availability & HPC geometry limits
BPR	-	20 - 30	HRSG heat availability & fan diameter
TIT	K	~1600	LPT cooling & condenser size
WAR	-	0.10 - 0.3	HRSG heat availability
Fan diameter	m	2 - 2.2	Integration & ground clearance

Intake, Fan and Compressors

Although steam is injected after the compressors, modifications might be needed for the intake, fan, and compressors of the WET engine with respect to the common design adopted in turbofan engines. Due to higher BPR values, the intake and fan must handle increased air mass flow. The nacelle dimensions likely increase when two extra HEXs are placed in the engine. This brings integration challenges as the current engine size margins are already low. Regarding the fan, a diameter similar to or higher than that of a conventional UHBR turbofan engine is expected because of future technical advancements. Therefore, fan pressure ratios are lower than in traditional turbofan engines, and the need for a gearbox is more relevant to reduce noise [16]. A smaller, lower-pressure-ratio HPC with fewer stages can be expected in the WET engine, with a possible complete removal of the booster compressor. However, the smaller HPC features a reduced surge margin by shifting the operating point closer to the stall boundary, especially at low-speed conditions. Although not studied in this report, the number of stages and the stage loading should be considered in more detail in future studies. A summary of the findings is tabulated in Table 2.3 below [16, 59, 60, 61].

Table 2.3: Summary of expected WET engine changes for the intake and compressors.

Component	Expected change in WET Engine	Engine impact
Intake	Slightly larger mass flow, lower inlet Mach number	Minor impact, integration challenge due to longer nacelle
Fan	Similar or slightly larger diameter, lower FPR	Higher propulsive efficiency, lower specif thrust, similar fan efficiency and noise
LPC / booster	Likely removed or reduced stage count	Shorter engine, weight reduction
HPC	Lower OPR, fewer stages, smaller annulus heights because of reduced core mass flow	Lower thermal stress, possible turbomachinery efficiency loss, surge margin challenges

Water Injection & Combustion Chamber

Superheated steam needs to be injected before the turbine inlet of the WET engine. The injection point can be before, in, or after the combustor. Steam injection in the core of the gas generator has already been applied for stationary applications and implies several changes in the gas turbine performance and characteristics. The so-called simple Steam-Injected Gas Turbine (STIG) engine has been studied before, and the most relevant implications on performance are summarized below:

- **Power augmentation:** by the injection of steam close before or in the combustor, the C_p increases as steam has a higher specific heat compared to (compressed) air, ~2.0 vs. ~1.1 $J/kg/K$, respectively. Moreover, the relative mass flow through the turbine is larger than through the compressor. This results in higher power output than a simple dry cycle per unit of intake mass [63, 64, 65]. In other words, the specific work of a wet gas turbine is expected to be higher compared to a dry turbine.
- **Thermal efficiency:** when considering the cycle thermal efficiency, defined in Equation 2.2

below [66] (both for turbofan and turboshaft engines), steam injection affects this performance parameter as well, depending on the cycle configuration [67, 63, 65]. The steam injection temperature and the steam quantity largely dictate the fuel flow to reach the prescribed TIT. However, for a similar TIT, the specific work increases when injecting more water in the core. Both contribute to higher thermal efficiency values. A combination of steam injection and thermal recuperation aft of the last turbine stage has a beneficial effect on the efficiency if pressure drops in the bypass and core flows are neglected [68].

$$\eta_{th} = \frac{\dot{P}_{prop}}{\dot{Q}_{fuel}} = \frac{\dot{W}_{net}}{\dot{Q}_{fuel}} \tag{2.2}$$

As this study focuses on a preliminary thermodynamic assessment of the WET engine, the practical implications of injecting steam close to the combustor are beyond the scope of this work. However, for completeness, a short summary of the literature about two steam injection methods for aircraft engine applications is provided at the end of this section [69].

Wet combustion, i.e., combustion with compressed air, fuel, and additional steam, has several benefits, briefly discussed below. The amount of water present at the combustor exit is called the water-to-air ratio (WAR) and is a relevant parameter in the design of WET engines. The equations for FAR and WAR are provided in the Equation 2.3 and Equation 2.4.

$$FAR = \frac{\dot{m}_{fuel}}{\dot{m}_{air}} \tag{2.3}$$

$$WAR = \frac{\dot{m}_{water}}{\dot{m}_{air}} \tag{2.4}$$

Besides the effect on the engine's work and thermal efficiency, water injection also influences the combustion process. With the TIT assumed to be constant and dependent on turbine material limitations, the following statements can be made regarding wet combustion:

- **Fuel consumption:** depending on the temperature of the steam, the fuel flow can be higher or lower.
- **Reaction kinetics:** with steam addition, the dynamics of the combustion process change. Large water shares have proven to slow down the total combustion reaction. As a result, the volume of the combustor may need to be slightly larger to compensate for this [7, 70]. On the other hand, water has a relatively high specific heat capacity and can, thus, ensure more homogeneous combustion. As a result, temperature peaks are expected to be lower, and endothermic processes that thrive due to the temperature peaks are counteracted.
- **Oxygen availability:** a larger water share reduces the oxygen concentration in the combustor. The larger the water share, the more the combustion process goes toward stoichiometric conditions rather than lean conditions [70].
- **Combustion products:** Steam dilution causes the exhaust composition at the combustor outlet to differ from a conventional dry gas turbine engine. The lower oxygen concentration together with lower temperature peaks results in a significant reduction of NO_x, mainly due to lower thermal NO_x [69, 71, 72]. A steam share of 10% is reported to reduce NO_x emissions by already 90% [71]. Furthermore, CO and CO_2 concentrations are also affected by steam addition, but less compared to NO_x [72].

Naturally, the design of the combustor is to be revised for the case of large steam mass fractions. Ensuring stable combustion with avoidance of flashbacks is the primary concern for the combustor design, especially for future aviation fuels such as sustainable aviation fuel (SAF) and hydrogen. Lastly, it is still unclear where the superheated steam should be injected and the consequences of these design choices. Very little to nothing can be found regarding this topic. The possible injection locations can already be identified:

1. The steam is injected directly into the combustor separately from the fuel injection.
2. The steam is premixed with the fuel. The (liquid) fuel then evaporates when mixed with the superheated steam flow. The result is more homogeneous conditions in the combustion chamber, hence more optimal combustion with a significant reduction in NO_x and CO emissions [72].

3. Steam is injected between the LPC and HPC. This is equivalent to implementing compressor intercooling without the need to install a dedicated HEX. Because of steam injection, the compressed air temperature is lowered, and the specific work of the compressor is reduced.

4. Steam injection takes place between the HPC and the combustor inlet.

5. A combination of both points 3) and 4)

6. As proposed by MTU in a recent work, liquid water is injected aft of the HRSG to enhance heat transfer on the exhaust gas side of the condenser [59]. By injecting water before the condenser, saturated conditions may be reached thanks to the additional water evaporation.

Turbines

The addition of water in the combustion process increases the humidity of the exhaust stream because water is already part of the combustion products when kerosene or Jet-A is burned. As the exit temperature of the last turbine stage is significantly higher than the boiling point of water, the formation of liquid water droplets is most likely avoided. However, the effect of significant steam mass fractions in the exhaust flow on turbine material degradation and cycle performance should be examined more thoroughly. WET engines are found to operate at lower TIT, and this has a direct effect on cooling air demand in the turbines, improving efficiency. Lower specific work per unit mass of dry air can be achieved because of a relative increase in mass flow rate through the turbines compared to the compressors. The latter could lead to fewer HPT stages. The introduction of steam into the core also affects the LPT design. As the WET engine favors a high BPR and lower core flows, the power demand of the LPT would increase if the fan is connected to the low-pressure shaft. The WET engine shifts power extraction, namely more to the fan. This causes the turbine exit temperature (TET) to be lower. Nevertheless, the exit conditions are closer to saturation conditions, which could lead to enhanced degradation of the last LPT stages.

Heat Recovery Steam Generator

The HRSG is one of the core components of the WET engine. The purpose of this heat exchanger is to preheat, evaporate, and superheat the liquid water that is recovered from the cooled exhaust gases. The liquid water is heated with the thermal energy recuperated from the exhaust gases leaving the last turbine stage. For this reason, the heat exchanger, or recuperator, is often called the heat recovery steam generator (HRSG). A first analysis and assessment of the HRSG within the WET engine is provided by MTU [7]. Schmitz et al. positioned the HRSG aft of the LPT. This is done mainly because of simplicity and ease of integration. However, possible better cycle efficiencies can be obtained by placing the HRSG between the HPT and LPT or by a combination of both solutions [22]. Because the bottoming water cycle is assumed to be subcritical, evaporation occurs under constant temperature. The pinch point is a critical limitation for the heat transfer in the HRSG, as shown in Figure 2.14.

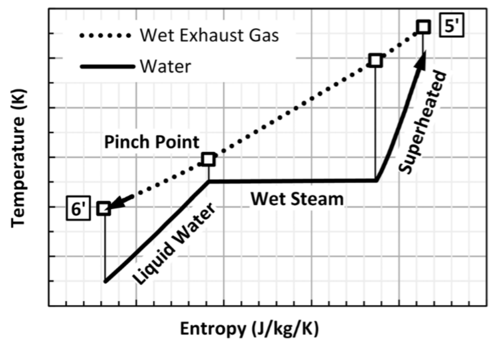

Figure 2.14: A (T,s)-diagram of the HRSG component proposed by MTU with the indicated pinch point [7].

In [7], the HRSG and condenser are modeled as a single HEX to investigate the magnitude of the total required thermal load of both components compared to the turbine work. Assuming all injected water is to be recovered, the study showed that the required thermal load and usable work ratio increase with the WAR. The effect of OPR on this ratio is also studied. In Chapter 5, these results are analyzed in more detail for verification. The HRSG for the WET engine needs to be both lightweight and compact to meet modern aviation requirements. Therefore, a compact tubular HEX is proposed by MTU featuring a small-diameter tube bundle [7]. The small tubes ensure a small pressure drop for the working fluid. Continuation of the research on specifically the HRSG is provided by DLR [73, 74]. *Schmelcher et al. (2023)* created a preliminary design tool for the HRSG covering preheating, evaporation, and superheating and applied the model to the WET engine. A cell-based approach (combined with the P-NTU method) is applied to divide the HEX tubes into smaller sections to calculate heat transfer properties. With this approach, a clear distinction between the three heating zones can be established along the tube length. The water mass flow rate in the water cycle greatly influences the heat exchange capabilities of the HRSG, where superheating can only be achieved for lower WAR values. If the water flow rate is too high, evaporation is barely possible, and two-phase flow exits the HRSG. Besides this, it is concluded that the operating points of the turbofan engine have a very high impact on HRSG performance. Cruise is shown to be the limiting operating point for water superheating, whereas HRSG pressure losses are much higher during take-off.

In the study by Chalmers University [75], a shell and tube heat exchanger is considered and designed as HRSG for the WET engine. The log-mean temperature difference (LMTD) method is used to design this HRSG, and the device is subdivided into an economizer, evaporator, and superheater. The weight of the HRSG is found to be 627kg. The shape of the HRSG is conical, where the flue gases flow radially outward when exiting the last turbine stage. A visualization of this HRSG layout is shown in Figure 2.15 [75].

The HRSG's effectiveness is also influenced by the BPR of the WET engine. A higher BPR reduces core mass flow and turbine exit temperature, limiting the available thermal energy for steam generation. This reduces the WAR, diminishing the cooling and efficiency benefits of the WET cycle. Thus, there is an optimal range of BPR (see Table 2.2) that balances fuel burn/TSFC savings with HRSG heat recovery effectiveness. The interaction between the HRSG and the condenser is another crucial design consideration. The condenser relies on sufficient exhaust cooling to ensure complete water recovery, but excessive heat extraction in the evaporator can lead to suboptimal condensation conditions. Higher TIT could improve evaporator performance but also affect the condenser operation. The interaction between the HRSG and the condenser should therefore be studied in more detail. In the Table 2.4 below, a summary is given concerning the key challenges associated with the HRSG design and their potential impact on the engine.

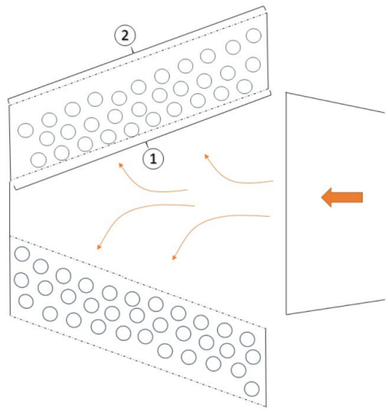

Figure 2.15: Cross-section of HRSG as proposed by Chalmers University [75].

Table 2.4: Summary of the HRSG limits, its performance effects, and possible solutions.

HRSG limitation	**Impact on WET engine performance**	**Possible mitigation strategy**
Pressure losses	Increases back pressure, reduction of performance	Optimize HRSG geometry and ensure minimization of pressure drop
Large size and weight	Larger, longer ang heavier engine, hence drag is increased. Also adds nacelle integration challenges	Use lightweight materials, optimize ducting, use hydrogen as fuel and heat sink.
Thermal energy availability	Reduce steam generation or results in too low HRSG exit temperatures.	Select lower WAR, optimize turbine exit temperature
Interaction with condenser	Hotter exhaust gases improves HRSG performance, effect on the condenser is not known.	Couple HRSG and condenser and optimize HEX arrangement

Condenser

After the HRSG, the temperature of the exhaust gases is still above the boiling point of water. A large share of the water in the exhaust stream must be recovered as a semi-closed water loop can be established. Otherwise, an extremely large water tank should be installed to provide water to the HRSG continuously. This would adversely affect aircraft drag and weight. To ensure (100%) water recovery, a condenser should be installed to reduce the temperature below the dew point of water. In Figure 2.12, a possible location for the condenser in the bypass duct is shown as proposed by MTU. The bypass air is the cooling flow in the condenser, whereas the hot exhaust flow from the HRSG is the heat source. Before looking at the condenser, it is noteworthy, to sum up all the possible sources through which water can enter the engine core exhaust:

1. **Through water injection:** for the WET engine, steam is injected directly into the engine's core. This increases the WAR within the engine (Equation 2.4).
2. **Through the combustion process:** because of the fuel oxidation in the combustor, water is a result of the chemical reaction process and is indirectly added to the gas mixture.
3. **Through the ambient:** water is added by the ambient humidity from the engine intake. This part is expected to be negligibly small compared to the previous two sources.
4. **Through turbine cooling:** it is possible that a small amount of water is used to cool the turbines because of cooling, especially in the first turbine stages as the temperature is high. This flow stream is expected to be relatively small compared to the first two sources.

The amount of water recovered from the exhaust can be expressed with a factor, called the water recovery ratio (WRR) which is the ratio of the recovered water and the total water mass added to the engine, as is shown below in Equation 2.5:

$$WRR = \frac{\dot{m}_{H_2O,rec}}{\dot{m}_{H_2O,inj}} \tag{2.5}$$

For the continuous supply of water to the HRSG without the need for a large water reservoir, a WRR of at least 1 is needed. This WRR can also be larger than one as combustion-induced water might also be recovered. The WRR is dependent on several factors, but as much water as possible must be in the liquid phase after the condenser. The phenomenon of supersaturation is said to greatly influence the WRR in the condenser [7]. When considering thermodynamic equilibrium, the relative humidity (RH) or dew point is an important indicator regarding the amount of water in the exhaust stream and potential condensation capabilities. The RH represents the amount of moisture in the air compared to the maximum amount of moisture that the air can hold at certain conditions. It is dependent on the steam quality $x_{H_2O,g}$, the static pressure of the gas p, and the temperature-dependent saturated vapor pressure, $p_{sat,vap}$ as shown below in Equation 2.6 and Equation 2.7.

$$RH = \frac{p_v}{p_{sat,v}} \tag{2.6}$$

$$p_v = x_{H_2O,g} \cdot p \tag{2.7}$$

Another way to describe the amount of moisture in the gas is the dew point temperature. The dew point is the temperature at which the RH is 100% for a given pressure, and the exhaust gas cannot hold more moisture considering thermodynamic equilibrium, i.e., the air is fully saturated with water vapor. If the temperature of the exhaust gas drops below the dew point, then condensation starts to occur as the exhaust cannot hold all the water vapor anymore. Therefore, the dew point is an important indicator for the condensation process. However, condensation does not necessarily occur in real processes exactly at a condition with RH equal to 100%.
The mixture can be temporarily or spatially supersaturated, i.e., the RH is larger than 100% or 1, and more water can be held compared to the equilibrium state. The process of supersaturation and condensation is illustrated in Figure 2.16 [76]. Starting from the initial state, a sudden change in temperature and pressure (adiabatic expansion) can cause the unsaturated vapor to become supersaturated. The formation of liquid water droplets causes the non-equilibrium mixture to be in equilibrium again ($RH = 1$). This type of condensation is called metastable condensation. The formation of liquid droplets starts when the so-called Wilson temperature is reached. The function of the condenser is clear, but some critical aspects should be mentioned. First, as much water as possible should be recovered continuously to reduce the size of the additional water reservoir. As soon as the water vapor is condensed and becomes liquid water, it should be extracted from the HEX or after the HEX in a

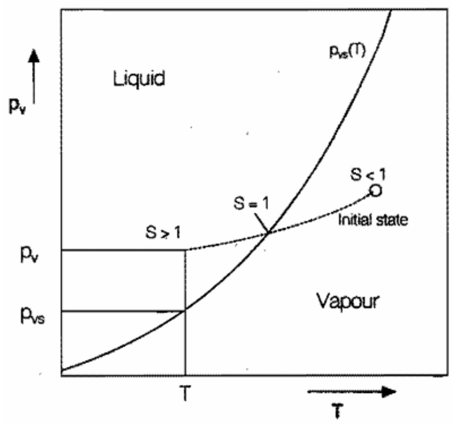

Figure 2.16: *p,T*-diagram of pure water with a qualitative representation of the supersaturation process [76].

water recovery device. If not, the water is blown out to the ambient. The condenser, therefore, also needs to feature easy water extraction, without affecting performance or weight too much. A cross-(counter)flow plate-fin HEX is proposed by MTU for the WET engine [7, 10]. The temperature of the bypass air has a significant effect on the cooling capacity of the condenser. During take-off conditions, the temperature difference between the heat source and heat sink is expected to be relatively small compared to flying at cruise altitude, where the air can reach -50 degrees Celsius. A very large HEX surface, i.e., volume and weight, is required for take-off. The design of the condenser generally comprises the trade-off between the ideal passage velocity to reduce pressure losses and the geometry and mass of the HEX. Although hardly any literature is available on the usage and integration of condensers in aero engines [7, 8], some information regarding the integration of air/air HEXs in the bypass duct is available. The intercooler is the best example for such bypass integrated HEX [77]. Additionally, constraints about the overall condenser design have been identified through the research on WET engines; however, these constraints are predominantly qualitative in nature [16, 59, 60, 61]. The main design challenges for the condenser are tabulated in Table 2.5 below.

Table 2.5: Summary of the condenser limits, its performance effects, and possible solutions.

Condenser limitation	Impact on WET engine performance	Possible mitigation strategy
Pressure losses	Increases back pressure, reduction of performance	Optimize condenser geometry and ensure minimization of pressure drop
Cooling requirements	Bypass air is cooling medium. Insufficient cooling reduces WRR. Higher BPR ensures colder bypass air.	Increase BPR optimize condenser design
Size and weight	Limiting component in WET engine. Adds significant nacelle integration challenges	Use lightweight materials, optimize configuration and bypass duct integration, use hydrogen as fuel and heat sink.
Nozzle velocity ratio	High nozzle velocity ratio improves cycle efficiency but lowers condenser effectiveness.	Balance nozzle velocity ratio for optimal condensation characteristics and propulsive efficiency

Water Recovery Unit

A large share of the exhaust stream's water is expected to be recovered in the condenser. However, this amount of water may not be sufficient to maintain continuous water injection during critical flight phases such as take-off. Additional measures should be taken to extract more water from the exhaust before exiting the core nozzle. This can be done in a duct between the condenser and the nozzle with the appropriate separating devices (see Figure 2.12). The main requirements of these devices are compactness and low-pressure losses. Several possibilities exist to separate the condensed liquid water from the exhaust stream in this flow duct. The most promising ones are summed below:

- **Swirl generator:** device that enhances turbulent flow through a duct, forcing the liquid particles to move towards the outer wall of the duct because of their larger inertia [78].
- **Vane-type separator:** wave-type flow channels are used to collect the liquid droplets more easily. Due to their relatively large inertia, droplets would be unable to follow the curved flow streamlines in the wave-type channel and tend to impinge on the wall. As a result, a liquid film forms on the lower vane surface and is collected because of gravity [79].
- **Micropin fin structures:** the addition of small fin structures on the wall surface aft of the condenser to collect the liquid water.
- **Electrostatic force usage:** water droplets are electrostatically charged. The electrostatic force ensures the movement of liquid droplets towards the wall, after which they can be collected [80].

A water tank should be integrated somewhere between the pump and the condenser and/or water-separating devices. The main purpose of this water tank is to provide a water buffer during critical flight phases. During take-off, the ambient air is relatively hot, and the condenser cooling capacity is low, so less water is recovered. An additional water tank may supply the required water so that superheated steam can be injected without interruption. The two following options can fill the water tank:

1. The tank is fully filled before take-off. As take-off is expected to be the most critical phase for water recovery, continuous supply is guaranteed.

2. During cruise, high WRRs are expected due to the cold ambient air in combination with relatively low fuel consumption. The water is stored in the reservoir and can be used for landing and (partly) for take-off mode.

The above points elucidate that a simple serial layout of the condenser, water tank, and feed water pump is not viable. During take-off, it is desired that the water flows directly from the recovery units to the pump, whereas for cruise, one part of the water should flow to the pump and one part to the reservoir to be stored.

Bottoming Water Cycle

A PFD of the proposed bottoming water cycle is given in Figure 2.17 below. Blue arrows represent a relatively cold flow, whereas the hotter flows are indicated with red arrows. The bottoming cycle is not closed (like the ORC / sCO_2 unit) but semi-closed. The recovered water is fed into the engine's core but is not guaranteed to be collected again. The combination of the open Brayton cycle and the parallel semi-closed water (Clausius) cycle can be seen as an alternative version of the Cheng cycle [81, 82]. Water is not fed from an external source but comes from the engine exhaust itself. The Cheng cycle idea is already realized for industrial applications with a significantly higher cycle efficiency compared to a simple cycle [82]. The liquid feed-water pump provides the driving force for transferring the liquid

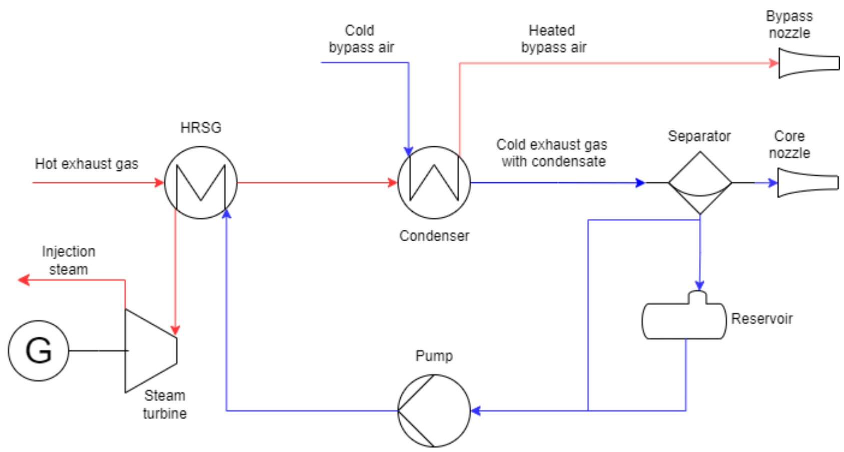

Figure 2.17: PFD of the bottoming water cycle for the WET engine.

water from either the water tank or the condenser to the HRSG. The work needed to compress the liquid water is significantly lower than the compression of steam or air, as liquid water is nearly incompressible. Besides this, the outlet pressure depends on the target pressure of the pressurized air at the water injection point in the LPC or HPC. The pump should deliver water with a high enough pressure so that a suitable pressure difference is available for injection. If a steam turbine is present after the HRSG, the pressure drop in the turbine should also be considered. To summarize, the water should be pressurized to overcome the pressure drops before the water injection, as shown in Equation 2.8.

$$\Pi_{pump} = \frac{p_{inj} + \Delta p_{turbine} + \Delta p_{HRSG} + \Delta p_{pipes}}{p_{pump,in}} \tag{2.8}$$

The superheated steam can be expanded in a steam turbine upstream of the injection point. Additional useful work can, therefore, be extracted from the steam, and this can be used for various ends as explained in Subsection 2.2.2.

2.3.4. Climate Effects

As said in the introduction, air transport accounts for 3-5% of anthropogenic climate change. During the COVID-19 pandemic, a strong decrease in aviation activities was seen. However, air transport recovered quickly again, with pre-pandemic emission levels expected shortly. Jet-A or kerosene is used as the main fuel source in modern civil aircraft and is designed for usage in aeronautical gas turbine engines. It consists of a mixture of several hydrocarbons (C_xH_y), and it is, therefore, difficult to assign a chemical composition to Jet-A. Nevertheless, approximately 8 to 16 carbon atoms are present per molecule. Jet-A is burned with compressed ambient air in the combustion chamber. According to the Equation 2.9 below, carbon dioxide CO_2, water vapor H_2O, and nitrogen oxides NO_x are the results of complete combustion at high temperature. However, complete combustion is hard to accomplish in reality and reaction products due to incomplete combustion should be taken into account as these can affect the climate or local air quality. Unburned hydrocarbons (UHC), particulate matter (PM), and soot are therefore also shown in the Equation 2.9 [3]. Lastly, kerosene often contains traces of sulfur compounds, and these can form sulfate aerosols in the combustion process.

$$C_xH_y + N_2 + O_2 \rightarrow CO_2 + H_2O + CO + NO_x + SO_x + UHC + PM + soot \tag{2.9}$$

All combustion products are expelled at the core nozzle into the ambient and this will affect the global atmosphere or local air quality, depending on the location (altitude) at which these products are expelled. However, their climate impact may not be directly noticeable. Aircraft emissions cause a temporal evolution of species concentration in the atmosphere. Depending on the location and time of the concentration change, it can affect the radiative forcing of the Earth, with a global temperature change as a long-term negative effect. The emission index (EI) is a metric that gives information about the amount of produced exhaust species per kilogram of fuel (Equation 2.10).

$$EI_i = \frac{m_i\ [g]}{m_{fuel}\ [kg]} \tag{2.10}$$

Based on this established climate metric, the aero engine emissions can be quantified and the results for Jet-A are shown in Table 2.6 [83]. It can be observed that the two primary exhaust species released by aero engines into the atmosphere are CO_2 and H_2O. The aforementioned important aircraft emissions are discussed below, focusing mainly on their climate impact.

Table 2.6: Emission index of the exhaust species for modern aero engines with Jet-A as fuel [83].

Exhaust species	EI [g/kg]
CO_2	3160
H_2O	1230
NO_x	12 - 16
CO	2 - 6
SO_2	0.6 - 1
C_xH_y	0.2 - 6
$Soot$	0.01 - 0.1

CO_2

Carbon dioxide is the main product of the combustion process in aero engines and is a greenhouse gas (GHG). Its exact amount depends on the exact composition of the fuel, especially the amount of carbon atoms in Jet-A. More CO_2 is formed for the combustion of $C_{12}H_{26}$ compared to C_8H_{18}, though the difference would be relatively small (3.11 compared to 3.09 kg/kg, respectively). As CO_2 is a direct GHG, its emission directly influences atmospheric CO_2 concentration. This may not necessarily lead to problems, but CO_2 is highly photochemically and thermodynamically stable, resulting in a lifetime of more than a century. Besides this, carbon dioxide is called a direct GHG because it directly impacts the trapping of heat in the atmosphere.

NO_x

NO_x emissions from aircraft originate from fuel combustion with air rather than pure oxygen. Among the several routes to form NO_x, thermal NO_x is the most significant contributor. The other sources for NO_x, namely prompt and fuel NO_x, are not extensively discussed here. Thermal NO_x is formed when diatomic nitrogen (N_2) is oxidized at sufficiently high temperatures. Temperatures higher than 1700K will accelerate the formation of thermal NO_x exponentially. Furthermore, residence time in the combustion chamber is a dictating parameter as a higher residence time results in a more significant possibility of dissociation of di-atomic nitrogen and oxygen and subsequent formation of NO_x by the Zeldovich mechanism [84].

The climate impact associated with the emission of NO_x is not as straightforward to evaluate as for carbon dioxide. In particular, NO_x is regarded as an indirect greenhouse gas. Depending on the location, the NO_x participates in chemical reactions that alters the concentrations of other GHGs such as methane (CH_4) and ozone (O_3). Higher NO_x concentration increases the ozone concentration in the troposphere, which enhances the greenhouse effect. The Equation 2.11 below summarizes ozone formation with NO_x as a precursor. The hydroperoxy radical is formed by the oxidation of CO and CH_4 [84]. The reactions represented by the equations below occur naturally in the atmosphere, but higher NO_x concentrations favor the ozone formation.

$$NO + HO_2 \rightarrow NO_2 + OH \tag{2.11a}$$
$$NO_2 + uv \rightarrow NO + O \tag{2.11b}$$
$$O + O_2 \rightarrow O_3 \tag{2.11c}$$

As mentioned earlier, the NO_x emissions also affect the methane concentration. CH_4 concentration is directly reduced if more NO_x is in the troposphere, i.e., at cruise altitude. The NO_x molecules tend to react to OH radicals and these radicals react with the methane molecules (warm air) or CO molecules (cold air) to form hydroperoxy molecules [84]. To summarize, the emission of NO_x from aircraft results in a net positive radiative forcing (RF) considering the concentration change of ozone, whereas a slight net negative RF is expected regarding methane. The slight decrease is only negligible compared to CH_4 emissions from the industry.

H_2O / Contrails

From Table 2.6 it can be observed that water (vapor) is the engine's second most important combustion product. Water is, just as CO_2, a direct GHG that is capable of absorbing heat and re-emitting it towards the Earth's surface. Compared to CO_2, water vapor has an even larger contribution towards global warming [62]. More water vapor emissions will, therefore, lead to higher atmospheric water concentrations, with a net positive RF as a result. However, the lifetime of H_2O in the atmosphere is in the order of weeks because of its removal by precipitation [85].

The formation of contrails due to water emissions also has a climate impact that may not be forgotten. Contrails are formed because of the temperature difference between the warm, moist engine exhaust and the cold, dry ambient air at high altitudes. Because of the lift-induced vortices, shown in Figure 2.18, the exhaust streams are continuously mixed with the ambient air, constantly decreasing temperature and relative humidity. Contrarily, the air gets saturated with liquid water, and droplets can form at the nucleation sites. Soot, (non) volatile organic compounds (VOC), and particulate matter (PM) from the engine exhaust act as primary nucleation site sources for the condensation process. When the droplets are supercooled, they freeze when temperatures are low enough. This initiates the formation of contrails. A visualization of the various stages of the formation of contrails is shown in the Figure 2.18 below [86].

Schmidt and Appleman derived a relation to predict whether contrails would be generated and this criterion is called the 'Schmidt-Appleman Criterion' (SAC). The ambient conditions determine whether the formed contrail is persistent or non-persistent, as the hot exhaust mixes eventually to ambient conditions. The mixing process of the core exhaust stream and the surrounding ambient is modeled as a straight line in the water partial pressure-temperature diagram (Figure 2.19). The intersection of this straight line, also called the mixing line, and the saturation curves concerning both ice and liquid phase allows one to predict the possibility of contrail formation. With reference to the diagram in Figure 2.19, the blue line represents the critical mixing line, and its slope (G) is determined by Equation 2.12 below. The slope G $[PaK^{-1}]$ is dependent on the emission index of water vapor, the ratio of molar masses of water and air, the c_p of the exhaust, the ambient pressure p_a, the propulsion efficiency η and the

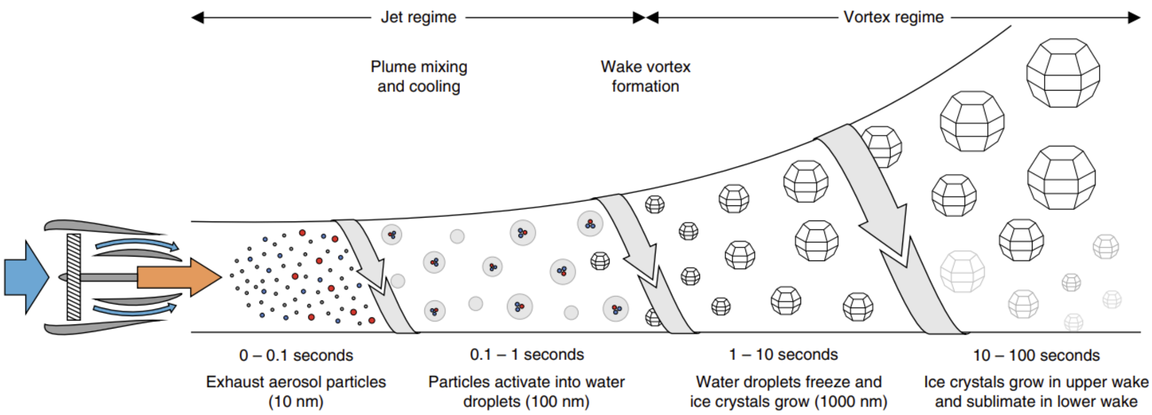

Figure 2.18: Processes and particles that affect the formation of contrails [86].

combustion heat Q in J/kg. The critical temperature point (at $RH = 100\%$) is defined as the point where the critical mixing line is tangent to the water saturation line. If the ambient is colder than this critical temperature, contrails will form.

$$G = \frac{EI_{H_2O} \cdot c_p \cdot p_a}{Q(1-\eta_{prop})} \frac{M_{air}}{M_{H_2O}} \tag{2.12}$$

The actual mixing line should cross the saturation line for liquid water to form droplets. Then, these droplets should crystallize to form contrails hence the mixing line should cross the ice saturation line. The ambient conditions determine whether the contrail is persistent or will disperse quickly. If the ambient point lies between the liquid water and ice saturation ice, a supersaturated atmosphere is obtained, and permanent crystals are formed, i.e., a persistent contrail. Conversely, an ambient point below the ice saturation line causes the ice particles to sublimate with a so-called 'threshold contrail'. The contrail dissolves promptly in the atmosphere [87].

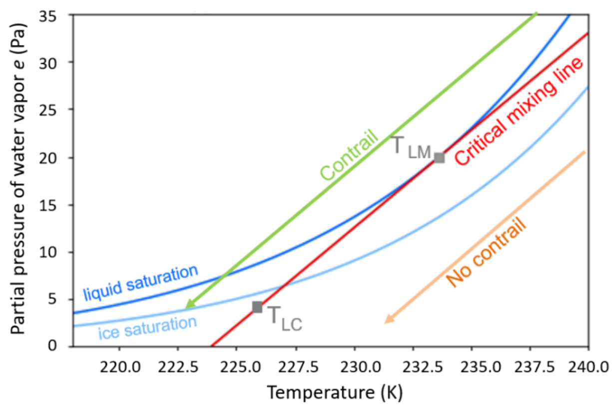

Figure 2.19: The Schmidt-Appleman criterion for the possible formation of (persistent) contrails [87].

Other emissions

A short note on other emissions (SO_x and soot) is given below:

- **SO_x**: SO_x emissions find its source in fuel impurities and account for several warming and cooling effects in the atmosphere. First, SO_x contributes to forming small particles that can act as nucleation sites for water particles to condense and form ice crystals. This enhances contrail formation and, therefore, has a net warming effect. Moreover, the sulfur oxides may react with H_2O to form sulfuric acid (H_2SO_4) and can be seen as having a cooling effect on the atmosphere [88]. Besides, the sulfate aerosols have a direct cooling effect as they reflect sunlight. It must, however, be said that the SO_x are generally negligibly small compared to other exhaust species.

- **Soot**: soot particles, or black carbon, have a direct warming effect as they absorb heat from solar radiation. Furthermore, the amount of soot particles strongly affects the ability to form contrails as these particles act as nucleation sources for water vapor particles to condense and form ice crystals.

Local air quality at airports is becoming more stringent to ensure healthy conditions. As the WET engine is only in its conceptual phase, engine emissions on the ground are not analyzed in this study.

Climate impact of WET engine

With the introduction of the WET engine, the emissions are likely to change depending on the exact conditions. The expected changes in emissions are discussed below for the most important exhaust species:

- **CO_2** : as the CO_2 emissions are directly proportional to fuel usage, lower CO_2 emissions are expected for the WET engine thanks to the lower SFC. The net positive RF is hence reduced if this engine type comes into service.

- **H_2O** : the effect of water injection on water vapor emissions is more difficult to predict compared to CO_2 emissions. An important aspect of the WET engine is the recovery of liquid water before entering the core nozzle. Without a water recovery system, more water is discharged at the nozzle, increasing the warming effect in the atmosphere. Depending on the WRR, the absolute water vapor emissions can be lowered, but this has to be investigated further. The WET engine does affect the probability of contrail formation. To qualitatively predict the likelihood, the parameters in Equation 2.12 should be considered. The EI_{H_2O}, Q, p_a, and both molar masses will not change for the wet engine as long as Jet-A is considered as fuel. However, the specific heat c_p and the propulsive efficiency are expected to change because of colder exhaust and the transfer of thermal energy to the bypass flow. Based on the above statements, no direct conclusions can be made regarding the formation of contrails. This has to be evaluated based on the WET engine results.

- **NO_x** : with the injection of water, temperature peaks are reduced in the combustor, leading to more homogeneous combustion. NO_x emissions are therefore expected to decrease for the WET engine. More information regarding the effect of water injection on NO_x can be found in Table 2.3.3. A further reduction in exhaust temperature due to the HRSG and condenser should facilitate a reduction in NO_x emissions.

Pouzolz et al. did a first evaluation on the climate impact of the WET engine compared to a baseline turbofan engine from 2015 and a future turbofan engine (2030-2035) [9]. They considered the most relevant aircraft emissions, i.e. RF due to CO_2, NO_x, and contrails, for a first-order estimation given a typical A320 mission. Building on this research, Kaiser et al. investigated the climate impact of the WET engine with a focus on the effect of different exhaust conditions on contrail formation [10]. Following the Schmidt-Appleman criterion, it is found that contrail formation could be reduced by 50% with adaptation of the WET engine. Even though the water share in the exhaust increases significantly by the water injection, it does not necessarily produce more contrails. The critical temperature for contrails to be formed is lower for the WET engine. As a positive result, aircraft can fly at higher altitudes without producing contrails. On top of this, if the core exhaust is mixed with the (warm) by-pass streams, the mixing line slope can be reduced even further. A smaller slope indicates a smaller possibility for the air to become saturated with water, subsequently forming crystals. The simulations from [10] are only performed for a cruise segment and do not consider taxiing and take-off. The WET engine promises to significantly reduce the climate impact of aircraft engines, but its climate effects depending on alternative fuels are not yet proven. Pouzolz et al. estimated the climate impact of a WET engine with SAF and found that total emissions could be reduced by more than 90% compared to a 2015 turbofan engine.

2.3.5. Liquid Hydrogen as Alternative Fuel

Apart from synthetic (or sustainable, depending on the production process) aviation fuel (SAF), hydrogen is also widely considered as an alternative fuel for aero engines. Focusing on the WET engine application, hydrogen shows an even bigger potential as an alternative to kerosene, because it has some additional advantages with respect to the implementation of the WET engine concept. For the sake of simplicity, it is assumed that hydrogen storage in its pure form is the only suitable method to efficiently store hydrogen in aircraft. Hydrogen storage in metal hydrides, adsorbents, or chemical carriers is not yet ready to be implemented in complex aircraft systems [89, 90]. The Figure 2.20 shows the density of hydrogen under various circumstances, with the areas for liquid hydrogen (LH2) storage, pressurized gaseous hydrogen, and cryo compressed hydrogen marked in blue[1]. In the automotive

[1]Kuhn, M., *ILK Dresden.*, Storage Density of Hydrogen

industry and for stationary applications the hydrogen is mostly stored as pressurized gas. However, as weight reduction is critical for aircraft performance, hydrogen should be stored as efficiently as possible without taking up too much volume. For this reason, liquid hydrogen is seen as more promising than compressed gaseous hydrogen because of the higher storage density. A major drawback of LH2 storage is the amount of energy that is required for the liquefaction process. Another disadvantage is the space that is required for the integration of the hydrogen tanks. Unlike kerosene, hydrogen is preferably stored in spherical or cylindrical tanks, and integration options are often limited to the fuselage of the aircraft as the tanks are too bulky for conventional wing designs. The main advantages of the use of LH2 as a fuel source in aircraft are summed below:

- **Climate impact:** with hydrogen combustion, the CO_2 emissions are eliminated, bringing aviation one big step closer to climate-neutral flying. The only products of hydrogen combustion are water and NO_x. The effects of direct H_2O emissions and contrail formation should be further investigated because water vapor is a critical GHG. Apart from water vapor, NO_x is also still one of the exhaust species due to the presence of diatomic nitrogen during the combustion process. From the literature, it is found that combustion of hydrogen lowers the NO_x emissions, but the effect of steam injection is not considered [91].

- **Enhanced bottoming cycle performance:** as the water share in the exhaust stream significantly increases, water recovery likely becomes more convenient. The size of the recovery system may become smaller. Furthermore, the LH2 can be used as a heat sink for the condenser to both evaporate and superheat the hydrogen and to cool the exhaust stream [13, 56, 58, 77]. The condenser size is expected to be much smaller as the temperature difference between the heat sink and source is bigger. The LH2 stream could potentially be used for intercooling as well.

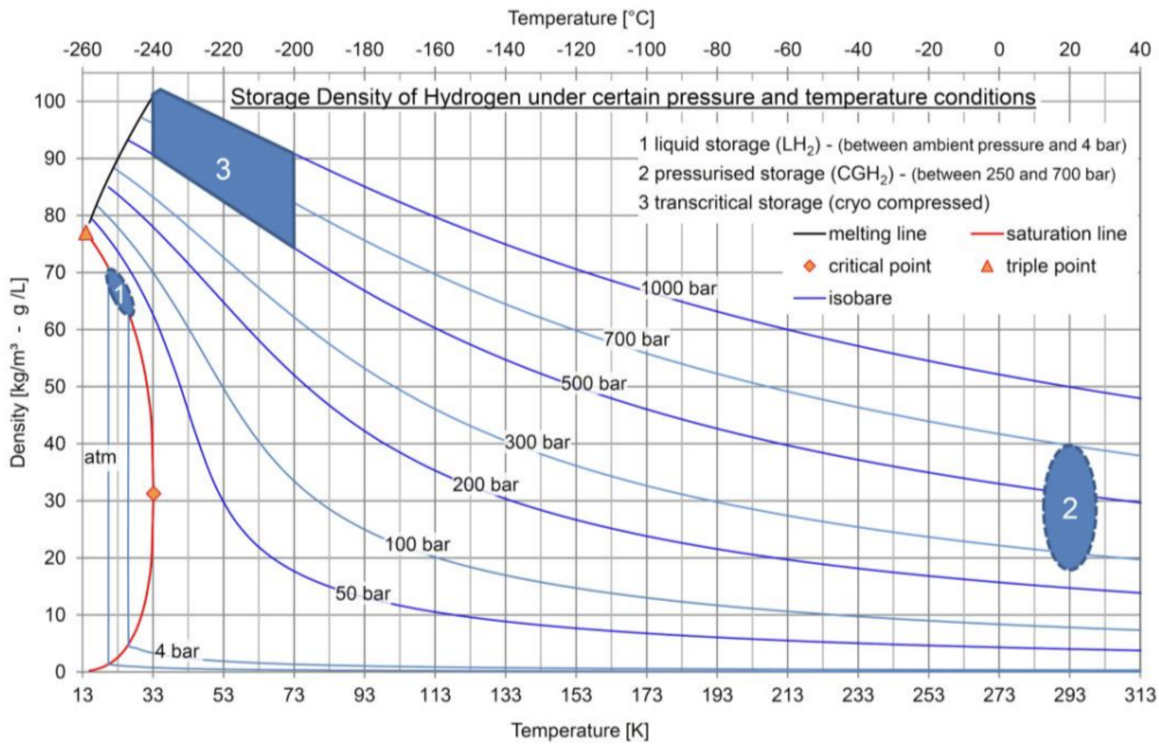

Figure 2.20: Hydrogen storage possibilities based on its density for various pressure and temperature conditions.

2.4. Summary & Research Gap

The aviation industry is a significant contributor to global greenhouse gas emissions, and its environmental impact is expected to grow with increasing air travel demand. To address this, the sector has set ambitious climate goals aimed at achieving net-zero carbon emissions by 2050. Key objectives include improving fuel efficiency, developing sustainable aviation fuels (SAFs), advancing electric and hydrogen propulsion technologies, and enhancing operational efficiencies. These goals align with the broader international efforts, such as the Paris Agreement, to limit global temperature rise and reduce the aviation sector's carbon footprint, driving innovation in aero engine technologies and sustainable practices.

To meet climate targets, both entirely new aircraft designs, such as the Flying-V, and innovative technologies that can be integrated into conventional turbofan engines are being developed. These novel engine technologies aim to reduce fuel consumption by employing unconventional solutions. The intercooled-recuperated aero engine (IRAE) is examined alongside combined cycle engines, including those incorporating an organic Rankine cycle or a supercritical CO_2 cycle. These cycle architectures have the potential to reduce emissions, enhance mechanical or electrical power generation, and lower fuel consumption. However, the benefits are often offset by the added weight and volume of the required heat exchangers and the increased complexity of the cycle. In 2021, MTU published an innovative cycle architecture, the water-enhanced turbofan engine, that uses a semi-closed (Cheng) cycle to inject and recover water from the engine's core. Although the HEXs still represent the biggest bottleneck, the relatively simple design and the working fluid of the secondary cycle (water) are a significant advantage. Unlike the ORC and sCO_2 cycle unit, the WET engine is not studied as much in detail and is therefore an interesting topic for research. First conceptual studies focus on the implementation of the concept for a turboshaft engine while the performance of the WET engine also in terms of emission reduction was studied using the NPSS software. However, the concept and its performance effects are not yet explored in detail for turbofan engines.

This thesis seeks to address the identified research gap by conducting a design exploration and parametric study on the Water-Enhanced Turbofan (WET) engine. The objective is to develop a turbofan model in pyCycle and openMDAO that serves as a robust simulation framework, facilitating future extensions with increased detail to enhance understanding of this innovative propulsion concept.

3

Aero Engine Modeling

The WET engine is an alternative engine architecture to replace the conventional high-bypass turbofan (HBTF) engine. An analysis tool is needed to model and simulate the WET engine. Besides this, the building blocks and fundamentals of turbofan engine simulation should be familiar to the reader. This chapter aims at providing background information regarding the used modeling framework in Section 3.1 and shortly discussing the modeling of the relevant aspects and components in an HBTF engine in Section 3.2 and Section 3.3, respectively. Lastly, the engine performance parameters are given in Section 3.4.

3.1. Modeling Framework

This section discusses the modeling and simulation tools that have been used to model and simulate the WET engine, namely OpenMDAO and pyCycle. Both tools have been developed by NASA and ensure the solving of complex (multidisciplinary) problems such as aero engine performance simulation and preliminary design.

3.1.1. PyCycle

PyCycle is an open-source (aero) engine cycle analysis tool that has been developed to overcome the limitations of the tool Numerical Propulsion System Simulation (NPSS) and to enable gradient-based optimization methods [92]. PyCycle uses the open-source framework OpenMDAO for Multidisciplinary Design Analysis and Optimization (MDAO) purposes. Modular component models form the basis of the pyCycle model library. These elements or basic component blocks can be linked together in random order to obtain and model a full aero engine system. The integration of analytical derivatives within the OpenMDAO framework reduces the computation costs significantly compared to the finite-difference derivatives used in NPSS [93]. The overall structure of pyCycle is shown by an extended design structure matrix (XDSM) in Figure 3.1 and it can be seen that the analysis tool consists of four main computational blocks:

- **Cycle:** this block consists of all thermodynamic equations that together form the heart of the software. The *Cycle* block represents multiple modular engine elements, such as compressors, turbines, and ducts, that can be connected to one another arbitrarily.

- **Balance:** only the interconnection of the individual component blocks does not give a valid aero engine system model. The *Balance* block comprises all the (physical) conservation equations and possible design requirements in the form of residual equations to close the system model. The balance equations are engine-specific and need to be defined in every *Cycle* both in the on-design and off-design calculation mode. PyCycle divides the balance equations into three types, namely conservation residual equations $\Re_c$, physical governing residual equations $\Re_p$, and design rule residual equations $\Re_d$ [94]. Equation 3.1 shows the typical form of a residual equation, where the target vector indicates the value that should be reached at the design point.

$$\Re_{c/d} = X_{state} - X_{target} = 0 \tag{3.1}$$

- **Solver:** all residual equations form a set of nonlinear equations. This set, together with all other cycle equations, is to be solved by a (numerical) *Solver*. Newton's method is typically used for finding solutions to a set of nonlinear equations [92].

- **Optimizer:** this block ensures minimizing or maximizing a certain problem objective by varying the design variables so that all (in)equality constraints are satisfied. The *Optimizer* is wrapped around an engine cycle, as shown in Subsection 3.1.1.

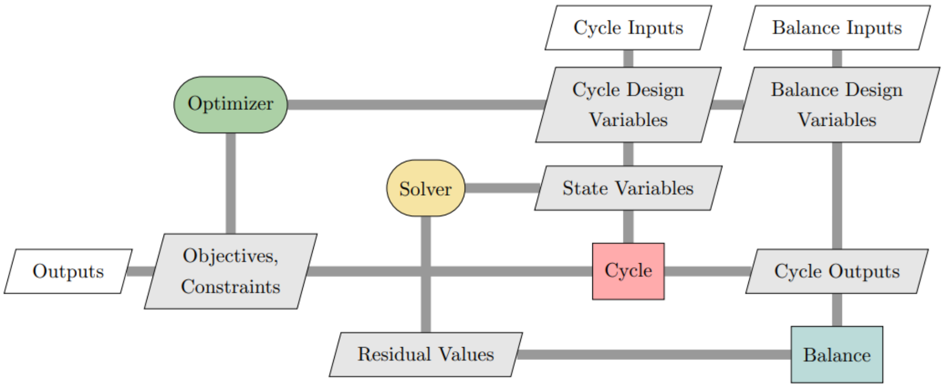

Figure 3.1: XDSM of the general lay-out of the pyCycle modeling framework [92].

In papers by NASA, the results of pyCycle are compared with the results of NPSS [92, 93, 94]. It was proven that pyCycle could calculate thermodynamic cycle data and cycle outputs with a (maximum relative) deviation of 0.03% with respect to the results of NPSS. Furthermore, the computational time reduces by approximately 3 orders of magnitude compared to NPSS, mainly because of a reduction in total derivative computational time [92]. This emphasizes the validity of the usage of pyCycle for aero engine modeling.

Apart from the abovementioned advantages, pyCycle has several other attractive functions, shortly summarized below:

- Each engine component is subdivided into sub-blocks, each having thermodynamic equations and corresponding derivatives. Hendricks et al. provide the exact structure of a compressor element in pyCycle [92]. Partial analytical derivatives are therefore easy to define at sub-component level.

- Both the single-point-design (SPD) and multiple-point-design (MPD) methods can be chosen to complete the cycle analysis. For MPD, cyclic data connections can be established between various flight operating points. Though the system becomes more complex, it matches real-life aero engine preliminary design better. SPD analysis is used in this study.

3.1.2. OpenMDAO

OpenMDAO is an open-source MDO framework that solves complex and coupled systems using Newton-type algorithms. The tool uses hierarchical techniques to maximize computing efficiency [94]. Again this software is developed by NASA. The OpenMDAO framework forms the basis for the implementation and application of the pyCycle library and has been chosen for several reasons. Firstly, the MDO software is a modular, object-oriented modeling structure with explicit and implicit computation objects (components). This provides flexibility, modularity, and ease of integration. Furthermore, the modular structure of OpenMDAO ensures the possibility of selecting various optimizers and (nonlinear) solvers that are capable of solving large, complex systems. Lastly, OpenMDAO features automatic computation of (analytic) derivatives across large, complicated models, allowing for efficient and accurate gradient-based optimization approach [92]. In Figure 3.2 the internal structure of the OpenMDAO is depicted with their corresponding hierarchies [94]. As can be seen, the tool consists of four fundamental classes, namely the *Problem*, *Group*, *Driver*, and *Component* class. The smallest class, i.e. the *Component* class, is subdivided into the *ExplicitComponent* and *ImplicitComponent* class. The interdependence and structure of the classes can be easily explained by Figure 3.2. The *Problem* class is the top-level block containing at least one object, in this case, a *Group* instance called 'model', and a single *Driver*. The model group comprises two sub-groups each containing two component instances. Based on the model inputs, that should be defined on the top-level *Problem* class, these inputs are assigned to the corresponding sub-groups and their components. The outputs of each *Component* instance are then passed together to the *Driver*.

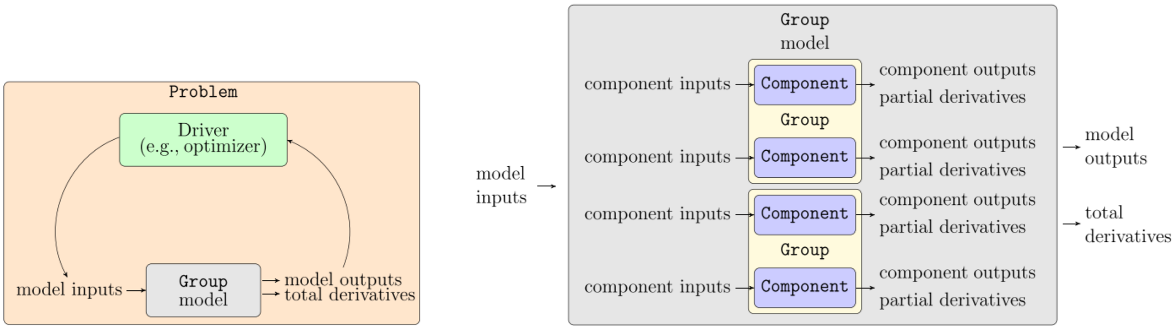

Figure 3.2: Hierarchical structure of the OpenMDAO framework containing the instances *Problem, Solver, Group and Component* [94].

OpenMDAO (and pyCycle) work with two types of derivatives that can also be identified in Figure 3.2:

1. **Partial derivatives:** the derivative of the *Component* output with respect to the *Component* input. These partial derivatives are directly coded in the component instances themselves. This improves computational speed significantly [92, 94]. When the derivatives are not defined, the software uses finite difference methods to define the component-specific derivatives. For the *ExplicitComponent*, derivatives are analytically computed in a straightforward matter. For the *ImplicitComponent* derivatives with respect to in- and outputs are calculated for the residual equation corresponding to the implicit component.

2. **Total derivatives:** the derivative of the model outputs with respect to the model inputs. Total derivatives are calculated in two steps, of which the first is the evaluation and collection of all partial derivatives from all components. Secondly, a system of equations containing all these partial derivatives is solved in either direct or adjoint form to obtain the total derivatives. The exact mathematical derivation for the total derivative computational approach can be found in the literature [92, 94, 95]. The total derivative for any objective function f w.r.t. the design variables x and implicit state variables y_i is shown in Equation 3.2. For the approach in [92] the total derivative is assumed to be taken around a converged point for which the residual equation ($\Re = 0$) is zero for any design variable. The final equation for both the direct and adjoint methods are given in Equation 3.3 and Equation 3.4, respectively [92].

$$\frac{df}{dx} = \frac{\partial f}{\partial x} + \frac{\partial f}{\partial y}\frac{dy}{dx} \tag{3.2}$$

$$\frac{df}{dx} = \frac{\partial f}{\partial x} + \frac{\partial f}{\partial y}\frac{dy}{dx} \quad with \quad \frac{dy}{dx} = -\left[\frac{\partial \Re}{\partial y}\right]^{-1}\frac{\partial \Re}{\partial x} \tag{3.3}$$

$$\frac{df}{dx} = \frac{\partial f}{\partial x} + \psi^T\frac{\partial \Re}{\partial x} \quad with \quad \psi = -\left[\frac{\partial \Re^T}{\partial y}\right]^{-1}\left[\frac{\partial f^T}{\partial y}\right] \tag{3.4}$$

To summarize, the derivatives are computed semi-numerically, where partial derivatives can be computed either numerically or analytically, and total derivatives are calculated by solving a system of equations.

3.2. Gas Composition & Thermodynamic Properties

A core part of the pyCycle software is the calculation of the thermodynamic properties at all stations between the various components. The standard pyCycle framework can accurately compute the properties of air and air-fuel mixtures. Several methods are available for these computations, but Chemical Equilibrium and Application (CEA) is integrated already in the pyCycle/OpenMDAO environment. The CEA library makes use of chemical equilibrium, given a thermodynamic state, to estimate the composition of a gas mixture, consisting of a user-defined number of chemical species [92, 93]. Because no chemical equilibrium library was found to be implemented directly within pyCycle/OpenMDAO, NASA integrated an adapted version of CEA within the framework. The implementation of the method has been verified against original CEA results [92, 93]. Before discussing the fundamentals of CEA method, it is worth mentioning that pyCycle can calculate the thermodynamic properties via two methods:

1. **CEA mode:** gas composition and properties are calculated with CEA during the cycle simulation.
2. **TABULAR mode:** properties are obtained from a generated thermodynamic table set through interpolation. Gas composition is not explicitly calculated, but determined by the fuel-to-air (FAR) ratio parameter.

PyCycle computes the gas properties in two steps using the CEA approach [96]. The method is visualized with the XDSM diagram in Figure 3.3. The first step comprises the minimization of Gibbs free energy that should result in chemical equilibrium composition among all species for a predefined thermodynamic state. This state is characterized by two independent state variables among temperature T, pressure p, density ρ, entropy S, and enthalpy h. In pyCycle, the *Thermo* class incorporates the CEA code and has three modes to calculate the properties: $Tp-mode$, $hp-mode$, and $Sp-mode$. The $Tp-mode$ is shortly explained below. Firstly, the Gibbs free energy is defined by multiplying the species concentration n_j and summing the result with the chemical potential μ_j for the number of species, N_s, as shown in Equation 3.5. The subscript j represents the jth species in the gas mixture.

$$g = \sum_{j}^{N_s}(\mu_j n_j) \quad where \quad n_j = \frac{1}{M_j} \tag{3.5}$$

The chemical potential of species μ_j in an ideal gas mixture is given by Equation 3.6.

$$\frac{\mu_j}{RT} = \frac{H_j^\circ(T)}{RT} - \frac{S_j^\circ(T)}{RT} + ln\Big(\frac{p}{p_a}\Big) + ln(n_j) - ln\Big(\sum_{k}^{N_s} n_k\Big) \tag{3.6}$$

The enthalpy H_j° and entropy S_j° relations are temperature dependent and are calculated with the so-called NASA polynomials defined by a set of coefficients $c_0, ..., c_8$. Coefficients for all species can be found in the paper of McBride et al. from NASA [97]. The general relation for both the enthalpy and entropy for the jth species are given in Equation 3.7 and Equation 3.8, respectively.

$$\frac{H_j^\circ(T)}{RT} = -\frac{c_0}{T^2} + \frac{c_1}{T}ln(T) + c_2 + \frac{c_3}{2}T + \frac{c_4}{3}T^2 + \frac{c_5}{4}T^3 + \frac{c_6}{5}T^4 + \frac{c_7}{T} \tag{3.7}$$

$$\frac{S_j^\circ(T)}{R} = -\frac{c_0}{2T^2} - \frac{c_1}{T} + c_2 ln(T) + c_3 T + \frac{c_4}{2}T^2 + \frac{c_5}{3}T^3 + \frac{c_6}{4}T^4 + c_8 \tag{3.8}$$

The minimization of free energy is a prerequisite for chemical equilibrium. A constraint concerning the mass balance (mb) for each atomic component of the species in the mixture should be imposed on the minimization (Equation 3.9). N_s is the number of species in the mixture, a_{ij} is the stoichiometric value for element i of species j and b_i° is the amount of element i per mass unit of the mixture composition [93, 96]. The Equation 3.9 provides one constraint per mixture element, hence a total of N_e constraints are given.

$$\Re_{mb,i} = \sum_{j=1}^{N_s}(a_{ij}n_j) - b_i^\circ = 0 \tag{3.9}$$

To solve and minimize the Gibbs free energy using the mass constraint (Equation 3.9), a Lagrangian is formed containing a Lagrange multiplier λ_i for each ith element. The Lagrangian and its derivative are given in Equation 3.10 and Equation 3.11, respectively.

$$G = \sum_{j=1}^{N_s}(\mu_j n_j) + \sum_{i=1}^{N_e}\lambda_i\Big(\sum_{j=1}^{N_s}(a_{ij}n_j) - b_i^0\Big) \tag{3.10}$$

$$\delta G = \sum_{j=1}^{N_s}\Big(\mu_j + \sum_{i=1}^{N_e}(\lambda_i a_{ij})\Big)\delta n_j + \sum_{i=1}^{N_e}\Big(\sum_{j=1}^{N_s}(a_{ij}n_j) - b_i^0\Big)\delta\lambda_i = 0 \tag{3.11}$$

The minimum of the Gibbs free energy is found by solving for the zeros of the derivative (with respect to the variables n and λ) of the Gibbs free energy. The Equation 3.10 can be split into two sets of equations, with one set similar to Equation 3.9 and the other is provided by Equation 3.12. The residual equation in Equation 3.12 represents the Gibbs free energy with the new Lagrange multiplier π.

$$\Re_{gibbs} = \frac{\mu_j}{RT} - \sum_{i=1}^{N_e}(\pi_i a_{ij}) = 0 \quad where \quad \pi_i = -\frac{\lambda_i}{RT} \tag{3.12}$$

The sets in Equation 3.9 and Equation 3.12 have $N_s + N_e$ residual equations with $N_s + N_e$ unknowns. The system can therefore be solved. This process is indicated in Figure 3.3 by the two most upper-left green blocks. Initial values for composition n and Lagrange multipliers π are fed to CEA and this gives the residual values as feedback to the solver.

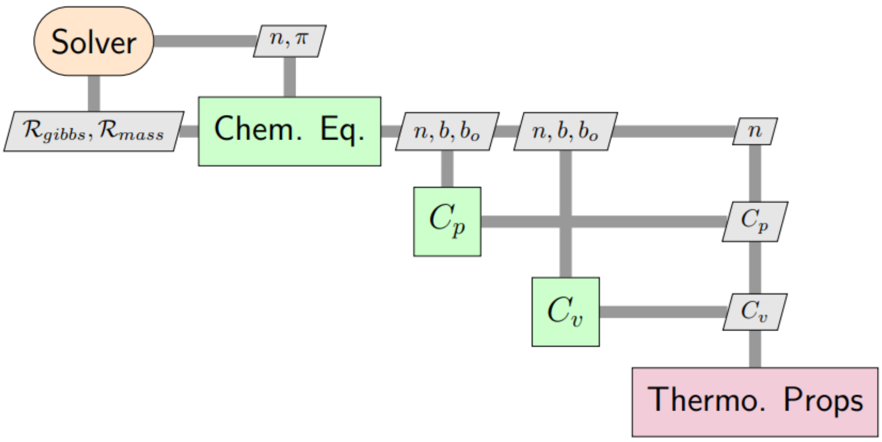

Figure 3.3: XDSM of Chemical Equilibrium and Application approach integrated in the pyCycle framework [93].

When the converged equilibrium composition is found, the vector $\mathbf{n}$ containing the concentrations for each species in the mixture is passed to the next class, see Figure 3.3. In this *Thermo. Props* class, the thermodynamic state of the mixture is calculated. The thermodynamic properties include nine quantities, listed in Table 3.1. When the *TABULAR* approach is used during simulation, nine table sets should be provided to pyCycle containing these thermodynamic properties as a function of temperature, pressure, and composition (FAR), i.e. three-dimensional table sets.

It is sufficient to provide the table for one set of independent set of thermodynamic states, e.g. temperature, pressure, and composition. All other properties can be computed accordingly. h, S and R are calculated by the summation of all species-specific properties. An exemplary calculation for obtaining the enthalpy of the gas mixture is given in Equation 3.13. N_s is the number of species in the gas mixture.

$$H_{mixture} = \sum_{j}^{N_s}(n_j H_j) \tag{3.13}$$

Table 3.1: Thermodynamic properties defined by pyCycle at each station.

Thermodynamic property	Description	Unit
T	Temperature	K
p	Pressure	Pa
h	Specific enthalpy	J/kg
S	Specific entropy	$J/kg/K$
γ	Ratio of specific heats	$-$
C_p	Specific heat at constant pressure	$J/kg/K$
C_v	Specific heat at constant volume	$J/kg/K$
ρ	Density	kg/m^3
R	Total specific gas constant	$J/kg/K$

The isobaric specific heat is calculated using a polynomial similar to that in Equation 3.7 and Equation 3.8. Equation 3.14 provides the polynomial form for C_p calculations.

$$\frac{C^{\circ}_{p,j}(T)}{R} = \frac{c_0}{T^2} + \frac{c_1}{T} + c_2 + c_3T + c_4T^2 + c_5T^3 + c_6T^4 \tag{3.14}$$

The other properties, γ, C_v, and ρ are calculated following the ideal gas law and formulated below.

$$C_v = C_p - R \tag{3.15}$$

$$\gamma = \frac{C_p}{C_v} \tag{3.16}$$

$$\rho = \frac{p}{RT} \tag{3.17}$$

3.3. Main Gas Path

A modern (ultra-)HBTF engine model is used as a basis for the development of the WET engine model in pyCycle. This section briefly discusses the fundamentals of the most relevant components of a regular turbofan engine, supported with some modeling equations as integrated in the pyCycle framework. Akba et al. also give a short explanation of some pyCycle components for the sake of completeness [98].

Flight conditions

Based on a user-defined altitude and Mach number, the (ambient) flight conditions can be calculated. Air temperature, pressure, density, viscosity, and speed of sound can be obtained from the United States standard atmosphere (1976) tabular data sets [1]. Total and static flow properties are outputs of this block and are used as inputs for the engine model.

Inlet

The inlet (or intake) component computes the flow conditions within the inlet cowl. The total pressure is slightly lower than the ambient one, because of various (aerodynamic/inflow/friction) losses. The pressure recovery in the intake is characterized by a recovery factor, i.e. a ram recovery factor. Both the ram recovery and the ram drag are formulated in pyCycle by Equation 3.18 and Equation 3.19, where the ram drag is defined as the ratio of air momentum at the inlet and gravity.

$$p_{t,2} = \eta_{ram} \cdot p_{t,0} \tag{3.18}$$

$$F_{ram} = \frac{\dot{m}_{in} V_{in}}{g} \tag{3.19}$$

Fan & Compressors

Calculations for the fan, LPC, IPC, and/or HPC are performed with one single *Compressor* class. Hendricks et al. gave a detailed explanation regarding the structure and equations of the compressor element [92]. The compressor is broken down into three sub-blocks: pressure rise, enthalpy rise, and power calculations. The pressure rise over a compressor, given a prescribed pressure ratio (PR), is given in Equation 3.20. Furthermore, Equation 3.21 shows that the total enthalpy after the last stage of the compressor is calculated with the isentropic efficiency relation. Lastly, the required power and torque are computed following Equation 3.22 and Equation 3.23, respectively. PyCycle requires a map

[1] https://www.digitaldutch.com/atmoscalc/

for each type of compressor in the model. Lastly, the default efficiency value is the isentropic/adiabatic one, but this can be changed to the polytropic efficiency. To do this, an extra balance equation per compressor should be added in the model.

$$p_{t,2} = PR \cdot p_{t,1} \tag{3.20}$$

$$h_{t,2} = h_{t,1} + \frac{h_{t,2,is} - h_{t,1}}{\eta_{is}} \tag{3.21}$$

$$\dot{W}_{comp} = \dot{m}(h_{t,2} - h_{t,1}) \tag{3.22}$$

$$\tau_{shaft} = \frac{\dot{W}_{comp}}{N_{mech,shaft}} \tag{3.23}$$

Combustor

In the combustor, fuel is added and ignited to heat the compressed air to a certain temperature. This is done with the *ThermoAdd* class where a reactant is added in the main flow. Its composition should be provided as well as the fuel's enthalpy of formation. The enthalpy of formation for a fuel is calculated assuming stoichiometric combustion in combination with either the lower or higher heating value (LHV/HHV), depending on the phase in which water is produced. For combustion processes, hence throughout this report, the LHV value is used. The conservation of energy for the burner is provided by Equation 3.24. The mass-averaged enthalpy at the inlet and outlet of the combustor together with the exit pressure are known. It follows that the other properties can be calculated through the function for property calculation as indicated by the $hp - mode$ in pyCycle.

$$\dot{m}_{air}h_{air} + \dot{m}_f h_{f,HOF} = \dot{m}_{exh}h_{exh} \tag{3.24}$$

Turbines

A similar methodology is used for turbines as has been explained for compressors. Contrary to the compressor component, the PR is used as an iteration variable to ensure zero net torque at the shafts (Equation 3.25). Moreover, the definitions for the total outlet enthalpy and power/torque of the turbine are slightly different as the enthalpy decreases through the turbine stages (Equation 3.26).

$$p_{t,2} = \frac{p_{t,1}}{PR} \tag{3.25}$$

$$h_{t,2} = h_{t,1} - \eta_{is}(h_{t,1} - h_{t,2,is}) \tag{3.26}$$

Bypass-duct and Heat-Exchangers

There are no detailed heat exchanger models available within the pyCycle framework. The *Duct* element partly solves this issue. The duct component can be seen as a simple heat exchanger where both a pressure loss factor and a heat flow $\dot{Q}$ can be set by the user. The outlet pressure is computed with Equation 3.25 and the total outlet enthalpy with an expression similar to that in Equation 3.22. The duct element is also used to model the bypass duct for TF engines.

Nozzle

The *Nozzle* element is an important part of aero engines for the generation of thrust force. The exit conditions for both the core and bypass nozzle are prescribed to be the ambient (static) pressure. A loss coefficient and nozzle type should be provided among the input parameters of this element in pyCycle. Regarding the nozzle losses, either a gross thrust coefficient or velocity coefficient should be provided. Finally, the gross thrust is computed for the nozzle section and its equation is given below (given a gross thrust coefficient $C_{f,g}$).

$$F_g = F_{g,ideal} \cdot C_{f,g} = \frac{\dot{m}_{nozz}V_{ideal}}{g} \cdot C_{f,g} \tag{3.27}$$

Bleeds & Turbine Cooling

Over the past 70 years, aero engine's TIT and OPR have been increased continuously to improve thermal efficiency [21]. However, maximum material temperatures still represent limitations for the operation of aero engines. Turbine cooling has been a mature technique to reduce the turbine blades' temperature without lowering the TIT. PyCycle contains a *Bleeds* class where pressurized air (or another stream) can be extracted from the main gas path and be inserted after the combustor in the turbine stages. Based on a pressure fraction, the cooling injection location can be chosen. Moreover, it can be chosen whether the bleed air contributes to the work extraction process or not. Similar to the *Bleeds* class, compressor elements can also be used for bleeds. A detailed cooling model is available in pyCycle as well, but this class is not used in this work for the sake of simplicity.

3.4. Engine Performance Parameters

The performance of an aero engine is dependent on several parameters. To consistently calculate the performance of the engine, this section clarifies the definition of aero engine performance parameters that will be used throughout this document. This is done for both the conventional turbofan engine and the new WET engine.

Overall Pressure Ratio

The overall pressure ratio (OPR) is defined as the ratio of stagnation (total) pressure after the last compressor stage and before the first compressor stage. For a conventional TF engine comprising a fan, LPC and HPC, the OPR is defined as in Equation 3.28. Regarding the CC engine, the same OPR definition as Equation 3.28 can be used.

$$\Pi_{overall} = \Pi_{fan}\Pi_{LPC}\Pi_{HPC} = \frac{P_{t,hpc}}{P_{t,intake}} \tag{3.28}$$

Thrust Specific Fuel Consumption

The thrust-specific fuel consumption (TSFC) is one of the most important aero-engine performance parameters. It describes how efficient the engine is in terms of fuel consumption and thrust generation. PyCycle calculates the TSFC for a turbofan engine following Equation 3.29 where F_g is the gross thrust of the nozzle. It is assumed that both the TF and WET engines have two nozzles: the core nozzle and the bypass nozzle.

$$TSFC = \frac{\dot{m}_f}{F_n} = \frac{\dot{m}_f}{F_{g,core} + F_{g,bypass} - F_{ram}} \tag{3.29}$$

Thermal Efficiency

The thermal efficiency of a TF engine can be seen as the kinetic energy increase achieved through the engine compared to the thermal energy that is inserted into the combustor [27]. Thermal efficiency can be split into three parts. The combustion efficiency, η_{comb}, is the conversion of chemical energy to heat. The thermodynamic efficiency, η_{thermo} is the conversion of heat to gas (generator) power. Finally, the jet generation efficiency, $\eta_{jet,gen}$ accounts for the conversion of the heat to a kinetic energy increase with respect to the inlet conditions. Based on these definitions, the thermal efficiency for a conventional turbofan engine is given in Equation 3.30.

$$\eta_{th} = \eta_{comb}\eta_{thermo}\eta_{jet,gen} = \frac{\sum \frac{1}{2}\dot{m}_{nozz}(V_{id,jet}^2 - V_0^2)}{\dot{m}_f \cdot LHV} = \frac{\sum P_{prop}}{\dot{m}_f \cdot LHV} \tag{3.30}$$

Regarding the WET engine, two heat exchangers are placed between the last turbine stage and the nozzle. Equation 3.30 can still be used.

Propulsive efficiency

The propulsive efficiency is the ratio of useful thrust power produced by a turbofan engine to the difference in kinetic energy between the nozzle inlet and the freestream conditions. A slight share of the energy exiting the nozzle is not used to generate thrust but goes in vortex generation/turbulence. Its mathematical formulation is given below in Equation 3.31.

$$\eta_{prop} = \frac{F_n \cdot V_0}{\sum \frac{1}{2}\dot{m}_{nozz}(V_{id,jet}^2 - V_0^2)} = \frac{\sum P_{thrust}}{\sum P_{prop}} \tag{3.31}$$

Overall efficiency

The (theoretical) total efficiency of the aero engine is the product of the thermal and the propulsive efficiency and is shown in Equation 3.32:

$$\eta_{tot} = \eta_{th}\eta_{prop} = \frac{F_n \cdot V}{\dot{m}_f \cdot LHV} \tag{3.32}$$

Other parameters

Other performance parameters that could give relevant performance information in the conceptual design phase are the specific thrust, thrust-to-weight ratio, and the velocity ratio of the engine. The first relates the performance of the engine to the intake mass flow rate (Equation 3.33). Specific thrust can indicate engine performance based on size, weight, frontal area, and volume, as well as technological level [27]. The second parameter represents the performance of the engine (thrust) compared to its weight and this indicator should be relatively high (Equation 3.34). Both equations are shown below. Lastly, the velocity ratio compares the (ideal) exit velocity of both the bypass and core nozzle and is provided in Equation 3.35.

$$F_s = \frac{F_n}{\dot{m}_{in}} \tag{3.33}$$

$$TW = \frac{F_n}{W_{engine}} \tag{3.34}$$

$$Velocity\ Ratio = \frac{V_{id,nozz,byp}}{V_{id,nozz,core}} \tag{3.35}$$

4

Model Development

Although pyCycle provides a good modeling framework to model aero engines, it is not always possible to model alternative engine architectures. This is also the case for the WET engine. Liquid water is, for example, not supported by pyCycle, which is an essential aspect of this type of engine. This chapter discusses the adjustments made in pyCycle & OpenMDAO so that the WET engine can be modeled. In Section 4.1 the thermodynamic data generation process and the changes regarding the thermodynamic model are addressed. The steam injection component as integrated in pyCycle is discussed in Section 4.2. Section 4.3 describes the combustor component using several fuels. Subsequently, Section 4.4 gives an overview regarding modeling the condensation process and the water separator. Lastly, the modeling of the heat exchangers and the water cycle is discussed in Section 4.5 and Section 4.6, respectively.

4.1. Thermodynamic Properties & Table Generation

It has already been mentioned in Section 3.2 that the user can select either 'CEA'-mode or 'TABULAR'-mode to simulate the engine cycle that has been created. The thermodynamic table sets required in the TABULAR mode should be created beforehand using CEA calculations. Accuracy between the two modes should not differ as long as the thermodynamic tables contain sufficient data points. Nonetheless, the computational time is expected to play a more significant role. Especially when facing (multidisciplinary) optimization of large, more complex aero engines, this CEA mode of calculating properties becomes increasingly disadvantageous. A short comparison is performed between the two calculation modes to assess the difference in computational time and the accuracy of engine performance parameters. The results are tabulated in Appendix A.1, Table A.1. Although the used tables are not very extensive and detailed, tabular results match already with CEA results. The discrepancy is lower than approximately 1.5%. Nevertheless, the improvement in computational time as the model becomes more complex can directly be observed. Calculations with the TABULAR mode are more than 70% faster compared to the CEA mode. This resulted in a preference to focus in this work on the TABULAR simulation mode and the generation of the required thermodynamic tables rather than working with the computationally expensive CEA mode.

4.1.1. Thermodynamic Table Set Generation Process

The TABULAR mode is only available if specific thermodynamic tables are generated. Based on temperature, pressure, and the fuel-to-air ratio (FAR) as inputs, all other thermodynamic properties (see Table 3.1) are calculated. In other words, the thermodynamic properties (h, S, C_p, C_v, γ, ρ and R) are calculated and stored in three-dimensional tables as a function of T, p, and FAR. To simulate the injection of water into the core flow, an additional table input is required, namely the water-to-air ratio (WAR). The dimension of the table sets should therefore be increased from three to four. Based on the 4D table set, five regions should be considered when calculating the thermodynamic properties:

- **FAR=0 & WAR=0:** air, default calculation method in pyCycle explained below.

- **FAR>0 & WAR=0:** exhaust gas, default calculation method in pyCycle explained below.
- **FAR=0 & WAR>0:** wet air, property calculation method explained in Subsection 4.1.3.
- **FAR>0 & WAR>0, no condensation:** wet exhaust gas, property calculation method explained in Subsection 4.1.4.
- **FAR>0 & WAR>0, condensation region:** partially condensed exhaust gas, property calculation method explained in Subsection 4.1.5.

The air and dry exhaust gas properties are computed via a two-step approach. This method is shown in Figure 4.1 below and is used as the default by pyCycle. First, in the more general case of exhaust gases, the gas composition is determined in the *ThermoAdd* class based on the fuel being used in the engine. With the new composition together with temperature, pressure, and the selected FAR, the thermodynamic properties are subsequently calculated. The enthalpy of formation for the fuel is not taken into account during the table generation process as this value should only be provided for each design point. To calculate the properties for air (FAR=0, WAR=0), the *Thermo* class is used only together with the composition of air.

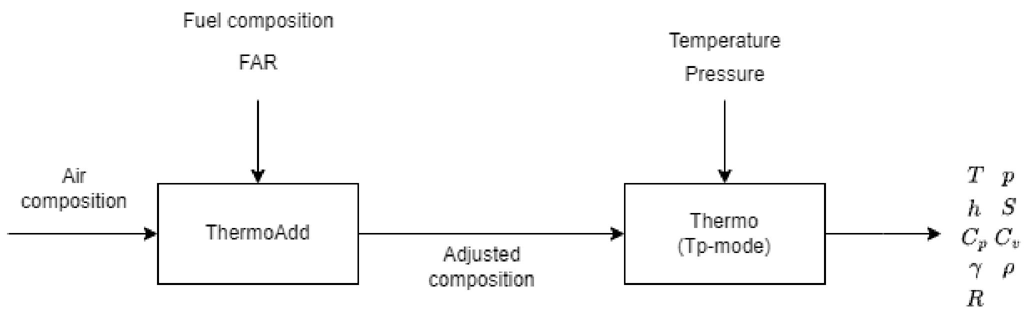

Figure 4.1: Table generation method for air and dry exhaust gas thermodynamic properties in pyCycle.

4.1.2. Thermodynamic Reference State

Within pyCycle, the reference state point is set to sea level conditions: $p_{ref} = 101325\ Pa$ and $T_{ref} = 298.15\ K$. The enthalpy values of all elements (Ar, C, H_2, N_2, O_2 in pyCycle) are assumed to be zero at the reference state point. This also implies that the reference enthalpy values of all molecules at this point are the enthalpies of formation. This information can be found in the publication of McBride et al. [97]. The reference values for the entropy are also provided in the work of NASA and coincide with the values found in pyCycle [97].

4.1.3. The Wet Air Model

Throughout this document, it is assumed that the water is mixed with the main gas path before the combustor entry. This means that the engine's core can be split into two parts: the part before the combustor where humid/wet air should be modeled and after the combustor where humid/wet exhaust gas should be considered. In this section, it is explained how the wet air is modeled in pyCycle.

The modeling of gas mixtures with high water vapor contents proved to be not accurate when using CEA [99]. To achieve more precise results, it is important to consider the non-ideal behavior of steam in the mixture. In literature, it is found that wet air cannot be modeled with the ideal gas law if the steam concentration is higher than 10% [99]. The assessment of the WET engine in this report considers steam concentrations between 0-40%, hence a new model should be adopted to accurately model the thermodynamic properties in the engine core. DLR investigated turbine exhaust flows with high steam concentrations to develop a gas model for the WET engine [100]. El-Soueidan et al. give an extensive literature study on the modeling of steam and various equations of state for real gas effects in turbomachinery flow [100]. Based on this state-of-the art analysis, DLR created a gas model accounting for real gas effects the steam in the gas-steam mixture. For this study, the core method of

DLR's gas model is used and adapted in the pyCycle framework to generate the thermodynamic tables. The gas model, hereafter named as wet air model (WA model), consists of two separate models, one for steam and the other for dry air, whose predictions are combined based on the ideal gas mixture approximation:

1. **Ideal exhaust gas mixture:** DLR uses Cantera to calculate the chemical equilibrium of the exhaust gas mixture[1]. Cantera and NASA CEA are different tools to calculate the chemical equilibrium composition based on temperature, pressure, and FAR. However, differences between the composition calculated by CEA and Cantera are assumed to be negligibly small [101]. Based on composition (defined by the molar fractions of the species) the molar mass of the mixture is calculated similarly as for the enthalpy (Equation 3.13).

2. **Real steam correction:** Since the non-ideal behavior of steam must be accounted for, the water properties provided by CEA/Cantera are not utilized. Instead, a highly accurate thermodynamic property model is employed: the IAPWS-95 formulation, developed by the International Association for the Properties of Water and Steam (IAPWS) [102]. Unlike the IF97 model, which is specifically designed for industrial applications and features region-dependent equations for computational efficiency [103], the IAPWS-95 model provides a single-region formulation valid over the entire phase diagram. This makes it particularly suitable for applications requiring high accuracy across a wide range of thermodynamic conditions, such as aero-engine turbine exhaust modeling. A key advantage of IAPWS-95 is its ability to serve as a fundamental equation of state (EoS), ensuring continuous and consistent property calculations, whereas IF97 relies on region-specific equations that introduce discontinuities at region boundaries [104]. Additionally, IAPWS-95 allows for reference state adjustments, which is not possible in CoolProp for IF97, making it more flexible in thermodynamic cycle simulations. However, IAPWS-95 has a significantly higher computational cost due to its complex implicit equations, whereas IF97 is optimized for rapid industrial calculations with explicit formulations [103, 105]. For aero engine applications, both IAPWS-95 and IF97 can predict steam properties with high accuracy. However, due to the need for a consistent and adaptable reference state, IAPWS-95 is preferred in this study despite its increased computational demand.

A general schematic overview of the wet (exhaust) air model that is used for both the wet air and wet exhaust gas property calculation is given in Figure 4.2 below.

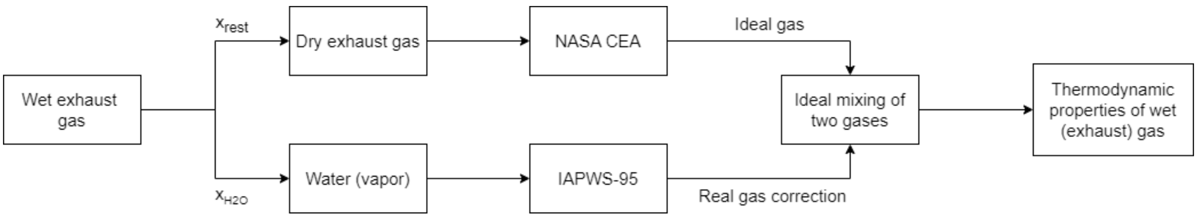

Figure 4.2: General structure of the wet (exhaust) gas model applied for the WET engine in this study.

The gas properties for superheated wet air are hence a combination of dry air and steam properties. To combine these parameters, both molar fraction and mass fraction have to be defined for the wet air, see Equation 4.1 and Equation 4.2, respectively. Based on the selected WAR, the mass fraction is calculated, and subsequently all the thermodynamic properties.

$$x_j = \frac{n_j}{n_{gas,tot}} \quad (4.1) \qquad k_j = \frac{m_j}{m_{gas,tot}} = \frac{WAR}{WAR+1} \quad (4.2)$$

To compute the thermodynamic property of a species in a gas mixture, the temperature and its (partial) pressure should be known. The partial pressure is defined according to Dalton's law, which states that the total pressure of a gas mixture is equal to the sum of the partial pressures of the individual species in the gas mixture (Equation 4.3 for wet air). Based on Dalton's law and the definition of molar fraction and WAR in Equation 2.4, the relation between WAR and p_{H2O} can be established via

[1]https://cantera.org/

Equation 4.4. Knowing the pressure of the gas mixture and the WAR is sufficient to rewrite Equation 4.4 to find the partial pressure of water.

$$p_{wet,air} = \sum_{j=1}^{N_s} p_j = p_{dry,air} + p_{H2O} = (x_{dry,air} + x_{H2O}) \cdot p \tag{4.3}$$

$$WAR_{wet,air} = \frac{m_{H2O}}{m_{air}} = \frac{n_{H2O} \cdot M_{H2O}}{n_{air} \cdot M_{air}} = \frac{M_{H2O}}{M_{air}} \frac{x_{H2O}}{x_{air}} = \frac{M_{H2O}}{M_{air}} \frac{p_{H2O}}{p_{air}} = \frac{M_{H2O}}{M_{air}} \frac{p_{H2O}}{(p - p_{H2O})} \tag{4.4}$$

The wet air properties needed for the table generation in pyCycle (Table 3.1) are calculated following Equation 4.5a until Equation 4.5g The specific heat values, the density, enthalpy and entropy values for water are obtained through CoolProp given the temperature of the wet mixture and the partial pressure of water. The specific heat at constant air pressure is calculated in pyCycle using NASA polynomials and is therefore pressure-independent. Real gas effects are accounted for by the IAPWS-95 model. Thus, the specific heat of water is pressure-dependent. The density is calculated using the ideal gas law (Equation 3.17). As both the density for air and water are calculated given the partial pressures, the values can be added up to find the mixture density. Lastly, the reference state for the enthalpy and entropy is the same for both models (CEA and IAPWS-95). The reference state in CoolProp is adjusted and set with the *set-reference-state* and *DMOLAR* functions.

$$C_{p,wet,air} = k_{air}(WAR) \cdot C_{p,air}(T) + k_{H2O}(WAR) \cdot C_{p,H2O}(T, p_{H2O}) \tag{4.5a}$$

$$C_{v,wet,air} = k_{air}(WAR) \cdot C_{v,air}(T) + k_{H2O}(WAR) \cdot C_{v,H2O}(T, p_{H2O}) \tag{4.5b}$$

$$\rho_{wet,air} = \rho_{air}(T, p_{air}) + \rho_{H2O}(T, p_{H2O}) \tag{4.5c}$$

$$\gamma_{wet,air} = \frac{C_{p,wet,air}}{C_{v,wet,air}} \tag{4.5d}$$

$$R_{wet,air} = x_{air}R_{air} + x_{H2O}R_{H2O} \tag{4.5e}$$

$$h_{wet,air} = k_{air}(WAR) \cdot h_{air}(T, p_{air}) + k_{H2O}(WAR) \cdot h_{H2O}(T, p_{H2O}) \tag{4.5f}$$

$$S_{wet,air} = k_{air}(WAR) \cdot S_{air}(T, p_{air}) + k_{H2O}(WAR) \cdot S_{H2O}(T, p_{H2O}) \tag{4.5g}$$

This part of the thermodynamic model ($WAR > 0$, $FAR = 0$) will be verified in Section 5.1. More details regarding the implementation of the new thermodynamic tables and the limitations can be found in Subsection 4.1.6.

4.1.4. Humid Exhaust Gas Model

The humid exhaust gas model is needed to estimate the thermodynamic properties downstream of the combustor. For conventional aircraft, the fuel-induced water in the exhaust is relatively small (generally smaller than 5%). This supports the assumption in pyCycle that water vapor can be modeled as an ideal gas downstream of the combustor. However, when large water shares are present in the core flow due to the water injection, this assumption may not be valid anymore as real gas effects are not negligible [99]. A new method has been developed in pyCycle where the exhaust gas properties are corrected to account for the real gas effects of steam. A similar approach as in Subsection 4.1.3 is used. Some modifications are, however, needed because additional fuel-induced water is present in the exhaust gases. Figure 4.2 also represents the general structure for the wet exhaust gas property calculation method following the ideal mixing of two gases. A schematic overview of the approach used to generate the thermodynamic data for the wet exhaust gas is shown in Figure 4.3. The exhaust gas mixture composition is first determined, given the fuel composition, the fuel-to-air ratio, and the water-to-air ratio. The $Tp - mode$ is used to calculate the species' mole fractions in the exhaust gas mixture. The species' molar fractions are used to calculate the mass fraction of the water and the dry exhaust gas in the wet exhaust gas mixture, following Equation 4.6 and Equation 4.7, respectively. Based on the mole fractions and the pressure, the partial pressure of the water vapor and the dry exhaust gas are computed using Dalton's Law. The dry exhaust gas properties are then calculated for the given composition, partial pressure, and temperature in the $TabThermoGenAir$ class. Considering the steam properties, these are calculated by CoolProp using the partial water pressure and the temperature.

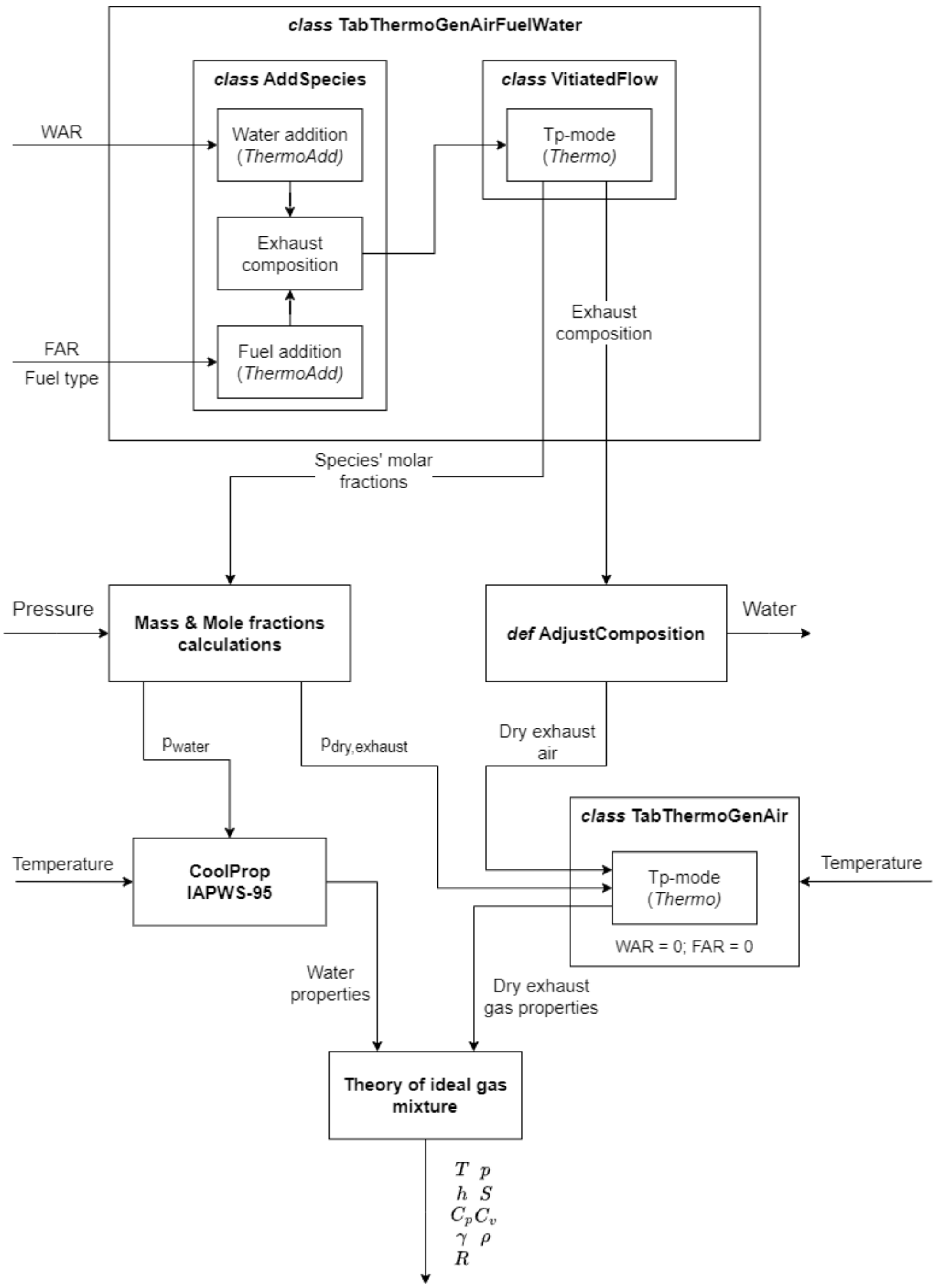

Figure 4.3: Flow diagram of the thermodynamic table generation method for the humid exhaust gas model.

Lastly, the wet exhaust gas mixture properties are found based on the ideal gas mixture approximation as already shown in Subsection 4.1.3 (Equation 4.5a until Equation 4.5g).

$$k_{H2O} = x_{H2O} \cdot \frac{M_{H2O}}{M_{mixture}} \qquad (4.6) \qquad\qquad k_{dry,exh} = 1 - k_{H2O} \qquad (4.7)$$

4.1.5. Thermodynamic Properties in the Condensation Region

After the condenser, part of the water vapor has condensed to liquid water. Therefore, the thermodynamic properties of (partially) condensed exhaust gas should be computed and stored in the thermodynamic tables. This section describes how these thermodynamic properties in the condensation region are calculated. Considering this is a preliminary design study for the WET engine, the modeling of detailed phase-changing phenomena is not required. A relatively simple approach is therefore used to model condensation. In Figure 4.4, the phase diagram of pure water is shown with both the critical and triple point indicated [106]. Water condensation is only possible within a certain temperature and pressure range, namely in the region above the saturation line presented in Figure 4.4. Hence,

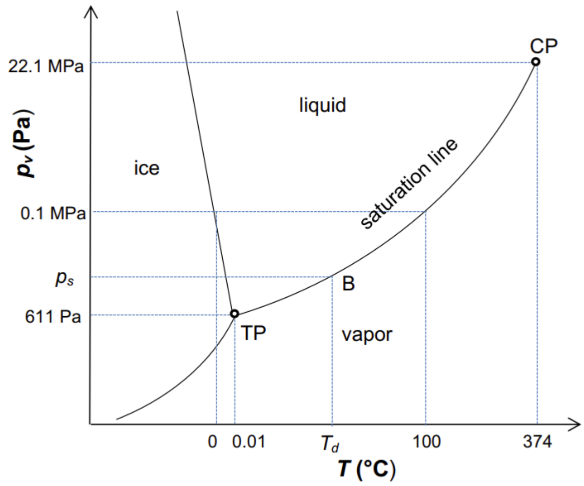

Figure 4.4: Temperature-pressure diagram, or phase change diagram, for pure water [106].

a condition is imposed in the property table generation process where condensation can only occur between $0.01°C$ (273.16K) and $373.99°C$ (647.10K). Suppose the temperature is between the triple point and the critical point. In that case, it has to be checked whether the partial pressure of water in the exhaust gas mixture is above or below the water saturation pressure at a given temperature. The possible thermodynamic states are listed below in terms of the supersaturation parameter:

$$\text{water state} = \begin{cases} \text{liquid}\,, & \text{if } SS > 1 \\ \text{gaseous}\,, & \text{if } SS < 1 \\ \text{saturated}\,, & \text{if } SS = 1 \end{cases}$$

The (super)saturation parameter (SS) is a parameter with a meaning is similar to that of the relative humidity, whose definition is reported in Equation 2.6. However, a relative humidity larger than unity is not possible. Given the saturation pressure, a larger share of water in the mixture would mean that the excess water would condense. The details of this mechanism are explained in Subsection 2.3.1. Similar to the RH, the saturation parameter is formulated in Equation 4.8, based on Raoult's law for ideal mixtures.

$$SS = \frac{p_{H2O}}{p_{sat,H2O}} = \frac{x_{H2O} \cdot p}{p_{sat,H2O}} \qquad (4.8)$$

The mole fraction of the water x_{H2O} is provided by CEA, but the saturated (vapor) pressure of the water is still to be calculated, given the mixture temperature. The saturated vapor line can be approximated by various correlations, each with documented accuracy. Values for the water vapor pressure are found in the Handbook of Chemistry and Physics and are generally used as a comparison for approximation formulas [107]. Several relations that are proposed to model the saturation water curve are the August equation, the Antoine formulation, the Magnus approximation, the Tetens approximation, the Buck equation, and the Goff-Gratch approximation [108]. Based on relative error estimations, an improved version of the Magnus formulation (Equation 4.9) is recommended for temperatures ranging from -40 to 50 degrees Celsius with low errors above 50 degrees.

$$p_{sat,H2O} = 0.61094 \cdot \exp\left(\frac{17.625T}{T + 243.04}\right) \tag{4.9}$$

It is also possible to calculate the saturated water vapor pressure using CoolProp. The IAPWS-95 model uses a polynomial approximation to model this line and is given below, where the coefficients a_1 to a_6 are given in the literature [109]. In Equation 4.10, τ is equal to $1 - T/T_c$.

$$\ln\left(\frac{p}{p_c}\right) = \frac{T_c}{T}\left[a_1\tau + a_2\tau^{1.5} + a_3\tau^3 + a_4\tau^{3.5} + a_5\tau^4 + a_6\tau^{7.5}\right] \tag{4.10}$$

Dias et al. conducted a study regarding consistency in water vapor pressure predictions. The authors compared eight saturated vapor line expressions [110]. Until 150 degrees Celsius, the Buck approximation has the lowest relative error compared to the IAPWS-95 relation. However, Magnus' approximation also shows good accuracy and outperforms Buck's relation for higher temperatures. In addition, Magnus' equation is simpler and, therefore, easier to use in preliminary design models. Unfortunately, CoolProp does not converge for temperatures larger than the critical temperature for calculating saturation conditions, which could represent a problem for the Newton solver in pyCycle. The Magnus polynomial approximation is, unlike CoolProp, continuous and, hence, easier to handle in the pyCycle framework, although the vapor pressure values are not as accurate as computed by CoolProp. The continuity of the Magnus approximation may help the Newton Solver to converge. Therefore, the Magnus approximation is also used to determine the water saturation pressure in the table generation process given a prescribed temperature.

Having evaluated the saturated vapor pressure at a given mixture temperature, the rate of (super-) saturation can be computed following Equation 4.8. Subsequently, a recovery factor is introduced to estimate the amount of liquid water that can be obtained based on the supersaturation parameter. The recovery factor is defined in Equation 4.11 with an extra efficiency factor, $\eta_{rec,H2O}$, to account for potential losses during the water recovery process [7].

$$\zeta_{rec} = \left(1 - \frac{1}{SS}\right) \cdot \eta_{rec,H2O} \tag{4.11}$$

Based on Equation 4.11, it is obvious that only liquid water can be recovered if the saturation parameter exceeds unity and supersaturation occurs. If $SS = 1$, then no water is to be recovered as the water is in the saturated state. When the water partial pressure is lower than the saturated vapor pressure, the recovery factor becomes negative, and no water is liquefied. When $SS > 1$, the exhaust flow consists of dry exhaust gas, liquid water, and water vapor. In the property table generation process, the thermodynamic properties should be computed given a temperature, pressure, FAR, and WAR. When the temperature is below the critical temperature ($T_{triple} < T < T_{crit}$), it must be checked whether part of the water in the exhaust gas mixture is condensed. This is done by comparing the partial water pressure to the water saturation pressure. If the partial water pressure is higher than the saturation pressure, part of the water will condense, and this should be accounted for in the property table generation process. To do this, the water mass fraction can be split up into a liquid and a gaseous/vapor part:

$$z_{liq,H2O} = k_{H2O,exh} \cdot \zeta_{rec} \tag{4.12}$$

$$z_{vap,H2O} = k_{H2O,exh} \cdot (1 - \zeta_{rec}) \tag{4.13}$$

$k_{H2O,exh}$ is the mass fraction of all water in the exhaust gas, whereas $z_{liq,H2O}$ is the mass fraction of liquid water in the exhaust gas. The last step is to compute the seven thermodynamic properties included in the tables. The specific heat ratio γ is calculated similarly to Equation 4.5d. Enthalpy, entropy, specific heats, and density are calculated following Equation 4.14a to Equation 4.14e.

$$C_{p,cond} = k_{air,exh} \cdot C_{p,air} + z_{vap,H2O} \cdot C_{p,sat,H2O} + z_{liq,H2O} \cdot C_{p,liq,H2O} \tag{4.14a}$$

$$C_{v,cond} = k_{air,exh} \cdot C_{v,air} + z_{vap,H2O} \cdot C_{v,sat,H2O} + z_{liq,H2O} \cdot C_{v,liq,H2O} \tag{4.14b}$$

$$\rho_{cond} = \rho_{air}(T, p_{air}) + \rho_{H2O,vap}(T, p_{H2O}) \; (+\rho_{H2O,liq}(T, p_{H2O})) \tag{4.14c}$$

$$h_{cond} = k_{air,exh} \cdot h_{air} + z_{vap,H2O} \cdot h_{sat,H2O} + z_{liq,H2O} \cdot h_{liq,H2O} \tag{4.14d}$$

$$S_{cond} = k_{air,exh} \cdot S_{air} + z_{vap,H2O} \cdot S_{sat,H2O} + z_{liq,H2O} \cdot S_{liq,H2O} \tag{4.14e}$$

Regarding the mass fractions, they should add up to one: $k_{air,exh} + z_{vap} + z_{liq} = k_{air,exh} + k_{H2O,exh} = 1$. A schematic overview of this part in the property table generation process is shown in Figure 4.5. The symbol X in Figure 4.5 represent one of the thermodynamic properties stored in the 4D tables (C_p, C_v, h, S).

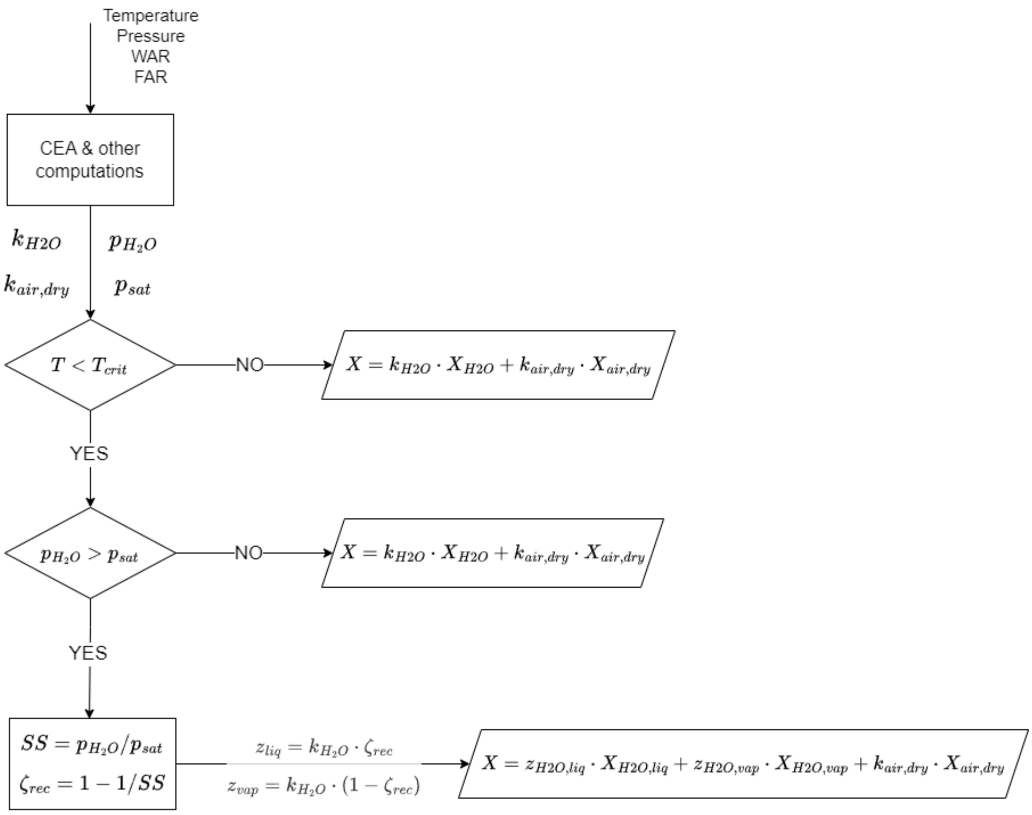

Figure 4.5: Schematic overview for calculating the thermodynamic properties in the condensation region.

The mixture properties are hence calculated as the weighted sum of the properties of three components: i) the ideal, dry exhaust gas, ii) the saturated water vapor, and iii) the condensed (liquid) water. The approach for calculating the dry exhaust gas properties is similar to the previously discussed method in Subsection 4.1.4. The partial pressure of water vapor in the exhaust cannot exceed the vapor pressure of saturated water at the specified temperature T. Should it surpass this threshold, the water vapor would undergo condensation until a state of equilibrium, consistent with the saturated vapor pressure, is attained.

Special consideration must be given to the density of the exhaust gas mixture in the condensation region (Equation 4.14c). Unlike other thermodynamic properties, the contribution of the liquid phase to the mixture density is omitted during the table generation process. This approach is necessary to maintain numerical stability and ensure convergence of the computational framework. If the liquid phase were included, unrealistically high mixture densities would be predicted immediately downstream of the condenser. For instance, liquid water has a density of approximately $1000 kg/m^3$, and even if only 1% of the water in the exhaust mixture condenses, the resulting mixture density would exceed $10 kg/m^3$. In reality, a significant portion of the condensed water would separate from the gas stream and accumulate along the duct walls rather than remaining suspended within the flow. To prevent numerical instabilities and ensure physically consistent results, the liquid-phase contribution to density is therefore neglected.

4.1.6. Implementation & Limitations

The default version of pyCycle only incorporates three-dimensional tables for the TABULAR method. These tables are dependent on pressure, temperature, and FAR. For the WET engine, a new parameter is introduced: the water-to-air ratio (WAR). The internal structure of pyCycle is adjusted such that the TABULAR mode also accepts four-dimensional tables, i.e. tables containing p, T, FAR, and WAR.

Furthermore, it is worth mentioning the ranges in which the wet (exhaust) air model is feasible and valid. To do this, the limitations of all the separate models have to be identified. All the thermodynamic models used in both the wet air and wet exhaust gas models are summarized below:

- **NASA CEA**: for calculating equilibrium gas mixture composition.
- **NASA polynomials**: for calculating the specific heat, enthalpy, and entropy based on temperature and composition of the gas mixture.
- **IAPWS-95 (CoolProp)**: water properties.

As transport properties are not considered in detail for this study, only the validity of thermodynamic properties has been investigated. For each model, pressure and temperature validity ranges are tabulated in Table 4.1. CEA makes use of the Gibbs free energy minimization whose definition is given in Equation 3.6. The enthalpy and entropy are computed by means of the NASA polynomial functions. As no information could be found regarding temperature and pressure validity ranges for the CEA program, it is assumed that the limitations are similar to those of the NASA polynomials. It is documented by McBride et al. that the maximum temperature range of these polynomials goes from 200 to 20000 Kelvin [97]. However, this range is not valid for each type of species. The lower temperature limit for ionic gases is 298.15 K and the upper limit of 20000 K is only valid for simple molecules and mono-atomic species. Looking at the species that are available in pyCycle, it can be concluded that the temperature range is set to 200-6000 K. This temperature range is large enough for aero engine applications, where TIT is generally not higher than 2000 K. In addition, the polynomials are pressure-independent and hence are valid for all pressures. Lastly, the limits of IAPWS-95 applied in CoolProp have to be identified. Minimum temperature and pressure are defined at the triple point, i.e. at 273.16 K and 611.65 Pa. The maximum temperature and pressure are documented to be 2000 K and 1000 MPa, respectively [102, 111]. If transport properties are needed, the maximum temperature and pressure limits are reduced to 773.15 K and 10 bar, respectively [100]. Based on Table 4.1, it can be concluded that the wet (exhaust) air model in pyCycle is valid from 273.16 to 2000 Kelvin and from 0 to 100 MPa, well suitable for aero engine applications. Lastly, the model is valid for $WAR = 0$ to $WAR = 0.4$ as documented by DLR [100].

Table 4.1: Overview of limitations regarding the various models applied within the WET engine.

Model	Temperature range [K]	Pressure range [MPa]	Source
NASA CEA	200 - 6000	independent	[92, 97]
NASA polynomials	200 - 6000	independent	[92, 97]
IAPWS-95 CoolProp	273.16 - 2000	0 - 100	[102, 111]
pyCycle exhaust gas model	273.16 - 2000	0 - 100	

4.2. Steam Injection

A new pyCycle element is implemented for modeling the steam injection into the main gas path. This element, called the water injector, is very similar to the combustor element in pyCycle. If fluid properties are calculated in the so-called CEA mode, the default mixer available in pyCycle could have been used for this purpose. However, in the TABULAR mode, one cannot set pure water as the input stream, as the tables are defined in pyCycle only for air ($FAR = 0$, $WAR = 0$) and exhaust gases ($FAR > 0$, $WAR \geq 0$). Water is injected similarly in the injector as the injection of fuel in the combustor. The inputs for this water injector component are the steam enthalpy at given pressure and temperature, and WAR, similar to the fuel enthalpy of formation and FAR in the combustor component, respectively.

The resulting mixed enthalpy of the wet air is calculated by a mass-averaged approach used within pyCycle, as shown in Equation 4.15 below.

$$h_{mix} = \frac{h_1 \cdot \dot{m}_1 + h_2 \cdot \dot{m}_2}{\dot{m}_1 + \dot{m}_2} \tag{4.15}$$

A requirement regarding mixing is that the static pressure of the injected steam should be at least equal to the static pressure of the compressed air. This, however, introduces a complication with the calculation of thermodynamic properties with the TABULAR approach. Normally, no heat or energy is assumed to be absorbed or generated in an ideal mixing process,. The molecular interactions are neglected. Following the approach from Greitzer et al., mixing is bound to the conservation of mass, momentum, and energy [112]. The equation of state should also be taken into account. The conservation of mass is ensured by utilizing the water-to-air ratio. The conservation of energy is satisfied with the summation of the total enthalpy of the input streams. Conservation of momentum is coupled to the impulse function. This function is related to the pressure of the stream, the duct area, the velocity of the flow, and the mass flow rate:

$$I = pA + \rho AV^2 = pA + \dot{m}V \tag{4.16}$$

Based on the theory of ideal mixing and Dalton's law, the total pressure of the mixture is given by the partial pressures of both streams, given that the Mach numbers, mass flow rates (and consequently, the duct area and volume), and pressures are known. When calculating the thermodynamic properties with the TABULAR approach in PyCycle, this presents a challenge, as only enthalpy and the WAR are needed as inputs in the water injector model. To address this limitation, a simplified method is employed to approximate the correct mixture properties. For an ideal gas, as computed in CEA, enthalpy is independent of pressure. However, the thermodynamic properties exhibit pressure dependence for steam, albeit with minimal impact under typical mixer conditions. The enthalpy difference between the main gas path and the bottoming water cycle is particularly relevant. Just before injection, the total enthalpy of the steam is considered at the corresponding injection pressure. This pressure must be at least equal to or greater than the incoming static pressure of the compressed air to ensure proper mixing. At the same time, the steam enthalpy at the mixer outlet observed in the main gas path should correspond to the partial pressure of the steam in the mixture. While this discrepancy is expected to be negligible for low WARs, it may become significant at higher WARs. Furthermore, the steam injection pressure just before the injection point is a critical parameter for determining the performance of the liquid water pump. All other mixing properties are estimated based on the $hp - mode$ with table interpolation within the component. The simplified approach of coupling the steam enthalpy from the water cycle and the input enthalpy value for the water injector is illustrated in Figure 4.6 and validated using a mixer-combustor model in Subsection 5.1.2. To summarize, ideal mixing is assumed in the mixer component in pyCycle, where the injection enthalpy is calculated using CoolProp with the partial pressure of the steam in the mixture.

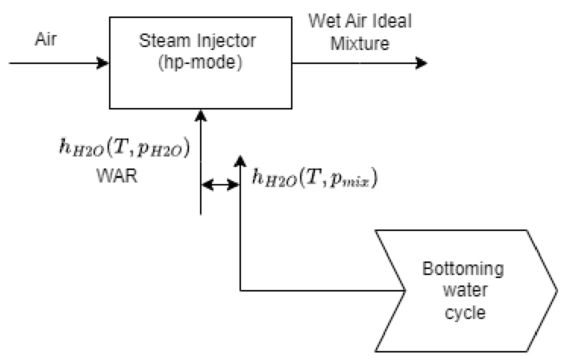

Figure 4.6: Simplified structure of the water injector component with the two different enthalpy values indicated.

4.3. The Combustor & Fuel-Specific Table Sets

Kerosene is the conventional fuel used in modern aero engines. It is already discussed in the literature study (Chapter 2) that this fuel entails important greenhouse effects. With the introduction of SAF, aviation is a small step closer to becoming more sustainable and meeting future emission goals. It is of vital importance, also for future WET engine analysis and/or optimization, that the effect of multiple fuels on the engine performance can be assessed. For each new, alternative fuel, a new thermodynamic data set should be generated. The enthalpy of formation together with the fuel composition are the two most important input parameters for modeling fuel injection in the combustor. Unfortunately, the enthalpy of formation (HOF) is not a property that can be directly measured. Instead, the enthalpy of formation of the fuel (with units J/g) can be derived from the lower heating value (LHV) assuming a stoichiometric combustion reaction. The general formula for stoichiometric combustion is shown below assuming that a fuel molecule comprises only carbon and hydrogen atoms:

$$C_xH_y + (x + \frac{y}{2}) \cdot O_2 \rightarrow x \cdot CO_2 + \frac{y}{2} \cdot H_2O \tag{4.17}$$

The LHV, the heat that is released for the combustion of 1 kg of fuel, can be measured more easily, and fuel-specific values are documented extensively in literature [113, 114, 115]. Below, a summary of the approach for finding the fuel HOF based on LHV is provided. Considering a combustion reaction, the enthalpy of reaction (i.e. enthalpy of combustion) is defined as the energy difference between the combustion products and the reactants:

$$\Delta H_r^0 = \sum^{N_{prods}} \nu_{stoich} \Delta H_{prods}^{f,0} - \sum^{N_{reacts}} \nu_{stoich} \Delta H_{reacts}^{f,0} \tag{4.18}$$

The coefficient ν_{stoich} represents the stoichiometric coefficients for each reactant and combustion product. $\Delta H^{f,0}$ is the standard enthalpy of formation and means the change in enthalpy to form one mole of a molecule from its constituent base elements, provided that all substances are considered in their standard states. The enthalpy of reaction, for which its value is derived from the LHV, is negative for combustion reactions as these are generally exothermic, where a large amount of heat is released. The enthalpy of formation of several species is already known and can be found in the literature. However, the enthalpy of formation for the fuel should be computed based on Equation 4.18.

Based on fuel composition, LHV, Equation 4.17, and Equation 4.18, the standard fuel enthalpy of formation is computed. All calculations should be performed with energy per mole units as a chemical reaction is considered. For its use in pyCycle, the obtained value should be expressed in energy per unit mass for which the molar mass of the fuel is needed. The resulting enthalpy of formation value is used in the pyCycle framework for each operating point. A set of fuels is already available in pyCycle and comprises *dodecane, methane, Jet-A types, and hydrogen*. For the simulation of the kerosene-fueled WET engine, the enthalpy of formation for kerosene is calculated to be $-1745\ kJ/kg$. For future usage, the enthalpy value of all fuels can be automatically calculated based on composition and used for engine simulations.

4.4. Water Condensation & Separation

In thermodynamic cycles with water injection & recovery, modeling of phase change phenomena and water separation is essential for performance prediction and system optimization. The methodology regarding the creation of the thermodynamic tables has been discussed in Subsection 4.1.1. The condensation region within this process is considered in Subsection 4.1.5. Using the generated thermodynamic tables, the thermodynamic properties after the condenser can be correctly computed. However, extra calculations should be performed during the simulation to ensure that a certain amount of water is condensed and can be subsequently removed in the water separator. The Subsection 4.4.1 describes these additional equations in the WET engine model to find the correct (below) dew point after the condenser so that enough water can be recovered. Additionally, the modeling approach for the water separator is explained in Subsection 4.4.2. The separator is responsible for extracting condensed liquid water from the flow.

4.4.1. Condensation Process

An important assumption for the WET engine in this study is that all the injected water should be recovered after the condenser. This assumption is particularly valid during the cruise phase when the ambient air is sufficiently cold to cool the exhaust gases [16, 60]. Given the above assumption, the below dew temperature after the condenser should be calculated in order to condense as much water as is being injected before the combustion chamber. Some extra equations should, therefore, be integrated into the WET engine model to find the correct below dew point temperature and pressure. The pressure aft of the condenser is a result of the LPT outlet pressure and the imposed pressure drops in the HRSG and condenser. Based on the condenser outlet pressure and the exhaust gas composition, the below dew temperature can be calculated. The method is described below.

The TABULAR simulation method is used to simulate the WET engine and may be computationally quicker, but the level of detail is lower than that of the CEA mode, with fewer thermodynamic variables available during runtime. The exact composition of the exhaust gas mixture is not stored in the thermodynamic tables. Instead, the specific gas constant R ($R = \bar{R}_c/M_{mix}$) is stored (see Table 3.1). To find the composition of the exhaust gas mixture during simulation, a designated new class component is developed. The WAR and FAR are used as inputs, whereas the mass- & mole fractions of the wet exhaust gas are the outputs. Based on the equivalence ratio, shown in Equation 4.19 below, these fractions for non-stoichiometric complete combustion can be computed following Equation 4.17. The total water amount should be estimated in the exhaust flow and comprise both injected and fuel-induced water.

$$\phi = \frac{FAR_{model}}{FAR_{stoich}} \tag{4.19}$$

The required saturation pressure to recover all the injected water can be computed by a combination of the (super)saturation parameter, Raoult's law (Equation 4.8) and the recovery factor (Equation 4.11) and is shown in Equation 4.20:

$$p_{H2O,sat} = \frac{x_{H2O}p}{SS} = \frac{n_{H2O,tot} \cdot p \cdot \left(1 - \frac{\zeta_{rec}}{\eta_{rec,H2O}}\right)}{n_{tot,exh}} \tag{4.20}$$

The total molar amount of the exhaust gases, $n_{tot,exh}$ is estimated using the (molar) specific gas constant of the exhaust gases, R_{exh}, the universal gas constant, $\bar{R}_c$, and the mass flow rate through the condenser. This is shown in Equation 4.21.

$$n_{tot,exh} = \frac{R_{exh} \cdot \dot{m}_{exh}}{\bar{R}_c} \tag{4.21}$$

The total chemical amount of water in the exhaust gases, $n_{H2O,tot}$, is computed by multiplying the water mole fraction and the total molar amount of the exhaust gases. The pressure p at the condenser outlet is known. The water recovery efficiency, η_{rec,H_2O}, represents which part of the condensed water can be effectively recovered in the water separator. Although it is likely that not all condensed water can be separated in reality, the water recovery efficiency is assumed to be equal to one throughout this study. The water recovery factor ζ_{rec} represents the ratio of actual recovered water and the total amount of water in the exhaust gas. The recovery factor can therefore also be formulated according to Equation 4.22.

$$\zeta_{rec} = \frac{\dot{m}_{H2O,rec}}{n_{H2O,tot} \cdot M_{H2O}} \tag{4.22}$$

Combining Equation 4.20 and Equation 4.22 gives a relation to estimate the required saturation pressure to condense the same amount of water that has been injected before the combustor. The relation is shown in Equation 4.23.

$$p_{H2O,sat} = \frac{n_{H2O,tot} \cdot p - \left(\frac{\dot{m}_{rec} \cdot p}{\eta_{rec,H2O} \cdot M_{H2O}}\right)}{n_{tot,exh}} \tag{4.23}$$

Finally, using the inverted Magnus equation, the temperature downstream of the condenser required to recover an amount of water equivalent to that injected can be determined. Since Magnus' equation is a continuous function, its derivatives can be efficiently evaluated through numerical differentiation, which is advantageous for the Newton solver employed in pyCycle.

4.4.2. The Water Separator

The implementation of the water separation process is simplified as this study focuses on the conceptual design of the WET engine. Just like the water injector explained in Section 4.2, a combustor-like component is used to extract the water. At this point, a new variable is introduced, namely the liquid water-to-air ratio, similar to the WAR and FAR. This term represents the amount of liquid water that can be recovered with respect to the amount of air that flows through the core and is formulated in Equation 4.24.

$$LWAR = -\frac{\dot{m}_{water,liq}}{\dot{m}_{air,in}} \tag{4.24}$$

The enthalpy of liquid water and the LWAR are the inputs for the water separator component. The enthalpy of liquid water is calculated by CoolProp using the condenser outlet temperature and pressure. Similar to Section 4.2, a mass-averaged approach is used to calculate the enthalpy aft of the separator. Based on the $hp - mode$ in pyCycle for property calculations, the thermodynamic properties are computed. Four situations are to be considered for the water separator:

1. $\mathbf{LWAR = 0}$: no water is condensed and the outgoing stream equals the incoming stream.
2. $\mathbf{-WAR < LWAR < 0}$: less liquid water is recovered than the amount injected. To maintain the continuous injection stream of steam, additional (liquid) water should be introduced utilizing a liquid water tank. The remaining water that has not been condensed will be expelled through the nozzle core.
3. $\mathbf{LWAR < -WAR}$: as fuel-generated water is also present in the wet exhaust gas, this water could theoretically also be recovered. Following Equation 4.24, this means that the WAR value would be reduced to negative values, which is not supported in the TABULAR property calculation method. In reality, this would be possible, and the extra water could be used to fill the water reservoir, i.e., during the cruise phase. The water is then used in a flight phase where not enough water can be recovered (take-off/landing).
4. $\mathbf{LWAR = -WAR}$: the amount of water that is condensed is equal to the amount of water that is being injected. *This situation is to be assumed for the turbofan engine model during cruise to simplify the calculations and to avoid taking into account the liquid water tank.*

Water Separation Correction Factor

The $LWAR$ parameter in Subsection 4.4.2 is introduced as all the thermodynamic property calculations in this study are performed using the TABULAR calculation mode in pyCycle. However, inaccuracies in thermodynamic station properties after the water separator may arise if all liquid water is removed from the exhaust. Given the assumption that all injector water is recovered in the separator, the $LWAR$ equals $-WAR$, and the WAR reduces to zero at and after the separator. Moreover, it is assumed that the temperature in the water separator does not change as the liquid water temperature is set equal to the bulk temperature. In reality, the temperature might be slightly different. As the enthalpy after the water separator is calculated based on the mass-averaged approach (Subsection 4.4.2), this could lead to a minor inconsistency in the thermodynamic property calculations. A correction factor is introduced to account for this and ensure a constant temperature over the water separator. For each operating point of the WET engine, the following conditions are assured:

- All water that has been injected in the water injector, is recovered in the water separator.
- The temperature over the water separator does not change.
- At the water separator outlet, saturated (exhaust gas) conditions are ensured.

4.5. Heat Exchangers

The heat recovery steam generator (HRSG) and the condenser are key components of the WET engine concept. The two heat exchanger's performance characteristics are evaluated using simple zero-dimensional (0D) methods and more detailed modeling techniques. While the overall features of the heat exchangers are initially assessed using a 0D approach for a preliminary investigation of the engine concept, the HRSG is further analyzed with higher fidelity using in-house software called Hexacode. This advanced modeling tool allows for more accurate modeling of the transfer processes, enabling a more precise evaluation of the HRSG's performance compared to the initial simplified models available in the pyCycle framework.

4.5.1. Simple HEX Design: HRSG and Condenser

Starting with the HRSG, heat is exchanged between the bottoming water cycle and the hot exhaust gas discharged by the LPT. Based on the desired injection temperature and pressure of the steam, the pressure drop at the cold side of the HRSG, and the condensation temperature, the heat duty of the HRSG can be computed. This thermal power should be equal to the heat flow on the hot side of the heat exchanger. The WET cycle requires that the HRSG outlet state is still superheated and no condensation is allowed. However, in the simple 0D approach, it cannot be checked whether this condition is satisfied. Therefore, once all results are generated and given a fixed WAR, the solutions should be carefully checked to verify that the design of the HRSG is feasible. More information regarding the WET engine design space exploration is given in Chapter 6 and Chapter 7. In pyCycle, the heat exchangers are modeled as simple ducts in which a pressure drop and a heat flow can be set. Both parameters can be set as cycle parameters or used as iteration variables in the balance equations. In the preliminary design of the WET engine, a prescribed, constant pressure drop is used for the hot and cold sides of the HRSG. The heat flow is instead determined according to the thermal input required in the water cycle. A more detailed description of how the HRSG heat duty is specified in the pyCycle model is provided in Section 4.6. Similarly, a pressure drop is set for both the hold and cold sides of the condenser based on values found in relevant literature. However, the heat duty $\dot{Q}_{cond}$ is an iteration variable in the balance equation as a certain dew point temperature should be reached after the condenser to recover as much water as is injected upstream of the combustor.

The HEX effectiveness is a critical parameter in thermal system design. It quantifies the ability of a heat exchanger to transfer thermal energy relative to its maximum theoretical potential. By setting constraints on the HEX effectiveness designers can avoid overestimating system gains, reduce the need for later-stage modifications, and ensure the feasibility of the HEX design. The effectiveness of both the HRSG and the condenser is defined following Equation 4.25 below.

$$\epsilon_{HEX} = \frac{\dot{Q}_{actual}}{\dot{Q}_{max}} \tag{4.25}$$

The effectiveness is not a limiting parameter for generating WET engine cycle results but it is for the feasibility of the identified solutions. Therefore, during the design exploration, the effectiveness of the HEXs for each design option is calculated and those with effectiveness values higher than unity are considered unfeasible and discarded. Looking at Equation 4.25, the actual heat transfer is calculated by the enthalpy difference multiplied by the mass flow rate on one HEX side as shown in Equation 4.26.

$$\dot{Q}_{actual} = \dot{m}\Delta h = \dot{m}_h C_{p,h}(T_{h,in} - T_{h,out}) = \dot{m}_c C_{p,c}(T_{c,out} - T_{c,in}) \tag{4.26}$$

The maximum allowable heat transfer $\dot{Q}_{max}$ depends on the fluid heat capacity rates and the inlet temperatures. Maximum heat transfer is restricted to the minimum heat capacity rate, CRR_{min}, and is formulated as shown below in Equation 4.27.

$$\dot{Q}_{max} = CRR_{min}(T_{h,in} - T_{c,in}) \quad \text{where} \quad CRR_{min} = \min(\dot{m}_c C_{p,c}, \dot{m}_h C_{p,h}) \tag{4.27}$$

A disadvantage of the Equation 4.27 is that it is valid for constant specific heats. This is not necessarily true for both the HRSG and the condenser, especially in the case of phase change processes. To capture these phenomena more effectively Equation 4.27 is rewritten with enthalpy values, rather than with specific heats. Equation 4.28 gives the adjusted method for computing the maximum heat transfer for both HEXs. Two terms have to be clarified further, namely $h_{c,T_{h,in}}$ and $h_{c,T_{h,in}}$. The first term indicates the enthalpy of the cold flow calculated at the hot inlet temperature. In contrast, the second term is the enthalpy of the hot flow assessed at the cold flow inlet temperature.

$$\dot{Q}_{max} = \min\Big(\dot{m}_c \cdot \big(h_{c,T_{h,in}} - h_{c,in}\big),\ \ \dot{m}_h \cdot \big(h_{h,in} - h_{h,T_{c,in}}\big)\Big) \tag{4.28}$$

Again, this is a simplified approach acceptable in a conceptual design phase. Besides the heat transfer $\dot{Q}$, the pressure drop over the heat exchanger is another important variable. Initial guesses are first used to solve the WET cycle. Afterwards, an updated pressure drop is fed to the HRSG model based on the results of the detailed evaporator design performed with Hexacode.

4.5.2. Hexacode

The in-house software HeXacode, developed in Python, is employed for sizing heat exchangers and its functionality has been verified by comparing its output against results from a commercial code for heat exchanger design and analysis [116]. The sizing process entails calculating the required heat transfer surface area to achieve a given heat duty, based on the inlet temperature, pressure, and mass flow rates of the hot and cold streams. Key outputs of the program include the physical dimensions, mass, and pressure drops on both the hot and cold sides. For the evaporator and condenser, the frontal area is predefined, while the depth is adjusted to meet design requirements.

The evaporator is configured as an annular, multi-pass, bare-tube bundle with a cross-counter flow arrangement relative to the exhaust gas flow. After the LPT diffuser, the wet exhaust gas makes a turn and flows radially outward. The water will flow in the same direction as the engine axis (see Figure 4.8). The integration of the HRSG in a turbofan engine is according to what is proposed by both MTU and DLR and is shown in Figure 2.12 and Figure 4.8, respectively [10, 60]. A visualization of the evaporator topology used for the WET engine is shown in Figure 4.7. This configuration includes tubes aligned with the engine axis and is constructed out of a nickel-based alloy, which offers excellent resistance to oxidation, high-temperature strength, and ease of fabrication. The tubes have a fixed outer diameter, while their wall thickness is determined by the pressure differential between the exhaust gases and the working fluid [46]. Moreover, it is found that in-line tube bundles generally have a higher mass compared to staggered configurations for the same frontal area, but their lower hot-side pressure drop contributes to improved cycle efficiency. This efficiency gain outweighs the drawback of the increased heat exchanger mass, making the in-line arrangement the preferred choice [116, 46].

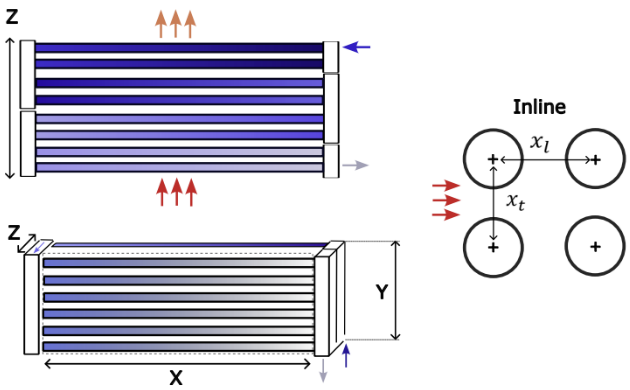

Figure 4.7: Lay-out of the multi-pass tube bundle HRSG (evaporator) used in the WET engine cycle.

For simplicity and convergence reasons, the heat duty distribution across the different control volumes of the HEX model is assumed to be logarithmic. This assumption likely results in an underestimation of pressure drop and an overestimation of heat transfer performance but is sufficient for a preliminary design analysis. To summarize, Hexacode is only used after the design exploration phase and is not coupled to pyCycle directly. Once an optimal, feasible WET engine design has been found, the effect of the evaporator size and performance is more closely investigated with the help of Hexacode. The possible integration of the HRSG (black) and the condenser (light blue) is illustrated in Figure 4.8 and proposed by DLR [16].

4.6. Bottoming Water Cycle

The liquid water is delivered to the HRSG by means of a pump. The pressure head should be such that the pressure drops in the piping and the HRSG are overcome and the required pressure at the steam injection point is reached. A PFD of the bottoming water cycle is given in Figure 2.17 with the required pressure ratio of the pump formulated in Equation 2.8. Tables are generated for all water properties. These tables have temperature and pressure as entries as the FAR and WAR are always set to zero as pure water is considered. CoolProp and the IAPWS-95 model are used to generate these tables. The state of the water cycle inlet, i.e. the recovered water, and the injection conditions

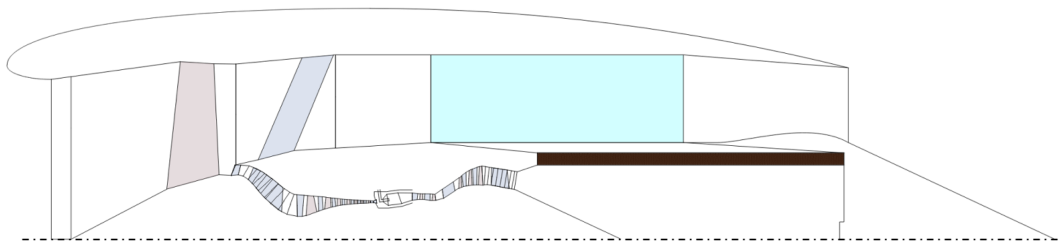

Figure 4.8: Possible integration of HRSG (black) and condenser (light blue) in a HBTF engine as proposed by DLR [60].

are known. The performance of both the water pump and the HRSG can be evaluated based on the specified inlet and outlet conditions. The state of the water, after it passes through the liquid pump, dictates the heat duty required by the HRSG. The exhaust gas outlet temperature can be determined by solving an energy balance. Unfortunately, pyCycle struggles to converge a model integrating an engine cycle with a bottoming water cycle. A simplification was then introduced to make the solver converge more easily as explained in the following. For the design exploration of the WET engine, the degree of superheating is fixed together with the HPC discharge pressure aft (for a fixed OPR). The steam injection temperature and pressure are therefore fixed and only inlet conditions of the water cycle should be provided. Normally, the water cycle inlet conditions are dictated by the separator water outlet conditions. It was noticed that if the temperature of the condensate is kept fixed, regardless of the condensate temperature, then the solver convergence is facilitated. Later in the report, the validity of this simplification will be evaluated. In the literature, it is reported that the core nozzle exit temperature for the WET engine varies between 290-330 Kelvin [16] and this temperature depends on the operating point and velocity ratio. During cruise phase, the core nozzle temperature is reported to be lower than 300K because of the higher cooling capacity of the condenser [16]. The temperature is, therefore, expected to change at the core nozzle inlet in a range of roughly only 10 Kelvin. Moreover, the collected water from the separator could flow to a water tank whose bulk temperature may differ from that at the separator outlet. Both observations support the hypothesis of fixing the water pump inlet temperature. The impact of this simplification is further discussed in Section 6.2.

The performance of the condenser is contingent upon the availability of the necessary cooling flow to reduce the HRSG outlet temperature to a level below the dew point. With known values for the bypass cooling temperature, mass flow rate, and the type of heat exchanger, it is possible to assess whether adequate cooling capacity to achieve the desired exhaust gas temperature is available.

5

Verification and Validation

Verification and validation are essential to ensure the accuracy and reliability of the water-enhanced turbofan (WET) engine model. In the verification process, the model is assessed to confirm the correct implementation of the code used to model the thermodynamic properties and physical phenomena, such as water injection and combustion effects. Section 5.1 presents a series of cases by which the new thermodynamic tables are verified. Validation involves comparing model results with reference data to assess the model's accuracy. By evaluating performance against existing engine models, the reliability of the WET engine model is established for further analysis and optimization studies. In Section 5.2, a conventional turbofan engine is provided that serves as a reference to validate the model results.

5.1. Verification

In this section, the thermodynamic model and its implementation are to be verified. Three types of verification tests have been performed to ensure that the implemented thermodynamic model is sufficiently accurate. First, the specific heat C_p and density ρ for wet air are analyzed for both the superheated and below dew point regions, see Subsection 5.1.1. Next, in Subsection 5.1.2, the thermodynamic model predictions are compared with those of Aspen and CEA tools for the simple test case of a mixer-combustor isolated subsystem. Lastly, a simple WET turboshaft model is set up in Subsection 5.1.3 so that the pyCycle results can be compared against those reported by MTU in their seminal work [7].

5.1.1. Thermodynamic Properties

In 2024, DLR published a paper in which a new gas model is implemented in CFD software to model exhaust gas flow with high steam loads [100]. This gas model formed the basis for the model established in Section 4.1. To assess the model's validity, some gas properties are compared against the results from DLR and the humid air (HA) model from CoolProp [117]. Some key notes have to be made before considering and comparing the three models:

- The validity of the HA model in Coolprop is limited. The model is only valid for temperatures up to 623.5 Kelvin [118]. The expected temperatures in the WET engine exceed this maximum value easily ($TIT > 1500K$), reducing its suitability for aero engine simulation purposes. Moreover, the HA model does not incorporate combustion products in its thermodynamic model, whereas this would certainly be required if hot turbines and/or evaporators downstream of the combustor are considered. Despite its limitations, the HA model can still be used to check the validity of the new thermodynamic model within its functional limits.

- As the reference state of the IF97 model could not be modified, the new thermodynamic model is made using the IAPWS-95 model (see Subsection 4.1.3).

- DLR used Cantera for estimating the exhaust gas composition, whereas pyCycle uses NASA CEA for computing the equilibrium composition.

- The DLR study does not provide any data about thermodynamic properties of wet exhaust gases, i.e. $WAR > 0$ & $FAR > 0$, but only for wet air ($WAR > 0$ & $FAR = 0$). Additional verification tests are therefore needed to assess the calculations of the wet exhaust gas properties. This is done in Subsection 5.1.2.

In Figure 5.1, the isobaric specific heat (left) and the density (right) of the wet air mixture are shown for various water-to-air ratios at a pressure of 1 bar. Considering Equation 4.4 and the highest WAR, the partial pressure of the water is computed to be 0.39 bar. The dew temperature, i.e., saturation temperature, is then computed using the IAPWS-95 model in CoolProp, which is approximately 348.5 Kelvin. Considering the HA model's upper limit in CoolProp, the temperature region used for investigating C_p and ρ is between 350 and 600 Kelvin. All values, therefore, belong to the superheated region. The blue dots in Figure 5.1 are the model values from the MTU gas model as retrieved from their work [100]. Furthermore, the black dotted lines represent the values predicted by the HA model in CoolProp. The orange line, lastly, illustrates the model ("pyCycle wet/humid gas model" is used after this point to indicate this model) created in pyCycle. Comparing the three different models for both C_p and ρ, the pyCycle wet gas model shows very good agreement with the MTU and HA CoolProp models. Notice also that the steam has a higher specific heat compared to air, and increasing the water share in wet air will yield a higher C_p. A similar statement can be made for the density. Extending Equation 3.17, the mixture density is dependent on the molar mass of the individual species (assuming constant temperature and pressure) as shown in Equation 5.1. The molar mass of water is lower than that of air, resulting in a lower density for gas mixtures with high water shares. This is confirmed by the right-hand side of Figure 5.1.

$$\rho = \frac{p}{R \cdot T} = \frac{p}{\frac{\bar{R}_C}{M} \cdot T} \tag{5.1}$$

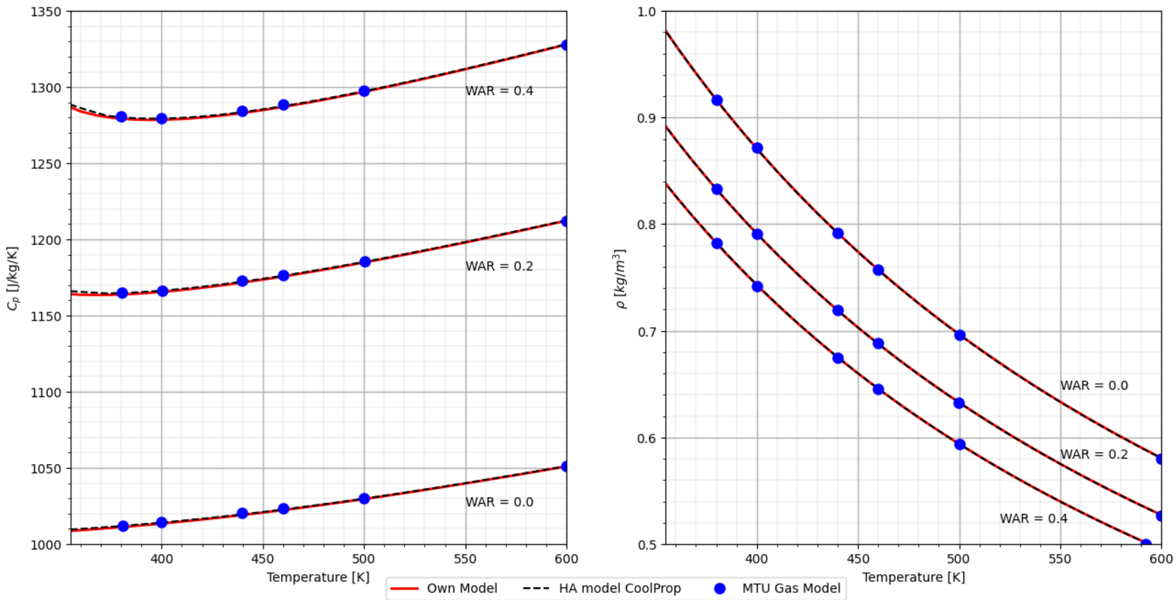

Figure 5.1: Comparison of the specific heat (left) and density (right) between the pyCycle wet gas model, the gas model from MTU and the humid air model from CoolProp ($p = 1\ bar$ and $FAR = 0$).

Figure 5.2 shows how the specific heat (left) and density (right) vary for pressures between 0.5 and 1.5 bar. These are the pressure ranges that are also considered in the paper by MTU. Once more, the results of the pyCycle wet gas model are very accurate when compared against MTU and the HA model and, hence, verified for this narrow pressure region. Besides this, the specific heat plot shows pressure-independent behavior for all WARs. For large WARs, there is a small positive correlation between pressure and C_p as visible in the top line of the right plot in Figure 5.2. Contrarily, there is a linear correlation between the pressure and density through the ideal gas law (Equation 5.1), which is illustrated in Figure 5.2.

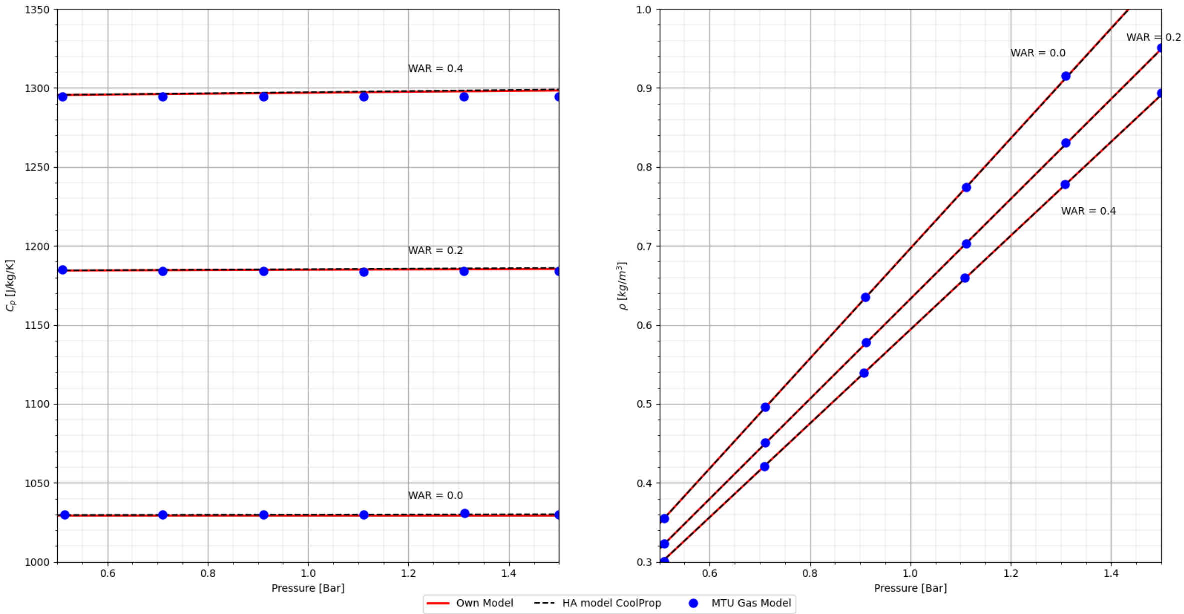

Figure 5.2: Comparison of the specific heat (left) and density (right) between the pyCycle wet gas model, the gas model from MTU and the humid air model from CoolProp ($T = 500\ K$ and $FAR = 0$).

Although wet air properties in the superheated region are verified, thermodynamic conditions below dew temperatures should also be considered as the condensation phenomenon is important for the WET engine. Figure 5.3 shows the specific heat for several WARs and pressures of 1 (left) and 10 bar (right), including the condensation region. At 1 bar and WAR = 0.4, the dew temperature is 348 Kelvin, whereas this is 471 Kelvin for 10 bar. Several considerations can be deduced from the figure:

- Considering temperatures higher than the dew point, the specific heat increases with temperature. However, when approaching the dew point, the specific heat value reaches a minimum value before starting to increase rapidly when the dew point is reached. This increase in C_p is enhanced for higher WARs and pressures. At higher pressures, the latent heat of evaporation (or condensation) is lower, smoothing the change in thermodynamic properties in proximity to the dew point.

- Below the dew point temperature, water starts to condense. Liquid water has a specific heat of more than 4000 $J/kg/K$, being approximately twice as high compared to that of steam. When water condenses, the C_p of the mixture strongly increases. This is the reason for the steep gradient on the left-hand side of the C_p charts in Figure 5.3.

- As the C_p of the mixture is computed through mass fractions, the C_p of a mixture with high water content is higher compared to that with low water content.

- From both charts, it can be concluded that the dew point temperature is affected by two parameters: the pressure and the water mass fraction. *At higher pressures, the dew point temperature is higher for the same WAR.* This is because an increased pressure raises the saturation temperature. Condensation starts, therefore, earlier when reducing the mixture of the gas mixture. *Moreover, the dew point temperature also increases with water-to-air ratios* as the partial pressure of water is dictated by WAR.

- At high temperatures, the C_p value of the wet mixture, for a given WAR, is independent of pressure. This is correct because the mixture's thermodynamic properties typically vary according to the ideal gas law at high temperatures. As the intermolecular forces become negligible, the influence of pressure on the specific heat at constant pressure tends to vanish.

As mentioned in the methodology section, the modeling of phase change phenomena such as condensation is not an easy task. As this study considers the preliminary design and performance assessment of the WET engine, phase change phenomena are modeled in a rather simplified manner, as explained in Section 4.4.

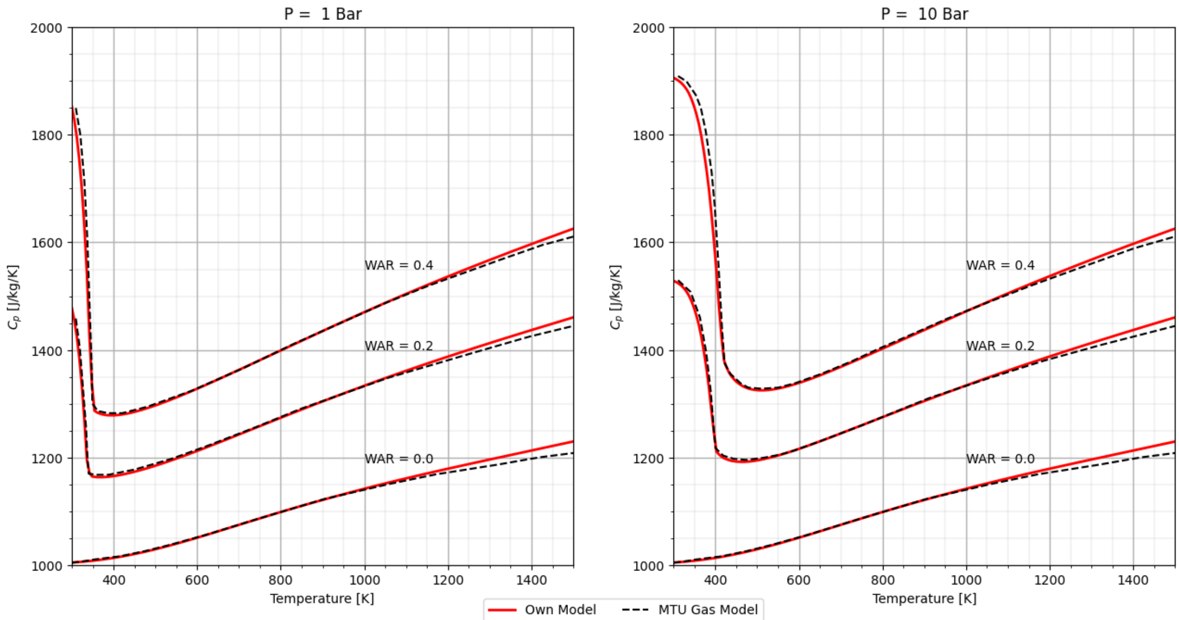

Figure 5.3: Specific heat capacity at constant pressure of wet air for pressures of 1 and 10 bar, and WAR up to 40% including the condensation region.

Lastly, the specific heat capacity of the exhaust gas mixture should approach the value of C_p for humid air (FAR = 0) as FAR decreases. Figure 5.4 illustrates this trend at pressures of 10 bar and 40 bar, showing a reduction in C_p for lower FARs. This decrease is attributed to a lower water fraction in the exhaust mixture, as reduced fuel flow results in less water formation. Since water has a relatively high specific heat capacity compared to other combustion products, its reduction leads to a corresponding decrease in C_p. Additionally, the figure highlights the influence of pressure on the specific heat capacity. At constant WAR and FAR, it is demonstrated that the pressure does not play a significant role for the specific heat C_p at temperatures sufficiently far from the dew point.

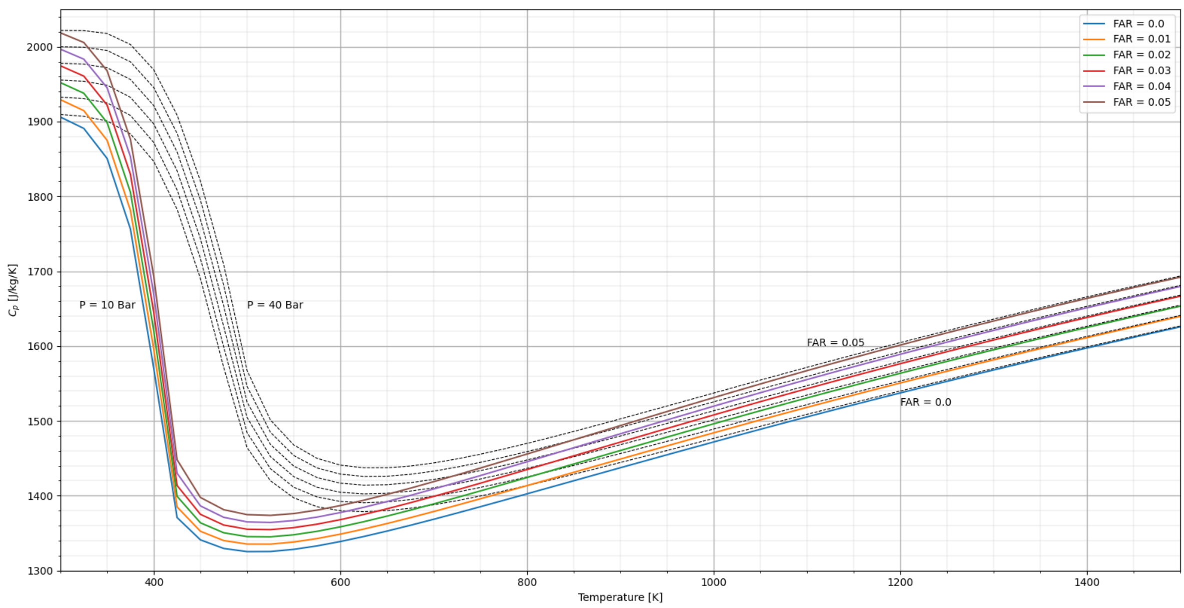

Figure 5.4: Effect of FAR variation on C_p for pressures of 10 and 40 bar (WAR = 0.4) and on the condensation region.

5.1.2. Wet Exhaust Gases

Various wet air thermodynamic properties have been verified in superheated or condensation regions. Unfortunately, no data for turbine exhaust gas properties with water shares up to 40% is available. To gain some insights into the gas properties aft of the combustor, a mixer-combustor model is created in pyCycle and Aspen Plus software. Aspen is one of the leading process simulation software that is being used for chemical applications [119]. The mixer-combustor model created in both frameworks to verify wet air and wet exhaust gas properties is shown in Figure 5.5. Compressed air enters the water injector, or mixer, where steam is added. As a result, wet compressed air (station [1] in Figure 5.5) flows out of this component and is led to the combustor. In this component, fuel is introduced and ignited, resulting in the formation of combustion products. The exhaust gases exit the combustor at station [2] in Figure 5.5.

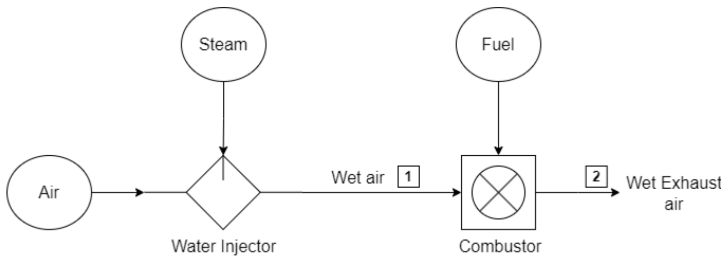

Figure 5.5: PFD of mixer-combustor model that is used for verification of the wet air and wet exhaust models in pyCycle.

The model is simulated in Aspen with appropriate settings and in PyCycle with both the CEA model and the TABULAR mode of calculating thermodynamic properties. In Aspen, the gas properties are modeled according to the ideal gas law in combination with the ideal gas mixture approximation as mixing rule. The expectation is that the results obtained with the CEA routine should be close to the results of Aspen, while the TABULAR mode predictions will be slightly different. The latter is likely caused by the fact that properties of water in the generated tables are calculated with the IAWPS-95 model, and by interpolation errors. Besides, some modeling details and/or assumptions are given regarding the model in Figure 5.5:

- As water is injected just before the combustor and after the last compressor stage, the Mach number in this component is likely to be very small. For this verification analysis, it is therefore assumed that the static pressure in the mixer is roughly equal to the total pressure.
- The class for calculating molar and mass fractions, based on WAR and FAR from the thermodynamic tables, was created after this test. It was not possible to provide these fractions for the TABULAR calculation mode in pyCycle. The fractions will, therefore, be given for CEA but not for TABULAR.
- Newton solver is used for convergence, and both absolute and relative error tolerances are set to $1e-6$.
- No pressure losses are assumed in the water injector and the combustor.
- Dodecane ($C_{10}H_{22}$) is used as fuel for the verification study. This fuel has been selected as it is a pure substance included in the Aspen Software fluid database, differently from Jet-A fuel, which is a blend of different molecules. At the same time, a new table set is easily generated for an arbitrary fuel in pyCycle. The properties used for Dodecane are tabulated in Table 5.1.

The three cases that are used for the verification of the thermodynamic model implemented in pyCycle are tabulated in Table 5.2. All three cases consider compressed air at 15 bar and 800 K as input with a mass flow rate of 10 kg/s. The steam is injected at various $WARs$ and temperatures to assess the calculation of the thermodynamic properties and composition of the exhaust gases for both high and low water content. The detailed results of all cases are tabulated in Appendix A.2, whereas a summary of the most important findings is presented below.

Firstly, the properties of the air, modeled as a mixture of N_2, O_2, Ar, and CO_2, are compared. The properties of compressed air for the three modes are summed in Table A.2. The second column

Table 5.1: Fuel characteristics for the mixer-combustor model.

Fuel specification	Value
Fuel type	Dodecane ($C_{12}H_{26}$)
T_{inj} $[K]$	298
Injection phase	Liquid
ΔH_f^0 $[kJ/mole]$	-352.373
M $[g/mole]$	170.338
ρ $[kg/m^3]$	746.080

Table 5.2: Verification cases details regarding the mixer-combustor model set-up.

	Air			Steam			
Case	**p [bar]**	**T [K]**	**MFR [kg/s]**	**p [bar]**	**T [K]**	**MFR [kg/s]**	**WAR**
1	15	800	10	15	500	1	0.1
2	15	800	10	15	800	1	0.1
3	15	800	10	15	1100	4	0.4

represents the absolute results from the Aspen simulation, whereas the third and fifth columns give the results for the CEA and TABULAR modes, respectively. The fourth column provides the relative difference between CEA and Aspen, whereas the sixth and seventh columns give the relative error between TABULAR mode and Aspen, and CEA, respectively. The relative error is calculated as follows:

$$RE = \frac{X_{mode,B} - X_{mode,A}}{X_{mode,A}} \cdot 100\% \tag{5.2}$$

The comparison shows that the CEA model reproduces the results of Aspen quite accurately within a relative percentage difference of a maximum of 0.018% (neglecting the entropy offset). The TABULAR mode yields results similar to those obtained with the CEA approach, which is understandable given that the tables are created using the CEA model. It can be said that, based on a comparison against CEA and Aspen results, the thermodynamic tables are sufficiently accurate to model (compressed) air.

Regarding steam property calculation, Table A.3 tabulates the results for the three models. Enthalpy discrepancies are all within 0.5%, which is higher than for the air, but this is expected as different models are used for modeling the water properties. Nevertheless, significant differences can be identified between mass density and isobaric-specific heat. Comparing CEA against Aspen, these changes are negligible as both rely on the ideal gas law. The TABULAR results show differences up to 28.4% and 7.3% for specific heat and density, respectively, compared to the other models. This is where real gas effects come into play. From CoolProp, it is found that the water saturation temperature at 15 bar is 471 Kelvin, slightly below the steam injection temperature for case 1 (500 Kelvin). The gradual increase in the isobaric-specific heat is the cause of the large discrepancy between the TABULAR mode and other models. The same consideration does apply to the differences in the mass density. Supporting graphs showing the differences among the three models for enthalpy, entropy, density, and isobaric specific heat in the temperature range 500-1100K can be found in Appendix A.3. As mentioned for the results in Table A.3, the largest relative error concerns the test case with temperatures near the saturation point, i.e. for case 1 in Table 5.2.

The results for the wet air properties estimated by all three modes are shown in Table A.4. As expected, the deviation after mixing is the highest when the steam injection temperature is 500 Kelvin, where the resulting temperature difference is 0.06%. However, the C_p relative error is not necessarily larger compared to the other two cases. This can be explained because two main aspects affect the estimation of the C_p (and density) of the mixture:

1. The temperature of the mixture
2. The water content in the mixture

The water share is relatively low for case 1 (10%) and high for case 3 (40%). Comparing case 1 and case 3, it can be said that the water share affects the estimate of C_p more than the temperature difference. The opposite is true for the density. Among the other thermodynamic properties, enthalpy is one of the most important as it is a crucial input state for the TABULAR mode in pyCycle. Differences are all smaller than 0.1%, even though IAPWS-95 has been used to predict the steam properties while generating the tables for the TABULAR calculation mode. The entropy differences are larger for the reason already mentioned before, namely a difference in reference state between Aspen and the CEA/TABULAR model. However, the differences in results between CEA and TABULAR calculation modes can be compared as both have the same reference state. All relative differences are smaller than 0.03%, where the entropy of the TABULAR method is smaller in all cases. This is because the value of water entropy estimated by CoolProp is lower throughout the considered temperature range, despite the two models having the same reference state. In summary, the comparison in Table A.4 shows small differences in the predictions of the CEA and TABULAR calculation modes, and Aspen: considering the thermodynamic properties for the three model results in Table A.4, a maximum relative error of 0.2% is observed. It can, therefore, be concluded that the TABULAR wet air model in pyCycle is verified.

The remaining part of the thermodynamic tables that have to be verified is that related to the predictions of the thermodynamic properties of wet exhaust gas after the combustor. The results for the three models are given in Table A.5. The combustor outlet temperature and pressure in the test cases of Table 5.2 are fixed at 1500 Kelvin and 15 bar, respectively, while the fuel mass flow rate is a model output. The relative error for $\dot{m}_f$ is larger for case 1, as expected. The temperature of the wet air at the combustor inlet estimated in the TABULAR calculation mode is slightly lower compared to the CEA and Aspen models. Thus, more fuel is required to reach a temperature of 1500 Kelvin at the combustor outlet. Still, the relative difference between the results obtained with the TABULAR calculation mode and those of the other models is smaller than 0.5% and is deemed acceptable for this study. Values for density, specific heat, and enthalpy all have a relative difference smaller than 0.1%, and the relative differences in entropy values are similar to those observed for humid air. Nevertheless, the largest discrepancy is found for the oxygen mass fraction in the mixture (CEA w.r.t. Aspen), being more than 0.5% for all three cases. This reduced oxygen fraction is likely caused by the relatively higher fuel consumption as the corresponding values for the CO_2 and H_2O mass fractions are higher than those according to the estimates of the Aspen model. Regarding C_p, it was shown that the water share and temperature of the mixture are most likely to cause errors for the thermodynamic tables. Because of the relatively large differences in the composition, this is a third factor that influences not only C_p, but also density, entropy, and enthalpy. Nevertheless, all discrepancies are lower than 0.5%, apart from the entropy. The deviations for this thermodynamic quantity among the three models are similar to those found in the verification cases involving wet air. To summarize, it can be said that for all three cases, the estimation of the thermodynamic properties of humid exhaust gases with the lookup tables implemented in pyCycle has the accuracy similar to those of the CEA and Aspen models, with relative deviations lower than 1% with most of these deviations being lower than 0.1%.

The last thing worth comparing for this simplified test case is how the computational speed varies depending on the chosen method for thermodynamic property calculation. This comparison is shown in Table 5.3. It can be concluded that the TABULAR calculation mode is approximately 10 times quicker than the CEA mode.

Table 5.3: Computational speed of CEA and TABULAR mode for the three mixer-combustor model cases.

	CEA mode	**TABULAR mode**
Case 1	9.042 sec	0.756 sec
Case 2	13.772 sec	0.708 sec
Case 3	8.008 sec	0.879 sec

5.1.3. WET Turboshaft Engine

In their first paper regarding the water-enhanced engine, MTU performed a thermodynamic analysis of a simplified WET engine configuration [7]. The considered engine architecture is the same as already shown in Figure 2.11. This section describes the steps taken to model a similar engine architecture and reproduce the results from the MTU study as accurately as possible.

Engine Lay-out & Assumptions

The WET engine configuration considered by MTU researchers in their seminal study is based on a simple turboshaft-type engine, as shown in Figure 2.11. This engine cycle is, therefore, referred to as the water-enhanced turboshaft (WETS) engine. Both the relevant assumptions and modeling choices that MTU has made in their study are listed below.

- The engine operation is simulated for standard sea level (SSL) conditions where the Mach number is set to zero.
- All turbomachinery efficiencies are assumed to be isentropic and set to 90%.
- Steam is injected at a temperature close to that at the compressor outlet.
- The TIT is fixed at 1650K, while the combustion efficiency is equal to 100%.
- All duct pressure losses, except those caused by the HEXs, are negligibly small, i.e., fixed to zero.
- The free power turbine (FPT) expands the exhaust gas to ambient pressure conditions. Moreover, the required power output is the same for all analyzed design solutions and is set to a fixed value of 25 MW.
- Regarding turbine cooling, it is assumed that 20% of the compressor discharge air is used to cool the turbine stages. 50% of this cooling mass contributes to the turbine work extraction process. Thus, 50% of the cooling air mass flow rate is injected before the first HPT stage, whereas the other half is injected after the last stage.
- Both the HRSG and the condenser are modeled as a simple HEX device (duct), where a thermal duty is imposed. The combined pressure loss over both HEXs is assumed to be 10% w.r.t. the total inlet pressure of the exhaust gases.
- No thrust generation is generated by this engine.
- In the MTU study, all thermodynamic properties are estimated using the NASA CEA approach. This means that all gases are treated as ideal gases. In pyCycle, the dry exhaust gas is modeled as an ideal gas, while the steam properties are calculated with the IAWPS-95. Some discrepancies are, therefore, expected between the results of MTU and those obtained with pyCycle.
- Kerosene (Jet A-1) is selected as fuel. The stoichiometric air-fuel ratio is reported to be 15:1, but no exact composition is mentioned.

The WETS engine model made in pyCycle is shown in Figure 5.6 and is similar to the MTU model. The yellow boxes indicate those quantities specified as inputs of the WETS engine model, while the blue boxes represent the dependent variables which are varied by the solver to satisfy the balance equations and to reach the engine's design specifications, or in other words, to minimize the residual equations of the engine model (Equation 3.1).

MTU WETS Results

One of the main advantages of the WETS engine compared to a conventional TF engine is the improved specific work of the core. Because steam has a higher specific heat than dry (exhaust) air, more work can be extracted from the turbines for a given inlet mass flow rate. As all design solutions should deliver the same power output, i.e. 25 MW, the core size of the WETS engine is expected to decrease for higher water shares in the core flow. MTU analyzed the heat capacity rate ratio of the HPT and the compressor. This heat capacity rate ratio (CRR) represents the enhanced turbine work potential compared to a reference Brayton cycle. It is formulated in Equation 5.3 with the stations as indicated in Figure 2.11. $\bar{C}_p$ is the average heat capacity of the exhaust between the inlet and outlet of the HPT. The mass flow rate in the numerator accounts for the cooling air mass flow rate that contributes to the work extraction process.

$$CRR = \frac{(\dot{m} \cdot \bar{C}_p)_{4-45}}{(\dot{m} \cdot \bar{C}_p)_{2-3}} \tag{5.3}$$

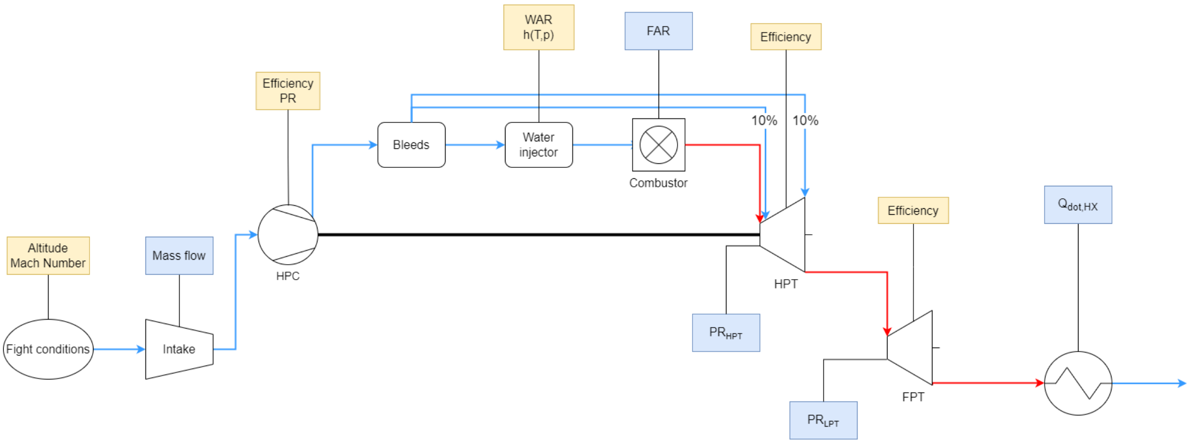

Figure 5.6: PFD of the WETS engine as modeled in the pyCycle framework with the blue and yellow boxes containing the state variables and cycle inputs, respectively.

Figure 5.7 shows the behavior of the CRR for various steam injection rates. The CRR increases linearly with WAR and the turbine work potential is, considering $WAR = 0.4$, 82% higher compared to the Brayton cycle. The result of pyCycle shows a similar linear behavior but the CRR is slightly underestimated compared to the results in the MTU paper. This can be explained by the different method adopted to calculate steam properties. Observe the C_p variation with temperature and the relative difference in the estimated values with the ideal gas model (CEA) and IAWPS-95 (pyCycle) in Figure A.5 and Figure A.6, respectively. The C_p returned by the IAPWS-95 model is lower than the value estimated by the CEA tool at high temperatures, above approximately 1400 K.

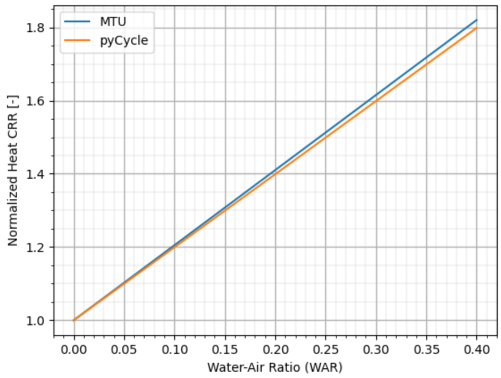

Figure 5.7: Normalized heat CRR of the WETS engine compared to a regular gas turbine engine cycle.

The effect of OPR and WAR on the compressor inlet mass flow rate is shown in Figure 5.8, where the colored lines represent the results in pyCycle and the black dotted lines are the equivalent results found in the MTU paper[7].
A noticeable impact of the water injection on the core mass flow rate, and thus on the core size, can be seen. The mass flow rate reduces significantly with the injection of steam, though this favorable effect reduces with increasing WAR. Moreover, the non-linear trend in the graph reflects the typical Joule-Brayton cycle variation of specific work with OPR for a fixed TIT. For $WAR = 0.4$ and $OPR = 30$, a mass flow rate decrease of 61% is predicted by MTU, which is similar to the value predicted by the pyCycle model, namely 61.28%. Although the predicted trends are almost identical to those reported in the MTU study for WAR values of 20% and higher, the baseline engine curve differs substantially from that reported by MTU. These discrepancies are reduced by increasing the amount of water injected into the en-

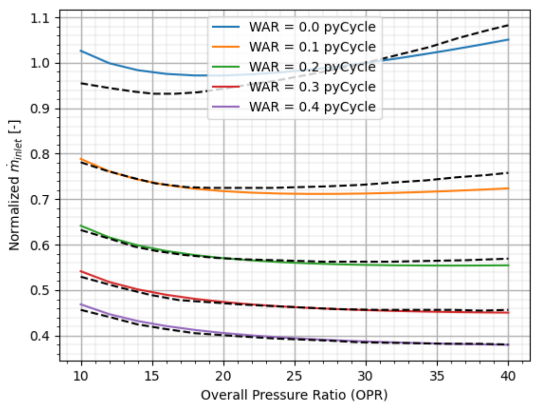

Figure 5.8: Normalized inlet mass flow rate of the WETS engine for various WARs and OPRs with the reference point at $WAR = 0$ and $OPR = 30$. Black dotted lines are MTU data retrieved from their work [7].

gine core. The exact cooling implementation by MTU is unknown, and a simple bleed component is used in pyCycle to imitate this. However, it is found that the results are quite sensitive to changes in the parameters of this simple cooling model. This could be the reason for the discrepancy between the two curves in Figure 5.8 for $WAR = 0$. Furthermore, in their seminal work on the WET engine, Schmitz et al. do not mention that the same simulation settings are used for both the conventional and steam-injected gas turbine engines. Exact steam injection conditions are also not mentioned in the original MTU study. Based on the reported *T,s*-diagram, steam is injected at a temperature similar to that of air at the compressor outlet. The influence of the assumptions regarding the gas turbine cycle reduces for higher water-to-air ratios. This makes sense as the impact of steam injection on the specific work of the thermodynamic cycle becomes more dominant and other factors, such as turbine cooling, reduce in importance. The model used to predict the performance of the baseline engine has, thus, been validated by comparing the model predictions with data available in the literature for an actual turbofan engine, see Section 5.2.

Previous analyses have demonstrated that injecting steam into the engine core reduces the core mass flow rate while increasing the engine's specific work. This factor is expected to influence also the core thermal efficiency of the WETS engine. In this regard, it is worth recalling that thermal efficiency is inversely proportional to the fuel mass flow rate (see Equation 3.30), and that any variation in $\dot{m}_f$ directly affects the efficiency, given that the lower heating value (LHV) and the engine's power output are held constant in the analysis. With a reduction in core size and a lower exhaust gas temperature at the engine outlet, fuel consumption is expected to decrease as the WAR increases. This expectation is supported by the results presented in Figure 5.9, illustrating the influence of WAR and OPR on fuel consumption. The black dotted lines represent the MTU results, which indicate a reduction in fuel flow of about 30% compared to the baseline engine. The results obtained with the pyCycle model exhibit a similar trend, predicting a reduction of 29.1% for a water-to-air ratio of 0.4. Notably, the pyCycle results align well with MTU data for WAR values of 0.2 and higher but show discrepancies at lower WAR values. Potential causes for this deviation have been previously discussed, though additional factors, such as fuel composition, may also contribute. Apart from mentioning the use of Jet A-1, no further details on fuel properties are provided in the work of MTU [7]. Analyzing Figure 5.9, the fuel flow rate exhibits a downward trend with respect to OPR, similar to that observed for the core mass flow rate: the fuel mass flow rate decreases with increasing OPR, due to improved thermal efficiencies achieved for the chosen TIT at higher pressure ratios. Moreover, the diminishing gap between the curves at higher WARs indicates that fuel savings eventually plateau, likely due to reduced oxygen availability for combustion.

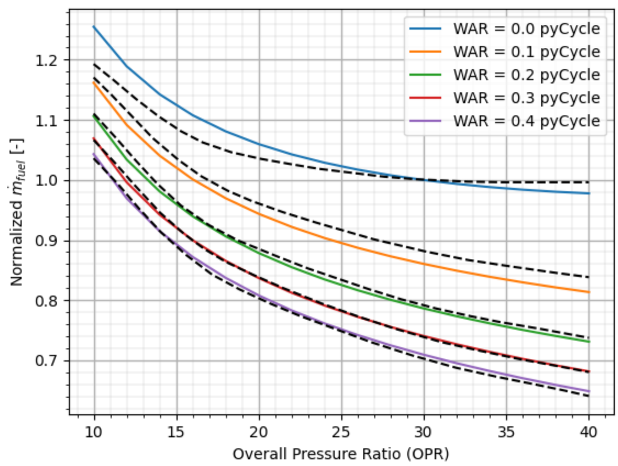

Figure 5.9: Normalized fuel mass flow rate of the WETS engine for various WARs and OPRs with respect to a reference engine with $WAR = 0$ and $OPR = 30$. Black dotted lines are taken from the study of MTU [7].

Overall, these preliminary results confirm the effectiveness of steam injection in reducing fuel consumption and prove the accuracy of the pyCycle model in predicting WET engine performance.

It is also worth investigating the variation of the equivalence ratio ϕ so that the effect of steam injection on the combustion process can be studied. The air-fuel equivalence ratio gives information about the amount of air that is needed to burn one mass unit of fuel and is defined by the ratio of the actual air-to-fuel ratio (AFR) and the stoichiometric AFR as shown in Equation 5.4. An equivalence ratio equal to one indicates a stoichiometric combustion process; a $\phi > 1$ corresponds to lean combustion process, as an excess of air (oxygen) is present with respect to the fuel; a $\phi < 1$ condition implies an excess of fuel and is referred to as rich combustion.

$$\phi = \frac{AFR}{AFR_{stoich}} \tag{5.4}$$

Kerosene (Jet A-1) is selected as fuel with a composition and LHV equal to $C_{11}H_{22}$ and 43.12 MJ/kg, respectively [113]. Based on these characteristics, the stoichiometric AFR is computed to be 14.62, approximately the same as the 1:15 value documented by MTU. The air-fuel equivalence ratio for the WETS engine as a function of WAR and OPR is presented in Figure 5.10. The results obtained with the pyCycle model (colored lines) almost perfectly match the results from MTU (dashed black line). Small deviations can be explained by differences in fuel characteristics. Still, it may be concluded that the deviations for low WAR values in Figure 5.8 and Figure 5.9 are not caused by the modeling of the fuel combustion process. Introducing steam in the core lowers the equivalence ratio as the mixture's oxygen (air) fraction reduces and approaches stoichiometric conditions for high WAR values. The increase in the equivalence ratio for higher OPR values can be also attributed to the lower temperature difference between the compressor outlet temperature and the TIT: less fuel is needed to heat up the core flow.

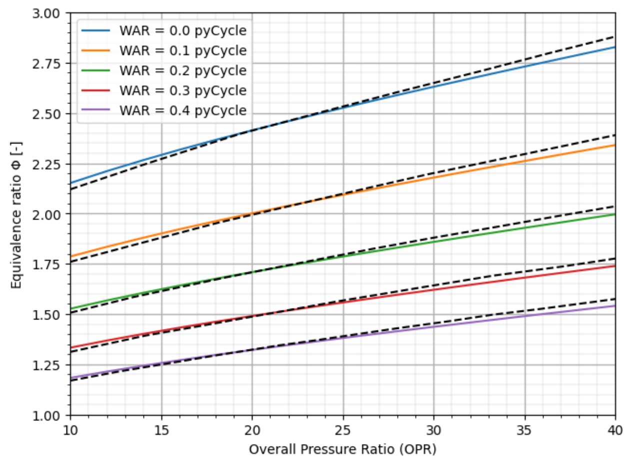

Figure 5.10: The air-fuel equivalence ratio (Φ) as function of WAR and OPR. Black dotted lines are taken from the study of MTU [7].

The last verification test is aimed at estimating the thermodynamic properties after the heat-exchanging devices. Modeled as a simple, single heat exchanger, the HRSG and condenser should cool the exhaust gases below the dew point so that all the water injected into the core is recovered and reinjected upstream of the combustor. The overall thermal load of the HEXs compared to the targeted turboshaft power output and the enthalpy change over the HEXs provides a first understanding of the HEX performance. In pyCycle, an extra balance equation is included in the engine model such that the heat flow $\dot{Q}_{HX}$ is determined according to the prescribed condenser outlet temperature. This temperature is calculated based on the partial and saturation pressure of the water in the exhaust stream. Referring back to Figure 2.11, thermodynamic properties at stations 5 and 7 are used to analyze the performance of the heat exchangers. The results are presented in Figure 5.11. Some important trends can be identified:

- For constant OPR, higher water shares in the core flow lead to a larger enthalpy drop in the exhaust gases across the HEXs. The increased turbine work potential results in hotter exhaust gases at the LPT outlet in a conventional engine. Although the heat duty of the heat exchangers required to cool the exhaust gas below the dew point will be higher, the recovered water can be heated up to higher temperatures. This would be beneficial for engine performance. The higher enthalpy change, multiplied by the mass flow rate, represents the HEX heat duty, which is therefore directly proportional to Δh.

- Wetter exhaust gases must be cooled more to recover all the injected water than dryer exhaust. The temperature at the LPT outlet is higher for higher WAR values, and the ratio $\dot{Q}_{HX}/W_{LPT}$ therefore increases.

- Higher OPR values causes the ratio $\dot{Q}_{HX}/\dot{W}_{FPT}$ to decrease. By setting a high OPR, the compressor discharge air is at a higher temperature, and less fuel needs to be added to achieve the prescribed TIT. More energy is to be extracted in the turbines to power the compressor and lower turbine outlet temperatures are achieved. This lowers the ratio $\dot{Q}_{HX}/W_{LPT}$.

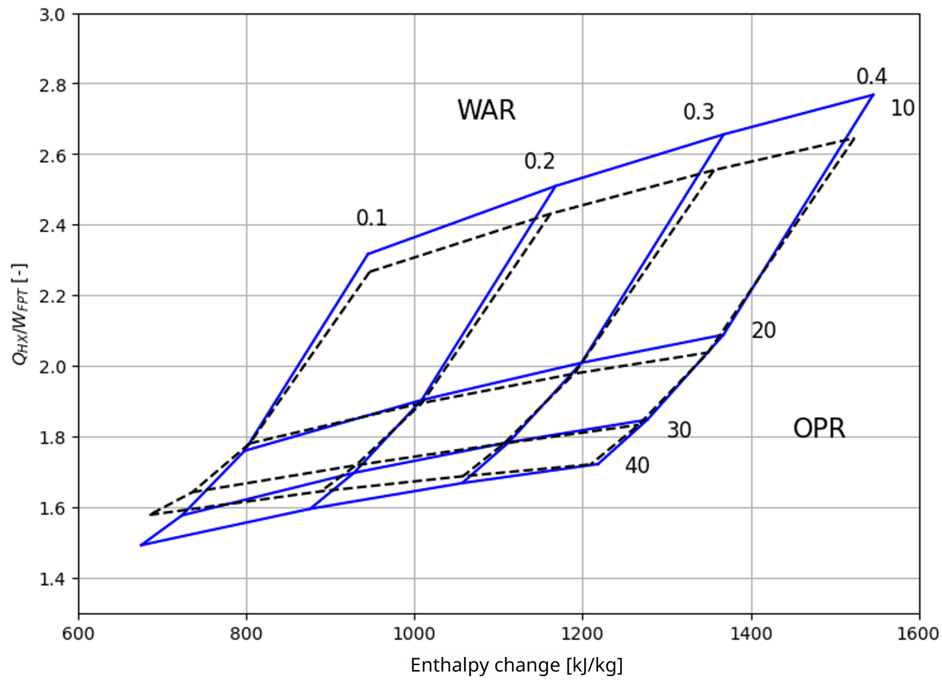

Figure 5.11: Ratio of the HEX thermal load and the FPT usable power as a function of the enthalpy change over the HEX. All points have been calculated assuming a 100% recovery of the injected water. Black dotted lines are taken from the study of MTU [7].

The results of the thermodynamic model and those of MTU in Figure 5.11 show similar trends. First, the trends, as discussed above, are similar to those found by MTU. The enthalpy drop of the exhaust gases over the heat exchangers is consistent in the two models for all design points. However, an offset is observed for low OPR values and all WARs. Referring to the results in Figure 5.8 and Figure 5.9, the (relative) deviation is the largest at low WARs for both very small and very large OPR values. Moreover, for $WAR = 0.1$, a constant underestimation of the fuel can be seen. However, these deviations can not be directly linked to the discrepancies in Figure 5.11. No explanation could be provided for the offset at low WAR and high OPR conditions. This offset is found for various modeling assumptions. Given the limited information provided in the MTU paper, different modeling assumptions were tested regarding the cooling model or the Mach number aft of the HEXs. However, the deviation with respect to the MTU results remained. The best match with the data in the first paper by MTU is obtained for an $OPR = 30$ and $WAR = 0.4$. For these conditions, MTU estimated that $\dot{Q}/\dot{W} = 1.83$, while the pyCycle model developed in this work returned a value of 1.847. Furthermore, the dew points estimated by the pyCycle model and those from MTU are compared. The dew point temperature after the condenser in the MTU study is approximately 311 Kelvin, whereas pyCycle model predicted a dew point temperature of 308 Kelvin.

5.2. Validation of the Baseline Engine Model

To verify the accuracy of the newly established thermodynamic model for humid gases, several verification tests were conducted in Section 5.1, which demonstrated that the model provides good predictions when compared to results from other software packages and relevant literature. However, in the case of no water injection, some discrepancies were observed between the pyCycle model results and those reported by MTU. To prove the model's validity despite these differences, a validation study is performed by modeling the performance of a turbofan for which detailed experimental data is available, namely a CFM56-3 turbofan engine [66].

A turbofan model, which will also form the basis for the WET engine, is created in pyCycle. A schematic layout of the turbofan engine that is being studied can be found either in the book of Kurzke [66] or in Figure 6.1 of Chapter 6. Only the engine on-design reference point is simulated. This reduces the complexity of the model, which is not affected by the choice of calibration of the turbomachinery maps or shaft speeds. Kurzke simulated the CFM56-3 in GasTurb and recreated a cycle reference point based on experimental data from the TAP report [66]. The inputs of the TF engine model implemented by Kurzke and in this study are tabulated in Table 5.4. The Kurzke model is replicated as closely as possible to avoid inaccuracies caused by differences in the engine configuration. The same isentropic efficiencies documented by Kurzke have been set in the pyCycle model. The TAP report does not provide the composition of the fuel. This information is needed to calculate the enthalpy of formation that should be inserted in the combustor model. The fuel composition has thus been modeled by specifying the chemical formula of an equivalent average fuel molecule. This is $C_{12}H_{23}$. Moreover, SLS conditions are considered for which a maximum (net) thrust force of almost 100kN ($\approx 22350 lbs$) was measured in the engine tests. Engine manuals of the CFM56-3 document similar maximum thrust values [120, 121].

Table 5.4: Input parameters for the cycle reference point of the CFM56-3 turbofan engine.

	Input value
BPR [-]	4.9373
Fn [kN]	99.43
TIT [K]	1577.55
$\mathbf{PR_{fan}}\ [-]$	1.655
$\mathbf{PR_{LPC}}\ [-]$	1.317
$\mathbf{PR_{HPC}}\ [-]$	11.069
$\mathbf{LHV_{fuel}}\ [\mathbf{MJ/kg}]$	42.769
Fuel	$C_{12}H_{23}$
Loading [%]	99.98

The simulation process in pyCycle differs from that applied in Gasturb. Kurzke used the isentropic efficiencies, TIT, and bypass ratio as iteration variables. This was chosen because temperatures were accurately measured at various stations and are therefore used as target values for the calibration of the model. Moreover, the fuel flow was measured and could therefore also be used as a target value, as well as the nozzle areas (fixed engine geometry). In pyCycle, all efficiencies have been fixed, and the pressure ratios of the turbines are used as iteration variables. Moreover, the FAR is varied to match the prescribed TIT. Lastly, the mass flow rate is used as iteration variable to match the measured corrected thrust. The outcomes for both engine models and their relative difference (Equation 5.2) are summarized in Table 5.5.

Table 5.5: Comparison between the results reported by Kurzke for the CFM56-3 engine and predictions of the two-shaft turbofan engine model implemented in PyCycle for a reference cycle point corresponding to SLS and maximum thrust conditions.

	Results in [66]	**Results pyCycle**	**Relative error [%]**
TSFC [g/kNs]	11.0146	11.0052	-0.085
$\mathbf{W_{fuel}}\ [\mathbf{kg/s}]$	1.0952	1.0942	-0.091
$\mathbf{m_{in}}\ [\mathbf{kg/s}]$	313.798	315.392	0.508
OPR [-]	24.16	24.13	-0.124
$\mathbf{T_{LPC,out}}\ [\mathbf{K}]$	369.92	369.66	-0.070
$\mathbf{T_{HPC,out}}\ [\mathbf{K}]$	770.82	770.34	-0.062
$\mathbf{T_{LPT,out}}\ [\mathbf{K}]$	862.58	867.68	0.591
$\mathbf{p_{LPT,out}}\ [\mathbf{kPa}]$	148.131	149.103	0.656
$\mathbf{A_{core}}\ [\mathbf{m^2}]$	0.29325	0.28666	-2.247
$\mathbf{A_{bypass}}\ [\mathbf{m^2}]$	0.74236	0.74036	-0.269

As the outcome of the pyCycle model indicates, this provides realistic results for a conventional turbofan engine. Analyzing the results of Table 5.5 in more detail, all pyCycle model outputs, except the core cross-sectional area, show relative errors lower than 0.65%. Especially, the engine performance parameters $TSFC$ and W_{fuel} show good accuracy with respect to the CFM56-3 data reported by Kurzke. The temperatures at the LPC, HPC, and LPT outlets and the pressure aft of the LPT also show good precision. The small differences can be attributed to a simplification applied in the pyCycle model regarding the fan component. Kurzke et al. considered different compression ratios for the inner (core flow) and outer (bypass) of the fan [66]. In the pyCycle model, both streams are compressed to the same pressure level. Thus, the PR_{LPC} is reduced with respect to the model in GasTurb to maintain the OPR of the engine. As the fan and the LPC models have slightly different isentropic efficiencies, this could lead to small errors in the estimation of the thermodynamic properties of the core flow. This validation test indicates that the discrepancies observed for the baseline WETS engine, i.e. with WAR = 0, in Subsection 5.1.3 with respect to the MTU data are most likely caused by some modeling assumptions regarding the engine cycle rather than errors in the thermodynamic model.

Extensive verification and validation tests have been conducted to assess the accuracy of the thermodynamic model of the WET engine. The prediction of the model in terms of engine performance and thermodynamic states at the various engine stations was meticulously compared against experimental data or results in the relevant literature for both conventional turbofan and simplified WET engine configurations. The results confirm that the model accurately predicts engine performance and characteristics under various conditions. Consequently, the model is both verified and validated, and ready for further extensions to perform a more detailed analysis of WET turbofan engines.

6

Engine Models

This chapter provides relevant information regarding the WET model as well as that of the baseline engine, whose results are used as a benchmark for the WET engine performance. In Section 6.1, the WET configuration is briefly discussed, highlighting the differences between the conventional and the WET turbofan engine. Subsequently, all relevant assumptions for each engine layout are provided in Section 6.2. Input parameters, design conditions, and cycle constants are given in Section 6.4.

6.1. Reference Engine Configurations

Figure 6.1 depicts the PFD of the WET engine modeled in this work. The predicted WET performance is compared against that of a conventional two-spool turbofan engine whose layout can be retrieved from that of the WET by removing the condenser, HRSG, and the water injection before the combustion chamber.

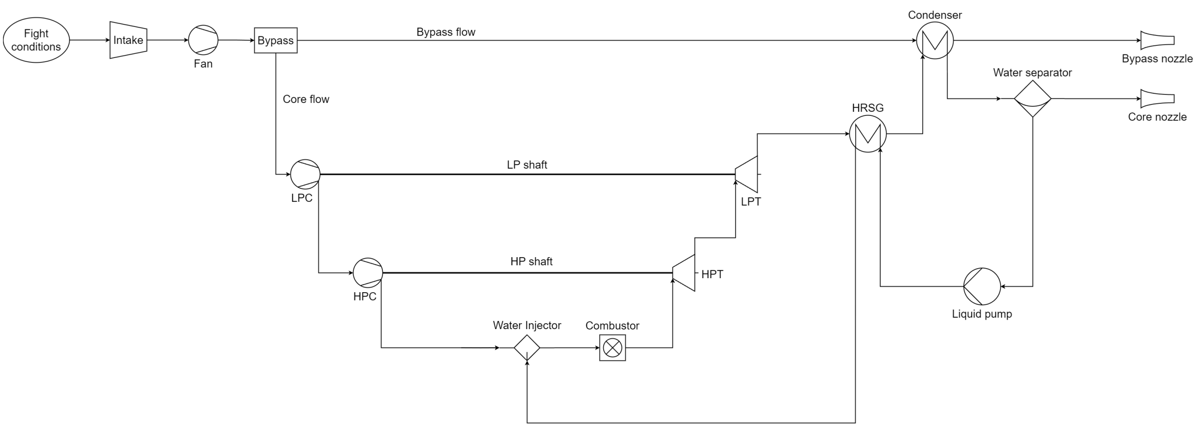

Figure 6.1: PFD of the water-enhanced turbofan engine architecture implemented in pyCycle.

Figure 6.2 gives an overview of the structure of the model as implemented in the OpenMDAO framework. The WET engine model consists mainly of three elements: the power unit that includes the two spool turbofan engine model (PU), the evaporator (HRSG), and a solver. Considering the first element, the PU integrates a simple two-spool turbofan engine model with a steam cycle. A non-linear Newton solver finds the solution of the balance equations pertaining to the PU group model. Subsequently, the evaporator is sized within Hexacode, an in-house heat exchanger tool made by Propulsion & Power group of TU Delft. Geometry, mass, and pressure drops are obtained from this model. Based on the computed pressure drop by Hexacode, this pressure drop is compared to the value assumed in the simple two-spool turbofan engine model in the Power Unit group.

Hexacode also includes models for condenser sizing, but this has not been included in the WET engine model yet. The reason is that Hexacode is not yet capable of capturing condensation in wet

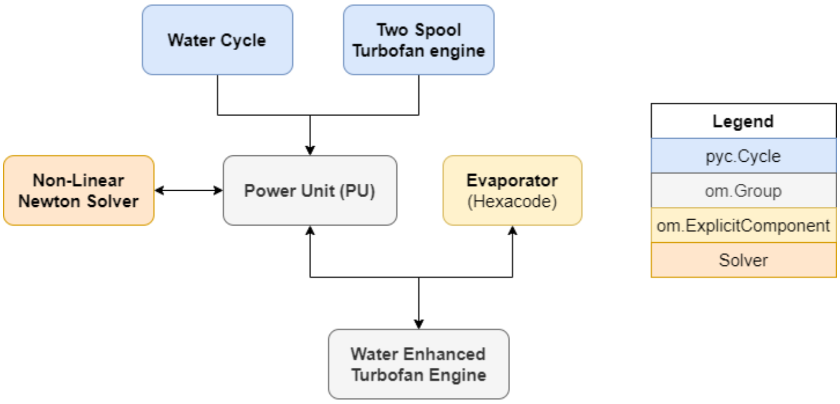

Figure 6.2: Structure of the complete water-enhanced turbofan engine model including the detailed heat exchanger models.

exhaust gases. It is possible to model the condenser as an air-to-air heat exchanger, but without accounting for water condensation in the exhaust gases. It means that the estimated pressure drops and HEX mass are not accurate for higher WAR values. Condensation of pure fluids is only available within Hexacode, which does not cohere with the WET engine condenser characteristics. Part of the exhaust gas mixture's water undergoes condensation. For the reasons stated above, detailed modeling and integration of the condenser (in Hexacode) is reserved for the future.

6.2. Assumptions & Simplifications

The following assumptions and simplifications apply to the WET engine:

- Turbine cooling has been neglected.
- The full water condensation process takes place in the condenser. It is assumed that the wet exhaust gas exiting the HRSG only contains water in the gaseous phase.
- Detailed condensation modeling has not been implemented at this stage and is reserved for future work.
- The condense recovery efficiency, $\eta_{rec,H2O}$, is assumed to be 1. This entails that the water separator recovers all the water that is being condensed.
- The temperature of the condensed water is assumed to be the same as that of the (dry) exhaust gases. However, this may not be the case in practice.
- A prerequisite of the WET engine is that all water that is being injected is recovered after the condenser. In other words, $LWAR = -WAR$ holds for the water separator (see Subsection 4.4.2).
- The combustion efficiency is considered to be 100%.
- The same engine net thrust is assumed in all cases to be analyzed. This holds for both the baseline and the WET engine cycle.
- Both HRSG and condenser are modeled in pyCycle as two separate ducts, which impose a given pressure drop and enthalpy variation in the corresponding cold and hot streams. The HRSG is sized by means of Hexacode afterward. The estimated pressure drops are fed back into the engine model to update the engine performance.
- Both the steam injector and the water separator work by the mass-averaged enthalpy principle. No detailed mixing or separation processes are considered for the sake of simplicity.
- It is assumed that the condenser will be placed in the bypass duct.
- Duct losses are set to zero unless stated otherwise in the subsequent Section 6.4. Additionally, each component's Mach number is chosen based on the guidelines provided by Kurzke [66].

- Polytropic efficiencies are prescribed for both the compressors and turbines. The isentropic efficiencies are determined using the PU's balance equations. This enables a fair comparison if the OPR is varied.
- As discussed in Section 4.6, fixed water temperature and pressure of 288.15 Kelvin and 0.5 bar are assumed at the pump inlet station. Because of the relatively high velocity ratio imposed in the WET engine, the core nozzle exit conditions do not vary significantly (290-330 K) [16]. When an optimal WET engine design has been found, the validity of this hypothesis will be checked.
- The steam injection temperature is defined by specifying the injection pressure and the degree of superheating at the HRSG cold side outlet. In this way, superheated steam conditions at the mixer inlet are guaranteed.

6.3. LEAP-1A-Type Engine as Comparison Benchmark

To evaluate the performance improvements of the WET engine, a conventional LEAP-1A-type engine is used as a benchmark. The LEAP-1A reference engine model described in Kurzke's work is the foundation for constructing this turbofan model [66]. This engine architecture is slightly different than the TF model built for validation purposes that was described in Section 5.2. The comparison is essential to assess the impact of steam injection on key performance metrics such as fuel consumption, thermal efficiency, and turbine work extraction. The relevance of this comparison lies in the fact that the LEAP-1A represents a state-of-the-art high-bypass turbofan widely used in commercial aviation. Furthermore, using a well-documented reference model facilitates direct performance comparisons, ensuring that any observed benefits or trade-offs of the WET cycle are grounded in a robust and industry-relevant context.

6.4. Input Parameters

This section briefly describes the considerations behind the chosen input parameters of the LEAP-1A-type benchmark engine and/or WET engine models.

Mach Numbers

Defining the Mach number for each engine component is needed to determine the thermodynamic state and flow properties at that station, since the Mach number relates the total and static properties of the flow. These are eventually needed to calculate the flow velocity, which are, in turn, required to assess the momentum and energy balance equations. Table 6.1 tabulates the selected Mach numbers at the engine stations. All Mach numbers are based on the values used by Kurzke [66].

Pressure Drops

A pressure drop should be imposed in each duct or combustor element in the engine cycle. It is assumed that most ducts have no pressure drop, but this may not be valid for some parts of the engine. The duct between the fan and the first stage of the LPC is relatively long, and a small pressure drop was chosen for this element. Pressure drop values for the combustor found in the literature are close to 5%, whereas a default value of 5.4% is found in the TF engine from pyCycle [21]. As these values are similar, a pressure drop of 5% is selected for the burner. A relative pressure drop of 1% is chosen for the bypass duct, based on [21]. Lastly, a guess has to be made for the pressure drop over both sides of the condenser and HRSG, as Hexacode is used for the preliminary design of the HRSG only. Moreover, this task is carried out only after the gas turbine and steam cycles have been defined. A ΔP of 5% is assumed for both sides of the HRSG. As the bypass ratio is relatively high for the WET engine, the pressure drop on the hot side (6%) is assumed to be slightly higher than the cold side (4%), based on the condenser geometry proportions shown in Figure 2.12. Unfortunately, no sources were identified that provide quantitative data or estimates concerning pressure losses within the condenser. All pressure drops are selected according to both the default values in pyCycle or the values documented by Kurzke or based on WET engine-related literature [7, 16, 59, 60, 66, 100]. A summary of the input parameters mentioned above can be found in Table 6.2.

Turbomachinery Polytropic Efficiencies

The efficiencies of turbomachines do have a significant effect on engine performance. Polytropic efficiencies are preferred over isentropic efficiencies in engine design and parametric analysis, particularly when evaluating changes in OPR. Samuelsson et al. developed a method to estimate the polytropic efficiencies based on the Entry-into-Service (EIS) year [122]. The efficiencies predicted for a 2030 EIS turbofan engine during the cruise phase are used for the WET engine in this study and are tabulated in Table 6.3.

Design Point & Fuel Characteristics

Cruise is considered as the design point for the WET engine. In this study, the off-design performance is not considered and is left for future research. The thrust is kept constant across all engine cycles and is comparable to values reported in the literature for narrow-body aero engines [10, 16, 123]. Moreover, kerosene is chosen as fuel with the corresponding properties as tabulated in Table 6.5.

Other Inputs

Other relevant inputs are tabulated in Table 6.4 for WET and conventional turbofan models. The ram recovery factor is based on the value used in pyCycle for an HBTF engine. Furthermore, the pressure ratio of the HPC and the core should also be chosen consistently with the prescribed OPR. As it is assumed that the performance of the HPC should be similar for all design points, the FPR is an iteration variable, and the LPC pressure ratio is a result of the OPR subtracted by the FPR and Π_{HPC}. A value of 12 is selected for Π_{LPC} based on values reported in the literature for modern or future conventional HBTF engines [56, 66, 124, 125]. Furthermore, the gross thrust coefficient is defined as the ratio of the real and ideal gross thrust. It quantifies nozzle efficiency by accounting for losses resulting from viscous effects and misalignments between the flow direction at the nozzle outlet and that in which the thrust has to be provided. Mattingly et al. reported values of C_{fg} between 0.9 and 1.0 depending on both nozzle area and pressure ratios [126]. Besides this, pyCycle also has values of C_{fg} stored in its default engine models, and these values are fixed for all engine cycles.

Table 6.1: Engine station Mach numbers in the engine cycle.

Engine Station	Mach Number [-]
Inlet	0.60
Fan	0.50
Duct fan-LPC	0.40
LPC	0.40
Duct LPC-HPC	0.40
HPC	0.30
Injector	0.30
Burner	0.20
HPT	0.40
Duct HPT-LPT	0.40
LPT	0.40
Duct LPT-HRSG	0.40
HRSG	0.35
Duct HRSG-Condenser	0.35
Condenser core	0.35
Water Separator	0.30
Duct bypass	0.50
Condenser bypass	0.45

Table 6.2: Pressure drops of various elements in the engine cycle.

Engine Component	Pressure drop [%]
Duct fan-LPC	0.5
Duct LPC-HPC	1.0
Burner (TF/WET)	5.0 / 4.0
Duct HPT-LPT	0.5
Duct LPT-HRSG	0.5
Duct bypass	1.0
HRSG core	5.0
HRSG water cycle	5.0
Condenser core	6.0
Condenser bypass	4.0

Table 6.3: Polytropic efficiency values of the fan, compressors and turbine.

Engine Component	Polytropic efficiency [%]
Fan (TF/WET)	91.00 / 95.60
LPC (TF/WET)	91.00 / 92.30
HPC (TF/WET)	91.00 / 93.00
HPT (TF/WET)	89.00 / 90.10
LPT (TF/WET)	91.00 / 92.40

6.5. Balance Equations and Solver Settings

The WET engine model is implemented within the PyCycle/OpenMDAO framework, which enables efficient modeling of thermodynamic cycles through a modular and optimization-driven approach. PyCycle,

Table 6.4: Other input parameters for both the reference and WET engine cycle.

Other input parameters	**Value**	**Unit**
Ram recovery	0.999	[-]
HPC pressure ratio (TF/WET)	18 / 12	[-]
Gross thrust coefficient core nozzle	0.993	[-]
Gross thrust coefficient bypass nozzle	0.993	[-]
HP shaft efficiency	99.5	[%]
LP shaft efficiency	99.5	[%]
ζ_{rec} / WRR	100	[%]
Pump inlet temperature	288.15	[K]
Pump inlet pressure	0.5	[bar]
Water pump isentropic efficiency	92	[%]

Table 6.5: Design point and fuel characteristics for both the reference and WET engine cycle.

Design point characteristics	**Value**	**Unit**
Design point	Cruise	
Altitude	35000	[ft]
Flight Mach number	0.78	[-]
Net thrust	22.8	[kN]
OPR (TF/WET)	45 / 35	[-]
Fuel characteristics		
Fuel composition	$C_{12}H_{23}$	
LHV	43.1	[MJ/kg]
Molar weight	167.3	[g/mole]
Combustion efficiency	100	[%]

built on OpenMDAO, provides a flexible environment for defining and solving complex engine configurations, making it well-suited for the iterative nature of aero-engine analysis.

Within this framework, solver settings are crucial in ensuring numerical stability and convergence. Balance equations are formulated to maintain consistency across thermodynamic states, with specific iteration variables adjusted to achieve predefined target conditions. By leveraging OpenMDAO's optimization and solver capabilities, the model is systematically solved in an iterative manner, enabling accurate prediction of the WET engine's performance under varying operating conditions.

The balance equations with the corresponding iteration variables and target values are tabulated in Table 6.6. For the sake of completeness, all target values are again shown. A cross in Table 6.6 means that the balance equation is not present in the reference engine model. This is only the case for the last balance equation, which expresses the relation between the heat duty of the condenser and the required dew temperature for recovering all injected water. The temperature at which all water is recovered depends on the pressure at the LPT outlet, hence on the corresponding design point. No fixed target value is therefore provided. Both the BPR and the TIT are varied in the design exploration phase. The range in which the TIT is varied for both engine architectures is shown in Table 6.6. The last difference between the conventional TF and the WET engine is the (ideal) nozzle velocity ratio, defined in Equation 3.35. Previous studies have established that a velocity ratio of 0.8 typically yields the minimum TSFC for conventional turbofan engines, making it a key design parameter in the conceptual design phase of aero engines. However, for WET engines, limited research has been conducted on the optimal velocity ratio. Three studies have examined the influence of velocity ratio on engine performance [16, 59, 60]. Among these, only the German Aerospace Center (DLR) has reported that an increased velocity ratio of 1.1 ensures minimum fuel burn. Based on this finding, a velocity ratio of 1.1 is adopted as the baseline value for the design space exploration of the WET engine. In the parametric study presented in Chapter 7, the impact of varying the velocity ratio on engine performance will be further analyzed.

Lastly, the solver settings are shortly summarized in Table 6.7 for both engine models. The absolute tolerance defines the maximum permissible residual error for the solver's convergence. It sets a fixed

Table 6.6: Balance equation in pyCycle used for the conventional TF engine and the WET engine.

Iteration Variable	Target Variable	Target Value	
		TF	WET
Intake mass flow rate (W_{in})	Net thrust (F_n)	22.8 kN	22.8 kN
Fuel-to-air ratio (FAR)	Turbine Inlet Temperature (TIT)	1500 - 1800 K	1500 - 1700 K
HPT pressure ratio (Π_{HPT})	HP shaft torque / power	0	0
LPT pressure ratio (Π_{LPT})	LP shaft torque / power	0	0
Fan isentropic efficiency ($\eta_{is,fan}$)	Fan polytropic efficiency ($\eta_{poly,fan}$)	0.910	0.956
LPC isentropic efficiency ($\eta_{is,LPC}$)	LPC polytropic efficiency ($\eta_{poly,LPC}$)	0.910	0.923
HPC isentropic efficiency ($\eta_{is,HPC}$)	HPC polytropic efficiency ($\eta_{poly,HPC}$)	0.910	0.930
HPT isentropic efficiency ($\eta_{is,HPT}$)	HPT polytropic efficiency ($\eta_{poly,HPT}$)	0.890	0.901
LPT isentropic efficiency ($\eta_{is,LPT}$)	LPT polytropic efficiency ($\eta_{poly,LPT}$)	0.910	0.924
Fan pressure ratio (FPR)	Nozzle velocity ratio	0.8	1.1
HRSG heat flow ($\dot{Q}_{cond}$)	Static condenser outlet temperature	x	Dependent

threshold below which the solution is considered sufficiently accurate, regardless of the variable magnitude. The relative tolerance is a convergence criterion based on the magnitude of the solution itself. It ensures that the solver stops when the residual error is sufficiently small compared to the current value of the variable, making it particularly useful for handling a wide range of variable magnitudes. Furthermore, the Armijo-Goldstein line search method improves the robustness of Newton solvers by ensuring that each iteration sufficiently reduces the residual error. It modifies the step size to maintain stability and prevent divergence, which is especially beneficial for highly nonlinear problems. Armijo-Goldstein line search is preferred over BoundsEnforce in nonlinear Newton solvers due to its ability to improve convergence stability, handle nonlinearities, and provide flexibility in constraint handling. Dynamically adjusting the step size prevents instability and overshooting, ensuring smoother convergence in highly nonlinear systems like turbofan engine models. Unlike BoundsEnforce, which strictly limits updates within predefined constraints and may cause stagnation near boundaries, Armijo-Goldstein allows for controlled step size reduction, increasing the likelihood of finding a valid solution within the feasible region. This makes it a more robust choice for solving complex balance equations.

Table 6.7: Solver settings for both conventional and water-enhanced TF engine.

Solver setting	TF	WET
Non-linear solver type	Newton Solver	Newton Solver
Absolute tolerance	1e-7	1e-4
Relative tolerance	1e-15	1e-15
Maximum iterations	30	50
Linesearch type	ArmijoGoldstein	ArmijoGoldstein

7
Results & Discussion

This chapter presents the performance analysis results of a conventional turbofan engine and the novel Water Enhanced Turbofan (WET) engine. Section 7.1 documents the performance of the benchmark engine (LEAP-1A-type), serving as a reference for comparison with the WET engine. Section 7.2 focuses on the WET engine, introducing its key characteristics and analyzing its performance across various configurations. The design space exploration (Subsection 7.2.1) provides an overview of potential design variations, while Subsection 7.2.3 reports the characteristics of the HRSG estimated with the high-fidelity Hexacode software. After checking all constraints and heat exchanger feasibility, the best WET engine configuration is presented in Subsection 7.2.4.

Subsequently, Section 7.3 presents a parametric study examining the influence of critical design parameters on engine performance. Finally, Section 7.4 provides a discussion, synthesizing the findings from the benchmark engine model, the WET engine design space exploration, and parametric studies. This section contextualizes the results within the broader scope of aero-engine technology and identifies key aspects for future research.

7.1. Benchmark: The Conventional Turbofan Engine (LEAP-1A)

To establish a reference for the WET engine, a baseline high-bypass turbofan (HBTF) model was developed. This benchmark engine is modeled after the LEAP-1A, based on the modeling guidelines from Kurzke's textbook, but neglecting turbine cooling. The TSFC map, shown in Figure 7.1, illustrates the variations in TSFC over a range of TITs and BPRs, providing key insights into fuel efficiency trends. All relevant input parameters can be found in Section 6.4. The TSFC map is generated for bypass ratio values between 8 and 20, each with a step size of $\Delta BPR = 0.5$, whereas the TIT ranges from 1500 to 1800 Kelvin, and is varied with a step size of $\Delta TIT = 10\ K$. For all design points, the nozzle velocity ratio is set to 0.8. The TSFC map presents contour lines of constant TSFC across different TIT and BPR values, where the darker blue region indicates designs with relatively low TSFC. Moreover, the dotted black lines show constant intake mass flow rate values.

It is worth looking at the TSFC trends in the Figure 7.1. For a given BPR, the TSFC initially decreases with increasing TIT but subsequently increases beyond a certain TIT value. At relatively low TIT values, increasing TIT enhances the thermal efficiency of the Brayton cycle. A higher TIT increases the available enthalpy for expansion in the turbine, allowing for more effective power extraction. This improves the overall thermal efficiency of the cycle, leading to a reduction in TSFC. However, as TIT continues to increase, the rate of efficiency improvement begins to diminish as the higher availability of thermal energy at the turbine inlet leads progressively to an increase in the exhaust gas temperature downstream of the LPT. A larger fraction of energy is therefore wasted in the exhaust gases. Additionally, the higher exhaust velocities associated with increased TIT can reduce propulsive efficiency, particularly in a high-bypass turbofan where lower exhaust velocities are preferred for maximizing efficiency. Beyond a critical TIT, these detrimental effects outweigh the benefits of increased thermal efficiency, causing TSFC to rise. If cooling effects were included in the analysis, the trend would become even more pronounced, as a portion of the compressed air would need to be diverted for turbine cooling rather than combustion, further reducing efficiency.

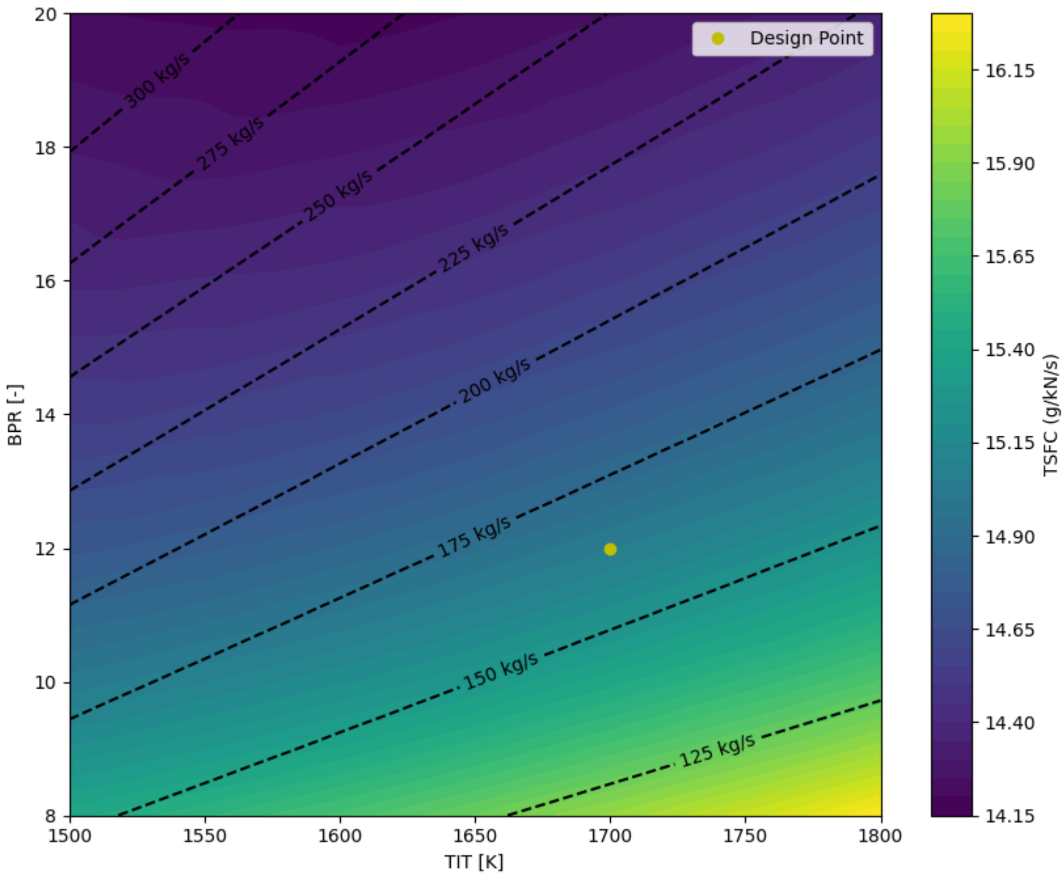

Figure 7.1: Design exploration map (TSFC) for a LEAP-1A-type engine with the green dot indicating the reference turbofan design.

Based on values found in the literature for the LEAP-1A engine for cruise conditions, the BPR and TIT are fixed, and the corresponding thermodynamic cycle can be simulated. It is documented that the BPR of the LEAP-1A engine is 11/12:1, while the TIT of the exemplary turbofan engine is between 1600 and 1700 Kelvin during cruise [127]. Kurzke also reports a similar BPR and TIT of 1700 Kelvin for an exemplary turbofan engine [66]. The reference LEAP-1A operating point (TIT = 1700 K, BPR = 12) is marked on the map with a green dot. This configuration lies within a region of relatively low TSFC but does not reach the absolute minimum. This aligns with design trade-offs balancing efficiency, thrust requirements, and operational constraints. A summary of the most relevant engine performance parameters for the chosen reference design is tabulated in Table 7.1. Besides this, the thermodynamic cycle data of the reference TF engine for each station are presented in Appendix A.4.1.

Table 7.1: Performance of the benchmark TF engine (OPR=45, TIT=1700K, BPR=12).

TF results	**Value**
TSFC [g/kN/s]	15.047
Intake mass flow rate [kg/s]	163.251
FPR [-]	1.680
FAR [-]	0.0273
Thermal efficiency [%]	48.54
Propulsive efficiency [%]	76.50
Total efficiency [%]	37.13

To support the results reported in Figure 7.1 and Table 7.1, a comparison has been made with the results documented in Kurzke [66]. Also, the efficiency trends are investigated in Figure 7.3. Lastly, the thermal and propulsive efficiencies are compared in Figure 7.4.

First, the TSFC is presented as function of BPR in Figure 7.2. The solid line represents the reference TF engine modeled in pyCycle, whereas the dashed line is the baseline engine data from Kurzke. The PyCycle engine model consistently shows higher TSFC (8%) than the Kurzke reference case across all BPR values, but has a similar trend. The discrepancies between the two models are given below:

- **No turbine cooling in the pyCycle model:** Kurzke's model includes realistic cooling flows for turbine blades, whereas the pyCycle model assumes an idealized setup without cooling. Generally, the TSFC is better without cooling, and this can therefore not explain the overestimation of TSFC for the pyCycle engine.

- **Fan pressure ratio:** Kurzke's model considers a lower pressure rise for the inner part of the fan compared to the outer part, whereas the pyCycle model considers the same pressure rise over both the core and outer fan. Because the polytropic efficiency of both the booster and the fan is equal (Table 6.3), this aspect does not cause the discrepancy in TSFC.

- **Nozzle expansion ideality:** Kurzke's model considers an ideal nozzle for both the core and bypass nozzle. This is not the case in the pyCycle model, where a gross thrust coefficient $C_{f,g}$ is imposed because this $C_{f,g}$ is also used for the WET engine. This is likely the primary contributor to the overestimation of TSFC observed in the PyCycle model results presented in Figure 7.2.

- **Other factors:** the pyCycle model does not account for bleeds or leakages, which may introduce minor deviations in the results. Additionally, slight discrepancies in fuel characteristics and air composition could contribute to variations in predicted performance. Furthermore, since pyCycle operates in TABULAR mode, small interpolation errors may affect the results. These interpolation inaccuracies could introduce minor deviations already at the intake, which may become more pronounced at higher pressure ratios due to the cumulative nature of numerical errors.

By addressing these factors, the PyCycle model could better match real-world engine performance and provide a more accurate baseline for comparison with the WET engine concept. However, a good comparison can still be made if the WET engine is based on the same modeling assumptions.

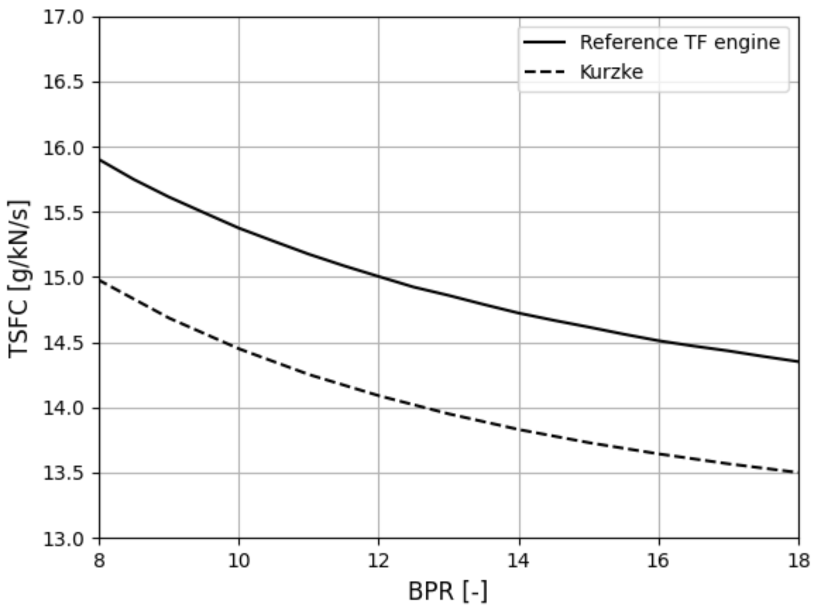

Figure 7.2: TSFC as function of BPR for both the reference engine in pyCycle and Kurzke's model [66].

Figure 7.3 presents the variation of thermal efficiency, propulsive efficiency, and overall efficiency as a function of BPR for the reference engine. Thermal efficiency remains relatively constant or slightly decreases with increasing BPR. Propulsive efficiency increases significantly with BPR. This is expected, as higher BPR results in a lower bypass exhaust velocity, reducing kinetic energy losses and making the propulsion system more efficient. Total (or overall) efficiency gradually increases with BPR. Despite the slight reduction in thermal efficiency, the strong improvement in propulsive efficiency dominates, leading to a net gain in total efficiency. This explains why modern turbofan engines favor higher BPR values to optimize fuel efficiency.

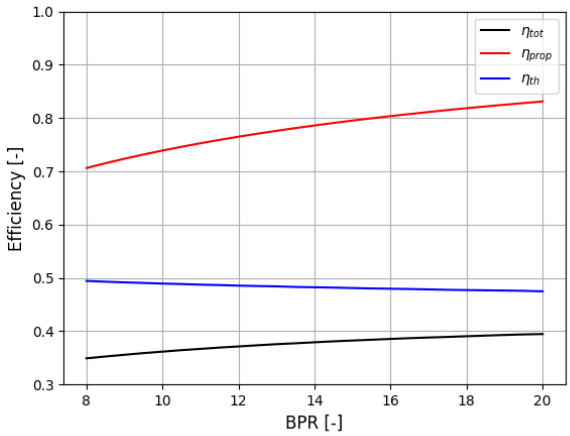

Figure 7.3: Turbofan reference engine efficiencies as function of BPR.

Figure 7.4 shows how the thermal efficiency of the TF baseline engine varies with OPR, BPR and TIT for constant propulsive efficiency. As OPR and TIT increase, thermal efficiency improves due to the higher power extracted from the turbine that more than compensates the extra power demand of the compressor. However, at a fixed propulsive efficiency, BPR has a weaker influence on thermal efficiency than OPR and TIT. As BPR increases, more power is allocated to the fan, reducing the core's specific work output. While this increases propulsive efficiency, it can slightly lower thermal efficiency due to a reduced pressure and temperature ratio in the turbines. Kurzke only provides results for $OPR = 40$ and $OPR = 50$, whereas the reference engine has an OPR of 45. It can be seen that the reference engine trend aligns between the lines of Kurzke in the depicted TIT range, although not exactly in the middle. Nevertheless, the offset in TSFC as shown in Figure 7.1 is directly coupled to the engine's efficiency and a small offset in Figure 7.4 is therefore expected.

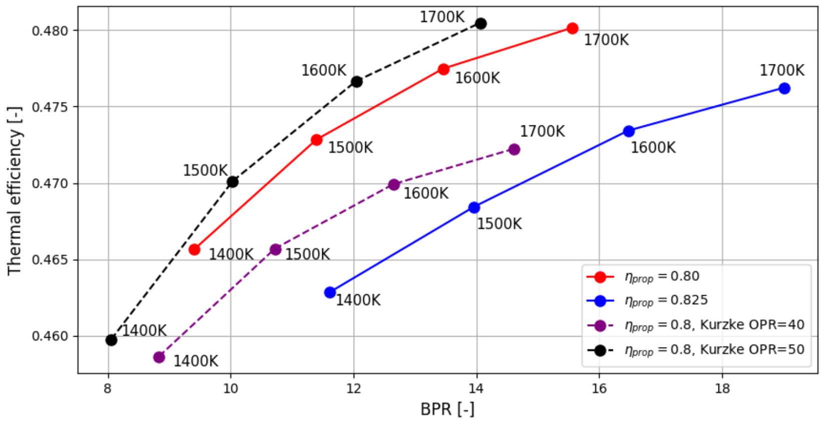

Figure 7.4: Comparison of the thermal efficiency of Kurzke's exemplary TF engine with that of the PyCycle TF model for a given propulsive efficiency.

This benchmark case provides a reference for evaluating the impact of water injection and recovering in the WET engine. The WET engine's optimal TIT-BPR combination can be evaluated against this benchmark to assess efficiency improvements. The TSFC map of the benchmark HBTF engine confirms well-established trends: increasing TIT and BPR improves fuel efficiency, but with diminishing returns. The chosen LEAP-1A-type operating point provides a reasonable trade-off between efficiency and engine size and will be used for comparison with the WET engine.

7.2. The Water Enhanced Turbofan Engine

This section presents the results of the design exploration for the WET engine. Following the approach outlined in the previous section, the TSFC variation with the relative amount of injected water is analyzed in Subsection 7.2.1. Based on design constraints, the most optimal solution in terms of (overall) fuel consumption is identified and selected for further analysis. Subsequently, the HRSG in this engine is modeled in greater detail in Subsection 7.2.3. The architecture and performance characteristics of the optimal WET engine cycle are examined in Subsection 7.2.4, with key performance trends discussed in Subsection 7.2.2.

7.2.1. Design Space Exploration

The TIT, BPR, and WAR have been varied to see their effect on fuel consumption. The range for each parameter with the corresponding step size is tabulated in Table 7.2 below. The ideal TIT is expected to be around 1600 Kelvin according to various studies [7, 16, 59, 60]. The range in Table 7.2 is therefore deemed sufficient. The lowest BPR is selected to be 10, with maxima ranging from 20 to 40, depending on the water injection point. Higher WAR values generally result in a higher BPR.

Table 7.2: Range of the three key input parameters with the step size considered for generating WET engine performance plots.

Input parameter	Range	Step size
TIT [Kelvin]	1500 - 1700	20
BPR [-]	10 - 20/40	1
WAR [-]	0.05 - 0.40	0.05

The TSFC maps for $0.1 < WAR < 0.35$ are shown in Figure 7.5 to Figure 7.10. Looking at the maps, they contain more information compared to the TSFC map from the reference engine (Figure 7.1). All design constraints are included and indicated with colored lines. The following constraints are considered for the WET engine model:

1. **Maximum mass flow rate:** Based on the specified thrust requirement of $22.8\ kN$ and the prescribed cycle parameters, including the TIT and BPR, a nominal intake mass flow rate of $153.251\ kg/s$ is determined. Literature suggests that future engine designs are expected to feature larger fan diameters and, consequently, higher intake mass flow rates. Görtz et al. report an expected increase in fan diameter from 2.00 meters to 2.20 meters [16]. To ensure a meaningful comparison, the intake mass flow rate is maintained constant for the WET engine, as an increased fan diameter would similarly reduce the TSFC of the reference turbofan engine. *In the TSFC maps, this condition is indicated with the red line.*

2. **Exhaust gas state after HRSG:** several studies on WET engines emphasize that the exhaust gases must remain superheated after passing through the HRSG, ensuring that no condensation occurs [7, 59, 60]. This requirement has also been adopted in the present study. To maintain these conditions, a minimum temperature margin of 50 Kelvin is imposed between the saturation temperature of water vapor and the exhaust gas temperature at the HRSG exit. *In the TSFC maps, this condition is indicated with the light blue line. All design points above this line are considered feasible.*

3. **HEXs effectiveness:** the HEX effectiveness, as defined in Equation 4.25, provides information regarding the actual heat transfer rate compared to the maximum allowable one. The effectiveness may not exceed unity (unfeasible HEX design) and a maximum value of 1.0 is chosen for the condenser. This value is high for a condenser. However, the literature indicates that the condenser is the most critical component in the WET engine. *In the TSFC maps, this condenser condition is indicated with the white line. All points above the white line are considered acceptable.* For the HRSG, the maximum effectiveness value is selected to be 0.85. *In the TSFC maps, this constraint on the HRSG effectiveness is indicated with the yellow line. All points below the yellow line are feasible.*

4. **Annulus height HPC outlet:** a key design constraint for WET engine is the annulus height at the HPC outlet, as documented in the literature [16, 60]. This parameter is critical for maintaining appropriate flow passage dimensions and avoiding excessive aerodynamic losses. A minimum height is proposed in both studies (10.5 & 11.5 mm). *For this study, the minimum HPC annulus height is set to 12 mm to remain conservative.*

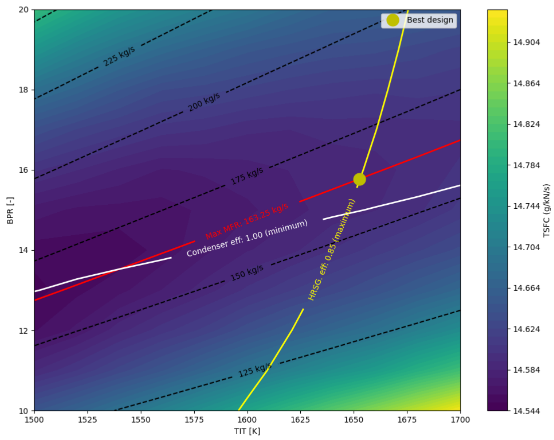

Figure 7.5: Design exploration map with constraint lines for WAR = 0.10.

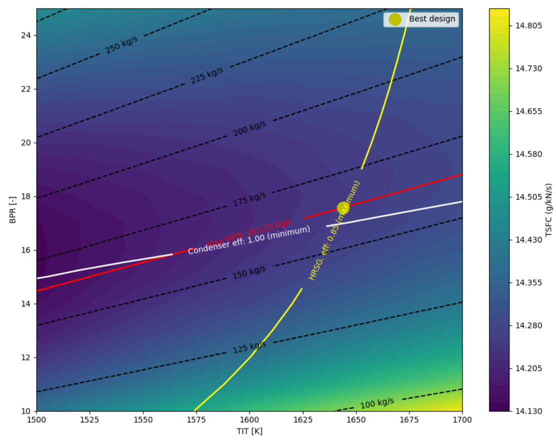

Figure 7.6: Design exploration map with constraint lines for WAR = 0.15.

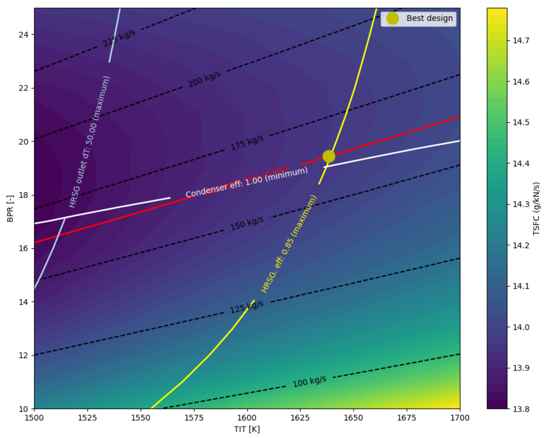

Figure 7.7: Design exploration map with constraint lines for WAR = 0.20.

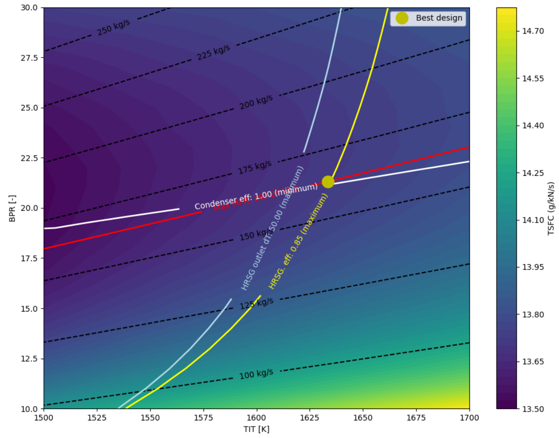

Figure 7.8: Design exploration map with constraint lines for WAR = 0.25.

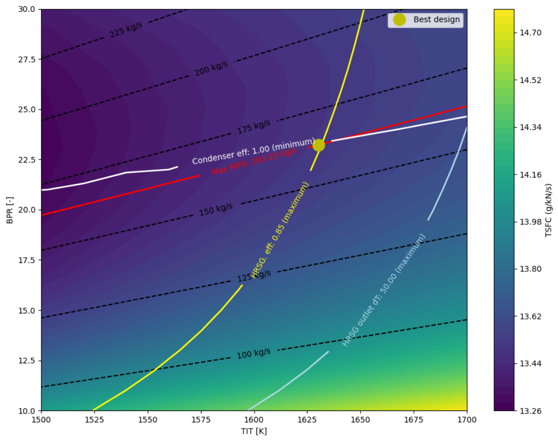

Figure 7.9: Design exploration map with constraint lines for WAR = 0.30. The best design is unfeasible.

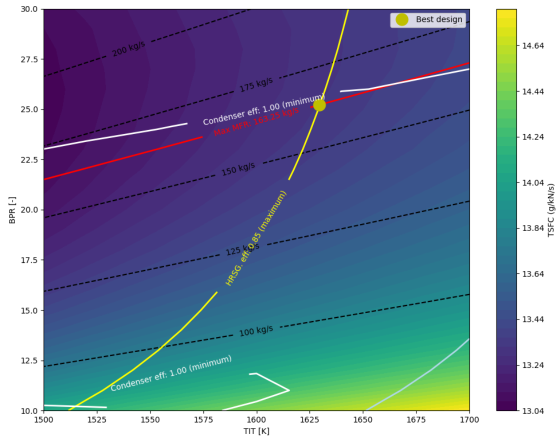

Figure 7.10: Design exploration map with constraint lines for WAR = 0.35. The best design is unfeasible.

As for the reference engine, constant mass flow rates are represented in the maps by black dotted lines, while the colored contours indicate constant TSFC values. From the Figure 7.5 and Figure 7.10, it is evident that the feasible design space is constrained to a relatively small region within the overall design space (top right area of the graph). The general trends observed in the TSFC maps are examined in Subsection 7.2.2.

Based on the abovementioned constraints, an optimal design can be chosen for the given water fraction, ranging from $WAR = 0.10$ to $WAR = 0.35$. The design space is bounded by multiple limiting factors, as indicated by the constraint lines in the TSFC contour plots. The condenser effectiveness limit (white line) defines the lower boundary, ensuring that the water recovery process remains theoretically feasible. The HRSG effectiveness limit (yellow line) represents the upper bound of the feasible design space. Additionally, the minimum HRSG outlet temperature constraint (light blue line) ensures that the exhaust remains superheated. The light blue line represents an upper bound of the design space. Lastly, the red line gives the mass flow rate found for the reference TF engine design point. To enable a fair performance comparison between the baseline TF engine and the WET engine, the design point of the WET engine should be located on the red line, representing configurations with equal intake mass flow rates and, consequently, comparable engine sizes. Looking at Figure 7.5 to Figure 7.9, the intersection of the red and yellow lines provides the best design point until a WAR of 0.3. At $WAR = 0.30$, the required condenser effectiveness to recover all the injected water becomes greater than one, and the exhaust temperature at the HRSG outlet falls below the prescribed minimum at the identified intersection point. A similar trend is observed in Figure 7.10 for $WAR = 0.35$. Consequently, design points corresponding to WAR values of 0.30 and higher are considered unfeasible. Conversely, in Figure 7.5, the absence of a blue constraint line indicates that the HRSG outlet temperature remains above the minimum threshold across the entire design space. At $WAR = 0.15$, the light blue constraint line appears in the upper left region of the map. Thus, it does not represent a critical limitation for the WET engine design. However, as WAR increases, this constraint shifts towards the right, limiting more and more the feasible design space. Similarly, with increasing WAR, the distance between the condenser effectiveness limit (white line) and the optimal design intersection point progressively decreases. This trend indicates that engine cycles with higher WAR levels are difficult to realize as the recovery of the injected water necessitates a cooling of the exhaust up to increasingly lower temperatures. This may not be feasible given the ram air temperature. Consequently, the design space becomes more restricted.

Looking at the maps in Figure 7.5 to Figure 7.10, the TSFC follows a specific trend with respect to both TIT and BPR. For a constant BPR, the TSFC increases with higher combustor exit temperatures. For a constant combustor inlet mass flow rate, this would correspond to an increase in fuel flow rate, directly affecting the TSFC. However, the combustor inlet mass flow rate slightly decreases as more work can be done by the turbines for higher-temperature exhaust flows. It is found that, overall, the fuel flow rate slightly increases, and thus the TSFC. This occurs despite the positive effect associated with the heating of the ram air in the condenser. The LPT outlet temperature tends to be higher for higher TIT values. The temperature differences in the HRSG are lowered, and the thermal load of the condenser becomes more critical. At the same time, more thermal energy is added to the bypass stream, reducing air density and hence increasing its velocity. However, it is also found that the FPR increases with TIT, implying that the heat addition to the bypass duct is not sufficient to reach the high velocities required to achieve the prescribed velocity ratio. It was found, indeed, that heat addition in the ram air duct does not have a significant effect on thrust generation. The higher FPR values also explain why the propulsive efficiency drops with increasing TIT values.

A similar trend is observed when TIT is held constant while BPR varies, with TSFC is initially decreasing to a minimum before rising again. Figure 7.11 to Figure 7.14 elucidate these trends. At low BPR, the core flow generates a substantial portion of thrust (Figure 7.14). Despite the reduced core nozzle velocity in the WET engine, the bypass jet velocity remains relatively high, limiting the increase in propulsive efficiency. This trend is similar to that observed for the conventional turbofan engines: propulsive efficiency increases but plateaus at higher BPR values (Figure 7.3 and Figure 7.11). Initially, increasing BPR reduces the core mass flow rate; however, this effect tends to disappear beyond a certain BPR value. HPC, HPT, and water mass flow trends are depicted in Figure 7.13. Since TIT remains constant, a reduction in core mass flow lowers fuel flow, thereby decreasing TSFC. The optimal balance of bypass thrust and reduced core flow leads to a TSFC minimum. Beyond this point, increasing BPR raises fan power requirements, lowers turbine outlet temperature, and reduces HRSG and condenser performance. As shown in Figure 7.12, higher BPR values cause the condenser pressure and the required dew point temperature to decrease. Increasing core mass flow counteracts these effects, but it results in higher fuel consumption. Ultimately, the increase in propulsive efficiency initially outweighs the decline in thermal efficiency, leading to an overall efficiency gain until this quantity plateaus and then declines. This TSFC minimum shifts toward higher BPR values with increased water injection as larger specific work is achieved in the core.

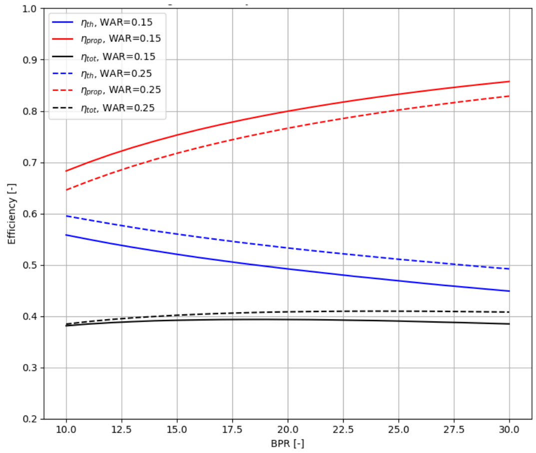

Figure 7.11: Variation of efficiencies as a function of BPR and WAR (TIT=1600K).

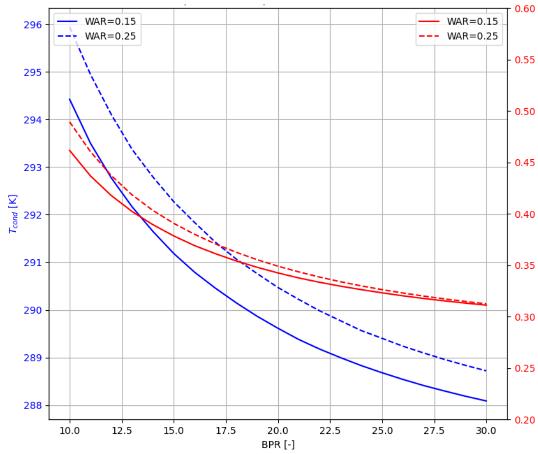

Figure 7.12: Variation of condensation temperature and pressure as a function of BPR and WAR (TIT=1600K).

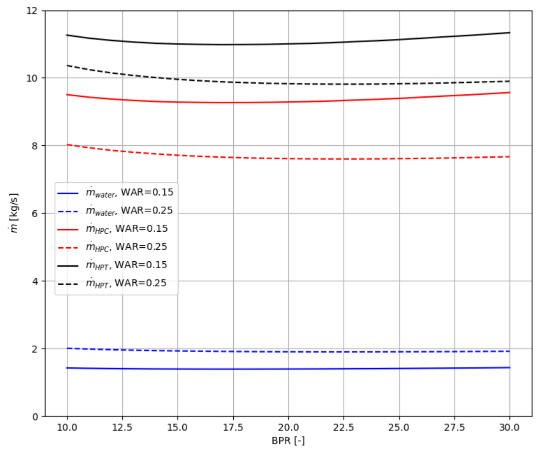

Figure 7.13: Variation of key mass flow rates as a function of BPR and WAR (TIT=1600K).

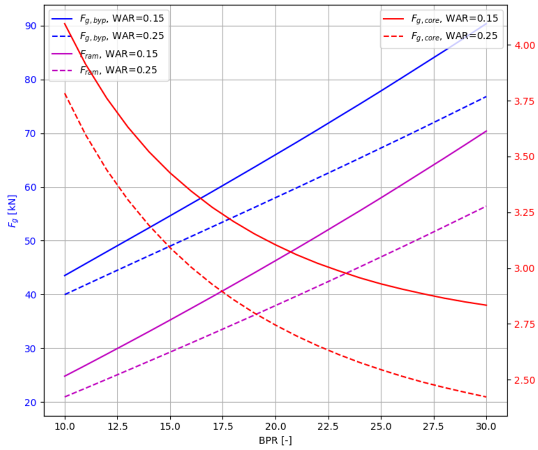

Figure 7.14: Variation of thrust components as a function of BPR and WAR (TIT=1600K).

The TSFC as function of WAR is shown in Figure 7.15 for $0.1 \leq WAR \leq 0.35$. For each design point, the HPC outlet annulus height is specified in red. The red dotted line indicates the minimum HPC annulus height. Additionally, the grey region represents the infeasible design region. The TSFC of the reference turbofan engine is indicated by the horizontal blue dotted line, serving as a benchmark for performance comparison. The minimum HPC outlet annulus height must not fall below 12 millimeters. This constraint is represented by the light grey region in Figure 7.15. By analyzing Figure 7.15, the optimal design point is identified at WAR = 0.2, as it yields the lowest TSFC while satisfying all previously established constraints. The performance characteristics of this design solution will be examined in detail in Subsection 7.2.4. Before this analysis, the feasibility of the HRSG design will be assessed in Subsection 7.2.3.

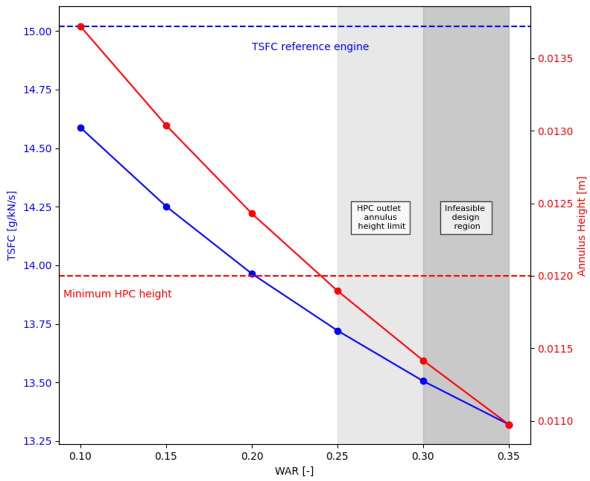

Figure 7.15: TSFC of the WET engine as a function of the water-to-air ratio (WAR).

7.2.2. Trends

This section discusses the trends that can be observed for the feasible design points emerging from Figure 7.15. The trends are hence provided for $0.10 < WAR < 0.25$.. The variation of TIT and BPR at WAR-dependent optimal design points is depicted in Figure 7.16. The figure shows an approximately linear increase in BPR with rising WAR, while TIT decreases non-linearly, aligning with trends reported in WET engine literature. Water injection increases the thermal capacity (C_p), enhancing core-specific work and reducing the required combustion temperature for a given energy extraction in the turbines. Consequently, TIT decreases with increasing WAR, consistent with findings in the literature [7, 16, 59]. As higher BPR values enhance propulsive efficiency, this trend becomes particularly relevant at higher WAR, where thermal efficiency gains plateau. Literature supports the preference for ultra-high BPR configurations in WET engines with increasing WAR [7, 16, 59, 60].

Figure 7.17 illustrates the variation in thermal, propulsive, and total efficiency as a function of WAR. Total efficiency increases with higher WAR, primarily driven by thermal efficiency, while propulsive efficiency remains relatively constant. As shown in Figure 7.19, the core mass flow rate decreases with increasing water injection (blue dotted line), as expected. Although a higher WAR leads to an increase in FAR (Figure 7.21), the dominant effect of reduced core mass flow results in a net decrease in fuel flow, thereby positively influencing thermal efficiency and TSFC. The pump inlet temperature remains stable at approximately 291 K, while the HRSG effectiveness forms the constraint on the feasible design space (Subsection 7.2.1). This limitation directly impacts the HRSG's required hot-side inlet temperature to maintain the prescribed effectiveness. Despite the increased thermal loads at higher WAR, the HRSG inlet temperature remains approximately constant, which can be attributed to a reduction in TIT (Figure 7.16). As more water is heated while maintaining a fixed degree of superheating, the total heat transfer within the HRSG increases. This trend is illustrated in Figure 7.18, which shows a rise in $\dot{Q}_{HRSG}$. Consequently, heat load in the condenser decreases, as the required dew-point temperature only marginally reduces at higher WAR values (Figure 7.20). Overall, the total heat flow increases due to the higher thermal capacity of the exhaust gases. However, the reduction in condenser thermal load limits the amount of energy that can be transferred to the ram air. At a WAR of 0.25, the heat duty in the HRSG and the condenser is roughly the same. Görtz et al. found a similar heat flow split and magnitude at a WAR of 0.245 for a similar engine configuration [16]. Furthermore, the trends are similar to those reported in the second study of DLR [60]. Regarding nozzle exit velocities in both the core and bypass streams (Figure 7.23), only a slight decrease is observed with the increase in WAR, with negligible impact on propulsive efficiency. To maintain a constant velocity ratio, the fan pressure ratio is slightly increased. This gradual FPR increase with WAR is depicted in Figure 7.22. In summary, the nozzle exit conditions are similar across all design points, resulting in a nearly constant propulsive efficiency over varying WAR. However, changes in core mass flow lead to a reduction in fuel flow at higher water shares, directly enhancing thermal efficiency. Consequently, total efficiency improves, yielding a reduction in TSFC.

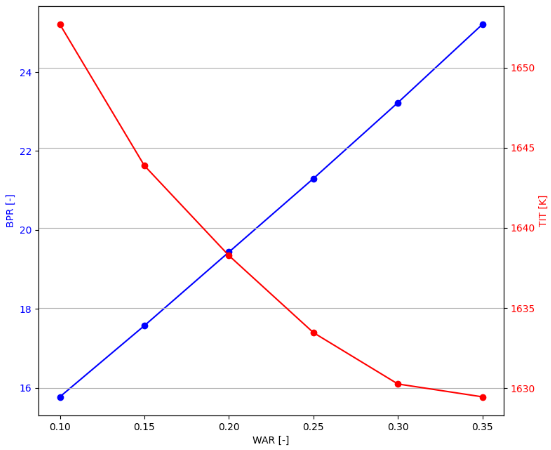

Figure 7.16: BPR and TIT as function of WAR for all optimal design points.

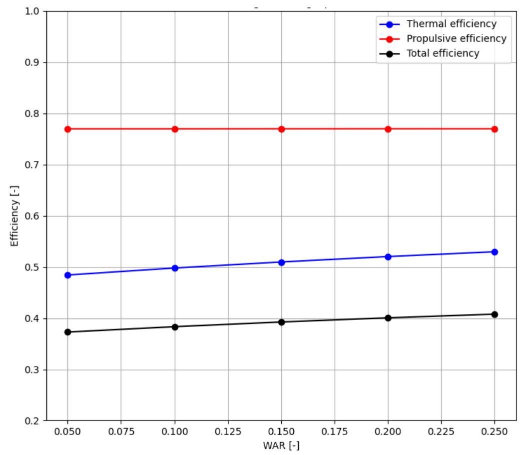

Figure 7.17: Engine efficiencies as function of WAR for all optimal design points.

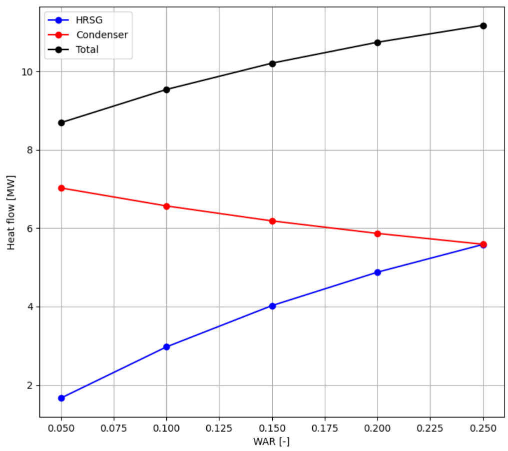

Figure 7.18: HEX thermal loads as function of WAR for all optimal design points.

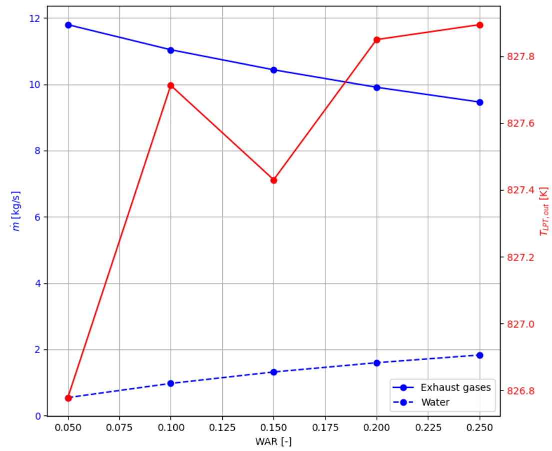

Figure 7.19: HRSG mass flow rates and hot side inlet temperature as function of WAR for all optimal design points.

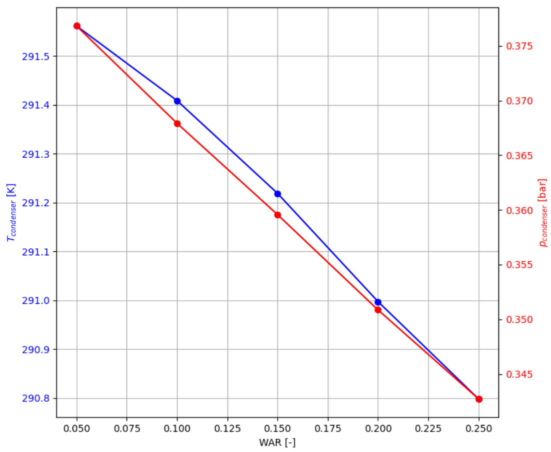

Figure 7.20: Static condensation outlet conditions as function of WAR for all optimal design points.

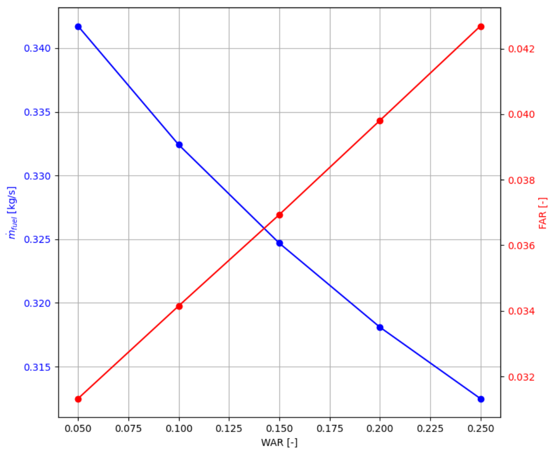

Figure 7.21: FAR and fuel mass flow rate as function of WAR for all optimal design points.

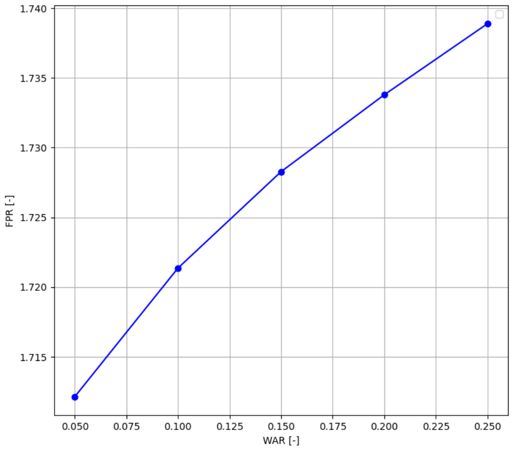

Figure 7.22: FPR as function of WAR for all optimal design points.

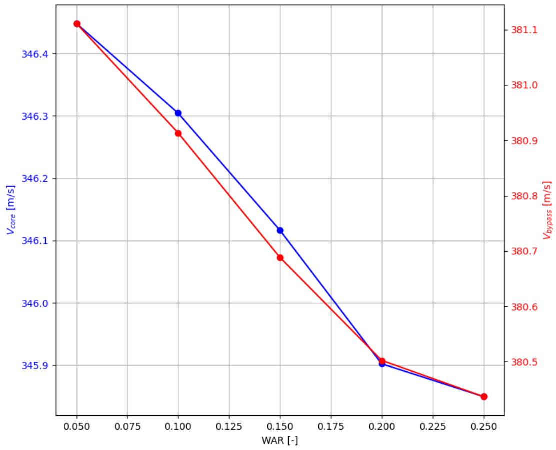

Figure 7.23: Ideal nozzle exit velocities as function of WAR for all optimal design points.

7.2.3. Hexacode

In Subsection 7.2.1, the best design solution corresponding to $WAR = 0.20$ was identified as the best design option for the WET engine as it yields the lowest TSFC while complying with the imposed constraints. The heat exchangers are modeled as simple ducts in pyCycle, and no information, except theoretical effectiveness, is given regarding the heat exchanger characteristics. To check its feasibility, the HRSG was modeled with the in-house code Hexacode. The objective is to perform a preliminary sizing of this HEX to estimate its weight and the pressure drops in the hot and cold streams, as these quantities affect the actual performance of the engine. It was not possible to perform the same check for the condenser as Hexacode does not feature a thermodynamic model for condensing humid gases. The extension of this tool was out of the scope of the present project. The HRSG topology and its integration in the nacelle are similar to those adopted for the combined-cycle turbofan (CC-TF) engine presented by Krempus et al. [128]. More details about the HEX geometry and the chosen design inputs are provided in Subsection 4.5.2 and Section 6.4, respectively. The thermodynamic conditions at the inlet of the HRSG are known from thermodynamic cycle calculations and can be specified as inputs to the Hexacode model. The inputs include the (static) temperature and pressure at both cold and hot sides, the mass flow rates, part of the geometry, the composition of the exhaust, and the heat duty. Hexacode calculates the mass, pressure drop, and remaining dimensions. An overview of the inputs for modeling the HRSG in Hexacode is provided in Table 7.3 below. The length of the HRSG, X_{hrsg}, is set to be equal to 0.60 meters, based on the optimization outcome in the study of Krempus et al. [128]. The inner HRSG perimeter, Y_{hrsg}, is computed given the annulus area and the hub-to-tip ratio at the LPT outlet (λ_{LPT}). A value of $\lambda = 0.45$ is chosen, following the recommendations by Kurzke [66].

Table 7.3: Input parameters for modeling the HRSG in Hexacode.

Input parameter	Value	Units
$T_{c,in}$	288.193	$[K]$
$T_{h,in}$	827.590	$[K]$
$p_{c,in}$	11.844	$[bar]$
$p_{h,in}$	0.384	$[bar]$
$\dot{m}_c$	9.908	$[kg/s]$
$\dot{m}_h$	1.598	$[kg/s]$
WAR	0.20	$[-]$
FAR	0.0398	$[-]$
$\dot{Q}_{hrsg}$	4.8790	$[MW]$
X_{hrsg}	0.60	$[m]$
Y_{hrsg}	2.15	$[m]$

Table 7.4 tabulates the results of the Hexacode simulation and the HRSG design specifications

estimated or assumed in the thermodynamic cycle analysis. The relative pressure drop, $dPqP$, has been assumed in the pyCycle model to be equal to 0.05 for both the cold and hot sides of the HRSG. The Hexacode software is used to check the validity of this assumption. The maximum relative error is almost 73% for the cold side. Although the magnitude of this relative error may seem large, its effects on the steam thermodynamic conditions are not significant. Considering outlet temperature, pressure, specific heat, and density, the maximum error is only 3%. Since the Mach number is a fixed input parameter, it directly influences the static conditions, thereby explaining the observed discrepancies in the temperature and pressure estimated by Hexacode at the HRSG outlet. When considering total pressures alone, the outlet conditions predicted by PyCycle align exactly with those obtained from Hexacode. Consequently, the discrepancies presented in Table 7.4 are not deemed significant for further discussion. The relative pressure drop for the hot side ($dPqP_h$) calculated by Hexacode shows only minor deviations from the initially assumed values. However, the pressure drop on the cold side is slightly overestimated by pyCycle when compared to the Hexacode output value. It must be said that the Hexacode results are very sensitive to inputs, especially the number of passes, N_{pass}. For the results in Table 7.4, N_{pass} is set to two. Increasing the number of passes would impose higher pressure drops in the cold side of the HRSG. Additionally, Table 7.4 provides an overview of the mass and depth of the empty HRSG. A representation of the temperature profiles, approximated based on Hexacode results, is presented in Subsection 7.2.4.

Table 7.4: Results of HRSG model in Hexacode and comparison with the simplified model in pyCycle.

HRSG outputs	Units	pyCycle	Hexacode	Rel. error [%]
$T_{s_{h,out}}$	$[K]$	451.102	438.100	-2.882
$T_{s_{c,out}}$	$[K]$	605.559	605.551	0.002
$p_{h,out}$	$[bar]$	0.373	0.365	-2.145
$p_{c,out}$	$[bar]$	11.687	11.683	-0.034
$C_{p_{h,out}}$	$[kJ/(kg \cdot K)]$	1207.01	1202.37	-0.369
$\rho_{h,out}$	$[kg/m^3]$	0.262	0.265	1.145
$dPqP_h$	$[-]$	0.05	0.0512	1.950
$dPqP_c$	$[-]$	0.05	0.0136	-72.886
m_{hrsg}	$[kg]$	-	103.71	-
Z_{hrsg}	$[m]$	-	0.14355	-

7.2.4. Best Design Solution

Based on the results presented in Subsection 7.2.1, Subsection 7.2.2 and Subsection 7.2.3 an optimum design can be established for the WET engine. The comparison between the conventional turbofan (TF reference) and the water-enhanced turbofan (WET) engine, as presented in Table 7.5, reveals significant differences in thermodynamic performance and cycle characteristics. Despite maintaining identical net thrust output (F_{net}) and intake mass flow rate ($\dot{m}_{intake}$), water injection fundamentally alters the engine's operating conditions.

Thermal and Combustion-related Changes

One of the most prominent changes is the reduction in TIT, which decreases by 3.63% from 1700 K to 1638.3 K in the WET engine. This reduction is a direct consequence of the increased thermal capacity of the core flow due to water injection. Adding water raises the specific heat capacity (C_p) of the working fluid, reducing the required combustion temperature for a given energy output. This aligns with findings in water-injected gas turbine literature, where similar trends are observed at elevated WAR levels. The OPR experiences a notable decline of 22.22%, decreasing from 45 in the conventional turbofan to 35 in the WET engine. The OPR is a critical design parameter for both engine architectures and its selection is based on established literature sources [16, 59, 60, 66]. In the case of the WET engine, a reduction in OPR is anticipated due to a decrease in core mass flow rate, which is a direct consequence of water injection and the associated thermodynamic cycle modifications. To quantify and analyze this effect, a parametric study is conducted, as detailed in Section 7.3, wherein the influence of OPR on engine architecture and performance is examined. Furthermore, FAR is significantly higher (+45.79%) in the WET engine. The increase in the specific work of the engine and thus the reduction

Table 7.5: Comparison of key engine parameters for the reference TF design and the optimum WET design.

Engine parameter	Units	TF reference	WET engine	Rel. Diff. [%]
F_{net}	$[kN]$	22.8	22.8	0
$\dot{m}_{intake}$	$[kg/s]$	163.344	163.344	0
$\dot{m}_{core,exh}$	$[kg/s]$	12.901	9.905	-23.22
$\dot{m}_{fuel}$	$[kg/s]$	0.3431	0.3179	-7.34
TIT	$[K]$	1700	1638.277	-3.63
BPR	$[-]$	12	19.439	+61.99
OPR	$[-]$	45	35	-22.22
FPR	$[-]$	1.680	1.734	+3.21
FAR	$[-]$	0.0273	0.0398	+45.79
$TSFC$	$[g/kN/s]$	15.047	13.952	-7.28
η_{th}	$[\%]$	48.54	52.03	+7.19
η_{prop}	$[\%]$	76.49	77.00	+0.67
η_{tot}	$[\%]$	37.13	40.06	+7.89

in the core mass flow rate with increasing WAR is the main reason of this trend. It is also documented by Schmitz et al. that combustion approaches stoichiometric conditions for higher WAR values [7].

Bypass Ratio and Fan Performance

The BPR exhibits the most substantial relative increase, rising by 61.99% from 12 to 19.44. This increase is a direct consequence of the increased specific work of the engine. In conventional TF engines, an increase in the BPR typically reduces the bypass nozzle velocity. However, in the case of the WET engine, this velocity reduction is offset by a higher FPR. This compensation arises from the nozzle velocity ratio, which is inherently higher for WET engine configurations. As a result, the bypass nozzle velocity, and consequently the propulsive efficiency, is directly influenced by this parameter, as further discussed in this section. While existing literature generally associates WET engines with lower FPR values, this dependency is strongly linked to the selected nozzle velocity ratio. In this study, a relatively high nozzle velocity ratio of 1.1 is adopted [60], leading to increased ram air nozzle velocity values compared to the core nozzle velocity. Beyond the effects of heat addition in the condenser, the FPR is a key parameter for further increasing nozzle velocity. Consequently, for the WET engine, the FPR increases by 3.21%, indicating enhanced work extraction by the fan to accelerate the higher bypass mass flow rate.

Fuel Efficiency and Overall Efficiency Gains

A key performance enhancement is the reduction in TSFC, which decreases by 7.28% in the WET configuration. This improvement stems from the combined effects of higher thermal efficiency (η_{th}) and increased propulsive efficiency (η_{prop}). Besides this, the mass flow rate through the combustor decreases, leading to a reduction in fuel flow for a given TIT, despite a significant increase in the FAR (see Table 7.5). The thermal efficiency rises from 48.54% to 52.03% (+7.19%), driven by the enhanced energy utilization within the cycle and the increased specific heat capacity and turbine work extraction. To summarize, some thermal energy is recuperated. Similarly, propulsive efficiency sees a marginal improvement of 0.67%, attributed to the higher BPR. Propulsive efficiency generally tends to increase significantly with BPR, as demonstrated in Figure 7.3. However, in the case of the WET engine, the elevated nozzle velocity ratio results in a higher fan pressure ratio (FPR), leading to an increased exhaust velocity of the ram air. Consequently, this results in greater kinetic energy losses within the bypass duct, partially offsetting the efficiency gains associated with higher BPR values. Overall, the total efficiency (η_{tot}) experiences a notable increase of 7.89%. The water-enhanced cycle thus demonstrates a clear advantage in reducing fuel consumption and improving overall engine performance, albeit at the cost of increased system complexity, weight, and potential modifications in compressor and turbine design.

The observed trends of the main engine characteristics align with theoretical expectations and previously published research on water-enhanced aero-engine cycles. However, further considerations regarding relevant engine parameters, such as OPR, steam injection temperature, and velocity ratio, are to be investigated in relation to their effect on both engine and heat exchanger performance. This will be done in Section 7.3.

Based on the WET engine configuration and the corresponding optimal engine parameters, the preliminary design of the HRSG can be investigated using Hexacode. The results are tabulated in Table 7.4. Given its length and the perimeter, the depth or thickness of the cylindrical-type HEX is

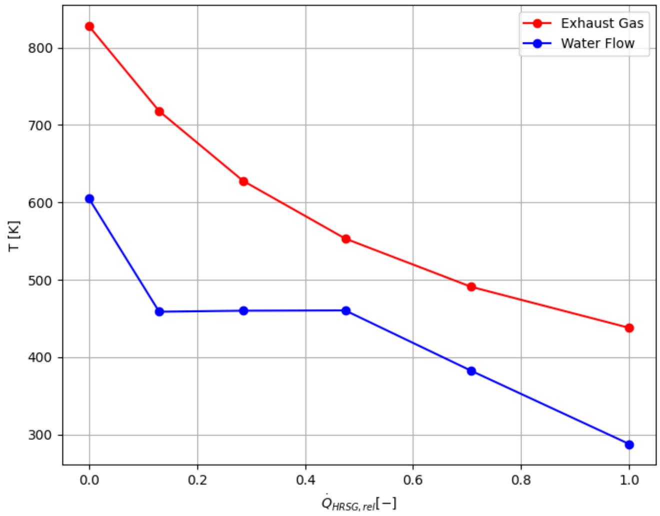

Figure 7.24: Hexacode HRSG temperature profiles for the WET engine design (N_{pass} = 5).

small. The system integration and its effects on engine geometry are not considered in this preliminary design phase and are left for future research. However, an approximation of the HRSG temperature profiles can be provided based on the station outputs of Hexacode and is shown in Figure 7.24. The horizontal axis represents the normalized cumulative heat flow ($\dot{Q}_{HRSG,rel}$), ranging from 0 to 1, while the vertical axis shows the temperature in Kelvin. The exhaust gas (red line) exhibits a steady decrease in temperature along the heat exchanger. In contrast, the water side (blue line) exhibits a typical phase-change profile, characterized by the temperature plateau during which water evaporates. The trend in the exhaust gas is not linear, probably caused by the settings used in Hexacode. Considering a multi-pass HEX, convergence is enhanced when selecting the logarithmic heat load distribution [116]. The minimum temperature difference, i.e., the pinch point, for the HRSG equals 92.79 K, with the exhaust gas outlet temperature significantly above the dew point at which water starts to condense (320.8 K). Similarly to results in the literature, the pinch point is located at the start of the evaporation phase, i.e. close to a relative cumulative heat load of 0.5.

Regarding the mean logarithmic temperature difference (LMTD) in each control volume of the HEX, the value ranges from 100.4 Kelvin in correspondence to the pinch point to 240.4 Kelvin at the left-hand side in Figure 7.24. A smaller pinch-point temperature difference enhances heat recovery. However, achieving this requires a larger heat exchanger surface area, increasing system complexity, weight, and cost. Conversely, a larger pinch point temperature difference reduces the heat exchanger size but limits the amount of recoverable heat, leading to lower thermal efficiency. It is worth pointing out that the pinch point temperature in this study is much higher than the values considered in previous works on the WET engine. Görtz et al. fixed the HRSG pinch point temperature to only 10 Kelvin, suggesting that the HEX is likely to be very heavy [16]. This value has been raised to 30 Kelvin in their second study [60].

Although the HRSG design satisfies all imposed constraints, the observed pinch point temperature remains relatively high compared to values reported in literature, indicating potential for further optimization to enhance the overall WET engine performance. One possible improvement involves increasing the WAR, enabling a greater mass of water to be heated to the prescribed injection temperature. However, this approach is constrained by the minimum HPC outlet annulus height, as illustrated in Figure 7.15, which limits the extent to which WAR can be increased. Alternatively, the steam injection temperature could be raised while maintaining a fixed WAR, potentially improving heat utilization and overall cycle efficiency. This approach is systematically explored in the parametric study presented in Section 7.3, where the influence of varying steam injection temperatures on HRSG performance and WET engine operation is further analyzed.

7.3. Parametric Study

A parametric study is conducted to comprehensively understand the WET engine's performance. The analysis is focused on three key parameters: OPR, degree of steam superheating, and nozzle velocity ratio. While these parameters were held constant during the design exploration process, their influence on the engine cycle, heat exchangers, and WET-specific performance metrics must be assessed to complete the analysis. By systematically varying these parameters, this study aims to identify their impact on cycle efficiency, thermal management, and propulsion characteristics, providing deeper insights into the trade-offs and optimization potential of the WET concept. The OPR range used for the parametric study is $25 < OPR < 45$, the degree of steam superheating range is $50 < \Delta T_{superheating} < 290\ K$, and the nozzle velocity ratio range is $0.7 < Velocity\ Ratio < 1.2$.

7.3.1. Effect of OPR

Figure 7.25 to Figure 7.32 illustrate the influence of OPR variation on key performance characteristics of the WET engine. Since the high-pressure compressor pressure ratio (Π_{HPC}) is maintained constant, changes in OPR primarily result in a trade-off between the low-pressure compressor pressure ratio (Π_{LPC}) and the FPR while ensuring a prescribed nozzle velocity ratio of 1.1. The principal benefit of increasing OPR, as depicted in Figure 7.25 and Figure 7.26, is an improvement in thermal efficiency, which translates directly into a reduction in TSFC. A reduction in TSFC of nearly 4% can be achieved compared to the optimal design presented in Table 7.5. However, this trend exhibits diminishing returns at higher OPR values, a behavior well-documented in literature [66, 126]. Furthermore, FAR and TSFC are inherently linked, as a lower FAR indicates improved fuel economy for a given net thrust and TIT. Variations in combustor inlet mass flow rate remain minimal, with the minimum at the design point (OPR = 35). Since TSFC directly correlates with overall efficiency, its trend closely follows that of thermal efficiency. Conversely, propulsive efficiency remains nearly constant due to the fixed BPR and nozzle velocity ratio. Despite these efficiency gains, OPR cannot be increased indefinitely due to practical constraints related to engine performance, mechanical and size limitations. These limitations

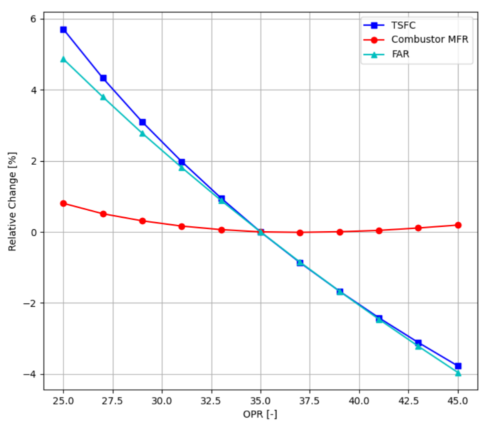

Figure 7.25: Effect of OPR variation on WET combustor parameters.

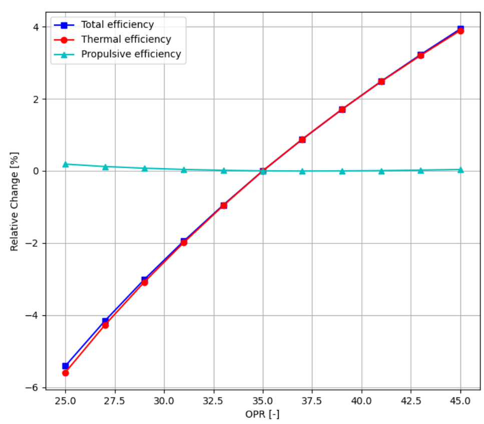

Figure 7.26: Effect of OPR variation on WET engine efficiencies.

are illustrated in Figure 7.27. The dashed, colored vertical lines represent the maximum constraint value for the corresponding constraint parameter. The critical constraint for the OPR is the HPC outlet annulus height. A minimum value of 12mm is used throughout this document, and $OPR = 37$ represents the maximum feasible value. Looking at other constraints, the intake mass flow rate does not change significantly, while the condenser effectiveness and the minimum degree of superheating of steam aft of the HRSG would play a role only for higher OPR values as shown by the dashed vertical lines in Figure 7.27. Turbine cooling is not incorporated in the model but does play a significant role and constraint when considering very high OPRs. Nevertheless, it is assumed that the cooling impact does not change significantly with an increase of OPR from 35 to 37.

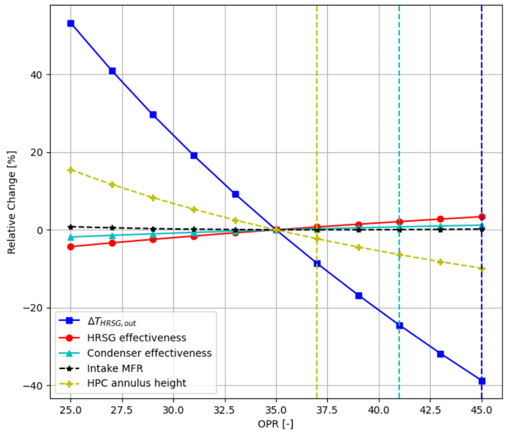

Figure 7.27: Effect of OPR variation on the imposed WET engine constraints. The dashed, colored lines are the associated maximum constraint values.

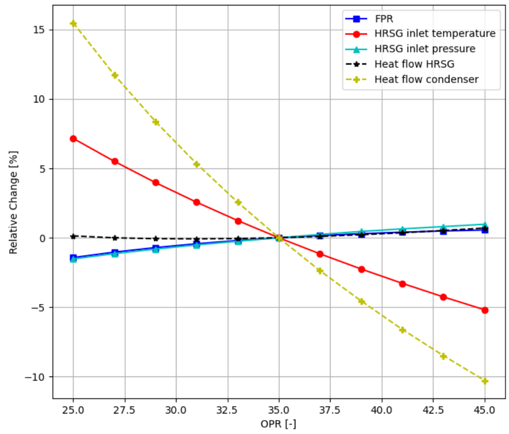

Figure 7.28: Effect of OPR variation on FPR, HEXs thermal loads, and LPT outlet conditions.

The FPR as function of OPR together with the LPT outlet conditions and the heat transfer for both the HRSG and condenser are provided in Figure 7.28. Since the core mass flow rate does not change significantly, the turbines have to extract more work to achieve a higher OPR. As a result, the LPT discharge temperature is expected to be lower. The required heat flow for evaporating and superheating the water remains similar, but increases slightly for higher OPR. This is a consequence of keeping the WAR constant for this analysis with a slightly higher core mass flow rate. The lower LPT exit temperature and the constant HRSG heat demand explain the reduced heat load in the condenser. Less heat for the ram air reduces its velocity, hence the gross bypass thrust. The FPR is slightly higher to compensate for this reduction. The effect of the marginal increase in HRSG heat duty on the HRSG size and pressure drops is illustrated Figure 7.29, where the Hexacode results are presented. The empty

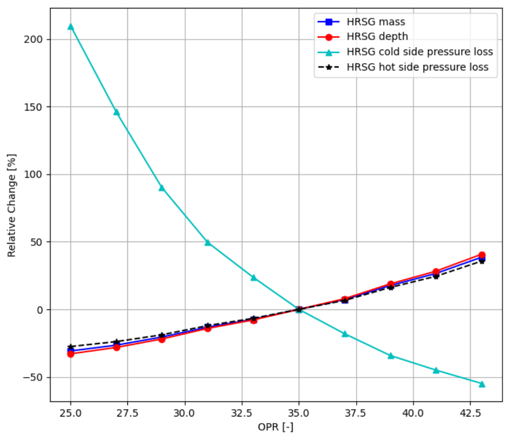

Figure 7.29: Effect of OPR variation on HRSG characteristics (Hexacode).

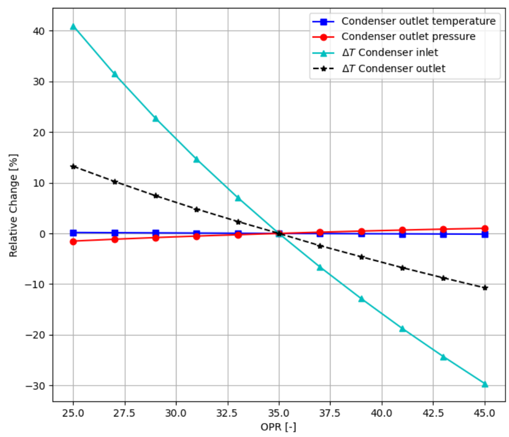

Figure 7.30: Effect of OPR variation on condenser performance characteristics.

mass and the depth of the HRSG exhibit a similar trend, increasing significantly with higher OPR values.

These results can directly influence the TSFC, while the greater depth introduces challenges related to system integration. The additional weight and associated pressure losses in the heat exchanger may thus offset the potential improvements in TSFC due to higher OPR. Furthermore, the increased HRSG depth results in a higher pressure drop, which negatively impacts core thrust and may further influence TSFC. In contrast, the pressure drop in the working fluid has an opposite trend. As the tube diameter and the mass flow rates are fixed, fewer tubes in parallel (i.e. flow area) are needed to achieve the required HRSG heat duty. Thus, the velocity of the water increases, adversely affecting the pressure drop according to the Darcy-Weinbach equation ($\Delta p \propto V^2$). In Figure 7.30, key condenser characteristics are provided, including the outlet conditions and the temperature difference between the inlets of both hot and cold side streams and outlets of both streams. The condenser outlet conditions remain largely unchanged since both the velocity ratio and BPR are fixed. However, preliminary observations suggest decreased condenser performance due to the lower HRSG outlet temperature. The reduced temperature difference between the hot and cold side inlets lead to lower heat transfer effectiveness. Similarly to the HRSG, this reduction in effectiveness is expected to result in increased weight, larger dimensions, and additional pressure losses for the condenser, penalizing overall system performance.

Lastly, the conditions at both the core nozzle (Figure 7.31) and bypass nozzle (Figure 7.32) are discussed. It immediately stands out that all relative changes are small ($< 1.5\%$), indicating that the OPR does not significantly affect nozzle operating conditions.

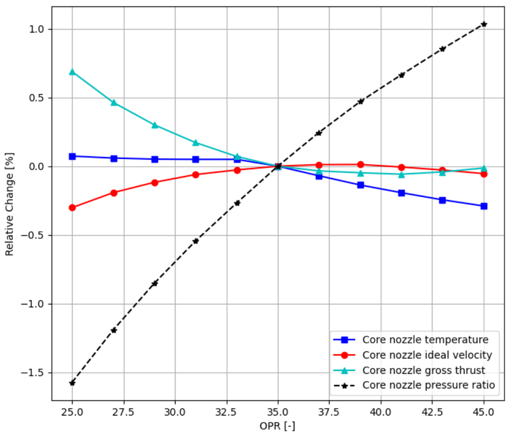

Figure 7.31: Effect of OPR variation on core nozzle parameters.

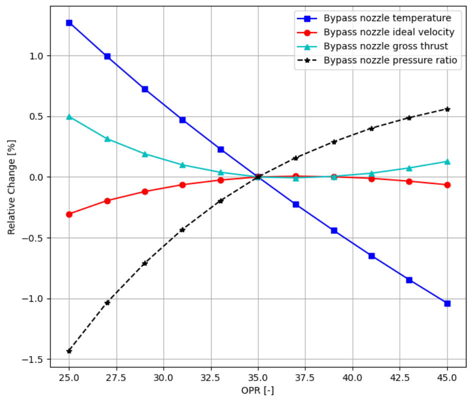

Figure 7.32: Effect of OPR variation on bypass nozzle parameters.

7.3.2. Effect of Injection Temperature

Figure 7.33 to Figure 7.40 illustrate the effect of varying the degree of water superheating on key performance parameters of the WET engine. As the degree of superheating increases, the temperature of the compressed wet air mixture rises, thereby reducing the fuel requirement to achieve a given TIT. This directly lowers the TSFC, as demonstrated in Figure 7.33. The observed trend in TSFC is primarily governed by the mass flow rate (MFR) entering the combustor and FAR. Several factors may contribute to the observed slight increase in core mass flow rate, and, consequently at the engine intake:

- A lower FAR results in a lower average molecular weight of the air-fuel mixture, influencing the exhaust gases' density and specific heat capacity. A corresponding increase in MFR could compensate for these changes while ensuring sufficient energy extraction by the turbines.
- A variation in the thermal energy transferred to the ram air duct modifies the bypass nozzle operating conditions. It results that adjustments in either the FPR or mass flow rate are needed to maintain the prescribed net thrust output.

In analogy to what was observed in Subsection 7.3.1, the reduction in TSFC is the result of an improvement in overall engine efficiency. Propulsive efficiency exhibits an upward trend, albeit less pronounced than the thermal efficiency gain. The slight increase in intake mass flow rate leads to a reduction in the required FPR, as depicted in Figure 7.36. The design constraints are again depicted in Figure 7.35. The HPC annulus outlet height, condenser effectiveness, and intake MFR do not change and will not prevent the adoption of higher steam injection temperatures. The HRSG effectiveness can be up to 10% higher compared to the baseline value as more water has to be heated to a higher temperature. This could potentially lead to convergence problems in Hexacode given the chosen design settings. As key engine parameters remain constant in this the parametric study, it is no surprise that the station conditions do not differ significantly as illustrated for the HRSG inlet (Figure 7.36), the condenser outlet (Figure 7.38), and both nozzles (Figure 7.39 & Figure 7.40). Nevertheless, the heat duty of the HRSG is severely affected by the degree of superheating. Although most of the heat is required for the phase-change process, the degree of superheating plays a role and can lead to heat duty changes of more than 10%. Thus, if the degree of superheating is increased, less heat remains available for the condenser. Both trends are shown in Figure 7.36.

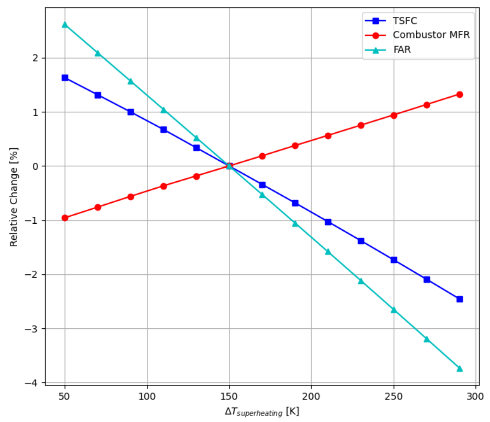

Figure 7.33: Effect of degree of steam superheating variation on WET combustor parameters.

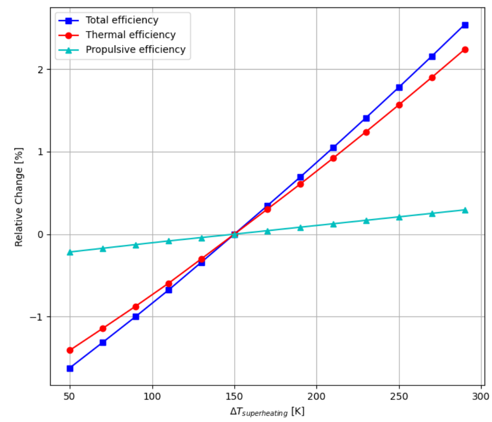

Figure 7.34: Effect of degree of steam superheating variation on WET engine efficiencies.

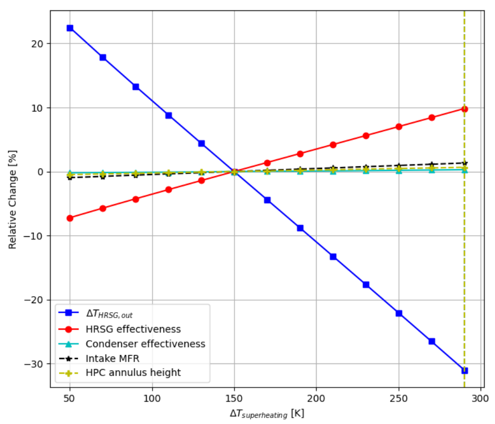

Figure 7.35: Effect of steam degree of superheating variation on the imposed constraints.

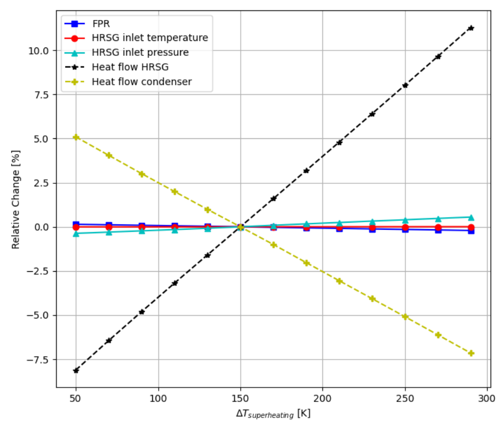

Figure 7.36: Effect of degree of steam superheating variation on FPR, HEX thermal loads, and LPT outlet conditions.

An analysis of the HRSG results obtained from Hexacode reveals that Figure 7.37 does not encompass the full range of investigated superheating degrees. Specifically, Hexacode encounters convergence issues for degrees of superheating exceeding 210 K, as the degree of superheating cannot be achieved in the HRSG. The HRSG mass, depth, and hot-side pressure drop increase significantly with a higher degree of superheating, following the same trend discussed Subsection 7.3.1. However, compared to OPR variation, the increase in steam degree of superheating appears less critical to realize. A critical consideration in interpreting the Hexacode results is that the HRSG configuration remained the same across all investigated cases. The number of water passes within the HRSG is set to two, which may impose a design limitation at higher superheating degrees. Increasing the number of passes would likely facilitate further superheating, albeit with a higher pressure drop due to the increased flow path length. To maintain consistency in the analysis, the number of passes has been kept constant, restricting the maximum feasible degree of superheating to 210 K. The degree of superheating does not influence the condenser outlet conditions, as these are predominantly dictated by pressure and exhaust gas composition. However, a lower FAR reduces water content in the exhaust stream, resulting in a slightly lower condenser outlet temperature, as depicted in Figure 7.38. Additionally, the temperature differences between the inlet and outlet flows of the condenser exhibit trends similar to those observed for OPR variation, albeit with a less pronounced effect.

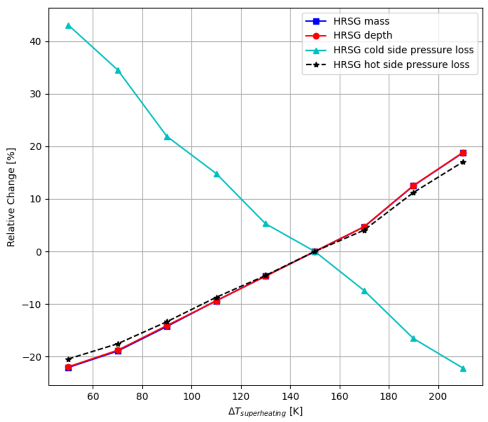

Figure 7.37: Effect of degree of steam superheating variation on HRSG characteristics (Hexacode).

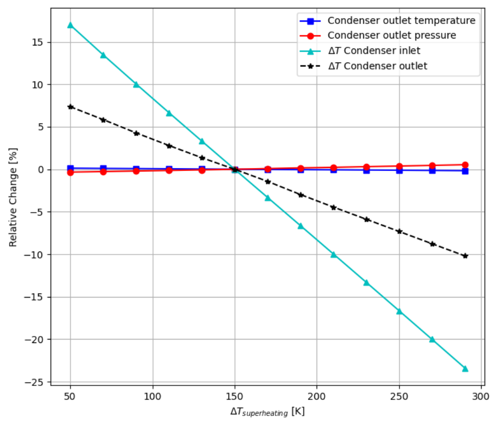

Figure 7.38: Effect of degree of steam superheating variation on condenser parameters.

Lastly, the core and bypass nozzle property sensitivities are illustrated in Figure 7.39 and Figure 7.40, respectively. Generally, the effects of superheating changes on nozzle conditions are even less compared to the variation in OPR. The increase in gross thrust in both nozzles can be explained by the higher intake mass flow rate. A larger gross thrust should compensate for the increased ram air drag, which is caused by the increased intake mass flow rate, to end up with the prescribed net thrust.

7.3.3. Effect of Velocity Ratio

Figure 7.41 to Figure 7.48 illustrate the impact of the nozzle velocity ratio variation on key performance characteristics of the WET engine. Based on analysis by several authors, the ideal nozzle velocity ratio for conventional turbofan engines is close to or equal to 0.8 [66, 126]. For the WET engine, an optimal velocity ratio of 1.1 is mentioned by DLR [60]. This value is also used in the design exploration described in Subsection 7.2.1. The nozzle velocity ratio is thus varied from 0.7 to 1.2 and the corresponding effect on mass flow rate and TSFC is shown in Figure 7.41. The combustor inlet conditions remain, unlike in the previous two parametric analyses, unchanged and the FAR is therefore constant. The reduction in TSFC associated with a change in velocity ratio is mainly due to a reduction in core mass flow rate. Consider the thrust equation below for a turbofan engine and that the thrust, free stream velocity V_0 are fixed.

$$F_n = \dot{m}_{core} V_{id,core} + \dot{m}_{bypass} V_{id,bypass} - \dot{m}_{intake} V_0 \tag{7.1}$$

The velocity ratio is defined in Equation 3.35 and the BPR is defined as the ratio of bypass and core MFR. Rewriting Equation 7.1 and integrating the dimensionless parameters above results in the adapted

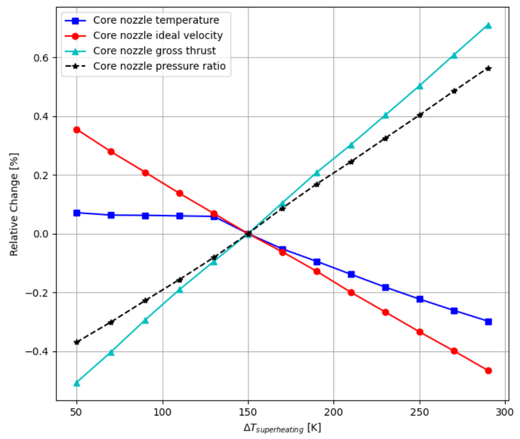

Figure 7.39: Effect of degree of steam superheating variation on core nozzle parameters.

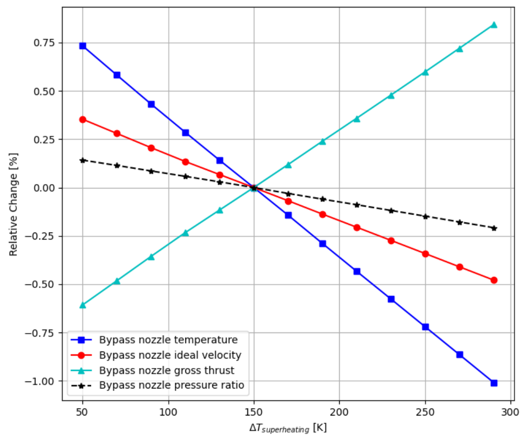

Figure 7.40: Effect of degree of steam superheating variation on bypass nozzle parameters.

thrust equation:

$$F_n = \dot{m}_{core} V_{id,core} (1 + BPR \cdot VR) - \dot{m}_{core} V_0 (1 + BPR) \tag{7.2}$$

A lower velocity ratio implies a reduction in bypass velocity relative to the core velocity. To maintain the required thrust level, the core mass flow rate—and consequently, the intake mass flow rate—must increase to compensate for this lower velocity ratio. Additionally, the FPR is the iteration variable to achieve the prescribed velocity ratio (Table 6.6). A reduction in bypass nozzle velocity ratio can thus be realized by lowering FPR. This trend is confirmed in Figure 7.44. Also the condenser heat duty slightly influences the bypass nozzle velocity. Figure 7.42 presents the efficiency trends as function of the velocity ratio. Total efficiency follows the same trend as TSFC, with thermal efficiency being the dominant factor. The propulsive efficiency is not significantly affected because the BPR remains fixed. As the FPR and heat addition in the bypass duct influence the ideal nozzle velocity, this quantity decreases at lower velocity ratios, approaching the freestream velocity. This reduction in velocity difference results in lower kinetic energy losses, thereby increasing propulsive efficiency. The trend of the bypass nozzle

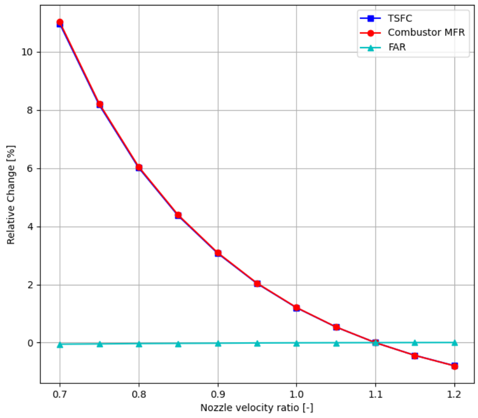

Figure 7.41: Effect of velocity ratio variation on WET combustor parameters.

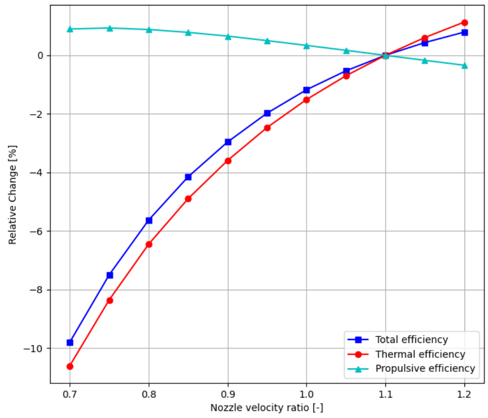

Figure 7.42: Effect of velocity ratio variation on WET engine efficiencies.

velocity is corroborated by Figure 7.48. Since the bypass flow in WET engine configurations generates an even larger share of the total thrust, the bypass nozzle characteristics essentially dictate the overall propulsive efficiency. The BPR is fixed in this analysis and large differences in propulsive efficiency are therefore not expected. Looking at the constraints in Figure 7.43, a velocity ratio equal to 1.1 is the optimal choice, because higher values exceed the condenser effectiveness maximum value. The HPC annulus outlet height is directly related to the mass flow rate, and its minimum value (12mm) is not reached within the velocity ratio range considered in this part of the study. Similarly, the HRSG outlet condition is not critical. Besides this, the LPT outlet conditions, FPR, and heat duties of both HEXs are provided in Figure 7.44. Compared to a conventional turbofan engine ($FPR \approx 0.7$) the WET engine has a lower FPR (>-10%) given a velocity ratio of 0.8. This is according to expectations as higher BPR is achieved for similar engine size, also documented in the literature [10, 16]. A reduction in FPR directly impacts the core flow, requiring the LPC to compensate for the lower pressure rise across the fan. Consequently, the pressure drop across the LPT decreases, leading to a higher LPT outlet pressure and temperature, as shown in Figure 7.44. Reducing the velocity ratio increases the heat load in both heat exchangers due to the higher mass flow rate. This effect is more pronounced for the condenser. The condenser's heat load is determined by the required saturation temperature to recover the injected water and the HRSG outlet conditions.

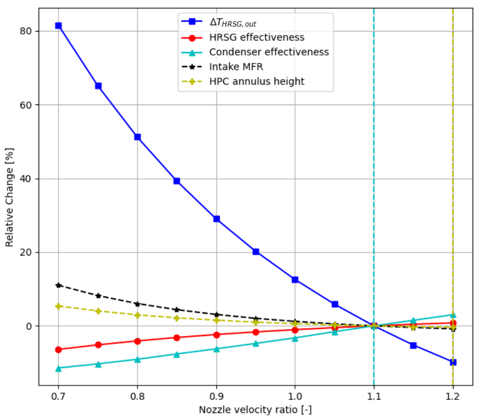

Figure 7.43: Effect of velocity ratio variation on the imposed WET engine constraints.

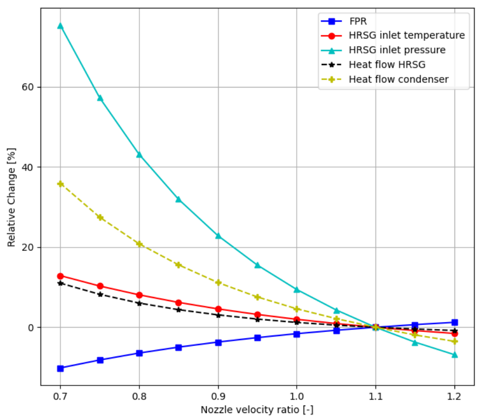

Figure 7.44: Effect of velocity ratio variation on FPR, HEX thermal loads, and LPT outlet conditions.

Regarding the heat exchangers, the trends in the HRSG characteristics shown in Figure 7.45 are according to expectations, as higher HEX inlet temperature differences enhance heat transfer. A lower velocity ratio decreases the HRSG's mass, size, and hot-side pressure drop, while significantly increasing the cold-side pressure drop. Given the more favorable inlet conditions for a fixed degree of superheating, the HRSG outlet temperature also rises. Although WAR primarily governs the condenser outlet temperature, pressure is also affected: a higher condenser outlet pressure is required to increase the core nozzle velocity and thus to lower the velocity ratio. Figure 7.46 illustrates how both pressure and temperature increase as the velocity ratio decreases. The combination of a lower FPR and higher exhaust temperature and pressure at the condenser inlet results in a greater temperature difference, enhancing heat transfer efficiency. While a lower velocity ratio raises the core nozzle temperature, the bypass temperature remains largely unaffected, increasing the temperature difference between the ram air and exhaust at the cold end of the condenser.

Finally, the nozzle exhaust conditions presented in Figure 7.47 and Figure 7.48 are analyzed. Compared to the results of the parametric studies discussed in Subsection 7.3.1 and Subsection 7.3.2, the impact of velocity ratio on nozzle operating conditions is considerably more pronounced, particularly for the core nozzle. A lower velocity ratio results in a significantly higher ideal core exhaust velocity than the bypass velocity. This is evident in both figures, where the core velocity increases by more than 40%, primarily driven by the higher core nozzle pressure ratio. Combined with the increased mass flow rate, this leads to greater core nozzle gross thrust. Regarding the bypass nozzle, the ideal velocity decreases at lower ratios, contributing to a slight improvement in propulsive efficiency. However, gross thrust still increases due to the higher mass flow rate. The reduction in ideal nozzle velocity is attributed to the lower FPR and the corresponding decrease in nozzle pressure ratio.

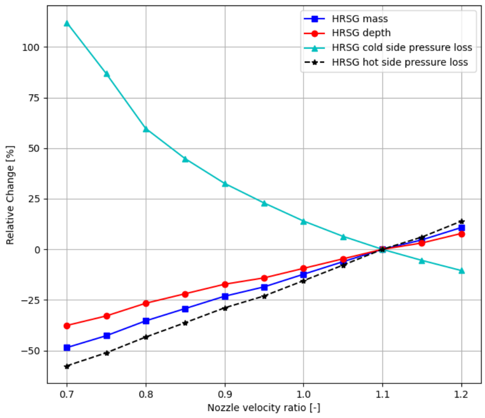

Figure 7.45: Effect of velocity ratio variation on HRSG characteristics (Hexacode).

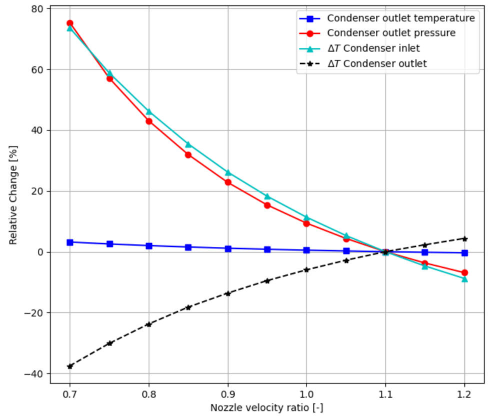

Figure 7.46: Effect of velocity ratio variation on condenser parameters.

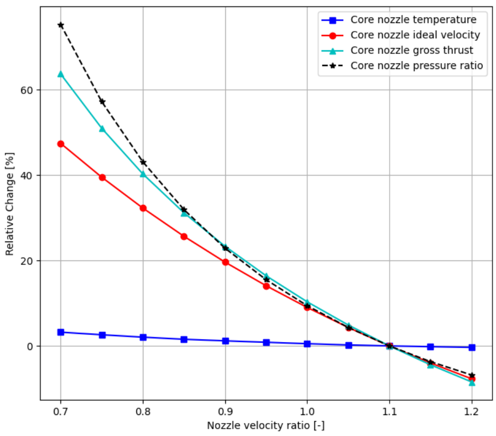

Figure 7.47: Effect of velocity ratio variation on core nozzle parameters.

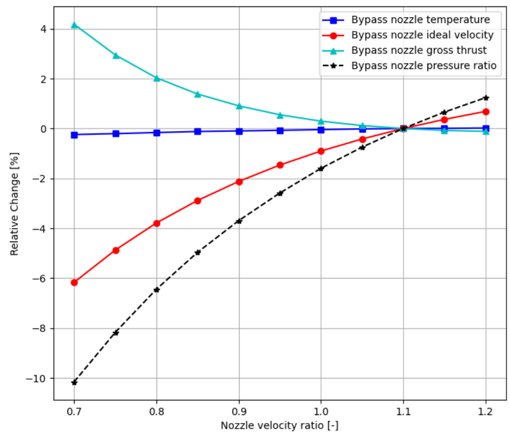

Figure 7.48: Effect of velocity ratio variation on bypass nozzle parameters.

This parametric study investigated the effects of three key parameters, namely OPR, the degree of superheating of injected steam, and the nozzle velocity ratio, on the performance, fuel efficiency, and other WET engine parameters.

- **OPR**: Increasing OPR generally improves thermal efficiency, hence TSFC, but leads to solutions that do not comply with the imposed design constraints. Although this study does not consider turbine cooling, the choice of the OPR significantly affects the required cooling mass flow rates. Besides this, the mall increase in performance achievable by selecting $OPR = 37$ instead of 35 will most likely be eroded by the larger and thus heavier HEXs required with this design option.
- **Degree of superheating:** Higher steam temperatures improve the thermal efficiency of the cycle by increasing the specific enthalpy of injected water. Although the effect of this design variable on TSFC is much smaller than OPR, it can have a beneficial cycle performance effect without significantly impacting the design constraints. However, the preliminary design of the HRSG performed in Hexacode reveals that the increase in degree of steam superheating higher

than 30% with respect to the baseline value is difficult to achieve with the chosen HEX configuration and that the mass and size become larger.

- **Nozzle velocity ratio:** A lower velocity ratio significantly increases intake mass flow rate and TSFC. The study confirms the findings reported in the literature (e.g., Görtz et al. [60]) that the optimum velocity ratio for fuel efficiency lies around 1.1. Beyond this point, performance gains diminish due to heat exchanger limitations.

Overall, the study highlights that OPR and superheating are the design variables, among those analyzed, yielding the highest potential increase in fuel efficiency, while varying the velocity ratio does not yield TSFC gains. These findings provide key design guidelines for optimizing WET performance.

7.4. Discussion

The performance analysis of the Water-Enhanced Turbofan engine reveals significant efficiency improvements compared to a conventional high-bypass turbofan, but these findings must be considered in light of the study's limitations and underlying assumptions. The design exploration demonstrated the potential of water injection and heat recovery to enhance thermal efficiency and reduce TSFC. However, the study also identified several constraints that limit the feasible design space, emphasizing the need for a trade-off between performance gains and design feasibility of the various engine components.

Design Exploration Process and Limitations

The design space exploration identified an optimal combination of TIT, BPR, and WAR that minimizes TSFC while complying with the prescribed engineering constraints. The key challenge in this process was balancing efficiency improvements with design feasibility. While future aero engines are expected to feature larger fan diameters [16], the WET engine's intake mass flow rate is maintained equal to that of the reference engine as the effect of larger engine nacelles on drag is not captured by the system model. The main limitations of the analysis concern the prediction of heat exchanger performance. The best design solution obtained in the design maps corresponds to the intersection of the curves representing the prescribed intake mass flow rate and HRSG effectiveness for WAR values up to and including $WAR = 0.25$. Beyond this point, the optimal design no longer satisfies the constraint on the HRSG superheating (indicated by the blue line in the maps). The HPC annulus height falls below the imposed minimum value at $WAR \geq 0.25$. It is also found that each map contains a minimum TSFC region. By increasing WAR, the minimum TSFC shifts towards higher BPR and lower TIT values. Initially, the total efficiency increases due to a rise in propulsive efficiency; however, at higher BPR values, the decline in thermal efficiency becomes the dominant factor. Additionally, the core nozzle inlet conditions hardly change in the solutions of the design as the velocity ratio is fixed to a high ratio. Due to the high velocity ratio, the FPR is relatively high and increases further with higher WAR values. The majority of the thermal energy recuperated from the exhaust gases is exchanged in the HRSG, while the pressure rise in the fan offsets the reduced thermal energy transferred to the ram air for higher WARs.

HRSG Modeling in Hexacode

The Hexacode software was used to model the HRSG with greater fidelity than in the pyCycle model. While it provided valuable insights into pressure losses, heat transfer effectiveness, and component sizing, analysis suffered from some inherent limitations, in particular related to the chosen HEX configurations. At the same time, the estimated pressure drops showed deviations from the assumed values in the pyCycle model, although not significantly. Moreover, the convergence issues for high degrees of steam superheating indicate that the model may require more attention and possible modifications to make it viable to thoroughly explore the whole design space of the WET cycle.

Comparison to the Conventional Turbofan Engine

To comply with the imposed constraints, the best WET engine design is found for $WAR = 0.20$. Compared to the benchmark LEAP-1A-like turbofan engine, the WET cycle demonstrated a 7.28% reduction in TSFC, primarily driven by an increase in thermal efficiency (+7.19%) and a modest gain in propulsive efficiency (+0.67%). This is achieved despite the reduced TIT (-3.63%) and lower OPR (-22.22%).

While these results suggest clear efficiency advantages, they must be interpreted with caution due to the modeling assumptions, the simplifications adopted to model the engine components such as the HEXs or the high-pressure turbine, whose cooling system is neglected, and the fixed fan diameter. Additionally, as this improvement is obtained at the cost of increased system complexity, engine weight and arguably low reliability, the reduction in fuel consumption should be weighted against these limitations. As in all previous studies documented in the literature, the condenser is found to be the component that affects the WET engine design the most both in terms of thermodynamic performance as well as in weight and system complexity.

Main Findings of the Parametric Study

A preliminary study of the WET engine cycle was performed to asses how key design variables - Overall Pressure Ratio (OPR), degree of superheating of steam, and nozzle velocity ratio - affects engine performance, particularly TSFC. The parametric study revealed that increasing OPR improves thermal efficiency. At the same time, the design solutions do not comply with some constraints such as annulus height limitations. The OPR could only be increased from 35 to 37. Otherwise, the annulus height constraint is reached. The impact on TSFC is a decrease in the order 1%. The steam degree of superheating has a marginal effect on engine performance and the increase of this design variable is limited by the HRSG design feasibility. 1% TSFC reductions could be reached when the degree of steam superheating is increased from 150 to 210 Kelvin without exceeding the constraints. The nozzle velocity ratio has a significant impact on mass flow distribution and TSFC, with lower velocity ratios significantly increasing the TSFC. The velocity ratio of 1.1 is found to be the most optimal and no further fuel consumption reduction could be achieved without exceeding constraints. These findings underline the sensitivity of the WET cycle performance to the imposed design constraints. Given that this study serves as a preliminary assessment of the WET engine's performance characteristics, identifying key design trends provides a foundation for more detailed future investigations.

8

Conclusions & Recommendations

8.1. Conclusions

This study has focused on the on-design modeling of the Water-Enhanced Turbofan (WET) engine within NASA's PyCycle and OpenMDAO framework. It explored how the injection of water in the engine core flow and its recuperation by cooling the exhaust gases impact the thermodynamic cycle efficiency and overall performance in comparison to a conventional turbofan engine.

A simplified WET engine cycle model has been developed in Python, featuring modular engine components. Cruise is considered as the design point throughout the simulation studies. This model extends that of a two-spool, high-bypass ratio turbofan engine, with the addition of WET-specific components, including a steam injector and a water separator. The heat recovery steam generator (HRSG) and condenser are modeled as simple ducts. A prescribed thermal energy input and pressure drop are imposed then to the flow passing through the duct. To enhance computational efficiency, the TABULAR calculation mode in pyCycle is used, significantly reducing simulation time. As the same suggests, this calculation mode makes use of thermodynamic tables. In the original version of pyCycle, these tables have three dimensions, namely two correspond to the chosen thermodynamic state variables, while the third one represents the fuel-to-air ratio. A fourth dimension, the water-to-air ratio (WAR), has been added in this work to accurately model wet air and wet exhaust gases. The developed tables also cover the condensation region of the mixture, facilitating the modeling of the WET engine. However, the thermodynamic model does not allow for the detailed modeling of the phase change phenomena in the wet exhaust gases. For the modeling of one of the key HEXs of the engine, namely the HRSG, the in-house software Hexacode is utilized.

The results show that the TSFC of the WET engine can be reduced by 7.3% compared to a LEAP-1A-type conventional high-bypass turbofan engine. This best design point is found at $WAR = 0.2$ as a result of the design exploration study. For a similar engine diameter, the bypass ratio is increased by 62%, resulting in a core mass flow rate reduction of 23%. With the injection of water in the core, the TSFC is minimized by reducing the TIT of 3.6% with respect to the reference engine. Given the increase in specific power of the cycle, lower OPR values can be reached at the HPC outlet to comply with the limitation on the minimum blade height of this component. The propulsive efficiency is barely improved by the increase in BPR as the air velocities in the bypass nozzle tend to be higher than in a conventional turbofan engine. The total efficiency improvement is therefore mainly achieved by the increase in thermal efficiency. A marginal increase in the degree of steam superheating and OPR has been shown in the parametric study to further reduce the TSFC by a few percentage points. The nozzle velocity ratio (VR) is a critical parameter in the performance for the WET engine. For the reference TF engine, an optimal VR of 0.8 has been documented in the literature, whereas the WET engine achieves its optimal performance at a significantly higher VR, namely 1.1. The condenser is identified as the most critical component, regardless of the considered WAR value, both in terms of performance and constraints related to size and weight. However, at higher WAR levels and increased degrees of steam superheating, the design of the HRSG also becomes challenging, as revealed by the analysis conducted with Hexacode and the parametric study.

While the WET engine demonstrates significant potential for fuel consumption reduction, this preliminary design study does not account for critical factors such as engine mass and size. Given the uncertainties introduced by the model simplifications and assumptions, as well as the limited availability of case studies in the literature, the projected mission fuel savings of a few percentage points may not, at this stage, justify full-scale development. Therefore, a further refinement of the analysis is necessary, including the investigation of engine size, weight, off-design performance, and more detailed heat exchanger modeling. A comprehensive assessment of these factors is essential to determine the feasibility of the WET engine as a viable propulsion concept for future aircraft applications.

8.2. Recommendations

Based on the findings of this study, several recommendations are proposed. These focus on addressing key limitations identified in the analysis and guiding future research and development efforts:

1. **Advanced Heat Exchanger Modeling and Integration:** the current modeling framework in pyCycle and OpenMDAO would benefit from the integration of more detailed heat exchanger models, particularly for the condenser. While Hexacode has been used to check and estimate the heat transfer and size constraints of the HRSG, a similar analysis should be performed for the condenser. This will require a thorough modeling of the condensation processes and phase change phenomena. The end goal is to achieve an accurate estimation of both performance and weight/size of the condenser. In general, a more comprehensive engine model would enable a better understanding of the trade-offs between heat exchanger efficiency, system weight, and fuel savings.

2. **Off-Design Performance**: the current analysis focuses only on the engine's design-point performance, though real-world operation involves a wide range of off-design conditions, including part-load operation, altitude variations, and transient behavior. A detailed off-design performance analysis would provide insights into the operational envelope of the WET engine, verifying that efficiency gains at cruise conditions do not come at the cost of significant performance penalties in other flight phases. This would also enable the optimization of the control setpoints for steam injection and water recovery throughout the flight envelope.

3. **Emissions Analysis for Environmental Impact Assessment**: with increasingly stringent environmental regulations, emissions are becoming a critical factor for future aircraft engine development. The WET engine has the potential to reduce nitrogen oxides (NO_x) emissions by more than 90% through lower combustion temperatures and the larger fraction of water in the exhaust gases, CO_2 by up to 10% as a result of the lower fuel consumption, and contrails by more than 50% thanks to the more favorable core nozzle exhaust conditions [10]. A more detailed emissions study, including the effects of water vapor on contrail formation and climate impact, would provide a comprehensive assessment of the environmental benefits of the WET concept.

4. **The Use of Alternative Fuels**: the use of alternative fuels, such as hydrogen, presents an opportunity to both improve fuel efficiency and enhance HEX performance. Liquid hydrogen, in particular, could serve as an effective heat sink, reducing reliance on ram air for cooling while simultaneously enabling ultra-low emissions operation. Future research should explore the thermodynamic benefits and integration challenges of hydrogen-fueled WET engines, considering both combustor modifications and fuel system implications.

5. **Cooling Strategies:** unlike conventional turbofan engines, where cooling is primarily required for the HPT, the WET engine experiences higher temperatures in the LPT due to the relatively high water share in the exhaust gas. Investigating novel cooling techniques, such as steam cooling or advanced thermal barrier coatings, is crucial for maintaining turbine longevity and efficiency in WET engine architectures.

By addressing these research areas, the feasibility and performance of the WET engine can be better understood, ensuring that its potential fuel savings and emissions benefits translate into a viable propulsion concept for future aircraft.

A

Appendix

A.1. Comparison of CEA and TABULAR Mode in pyCycle

Input data:

- **Turbojet**: PR = 15, F_n = 50 kN, TIT = 1400 K. Other input values are default values. Tabular set: AIR-JETA-TAB-SPEC (pyCycle default); enthalpy of fuel: 0 kJ/kg.
- **Turbofan**: TIT = 1400K, F_n = 50 kN. Other input values are default values. Tabular set: AIR-JETA-TAB-SPEC (pyCycle default); enthalpy of fuel: 0 kJ/kg.
- Default tabular set by pyCycle: FAR x p x T = 20 x 110 x 100 where $0 < FAR < 0.05$, $1 < p < 100e5$ Pa, and $100 < T < 3500$ K.

Table A.1: Comparison of the CEA and TABULAR mode in pyCycle for a simple turbojet and turbofan engine.

Parameter	**Turbojet**			**Turbofan**		
	CEA	**TAB**	**Δ%**	**CEA**	**TAB**	**Δ%**
t **[s]**	4.6200335	1.3671095	-70.409	47.644469	8.5718939	-82.009
$TSFC$ **[$g \cdot kN^{-1} \cdot s^{-1}$]**	23.292221	23.281012	-0.048	17.658158	17.481204	-1.002
F_n **[kN]**	49.999974	49.999950	0	49.999999	49.999999	0
$\dot{W}_{comp}$ **[MW]**	23.958401	23.802983	-0.649	43.078854	42.428887	-1.509
$\dot{m}_{in}$ **[$kg \cdot s^{-1}$]**	59.043375	58.894172	-0.253	385.19259	380.74423	-1.168
FAR	0.0197247	0.0197651	0.205	0.0190256	0.0190550	0.155

A.2. AspenPlus Test Engine Verification Results

In this section, the detailed results of the mixer-combustor comparison between Aspen, the CEA mode and TABULAR mode are tabulated. Temperature, pressure, enthalpy, entropy, density, isobaric specific heat, (mixture) molar mass and mass fractions are compared. Four tables are provided to provide the absolute values and relative errors of the three cases explained in Subsection 5.1.2:

- Table A.2 compares the thermodynamic properties of compressed air.
- Table A.3 compares the thermodynamic properties of steam.
- Table A.4 compares the thermodynamic properties of compressed wet air.
- Table A.5 compares the thermodynamic properties of compressed wet exhaust gas.

Table A.2: Comparison of thermodynamic properties for compressed air.

	Aspen Software	pyCycle CEA	Δ% Aspen	pyCycle TABULAR	Δ% Aspen	Δ% CEA
T $[K]$	800	800	0.000	800	0.000	0.000
P $[bar]$	15	15	0.000	15	0.000	0.000
$\mathbf{h_{mass}}$ $[kJ/kg]$	514.836	514.865	0.006	514.913	0.015	0.009
$\mathbf{S_{mass}}$ $[kJ/kgK]$	0.422	7.099	1581	7.099	1581	0.002
$\mathbf{D_{mass}}$ $[kg/m^3]$	6.562	6.562	0.003	6.563	0.007	0.004
$\mathbf{C_{p,mass}}$ $[kJ/kgK]$	-	1094.35	-	1094.41	-	0.006
M $[g/mole]$	29.098	29.100	0.004	29.098	0.001	-0.004
$\mathbf{k_{water}}$ $[-]$	6.19e-10	7.39e-8	0.000	-	-	-
$\mathbf{k_{nitrogen}}$ $[-]$	0.726854	0.726812	-0.006	-	-	-
$\mathbf{k_{oxygen}}$ $[-]$	0.254703	0.254735	0.013	-	-	-
$\mathbf{k_{argon}}$ $[-]$	0.017701	0.017713	0.018	-	-	-
$\mathbf{k_{CO2}}$ $[-]$	7.3354e-4	7.3356e-4	0.003	-	-	-

Table A.3: Comparison of thermodynamic properties for superheated steam at a pressure of 15 bar.

	Aspen Software	pyCycle CEA	Δ% Aspen	pyCycle TABULAR	Δ% Aspen	Δ% CEA
Case 1: T = 500K						
$\mathbf{h_{mass}}$ $[kJ/kg]$	-13038.698	-13038.905	-0.002	-13103.311	0.496	0.494
$\mathbf{S_{mass}}$ $[kJ/kgK]$	-2.728	10.220	-475	10.116	-471	-1.022
$\mathbf{D_{mass}}$ $[kg/m^3]$	6.500	6.500	-0.002	6.978	7.341	7.343
$\mathbf{C_{p,mass}}$ $[kJ/kgK]$	-	1955.32	-	2510.138	-	28.37
M $[g/mole]$	18.015	18.015	-0.001	29.0995	-0.005	0.000
Case 2: T = 800K						
$\mathbf{h_{mass}}$ $[kJ/kg]$	-12423.675	-12423.969	0.002	-12438.352	0.118	0.116
$\mathbf{S_{mass}}$ $[kJ/kgK]$	-1.768	11.180	-732.477	11.162	-731	-0.163
$\mathbf{D_{mass}}$ $[kg/m^3]$	4.063	4.063	-0.003	4.104	1.006	1.009
$\mathbf{C_{p,mass}}$ $[kJ/kgK]$	-	2149.74	-	2198.11	-	2.250
M $[g/mole]$	18.015	18.015	-0.001	29.0995	-0.005	0.000
Case 3: T = 1100K						
$\mathbf{h_{mass}}$ $[kJ/kg]$	-211630.748	-11747.126	-0.001	-11753.530	0.053	0.055
$\mathbf{S_{mass}}$ $[kJ/kgK]$	-1.051	11.897	-1231	11.887	-1231	-0.083
$\mathbf{D_{mass}}$ $[kg/m^3]$	2.955	2.955	-0.003	2.962	0.239	0.242
$\mathbf{C_{p,mass}}$ $[kJ/kgK]$	-	2363.23	-	2376.37	-	0.556
M $[g/mole]$	18.015	18.015	-0.001	29.0995	-0.005	0.000

Table A.4: Comparison of thermodynamic properties for wet, compressed air at a pressure of 15 bar.

	Aspen Software	pyCycle CEA	Δ% Aspen	pyCycle TABULAR	Δ% Aspen	Δ% CEA
Case 1						
$\mathbf{T_{mix}}$ $[K]$	752.76	752.79	0.004	752.35	-0.054	-0.058
$\mathbf{h_{mass}}$ $[kJ/kg]$	-717.303	-717.258	-0.006	-717.944	0.089	0.096
$\mathbf{S_{mass}}$ $[kJ/kgK]$	0.273	7.520	2657	7.518	2656	-0.018
$\mathbf{D_{mass}}$ $[kg/m^3]$	6.605	6.604	-0.005	6.611	0.096	0.101
$\mathbf{C_{p,mass}}$ $[kJ/kgK]$	-	1177.36	-	1177.92	-	0.047
M $[g/mole]$	27.557	27.557	0.001	27.564	0.023	0.023
$\mathbf{k_{water}}$ $[-]$	0.090909	0.090910	0.001	-	-	-
$\mathbf{k_{nitrogen}}$ $[-]$	0.660776	0.660739	0.001	-	-	-
$\mathbf{k_{oxygen}}$ $[-]$	0.231548	0.231578	0.013	-	-	-
$\mathbf{k_{argon}}$ $[-]$	0.016100	0.016103	0.013	-	-	-
$\mathbf{k_{CO2}}$ $[-]$	6.6686e-4	6.6687e-4	0.003	-	-	-
Case 2						
$\mathbf{T_{mix}}$ $[K]$	800.00	800.01	0.001	800.00	0.000	-0.001
$\mathbf{h_{mass}}$ $[kJ/kg]$	-661.392	-661.355	-0.006	-661.504	0.017	0.023
$\mathbf{S_{mass}}$ $[kJ/kgK]$	0.345	7.592	2102	7.591	2101	-0.008
$\mathbf{D_{mass}}$ $[kg/m^3]$	6.215	6.214	-0.002	6.217	0.042	0.045
$\mathbf{C_{p,mass}}$ $[kJ/kgK]$	-	1190.40	-	1190.91	-	0.043
M $[g/mole]$	27.557	27.557	0.001	27.564	0.024	0.023
Case 3						
$\mathbf{T_{mix}}$ $[K]$	936.11	936.17	0.006	936.35	0.026	0.020
$\mathbf{h_{mass}}$ $[kJ/kg]$	-2988.629	-2988.531	-0.003	-2989.238	0.020	0.024
$\mathbf{S_{mass}}$ $[kJ/kgK]$	0.245	8.713	3463	8.711	3462	-0.023
$\mathbf{D_{mass}}$ $[kg/m^3]$	4.770	4.769	-0.008	4.774	0.087	0.094
$\mathbf{C_{p,mass}}$ $[kJ/kgK]$	-	1444.83	-	1447.61	-	0.192
M $[g/mole]$	24.748	24.748	0.000	24.761	0.051	0.051
$\mathbf{k_{water}}$ $[-]$	0.285714	0.285717	0.001	-	-	-
$\mathbf{k_{nitrogen}}$ $[-]$	0.519181	0.519147	-0.007	-	-	-
$\mathbf{k_{oxygen}}$ $[-]$	0.181930	0.181945	-0.008	-	-	-
$\mathbf{k_{argon}}$ $[-]$	0.012650	0.012652	0.018	-	-	-
$\mathbf{k_{CO2}}$ $[-]$	5.23958e-4	5.23968e-4	0.002	-	-	-

Table A.5: Comparison of thermodynamic properties for wet, compressed exhaust gases at a pressure of 15 bar and TIT of 1500 Kelvin.

	Aspen Software	**pyCycle CEA**	**Δ% Aspen**	**pyCycle TABULAR**	**Δ% Aspen**	**Δ% CEA**
Case 1						
$\dot{\mathbf{m}}_{\mathbf{f}}$ $[kg/s]$	0.256601	0.257693	0.426	0.25772	0.438	0.012
$\mathbf{h}_{\mathbf{mass}}$ $[kJ/kg]$	-748.108	-748.192	0.011	-748.866	0.101	0.090
$\mathbf{S}_{\mathbf{mass}}$ $[kJ/kgK]$	1.166	8.487	628	8.486	628	-0.014
$\mathbf{D}_{\mathbf{mass}}$ $[kg/m^3]$	3.311	3.310	-0.006	3.311	0.002	0.008
$\mathbf{C}_{\mathbf{p,mass}}$ $[kJ/kgK]$	-	1406.11	-	1402.21	-	-0.278
M $[g/mole]$	27.525	27.525	0.000	27.525	0.002	0.001
$\mathbf{k}_{\mathbf{water}}$ $[-]$	0.120178	0.120272	0.078	-	-	-
$\mathbf{k}_{\mathbf{nitrogen}}$ $[-]$	0.645713	0.645177	-0.083	-	-	-
$\mathbf{k}_{\mathbf{oxygen}}$ $[-]$	0.147048	0.146238	-0.551	-	-	-
$\mathbf{k}_{\mathbf{argon}}$ $[-]$	0.015733	0.015734	0.008	-	-	-
$\mathbf{k}_{\mathbf{CO2}}$ $[-]$	0.071327	0.071590	0.369	-	-	-
Case 2						
$\dot{\mathbf{m}}_{\mathbf{f}}$ $[kg/s]$	0.241414	0.242512	0.455	0.242417	0.415	-0.039
$\mathbf{h}_{\mathbf{mass}}$ $[kJ/kg]$	-691.614	-691.712	0.014	-691.846	0.034	0.019
$\mathbf{S}_{\mathbf{mass}}$ $[kJ/kgK]$	1.165	8.482	628	8.481	628	-0.014
$\mathbf{D}_{\mathbf{mass}}$ $[kg/m^3]$	3.311	3.311	-0.001	3.298	0.002	0.004
$\mathbf{C}_{\mathbf{p,mass}}$ $[kJ/kgK]$	-	1403.163	-	1399.243	-	-0.279
M $[g/mole]$	27.527	27.527	0.000	27.527	0.002	0.001
$\mathbf{k}_{\mathbf{water}}$ $[-]$	0.118483	0.118578	0.080	-	-	-
$\mathbf{k}_{\mathbf{nitrogen}}$ $[-]$	0.646586	0.646041	-0.084	-	-	-
$\mathbf{k}_{\mathbf{oxygen}}$ $[-]$	0.151942	0.151118	-0.542	-	-	-
$\mathbf{k}_{\mathbf{argon}}$ $[-]$	0.015754	0.015755	0.008	-	-	-
$\mathbf{k}_{\mathbf{CO2}}$ $[-]$	0.067235	0.067502	0.398	-	-	-
Case 3						
$\dot{\mathbf{m}}_{\mathbf{f}}$ $[kg/s]$	0.298567	0.299903	0.447	0.299610	0.349	-0.098
$\mathbf{h}_{\mathbf{mass}}$ $[kJ/kg]$	-2969.419	-2969.239	-0.006	-2969.950	0.018	0.024
$\mathbf{S}_{\mathbf{mass}}$ $[kJ/kgK]$	0.975	9.486	873	9.484	872	-0.029
$\mathbf{D}_{\mathbf{mass}}$ $[kg/m^3]$	2.980	2.980	-0.002	2.980	0.003	0.005
$\mathbf{C}_{\mathbf{p,mass}}$ $[kJ/kgK]$	1652.6	1670.46	1.081	1663.393	0.653	-0.423
M $[g/mole]$	24.777	24.777	0.000	24.777	0.002	0.002
$\mathbf{k}_{\mathbf{water}}$ $[-]$	0.308457	0.308523	0.021	-	-	-
$\mathbf{k}_{\mathbf{nitrogen}}$ $[-]$	0.508340	0.507936	-0.079	-	-	-
$\mathbf{k}_{\mathbf{oxygen}}$ $[-]$	0.105564	0.104882	-0.646	-	-	-
$\mathbf{k}_{\mathbf{argon}}$ $[-]$	0.012386	0.012387	0.009	-	-	-
$\mathbf{k}_{\mathbf{CO2}}$ $[-]$	0.065252	0.065508	0.391	-	-	-

A.3. Real and Ideal Water Properties Comparison

In the Figure A.1 until Figure A.8, the differences for various thermodynamic properties, predicted by pyCycle and Coolprop, are plotted. The range 500-1100K is chosen to coincide with the temperatures used in the verification process (Subsection 5.1.2). The relative error / difference (RE) is calculated following Equation A.1.

$$RE = \frac{X_{CoolProp} - X_{CEA}}{X_{CEA}} \cdot 100\% \tag{A.1}$$

Close to the saturation point, the specific heat C_p shows a more gradual change, whereas the density, enthalpy and entropy perform a step change at the saturation temperature. This is not shown in the graph as the saturation temperature at 15 bar is approximately 471 Kelvin. The relative error for both enthalpy and entropy are smaller than 1%, whereas the maximum error is significantly higher for the isobaric specific heat ($\approx 28\%$) and the density ($\approx 7\%$).

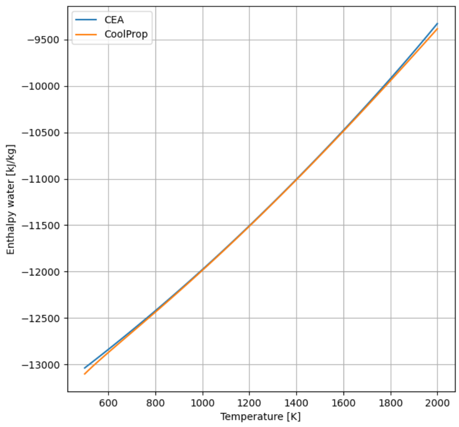

Figure A.1: Predicted water enthalpy by CoolProp and pyCycle CEA.

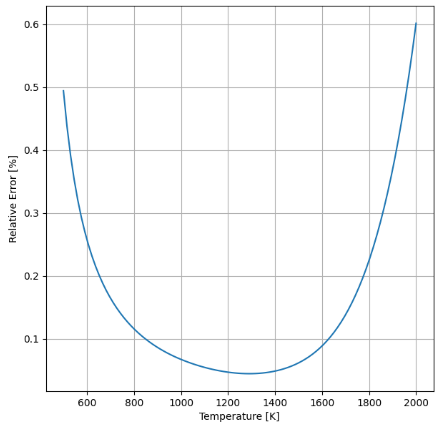

Figure A.2: Relative difference of the water enthalpy for both thermodynamic models.

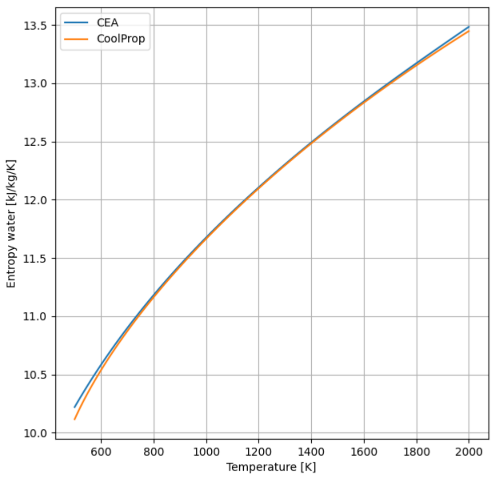

Figure A.3: Predicted water entropy by CoolProp and pyCycle CEA.

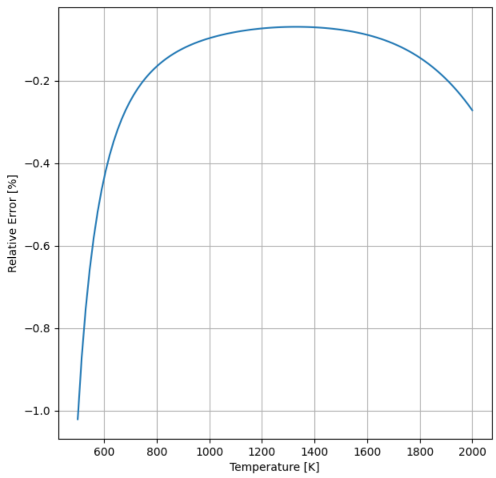

Figure A.4: Relative difference of the water entropy for both thermodynamic models.

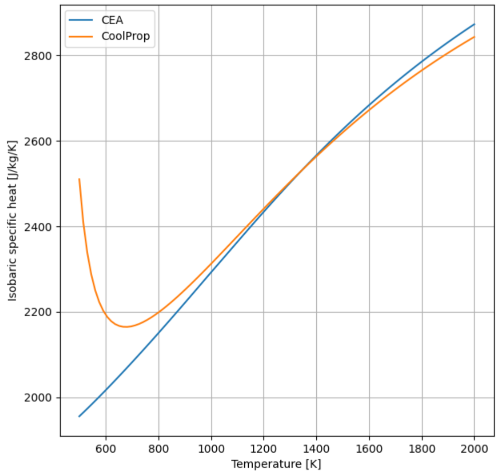

Figure A.5: Predicted water isobaric specific heat by CoolProp and pyCycle CEA.

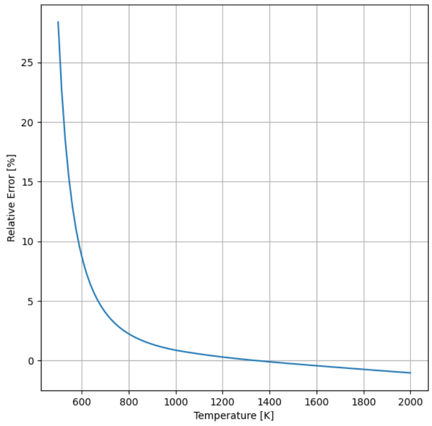

Figure A.6: Relative difference of the water isobaric specific heat for both thermodynamic models.

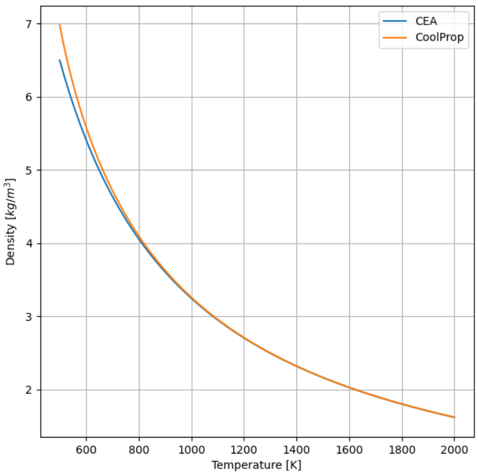

Figure A.7: Predicted water density by CoolProp and pyCycle CEA.

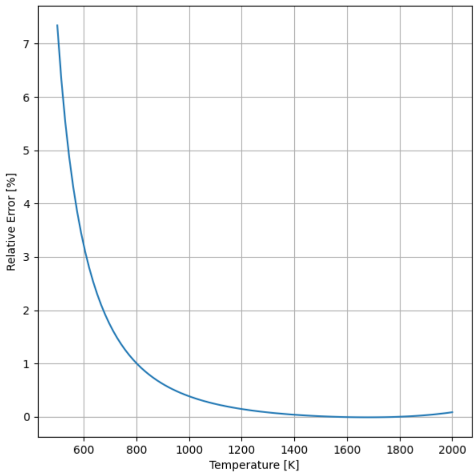

Figure A.8: Relative difference of the water density for both thermodynamic models.

A.4. Thermodynamic Cycle Data

This section gives the thermodynamic cycle data for both the reference TF engine (Appendix A.4.1) and the WETF engine (Appendix A.4.2). The flow stations are listed and the total pressure (bar), temperature (K), enthalpy (kJ/kg), and enthalpy ($kJ/kg/K$) are provided for each station. Furthermore, the static pressure (bar), the mass flow rate (kg/s), the Mach number, the velocity (m/s) and the nozzle area (m^2) are tabulated. Performance characteristics are given on top. Turbomachinery, burner, nozzle, and shaft properties are presented below the station properties with indicated units.

A.4.1. Reference TF Engine

POINT: DESIGN

PERFORMANCE CHARACTERISTICS

Mach	Alt	W [kg/s]	Fn [kN]	Fg [kN]	Fram [kN]	OPR	TSFC [g/kN/s]	BPR	eta_th	eta_prop	eta_tot
0.800	35000.0	163.251	22.80	61.55	38.75	45.080	15.047	12.000	0.485	0.765	0.371

FLOW STATIONS

Flow Station	tot:P	tot:T	tot:h	tot:S	stat:P	stat:W	stat:MN	stat:V	stat:area
DESIGN.fc.Fl_O	0.340	246.869	-55.822	6.995	0.238	1.000	0.800	237.357	0.012
DESIGN.inlet.Fl_O	0.339	246.869	-55.822	6.995	0.275	163.251	0.600	182.602	2.211
DESIGN.fan.Fl_O	0.570	292.482	-10.029	7.010	0.481	163.251	0.500	167.309	1.623
DESIGN.splitter.Fl_O1	0.570	292.482	-10.029	7.010	0.511	12.558	0.400	135.006	0.148
DESIGN.splitter.Fl_O2	0.570	292.482	-10.029	7.010	0.481	150.694	0.500	167.309	1.498
DESIGN.lpc.Fl_O	0.867	333.612	31.330	7.022	0.777	12.558	0.400	144.134	0.104
DESIGN.duct11.Fl_O	0.570	292.482	-10.029	7.010	0.511	12.558	0.400	135.006	0.148
DESIGN.hpc.Fl_O	15.297	801.689	521.300	7.110	14.402	12.558	0.300	166.184	0.012
DESIGN.bleeds.Fl_O	15.297	801.689	521.300	7.110	14.402	12.558	0.300	166.184	0.012
DESIGN.burner.Fl_O	14.533	1700.000	461.023	8.151	14.169	12.901	0.200	157.497	0.028
DESIGN.hpt.Fl_O	4.012	1316.711	-32.837	8.191	3.620	12.901	0.400	276.889	0.048
DESIGN.duct13.Fl_O	3.932	1316.711	-32.837	8.197	3.549	12.901	0.400	276.889	0.049
DESIGN.lpt.Fl_O	0.397	798.891	-655.698	8.256	0.357	12.901	0.400	218.591	0.369
DESIGN.duct14.Fl_O	0.393	798.891	-655.698	8.259	0.370	12.901	0.300	164.836	0.477
DESIGN.nozz_core.Fl_O	0.393	798.891	-655.698	8.259	0.238	12.901	0.891	464.303	0.235
DESIGN.duct01.Fl_O	0.564	292.482	-10.029	7.013	0.491	150.694	0.450	151.261	1.637
DESIGN.nozz_bypass.Fl_O	0.564	292.482	-10.029	7.013	0.306	150.694	1.000	313.048	1.115

COMPRESSOR PROPERTIES

Compressor	Wc [kg/s]	PR	eta_a	eta_p	Nc	pwr [MW]
DESIGN.fan	451.192	1.680	0.907	0.910	5041.160	-7.476
DESIGN.lpc	22.490	1.521	0.904	0.910	4631.416	-0.519
DESIGN.hpc	16.110	18.000	0.871	0.910	13667.033	-6.153

BURNER PROPERTIES

Burner	dPqP	TtOut [K]	Wfuel [kg/s]	FAR
DESIGN.burner	0.0500	1700.00	0.3431	0.02732

TURBINE PROPERTIES

Turbine	Wp [kg/s]	PR	eff_a	eff_p	Np	pwr [MW]
DESIGN.hpt	3.386	3.622	0.904	0.890	265.843	6.371
DESIGN.lpt	11.014	9.895	0.931	0.910	95.846	8.035

NOZZLE PROPERTIES

Nozzle	PR	Cv	Cfg	Ath [m2]	MNth	MNout	V [m/s]	Fg [kN]
DESIGN.nozz_core	1.650	N/A	0.993	0.235	0.891	0.891	464.303	5.950
DESIGN.nozz_bypass	2.367	N/A	0.993	1.115	1.000	1.000	313.048	55.599

SHAFT PROPERTIES

Shaft	Nmech	trqin [Nm]	trqout [Nm]	pwrin [MW]	pwrout [MW]
DESIGN.hp_shaft	14705.700	4137.217	-3995.474	6.371	-6.153
DESIGN.lp_shaft	4666.100	16444.735	-16362.512	8.035	-7.995

A.4.2. WETF Engine

POINT: DESIGN

PERFORMANCE CHARACTERISTICS

Mach	Alt	W [kg/s]	Fn [kN]	Fg [kN]	Fram [kN]	OPR	TSFC [g/kN/s]	BPR	eta_th	eta_prop	eta_tot
0.80000	35000.0	163.300	22.8	61.6	38.8	35.068	13.94403	19.439	0.521	0.770	0.401

FLOW STATIONS

Flow Station	tot:P	tot:T	tot:h	tot:S	stat:P	stat:W	stat:MN	stat:V	stat:area
DESIGN.fc.Fl_O	0.340	246.869	-55.822	6.995	0.238	1.000	0.800	237.357	0.012
DESIGN.inlet.Fl_O	0.339	246.869	-55.822	6.995	0.275	163.300	0.600	182.602	2.212
DESIGN.fan.Fl_O	0.589	292.959	-9.549	7.003	0.496	163.300	0.500	167.445	1.575
DESIGN.splitter.Fl_O1	0.589	292.959	-9.549	7.003	0.527	7.990	0.400	135.115	0.091
DESIGN.splitter.Fl_O2	0.589	292.959	-9.549	7.003	0.496	155.310	0.500	167.445	1.498
DESIGN.duct_core.Fl_O	0.586	292.959	-9.549	7.004	0.524	7.990	0.400	135.115	0.092
DESIGN.lpc.Fl_O	1.002	345.851	43.658	7.017	0.897	7.990	0.400	146.733	0.058
DESIGN.duct_lpc_hpc.Fl_	0.992	345.851	43.658	7.020	0.888	7.990	0.400	146.733	0.059
DESIGN.hpc.Fl_O	11.900	725.760	438.517	7.073	11.198	7.990	0.300	158.560	0.009
DESIGN.injector.Fl_O	11.900	692.386	-1773.710	7.856	11.207	9.588	0.300	161.498	0.011
DESIGN.burner.Fl_O	11.424	1638.277	-1772.800	9.114	11.144	9.905	0.200	160.586	0.028
DESIGN.hpt.Fl_O	5.224	1416.418	-2111.803	9.138	4.725	9.905	0.400	297.679	0.031
DESIGN.duct_hpt_lpt.Fl_	5.197	1416.418	-2111.803	9.140	4.701	9.905	0.400	297.679	0.031
DESIGN.lpt.Fl_O	0.428	848.073	-2921.621	9.200	0.386	9.905	0.400	233.824	0.287
DESIGN.duct_lpt_hrsg.Fl	0.425	848.073	-2921.621	9.201	0.384	9.905	0.400	233.824	0.288
DESIGN.hrsg.Fl_O	0.405	460.868	-3414.265	8.445	0.373	9.905	0.350	153.557	0.246
DESIGN.condenser.Fl_O	0.385	292.984	-4005.552	6.733	0.351	9.905	0.350	115.525	0.267
DESIGN.separator.Fl_O	0.385	292.880	-1725.034	7.208	0.369	8.308	0.300	101.415	0.187
DESIGN.nozz_core.Fl_O	0.385	292.880	-1725.034	7.208	0.260	8.308	1.000	312.617	0.078
DESIGN.duct_byp.Fl_O	0.583	292.959	-9.549	7.005	0.491	155.310	0.500	167.445	1.513
DESIGN.condenser_byp.Fl	0.559	330.466	28.163	7.138	0.487	155.310	0.450	160.736	1.810
DESIGN.nozz_bypass.Fl_O	0.559	330.466	28.163	7.138	0.295	155.310	1.000	332.725	1.249

COMPRESSOR PROPERTIES

Compressor	Wc [kg/s]	PR	eta_a	eta_p	Nc	pwr [MW]
DESIGN.fan	451.326	1.734	0.954	0.956	5041.160	-7.556
DESIGN.lpc	13.941	1.711	0.917	0.923	4627.640	-0.425
DESIGN.hpc	8.944	12.000	0.904	0.930	13423.028	-3.155

BURNER PROPERTIES

Burner	dPqP	TtOut [K]	Wfuel [kg/s]	FAR
DESIGN.burner	0.0400	1638.28	0.3179	0.03979

TURBINE PROPERTIES

Turbine	Wp [kg/s]	PR	eff_a	eff_p	Np	pwr [MW]
DESIGN.hpt	3.246	2.187	0.908	0.901	270.804	3.358
DESIGN.lpt	6.635	12.155	0.942	0.924	92.411	8.022

NOZZLE PROPERTIES

Nozzle	PR	Cv	Cfg	Ath [m2]	MNth	MNout	V [m/s]	Fg [kN]
DESIGN.nozz_core	1.613	N/A	0.993	0.078	1.000	1.000	312.617	2.855
DESIGN.nozz_bypass	2.346	N/A	0.993	1.249	1.000	1.000	332.725	58.706

SHAFT PROPERTIES

Shaft	Nmech	trqin [Nm]	trqout [Nm]	pwrin [MW]	pwrout [MW]
DESIGN.hp_shaft	14705.700	2180.551	-2048.591	3.358	-3.155
DESIGN.lp_shaft	4666.100	16416.542	-16334.459	8.022	-7.982

Bibliography

[1] International Energy Agency (IEA). *Aviation*. 2022. URL: https://www.iea.org/energy-system/transport/aviation.

[2] ICAO | Environment. *INNOVATION FOR A GREEN TRANSITION*. Tech. rep. ICAO, 2022, pp. 75–77.

[3] Volker Grewe et al. "Evaluating the climate impact of aviation emission scenarios towards the Paris agreement including COVID-19 effects". In: *Nature Communications 2021 12:1* 12.1 (June 2021), pp. 1–10. ISSN: 2041-1723. DOI: 10.1038/s41467-021-24091-y. URL: https://www.nature.com/articles/s41467-021-24091-y.

[4] M. Klöwer et al. "Quantifying aviation's contribution to global warming". In: *Environmental Research Letters* 16.10 (Nov. 2021), p. 104027. ISSN: 1748-9326. DOI: 10.1088/1748-9326/AC286E. URL: https://iopscience.iop.org/article/10.1088/1748-9326/ac286e%20https://iopscience.iop.org/article/10.1088/1748-9326/ac286e/meta.

[5] Frederico Afonso et al. "Strategies towards a more sustainable aviation: A systematic review". In: *Progress in Aerospace Sciences* 137 (Feb. 2023), p. 100878. ISSN: 0376-0421. DOI: 10.1016/J.PAEROSCI.2022.100878.

[6] Delft University of Technology. *Flying-V*. 2015. URL: https://www.tudelft.nl/en/ae/flying-v.

[7] Oliver Schmitz, Hermann Klingels, and Petra Kufner. "Aero Engine Concepts beyond 2030: Part 1-The Steam Injecting and Recovering Aero Engine". In: *Journal of Engineering for Gas Turbines and Power* 143.2 (Feb. 2021). ISSN: 15288919. DOI: 10.1115/1.4048985.

[8] Oliver Schmitz et al. "Aero Engine Concepts beyond 2030: Part 3-Experimental Demonstration of Technological Feasibility". In: *Journal of Engineering for Gas Turbines and Power* 143.2 (Feb. 2021). ISSN: 15288919. DOI: 10.1115/1.4048994.

[9] Regina Pouzolz, Oliver Schmitz, and Hermann Klingels. "Evaluation of the climate impact reduction potential of the water-enhanced turbofan (WET) concept". In: *Aerospace* 8.3 (Mar. 2021), pp. 1–12. ISSN: 22264310. DOI: 10.3390/aerospace8030059.

[10] Sascha Kaiser et al. "The Water-Enhanced Turbofan as Enabler for Climate-Neutral Aviation". In: *Applied Sciences (Switzerland)* 12.23 (Dec. 2022). ISSN: 20763417. DOI: 10.3390/app122312431.

[11] Peter N Atma, Andrew H R Lamkin, and Joaquim R R A Martins. "Comparing Hydrogen and Jet-A for a Ultra High-Bypass Turbofan with Water Recirculation." In: *AIAA AVIATION Forum* (June 2023). DOI: 10.2514/6.2023-4018. URL: http://arc.aiaa.org.

[12] Hamidreza Abedi et al. "Preliminary Analysis of Compression System Integrated Heat Management Concepts Using LH2-Based Parametric Gas Turbine Model". In: *Aerospace 2022, Vol. 9, Page 216* 9.4 (Apr. 2022), p. 216. ISSN: 2226-4310. DOI: 10.3390/AEROSPACE9040216. URL: https://www.mdpi.com/2226-4310/9/4/216/htm%20https://www.mdpi.com/2226-4310/9/4/216.

[13] Xiting Wang, Ai He, and Zhongzhi Hu. "Transient Modeling and Performance Analysis of Hydrogen-Fueled Aero Engines". In: *Processes 2023, Vol. 11, Page 423* 11.2 (Jan. 2023), p. 423. ISSN: 2227-9717. DOI: 10.3390/PR11020423. URL: https://www.mdpi.com/2227-9717/11/2/423/htm%20https://www.mdpi.com/2227-9717/11/2/423.

[14] Pratt & Whitney. *Hydrogen Steam and Inter-Cooled Turbine Engine (HySIITE)*. Nov. 2021. URL: https://arpa-e.energy.gov/technologies/projects/hydrogen-steam-and-inter-cooled-turbine-engine-hysite.

[15] Cranfield University and CORDIS EU. *ENABLEH2 H2020 project*. Sept. 2018. URL: https://www.enableh2.eu/.

[16] Alexander Görtz et al. "Water Enhanced Turbofan: Improved Thermodynamic Cycle Using Hydrogen as Fuel". In: *Volume 1: Aircraft Engine* (Sept. 2023). DOI: 10.1115/GT2023-100807. URL: https://dx.doi.org/10.1115/GT2023-100807.

[17] Colin F. McDonald et al. "Recuperated gas turbine aeroengines, part I: Early development activities". In: *Aircraft Engineering and Aerospace Technology* 80.2 (2008), pp. 139–157. ISSN: 00022667. DOI: 10.1108/00022660810859364/FULL/PDF.

[18] Colin F. McDonald et al. "Recuperated gas turbine aeroengines, part II: Engine design studies following early development testing". In: *Aircraft Engineering and Aerospace Technology* 80.3 (2008), pp. 280–294. ISSN: 00022667. DOI: 10.1108/00022660810873719/FULL/PDF.

[19] J. Privoznik Edward. *T63 REGENERATIVE ENGINE PROGRAM*. Tech. rep. Indianapolis: Allison Division - General Motors, May 1968.

[20] H. Grieb and B. Simon. "Pollutant emissions of existing and future engines for commercial aircraft". In: *Lecture Notes in Engineering* 60 (1990), pp. 43–83. ISSN: 01765035. DOI: 10.1007/978-3-642-51686-3{_}4/COVER. URL: https://link.springer.com/chapter/10.1007/978-3-642-51686-3_4.

[21] F. Yin and A. Gangoli Rao. "Performance analysis of an aero engine with inter-stage turbine burner". In: *Aeronautical Journal* 121.1245 (Nov. 2017), pp. 1605–1626. ISSN: 00019240. DOI: 10.1017/AER.2017.93.

[22] C. Salpingidou et al. "Thermodynamic analysis of recuperative gas turbines and aero engines". In: *Applied Thermal Engineering* 124 (2017), pp. 250–260. ISSN: 13594311. DOI: 10.1016/j.applthermaleng.2017.05.169.

[23] S. Pasini et al. "Heat recovery from aircraft engines". In: *35th Intersociety Energy Conversion Engineering Conference and Exhibit* (2000), pp. 546–553. DOI: 10.2514/6.2000-2901. URL: https://arc.aiaa.org/doi/10.2514/6.2000-2901.

[24] Guenter Wilfert et al. "Clean - Validation of a High Efficient Low NOx Core, a GTF High Speed Turbine and an Integration of a Recuperator in an Enviromental Friendly Engine Concept". In: *41st AIAA/ASME/SAE/ASEE Joint Propulsion Conference and Exhibit* (July 2005). DOI: 10.2514/6.2005-4195.

[25] Stefano Boggia and Klaus Rüd. "Intercooled Recuperated Gas Turbine Engine Concept". In: *41st AIAA/ASME/SAE/ASEE Joint Propulsion Conference and Exhibit* (July 2005). DOI: 10.2514/6.2005-4192.

[26] Nick Baker. "New Environmental Friendly Aero Engine Core Concepts". In: *newac.eu* (Jan. 2007). URL: https://www.academia.edu/16769881/New_Environmental_Friendly_Aero_Engine_Core_Concepts.

[27] J.P. van Buijtenen et al. *Aero Engine Technology AE4238*. Ed. by J.P. van Buijtenen, W. Visser, and A.G. Rao. 5th ed. Delft: Delft University of Technology, Aug. 2021.

[28] Konstantinos G. Kyprianidis et al. "Assessment of future aero-engine designs with intercooled and intercooled recuperated cores". In: *Journal of Engineering for Gas Turbines and Power* 133.1 (Jan. 2011). ISSN: 07424795. DOI: 10.1115/1.4001982/451225. URL: https://dx.doi.org/10.1115/1.4001982.

[29] Harald Schoenenborn et al. "Thermomechanical Design of a Heat Exchanger for a Recuperative Aeroengine". In: *Journal of Engineering for Gas Turbines and Power* 128.4 (Oct. 2006), pp. 736–744. ISSN: 0742-4795. DOI: 10.1115/1.1850510. URL: https://dx.doi.org/10.1115/1.1850510.

[30] Kyros Yakinthos et al. "Optimization of the design of recuperative heat exchangers in the exhaust nozzle of an aero engine". In: *Applied Mathematical Modelling* 31.11 (Nov. 2007), pp. 2524–2541. ISSN: 0307-904X. DOI: 10.1016/J.APM.2006.10.008.

[31] Dimitrios Missirlis et al. "Modeling an Installation of Recuperative Heat Exchangers for an Aero Engine". In: *Proceedings of the ASME Turbo Expo* 5 (Dec. 2010), pp. 281–289. DOI: 10.1115/GT2010-22263. URL: https://dx.doi.org/10.1115/GT2010-22263.

[32] A. Goulas et al. "Thermodynamics Cycle Analysis, Pressure Loss, and Heat Transfer Assessment of a Recuperative System for Aero-Engines". In: *Journal of Engineering for Gas Turbines and Power* 137.4 (Apr. 2015). ISSN: 15288919. DOI: 10.1115/1.4028584/373161. URL: https://dx.doi.org/10.1115/1.4028584.

[33] Christina Salpingidou et al. "Numerical modeling of heat exchangers in gas turbines using CFD computations and thermodynamic cycle analysis tools". In: *Chemical Engineering Transactions* 52 (2016), pp. 517–522. ISSN: 22839216. DOI: 10.3303/CET1652087.

[34] Z. Vlahostergios et al. "Efforts to improve aero engine performance through the optimal design of heat recuperation systems targeting fuel consumption and pollutant emissions reduction". In: *12th European Conference on Turbomachinery Fluid Dynamics and Thermodynamics, ETC 2017* (2017). DOI: 10.29008/ETC2017-356.

[35] Dimitrios Misirlis et al. "Optimization of Heat Exchangers for Intercooled Recuperated Aero Engines". In: *Aerospace 2017, Vol. 4, Page 14* 4.1 (Mar. 2017), p. 14. ISSN: 2226-4310. DOI: 10.3390/AEROSPACE4010014. URL: https://www.mdpi.com/2226-4310/4/1/14/htm%20https://www.mdpi.com/2226-4310/4/1/14.

[36] D. Misirlis et al. "INTERCOOLED RECUPERATED AERO ENGINE: DEVELOPMENT AND OPTIMIZATION OF INNOVATIVE HEAT EXCHANGER CONCEPTS". In: (2016).

[37] Florian Willi Jacob and V Sethi. "Performance and preliminary design of combined cycle aero engines utilising supercritical carbon dioxide". PhD thesis. 2018. URL: http://dspace.lib.cranfield.ac.uk/handle/1826/17432.

[38] H A Micak. "An introduction to the Kalina cycle". In: *International Joint Power Generation Conference*. American Society of Mechanical Engineers, New York, NY (United States), Dec. 1996. ISBN: 0-7918-1796-2.

[39] Christopher A. Perullo, Dimitri N. Mavris, and Eduardo Fonseca. "An integrated assessment of an organic Rankine cycle concept for use in onboard aircraft power generation". In: *Proceedings of the ASME Turbo Expo* 2 (2013). DOI: 10.1115/GT2013-95734.

[40] Luuk M.T. van Kleef, Oyeniyi A. Oyewunmi, and Christos N. Markides. "Multi-objective thermo-economic optimization of organic Rankine cycle (ORC) power systems in waste-heat recovery applications using computer-aided molecular design techniques". In: *Applied Energy* 251 (Oct. 2019), p. 112513. ISSN: 0306-2619. DOI: 10.1016/J.APENERGY.2019.01.071.

[41] Dabo Krempus et al. "On mixtures as working fluids of air-cooled ORC bottoming power plants of gas turbines". In: *Applied Thermal Engineering* 236 (Jan. 2024), p. 121730. ISSN: 1359-4311. DOI: 10.1016/J.APPLTHERMALENG.2023.121730.

[42] Piero Colonna et al. "Organic Rankine cycle power systems: A review". In: *ICOPE 2015 - International Conference on Power Engineering* (2015). DOI: 10.1299/JSMEICOPE.2015.12.E1.

[43] Khaled Zarati, Samer Maalouf, and Askin T. Isikveren. "Potential of the Bottom Organic Rankine Cycle to Recover Energy on Turboprop Engine Architecture". In: *ISABE*. Manchester, Sept. 2017. URL: https://www.researchgate.net/publication/319546494_Potential_of_the_Bottom_Organic_Rankine_Cycle_to_Recover_Energy_on_Turboprop_Engine_Architecture.

[44] G. E. Pateropoulos, T. G. Efstathiadis, and A. I. Kalfas. "Organic Rankine cycle for turboprop engine application". In: *The Aeronautical Journal* 125.1291 (Sept. 2021), pp. 1666–1686. ISSN: 0001-9240. DOI: 10.1017/AER.2021.32. URL: https://www.cambridge.org/core/journals/aeronautical-journal/article/organic-rankine-cycle-for-turboprop-engine-application/A8766E4C75EAF040D535CC7163827E9A.

[45] Momar Hughes and John Olsen. "Fuel Burn Reduction of Hybrid Aircraft Employing an Exhaust Heat Harvesting System". In: *Journal of Propulsion and Power* 38.2 (2022), pp. 241–253. ISSN: 15333876. DOI: 10.2514/1.B38393.

[46] Dabo Krempus et al. "ORC Waste Heat Recovery System for the Turboshaft Engines of Turbo-electric Aircraft". In: *Aerospace Europe Coference 2023 - 10th EUCASS*. 2023.

[47] Dabo Krempus et al. "Organic Rankine Cycle Waste Heat Recovery for Aircraft Auxiliary Power Units". In: 2022. URL: https://www.boeing.com/.

[48] C M De Servi et al. "EXPLORATORY ASSESSMENT OF A COMBINED-CYCLE ENGINE CONCEPT FOR AIRCRAFT PROPULSION". In: *Proceedings of the 1st Global Power and Propulsion Forum*. Jan. 2017.

[49] G. Angelino. "Carbon Dioxide Condensation Cycles For Power Production". In: *Journal of Engineering for Power* 90.3 (July 1968), pp. 287–295. ISSN: 0022-0825. DOI: 10.1115/1.3609190. URL: https://dx.doi.org/10.1115/1.3609190.

[50] Ladislav Vesely et al. "sCO2 Waste Heat Recovery System for Aircraft Engines". In: *AIAA Science and Technology Forum and Exposition, AIAA SciTech Forum 2022* (2022). DOI: 10.2514/6.2022-1407.

[51] Claire-Phonie Bury et al. "Impact of sCO2 Waste Heat Recovery System Air Cooler Integration on Aircraft Engine Thrust Performance". In: (Sept. 2023). DOI: 10.1115/GT2023-103166. URL: https://dx.doi.org/10.1115/GT2023-103166.

[52] Florian Jacob et al. "Performance of a supercritical CO2 bottoming cycle for aero applications". In: *Applied Sciences (Switzerland)* 7.3 (2017). ISSN: 20763417. DOI: 10.3390/APP7030255.

[53] Sam Yang and Juan C. Ordonez. "Aircraft weight reduction and onboard combined power cycle efficiency improvement—an integrative approach". In: *AIAA Aviation 2019 Forum* (2019), pp. 1–9. DOI: 10.2514/6.2019-3470.

[54] Pawel Ziolkowski, Knud Zabrocki, and Eckhard Müller. "TEG Design for Waste Heat Recovery at an Aviation Jet Engine Nozzle". In: *Applied Sciences 2018, Vol. 8, Page 2637* 8.12 (Dec. 2018), p. 2637. ISSN: 2076-3417. DOI: 10.3390/APP8122637. URL: https://www.mdpi.com/2076-3417/8/12/2637/htm%20https://www.mdpi.com/2076-3417/8/12/2637.

[55] B. Hånde and M. Førde. "Air Bottoming Cycle: Use of Gas Turbine Waste Heat for Power Generation". In: *Journal of Engineering for Gas Turbines and Power* 118.2 (Apr. 1996), pp. 359–368. ISSN: 0742-4795. DOI: 10.1115/1.2816597. URL: https://dx.doi.org/10.1115/1.2816597.

[56] T. Grönstedt and C. Xisto. "Conceptual design of ultra- efficient cores for mid-century aircraft turbine engines". In: (2019).

[57] Anders Lundbladh et al. "High Power Density Work Extraction from Turbofan Exhaust Heat". In: *ISABE-2015-20101* (2015). URL: https://research.chalmers.se/en/publication/229217.

[58] Guy Norris. *Pratt Outlines Hydrogen Steam-Injection Engine Concept*. Apr. 2022.

[59] Paul Ziegler, Sascha Kaiser, and Volker Gümmer. "Parametric Cycle Studies of the Water-Enhanced Turbofan Concept". In: *Proceedings of the ASME Turbo Expo* 5 (Sept. 2023). DOI: 10.1115/GT2023-100529. URL: https://dx.doi.org/10.1115/GT2023-100529.

[60] Alexander Görtz et al. "On the water enhanced turbofan concept: Part A - Thermodynamics and overall engine design". In: (2024). ISSN: 2958-4647.

[61] Jannik Häßy et al. "On the Water Enhanced Turbofan Concept: Part B - Flow Path and Mass Assessment". In: (2024). ISSN: 2958-4647.

[62] Gavin A. Schmidt et al. "Attribution of the present-day total greenhouse effect". In: *JGRD* 115.D20 (2010), p. D20106. ISSN: 0148-0227. DOI: 10.1029/2010JD014287. URL: https://ui.adsabs.harvard.edu/abs/2010JGRD..11520106S/abstract.

[63] Alistair Lloyd. "Thermodynamics of Chemically Recuperated Gas Turbines". PhD thesis. Princeton: Princeton University, Jan. 1991.

[64] J.H. Horlock and J.H. Horlock. "Chapter 6 – 'WET' GAS TURBINE PLANTS". In: *Advanced Gas Turbine Cycles* (2003), pp. 85–108. URL: http://www.sciencedirect.com:5070/book/9780080442730/advanced-gas-turbine-cycles.

[65] Robert J Stochl. *Assessment of steam-injected gas turbine systems and their potential application*. 1982.

[66] Joachim Kurzke and Ian Halliwell. "Propulsion and Power: An Exploration of Gas Turbine Performance Modeling". In: *Propulsion and Power: An Exploration of Gas Turbine Performance Modeling* (July 2018), pp. 1–755. DOI: 10.1007/978-3-319-75979-1/COVER.

[67] E. D. Larson and R. H. Williams. "Steam-Injected Gas Turbines". In: *Journal of Engineering for Gas Turbines and Power* 109.1 (Jan. 1987), pp. 55–63. ISSN: 0742-4795. DOI: 10.1115/1.3240006. URL: https://dx.doi.org/10.1115/1.3240006.

[68] J. B.W. Kok and E. A. Haselhoff. "Thermodynamic analysis of the thermal and exergetic performance of a mixed gas-steam aero derivative gas turbine engine for power generation". In: *Heliyon* 9.8 (Aug. 2023). ISSN: 24058440. DOI: 10.1016/j.heliyon.2023.e18927. URL: http://www.cell.com/article/S2405844023061352/fulltext%20http://www.cell.com/article/S2405844023061352/abstract%20https://www.cell.com/heliyon/abstract/S2405-8440(23)06135-2.

[69] David L. Daggett et al. *Water Injection on Commercial Aircraft to Reduce Airport Nitrogen Oxides*. 2010. URL: http://www.sti.nasa.gov.

[70] Oliver Krüger et al. "Large eddy simulations of hydrogen oxidation at ultra-wet conditions in a model gas turbine combustor applying detailed chemistry". In: *Journal of Engineering for Gas Turbines and Power* 135.2 (Feb. 2013). ISSN: 07424795. DOI: 10.1115/1.4007718/373367. URL: https://dx.doi.org/10.1115/1.4007718.

[71] A. G. Chen, Daniel J. Maloney, and William H. Day. "Humid Air NOx Reduction Effect on Liquid Fuel Combustion". In: *Journal of Engineering for Gas Turbines and Power* 126.1 (Jan. 2004), pp. 69–74. ISSN: 0742-4795. DOI: 10.1115/1.1615255. URL: https://dx.doi.org/10.1115/1.1615255.

[72] Sebastian Göke and Christian Oliver Paschereit. "Influence of steam dilution on NOx formation in premixed natural gas and hydrogen flames". In: *50th AIAA Aerospace Sciences Meeting Including the New Horizons Forum and Aerospace Exposition* (2012). DOI: 10.2514/6.2012-1272. URL: https://arc.aiaa.org/doi/10.2514/6.2012-1272.

[73] Marc Schmelcher et al. "Methods for the Preliminary Design of Heat Exchangers in Aircraft Engines". In: *Volume 5: Cycle Innovations* (Sept. 2023). DOI: 10.1115/GT2023-102959. URL: https://dx.doi.org/10.1115/GT2023-102959.

[74] Marc Schmelcher et al. "Integration of Heat Exchanger Models into the Performance Analysis of Innovative Aero Engine Architectures". In: ().

[75] Michal Nitulescu. *Steam generation and exhaust water recovery for the Water Enhanced Turbofan (WET) MERIM SAKIC*. Tech. rep. Gothenburg: Chalmers University of Technology, 2021.

[76] M.J.E.H. Muitjens. "Homogeneous condensation in a vapour/gas mixture at high pressures in an expansion cloud chamber". In: (1996). DOI: 10.6100/IR471316. URL: https://research.tue.nl/en/publications/homogeneous-condensation-in-a-vapourgas-mixture-at-high-pressures.

[77] Alexandre Capitao Patrao et al. "Compact heat exchangers for hydrogen-fueled aero engine intercooling and recuperation". In: *Applied Thermal Engineering* 243 (Apr. 2024), p. 122538. ISSN: 1359-4311. DOI: 10.1016/J.APPLTHERMALENG.2024.122538.

[78] Francesco Zonta, Cristian Marchioli, and Alfredo Soldati. "Particle and droplet deposition in turbulent swirled pipe flow". In: *International Journal of Multiphase Flow* 56 (Oct. 2013), pp. 172–183. ISSN: 0301-9322. DOI: 10.1016/J.IJMULTIPHASEFLOW.2013.06.002.

[79] Jia LI, Suyi HUANG, and Xiaomo WANG. "Numerical Study of Steam-Water Separators with Wave-type Vanes". In: *Chinese Journal of Chemical Engineering* 15.4 (Aug. 2007), pp. 492–498. ISSN: 1004-9541. DOI: 10.1016/S1004-9541(07)60114-1.

[80] S. Mhatre et al. "Electrostatic phase separation: A review". In: *Chemical Engineering Research and Design* 96 (Apr. 2015), pp. 177–195. ISSN: 0263-8762. DOI: 10.1016/J.CHERD.2015.02.012.

[81] Dah Yu Cheng. "The Distinction Between the Cheng and STIG Cycles". In: *Proceedings of the ASME Turbo Expo* 4 (Sept. 2008), pp. 101–116. DOI: 10.1115/GT2006-90382. URL: https://dx.doi.org/10.1115/GT2006-90382.

[82] Dah Yu Cheng and Albert L.C. Nelson. "The Chronological Development of the Cheng Cycle Steam Injected Gas Turbine During the Past 25 Years". In: *American Society of Mechanical Engineers, International Gas Turbine Institute, Turbo Expo (Publication) IGTI* 2 A (Feb. 2009), pp. 421–428. DOI: 10.1115/GT2002-30119. URL: https://dx.doi.org/10.1115/GT2002-30119.

[83] J.E. Penner et al. *Aviation and the Global Atmosphere*. Tech. rep. Cambridge: IPCC, 1999, p. 235.

[84] Melissa G. Michaud, Phillip R. Westmoreland, and Alan S. Feitelberg. "Chemical mechanisms of NOx formation for gas turbine conditions". In: *Symposium (International) on Combustion* 24.1 (Jan. 1992), pp. 879–887. ISSN: 0082-0784. DOI: 10.1016/S0082-0784(06)80105-0.

[85] Ulrich Schumann. *Aircraft Emissions*. Ed. by I. Douglas. Chichester, 2002.

[86] Bernd Kärcher. "Formation and radiative forcing of contrail cirrus". In: *Nature Communications 2018 9:1* 9.1 (May 2018), pp. 1–17. ISSN: 2041-1723. DOI: 10.1038/s41467-018-04068-0. URL: https://www.nature.com/articles/s41467-018-04068-0.

[87] Rebecca Dischl, Stefan Kaufmann, and Christiane Voigt. "Regional and Seasonal Dependence of the Potential Contrail Cover and the Potential Contrail Cirrus Cover over Europe". In: *Aerospace 2022, Vol. 9, Page 485* 9.9 (Aug. 2022), p. 485. ISSN: 2226-4310. DOI: 10.3390/AEROSPACE9090485. URL: https://www.mdpi.com/2226-4310/9/9/485/htm%20https://www.mdpi.com/2226-4310/9/9/485.

[88] Martin Schaeffer. "Methodologies for Aviation Emission Calculation - A comparison of alternative approaches towards 4D global inventories". PhD thesis. Berlin: DLR, May 2006.

[89] Anthony J. Colozza and Lisa Kohout. *Hydrogen Storage for Aircraft Applications Overview*. 2002. URL: http://www.sti.nasa.gov.

[90] Eytan J. Adler and Joaquim R.R.A. Martins. "Hydrogen-powered aircraft: Fundamental concepts, key technologies, and environmental impacts". In: *Progress in Aerospace Sciences* 141 (Aug. 2023), p. 100922. ISSN: 0376-0421. DOI: 10.1016/J.PAEROSCI.2023.100922.

[91] M. Anwar H. Khan et al. "The Emissions of Water Vapour and NOx from Modelled Hydrogen-Fuelled Aircraft and the Impact of NOx Reduction on Climate Compared with Kerosene-Fuelled Aircraft". In: *Atmosphere 2022, Vol. 13, Page 1660* 13.10 (Oct. 2022), p. 1660. ISSN: 2073-4433. DOI: 10.3390/ATMOS13101660. URL: https://www.mdpi.com/2073-4433/13/10/1660/htm%20https://www.mdpi.com/2073-4433/13/10/1660.

[92] Eric S. Hendricks and Justin S. Gray. "Pycycle: A tool for efficient optimization of gas turbine engine cycles". In: *Aerospace* 6.8 (Aug. 2019). ISSN: 22264310. DOI: 10.3390/AEROSPACE6080087.

[93] Justin Gray et al. *Thermodynamics of Gas Turbine Cycles with Analytic Derivatives in OpenMDAO*. 2016.

[94] Justin S. Gray et al. "OpenMDAO: an open-source framework for multidisciplinary design, analysis, and optimization". In: *Structural and Multidisciplinary Optimization* 59.4 (Apr. 2019), pp. 1075–1104. ISSN: 16151488. DOI: 10.1007/S00158-019-02211-Z/FIGURES/13. URL: https://link.springer.com/article/10.1007/s00158-019-02211-z.

[95] Tristan Hearn et al. *Optimization of Turbine Engine Cycle Analysis with Analytic Derivatives*. 2016.

[96] Sanford Gordon, Associates Cleveland, and Bonnie J Mcbride. *Computer program for calculation of complex chemical equilibrium compositions and applications. Part 1: Analysis*. 1994.

[97] Bonnie J. McBride, Michael J. Zehe, and Sanford Gordon. *NASA Glenn Coefficients for Calculating Thermodynamic Properties of Individual Species*. 2002. URL: http://www.sti.nasa.gov.

[98] Tufan Akba, Derek K. Baker, and M. Pınar Mengüç. "Off-design performance of micro-scale solar Brayton cycle". In: *Energy Conversion and Management* 289 (Aug. 2023), p. 117187. ISSN: 0196-8904. DOI: 10.1016/J.ENCONMAN.2023.117187.

[99] Filippo Rubechini et al. "The impact of gas modeling in the numerical analysis of a multistage gas turbine". In: *Journal of Turbomachinery* 130.2 (Apr. 2008). ISSN: 0889504X. DOI: 10.1115/1.2752187/451546. URL: https://dx.doi.org/10.1115/1.2752187.

[100] Mahmoud El-Soueidan et al. "Integration of a Gas Model Into Computational Fluid Dynamics Analysis for the Simulation of Turbine Exhaust Flows With High Steam Loads". In: *Journal of Engineering for Gas Turbines and Power* 146.3 (Mar. 2024). ISSN: 15288919. DOI: 10.1115/1.4063687/1169138. URL: https://dx.doi.org/10.1115/1.4063687.

[101] Stewart Youngblood. "Design and Testing of a Liquid Nitrous Oxide and Ethanol Fueled Rocket Engine". PhD thesis. URL: https://www.researchgate.net/publication/286916356_Design_and_Testing_of_a_Liquid_Nitrous_Oxide_and_Ethanol_Fueled_Rocket_Engine.

[102] W. Wagner and A. Pruß. "The IAPWS Formulation 1995 for the Thermodynamic Properties of Ordinary Water Substance for General and Scientific Use". In: *Journal of Physical and Chemical Reference Data* 31.2 (June 2002), pp. 387–535. ISSN: 0047-2689. DOI: 10.1063/1.1461829. URL: /aip/jpr/article/31/2/387/241937/The-IAPWS-Formulation-1995-for-the-Thermodynamic.

[103] Hans Joachim Kretzschmar and Wolfgang Wagner. "International steam tables: Properties of water and steam based on the industrial formulation IAPWS-IF97". In: *International Steam Tables: Properties of Water and Steam based on the Industrial Formulation IAPWS-IF97* (Apr. 2019), pp. 1–380. DOI: 10.1007/978-3-662-53219-5.

[104] W. Wagner et al. "The IAPWS industrial formulation 1997 for the thermodynamic properties of water and steam". In: *Journal of Engineering for Gas Turbines and Power* 122.1 (Jan. 2000), pp. 150–180. ISSN: 07424795. DOI: 10.1115/1.483186.

[105] R B Dooley. "The International Association for the Properties of Water and Steam". In: (2007). URL: http://www.iapws.org..

[106] Daniel Beysens. "The Physics of Dew, Breath Figures and Dropwise Condensation". In: Lecture Notes in Physics 994 (2022). DOI: 10.1007/978-3-030-90442-5. URL: https://link.springer.com/10.1007/978-3-030-90442-5.

[107] W.M. Haynes. *CRC Handbook of Chemistry and Physics*. CRC Press, June 2014. ISBN: 9780429170195. DOI: 10.1201/B17118. URL: https://www.taylorfrancis.com/books/mono/10.1201/b17118/crc-handbook-chemistry-physics-william-haynes.

[108] O.A. Alduchov and R.E. Eskridge. "Improved Magnus form approximation of saturation vapor pressure". In: *Journal of Applied Meteorology* 35.4 (1996), pp. 601–609.

[109] Wolfgang Wagner and A. Pruss. "International Equations for the Saturation Properties of Ordinary Water Substance. Revised According to the International Temperature Scale of 1990. Addendum to J. Phys. Chem. Ref. Data 16, 893 (1987)". In: *Journal of Physical and Chemical Reference Data* 22.3 (May 1993), pp. 783–787. ISSN: 0047-2689. DOI: 10.1063/1.555926. URL: /aip/jpr/article/22/3/783/241647/International-Equations-for-the-Saturation.

[110] Daniel Dias et al. "Consistency of Water Vapour Pressure and Specific Heat Capacity Values for Modelling Clay-Based Engineered Barriers". In: *Applied Sciences 2023, Vol. 13, Page 3361* 13.5 (Mar. 2023), p. 3361. ISSN: 2076-3417. DOI: 10.3390/APP13053361. URL: https://www.mdpi.com/2076-3417/13/5/3361/htm%20https://www.mdpi.com/2076-3417/13/5/3361.

[111] *Water — CoolProp 6.6.0 documentation*. URL: http://www.coolprop.org/fluid_properties/fluids/Water.html.

[112] E. M. Greitzer, C. S. Tan, and M. B. Graf. "Internal Flow: Concepts and Applications". In: *Internal Flow* (Apr. 2004). DOI: 10.1017/CBO9780511616709. URL: https://www.cambridge.org/core/books/internal-flow/14285A6FF068386CF4A1EBBA835319DE.

[113] Rui Xu et al. *Thermochemical Properties of Jet Fuels*. Tech. rep. Stanford University, 2015.

[114] Tim Edwards. "Reference jet fuels for combustion testing". In: *AIAA SciTech Forum - 55th AIAA Aerospace Sciences Meeting* (2017). DOI: 10.2514/6.2017-0146. URL: https://arc.aiaa.org/doi/10.2514/6.2017-0146.

[115] Donald R Jr. Burgess and Anthony Hamins. *Heats of Combustion and Related Properties of Pure Substances*. Technical Note (NIST TN), National Institute of Standards and Technology, Gaithersburg, MD, Aug. 2023. DOI: https://doi.org/10.6028/NIST.TN.2126. URL: https://tsapps.nist.gov/publication/get_pdf.cfm?pub_id=935736.

[116] F. Beltrame et al. "Reduced Order Modelling of Optimized Heat Exchangers for Maximum Mass-Specific Performance of Airborne ORC Waste Heat Recovery Units". In: *Proceedings of the 7th International Seminar on ORC Power System (ORC 2023)* (2024), pp. 563–573. DOI: 10.12795/9788447227457{_}93. URL: https://research.tudelft.nl/en/publications/reduced-order-modelling-of-optimized-heat-exchangers-for-maximum-.

[117] Ian H. Bell et al. "Pure and pseudo-pure fluid thermophysical property evaluation and the open-source thermophysical property library coolprop". In: *Industrial and Engineering Chemistry Research* 53.6 (Feb. 2014), pp. 2498–2508. ISSN: 08885885. DOI: 10.1021/IE4033999.

[118] Sebastian Herrmann, Hans Joachim Kretzschmar, and Donald P. Gatley. "Thermodynamic Properties of Real Moist Air, Dry Air, Steam, Water, and Ice (RP-1485)". In: *HVAC&R Research* 15.5 (2009), pp. 961–986. ISSN: 10789669. DOI: 10.1080/10789669.2009.10390874. URL: https://www.tandfonline.com/doi/abs/10.1080/10789669.2009.10390874.

[119] *Aspen Plus | Leading Process Simulation Software | AspenTech*. URL: https://www.aspentech.com/en/products/engineering/aspen-plus.

[120] Avellaneda Chavez. *cfm international CFM56-3 TRAINING MANUAL EFFECTIVITY CFMI PROPRIETARY INFORMATION*. URL: https://www.academia.edu/8851546/cfm_international_CFM56_3_TRAINING_MANUAL_EFFECTIVITY_CFMI_PROPRIETARY_INFORMATION.

[121] "OWNER'S & OPERATOR'S GUIDE: CFM56-3 SERIES". In: ().

[122] Sebastian Samuelsson, Tomas Gronstedt, and Konstantinos G. Kyprianidis. "Consistent Conceptual Design and Performance Modeling of Aero Engines". In: *Proceedings of the ASME Turbo Expo* 3 (Aug. 2015). DOI: 10.1115/GT2015-43331. URL: https://dx.doi.org/10.1115/GT2015-43331.

[123] Merijn Rembrandt van Holsteijn, Arvind Gangoli Rao, and Feijia Yin. "Operating Characteristics of an Electrically Assisted Turbofan Engine". In: *Proceedings of the ASME Turbo Expo* 1 (Jan. 2021). DOI: 10.1115/GT2020-15355. URL: https://dx.doi.org/10.1115/GT2020-15355.

[124] Mark D Guynn et al. "Refined Exploration of Turbofan Design Options for an Advanced Single-Aisle Transport". In: (2011). URL: http://www.sti.nasa.gov.

[125] Tomas Grönstedt et al. "Multidisciplinary assessment of a year 2035 turbofan propulsion system". In: *33rd Congress of the International Council of the Aeronautical Sciences*. Vol. 7. 2022, pp. 4981–4990. URL: https://research.chalmers.se,.

[126] Jack D. Mattingly, William H. Heiser, and David T. Pratt. *Aircraft Engine Design, Second Edition*. Reston ,VA: American Institute of Aeronautics and Astronautics, Jan. 2002. ISBN: 978-1-56347-538-2. DOI: 10.2514/4.861444.

[127] CFM. *LEAP Overview*. Tech. rep. 2017. URL: https://www.cfmaeroengines.com/wp-content/uploads/2017/09/Brochure_LEAPfiches_2017.pdf.

[128] D. Krempus. "Organic Rankine Cycle Waste Heat Recovery Systems for Aircraft Engines". In: (2025). DOI: 10.4233/UUID:5E565F99-A9F4-4208-95E9-2C542FD720F8. URL: https://research.tudelft.nl/en/publications/organic-rankine-cycle-waste-heat-recovery-systems-for-aircraft-en.